Imaging of Magnetic Nanoparticles using Magnetoelectric Sensors

Dissertation

zur Erlangung des akademischen Grades eines

Doktors der Ingenieurswissenschaften (Dr.-Ing.)

eingereicht an der

Technischen Fakultät

der Christian-Albrechts-Universität zu Kiel

vorgelegt von

Ron-Marco Friedrich

aus Kiel

Kiel, 2022

Ron-Marco Friedrich

Ph.D. Dissertation

submitted to obtain the degree of: Dr. Ing.

Technische Fakultät

Lehrstuhl für Materialverbunde

Christian-Albrechts-Universität zu Kiel

Faculty of Engineering

Chair for Multicomponent Materials

Kiel University

Kaiserstrasse 2

24143 Kiel

Germany

www.tf.uni-kiel.de

First examiner/Examination Committee member: **Professor Franz Faupel**, Chair for Multicomponent Materials, Faculty of Engineering, Christian-Albrechts-Universität zu Kiel

Second examiner/Examination Committee member: **Professor Gerhard Schmidt**, Digital Signal Processing and System Theory, Faculty of Engineering, Christian-Albrechts-Universität zu Kiel

Date of oral defense:

August 1, 2022

Abstract

Imaging of magnetic nanoparticles offers a variety of promising medical applications for therapeutics and diagnostics. Using magnetic nanoparticles as tracer material for imaging allows for the non-invasive detection of spatial distributions of nanoparticles that can give information about diseases or can be used in preventive medicine. Imaging biodistributions of magnetically labeled cells offers applicability for tissue engineering, as a means to monitor cell growth within artificial scaffolds non-destructively.

In the presented work, the capabilities of an imaging system for magnetic nanoparticles via magnetoelectric sensors are investigated. The investigated technique, called Magnetic Particle Mapping, is based on the detection of the nonlinear magnetic response of magnetic nanoparticles. A resonant magnetoelectric sensor is used for frequency selective measurements of the nanoparticles magnetic response.

Extensive modeling was performed that enabled proper imaging of magnetic nanoparticle distributions. Fundamental limitations of the imaging system were derived to describe resolution in correspondence to signal-to-noise ratios. Incorporation of additional parameters in the imaging system for the data analysis resulted in an algorithm for a more robust reconstruction of spatial particle distributions, increasing its imaging capabilities.

Experimental investigations of the imaging system show the capabilities for imaging of cell densities using magnetically labeled cells. Furthermore, resolution limitations were investigated and differentiation of different particle types in imaging was shown, referred to as "colored" imaging.

The imaging of biodistributions of magnetically labeled cells thus enable exciting perspectives on further research and possible applications in tissue engineering.

Zusammenfassung

Die Bildgebung von Verteilungen magnetischer Nanopartikel bietet eine große Auswahl an vielversprechenden medizinischen Anwendungen für die Therapeutik und Diagnostik. Die Verwendung von magnetischen Nanopartikeln als Tracermaterial für die Bildgebung ermöglicht die nicht-invasive Detektion von Verteilungen von Nanopartikeln, welche Informationen zu Krankheiten liefern bzw. in der präventativen Medizin genutzt werden kann. Bildgebende Verfahren für Verteilungen magnetisch markierter Zellen bietet die Möglichkeit in dem Gebiet des *Tissue Engineerings* das Wachstum von Zellverteilungen in artifiziellen Zellgerüsten nicht-destruktiv zu überwachen und zu bewerten.

In der vorliegenden Arbeit werden die Eigenschaften eines neuartigen bildgebenden Systems für magnetische Nanopartikel mittels magnetoelektrischer Sensoren untersucht. Die zu untersuchende Methode nennt sich *Magnetic Particle Mappging* und basiert auf der Detektion der nichtlinearen magnetischen Antwort der magnetischen Nanopartikel. Resonante magnetoelektrische Sensoren werden für frequenzselektive Messungen der magnetischen Nanopartikelantwort genutzt.

Umfangreiche Modellierungen des bildegebenden Systems werden ausgeführt, welche die korrekte Bildgebung von magnetischen Nanopartikeln ermöglichen. Fundamentale Limitierungen des Systems zur Beschreibung der Auflösung in Abhängigkeit der Signalstärke werden hergeleitet. Weiterhin wird durch die Berücksichtigung zusätzlicher Parameter des bildgebenden Systems ein Algorithmus entwickelt, welcher mit einer deutlich robusteren Rekonstruktion der räumlichen Partikelverteilung einhergeht, wodurch die Bildgebung verbessert wird.

Experimentelle Untersuchungen des bildegebenden Systems zeigen die Möglichkeit zur Bildgebung von Zelldichten mittels magnetisch markierter Zellen. Des Weiteren werden die Auflösungsgrenzen aufgezeigt und die Möglichkeit zur Bildgebung unterschiedlicher Partikelarten wird experimentell bewiesen.

Die so gezeigte Bildgebung von magnetisch markierterten Zellen bietet spannende Perspektiven in Hinsicht auf weitere Forschung und mögliche Anwendungen im *Tissue Engineering*.

Declaration of Authorship

This doctoral dissertation was prepared at the Department of Engineering at Kiel University (Christian-Albrechts-Universität zu Kiel) in fulfillment of the requirements for acquiring the degree of Dr.-Ing in Materials Science and Engineering.

I hereby declare that, apart from my supervisor's guidance, I authored and composed the content and design of this thesis and the respective research independently.

This work complies with the Rules of Good Scientific Practice of the German Research Foundation.

All content and ideas drawn directly or indirectly from external sources are clearly indicated. This thesis has not been published or submitted to any other examining body and all related research items that have been composed and published in peer-reviewed journals are clearly indicated as such.

I declare that no academic degree has been withdrawn from me.

Kiel, August 31, 2022

Ron-Marco Friedrich

Contents

Abstract

Zusammenfassung

Declaration of Authorship

Contents i

Acknowledgements v

Mathematical Notation vii

Abbreviations ix

Latin Symbols xi

Greek Symbols xv

List of Figures xvii

List of Tables xxiii

1 Introduction 1

1.1 Motivation and Scope of the Thesis 1

1.2 Structure of the Thesis 2

2 Theoretical Background and State of the Art 5

2.1 Magnetoelectric Sensors 5

2.2 Magnetic Nanoparticles 10

2.3 Imaging Systems for Magnetic Nanoparticles 17

2.4 Magnetoelectric Sensors for Detecting Magnetic Nanoparticles 21

3 Magnetic Particle Mapping **23**
3.1 Introduction . . . 23
3.2 Forward Modeling . . . 25
3.3 Inverse Problem . . . 35
3.4 Model Estimation . . . 45
3.5 Resolution Limits . . . 62
3.6 Summary . . . 67

4 Simulation **69**
4.1 Introduction . . . 69
4.2 Magnetic Particle Mapping . . . 70
4.3 Colored Magnetic Particle Mapping . . . 72
4.4 Model Estimation . . . 76
4.5 Resolution . . . 84
4.6 Resolution in Depth Imaging . . . 86

5 Experimental Investigation **93**
5.1 Objectives . . . 93
5.2 Experimental Setup, Sensor and Calibration . . . 94
5.3 Particle Characterization . . . 99
5.4 Imaging Cell Distributions . . . 101
5.5 Colored Magnetic Particle Mapping . . . 109
5.6 Resolution and Limitations . . . 116
5.7 Summary . . . 125

6 Conclusion and Outlook **127**
6.1 Conclusion . . . 127
6.2 Outlook . . . 128

A Appendix A **131**
A.1 Multicriteria Problem . . . 131
A.2 Projection onto L2 ball . . . 131
A.3 Projection onto L1 ball . . . 133
A.4 Projection into Nonnegative Orthant . . . 133
A.5 Projection into a Box . . . 134
A.6 Projection into a Cone . . . 134

B Appendix B **137**
B.1 Sensor Behavior 137
B.2 Fitting a Single Dipole 145

List of Publications **149**

Bibliography **151**

Acknowledgements

I would like to give many thanks to my Doktorvater, Prof. Franz Faupel, for giving me the opportunity to engage in this interesting research topic during my time as a PhD and the research environment in his group and the Collaborative Research Center 1261. He always had open doors for problems and he guided me through his supervision, while also giving me freedom to pursue many interesting things related to my research. The possibility to take part in teaching the Solid State Physics via the lectures and exercises gave me deepened insight to many areas of science and made me able to present complex topics with ease. Many thanks, Franz.

The work done in this thesis was part of the Collaborative Research Center 1261 "Biomagnetic Sensing" via the project B7, funded by the German Research Foundation and thanks goes to them for funding the project.

To Dr. Bill Brook Shurtleff, with whom I was always talking about anything. Through our discussions we both were able to sort our thoughts regarding our research. He could mentor me in many things due to his experience before coming back to the university. I have gained a close friend whose friendship I do not want to miss. Thank you.

I want to thank Dipl.-Ing. Stefan Rehders for his help in designing and building the setup used in this thesis. He was always very supportive and his insight to details made my research much easier. His calm and kind demeanor was always pleasant to work with. Thank you for your help.

Thanks to Dr. Jan-Martin Wagner, who was of great help during my time of my master's thesis. Due to his intricate guidance of writing, he has made a lasting effect on my approach to write. This has helped me throughout my thesis. Much thanks to you.

To Dr. Sebastian Zabel, who initially proposed this thesis project, and being my supervisor during my Master thesis. Without him, I would not have done this project for my PhD. Thank you.

To Benjamin Spetzler, whose outstanding drive for scientific understanding resulted in many interesting discussions regarding our PhD topics. Rambling about ideas lead

to deeper insight and questions that needed to be answered. Thank you.

Thanks goes to Dr. Nils Lukat, who always came up with new ideas, and working together with him in this project.

To Prof. Gerhard Schmidt for always having an open door to discuss current projects and problems.

To Wiebke Reichstein for continuous support during our studies and PhD hardships.

To all people in the Collaborative Research Center with whom I had the luck to talk and work with. And to the rest of the group and technical faculty who I may have forgotten.

Mathematical Notation

Notational conventions help the reader to quickly determine whether a given quantity is a scalar, vector or matrix. These conventions are not standardized and must therefore be explicitly mentioned beforehand.

In this thesis, the following conventions will be used:

Scalars

Scalar quantities are given in normal letters (Greek and Latin). They can be either uppercase or lowercase letters.

Vectors

Vectors are given in lowercase bold letters, e.g. $\boldsymbol{a}$. Some exceptions are given for physical quantities such as the magnetic field $\boldsymbol{H}_{\mathrm{m}}$, but this will be clear from the context.
Indexing of vectors is given by lowercase letters and the positional subscript starting from 1. For example the ith component in the vector $\boldsymbol{a}$ is a_i.
Unit vectors are given with an additional hat, i.e. $\hat{\boldsymbol{e}}$.
A vector in $\mathbb{R}^n$ with all ones or zeros is given as $\mathbf{1}_n$ or $\mathbf{0}_n$.
The transpose vector of $\boldsymbol{a}$ is denoted $\boldsymbol{a}^\intercal$.
An inner product of two vectors is given by $\boldsymbol{a}^\intercal\boldsymbol{a}$ and an outer product as $\boldsymbol{a}\boldsymbol{a}^\intercal$.

Matrices

Matrices are given in uppercase bold letters, e.g. $\boldsymbol{A}$.
Identity matrices in $\mathbb{R}^{n\times n}$ are given with the appropriate subscript $\boldsymbol{I}_{n\times n}$.
A matrix $\boldsymbol{A} \in \mathbb{R}^{m\times n}$ can be understood as a collection of vectors $\boldsymbol{a}_j \in \mathbb{R}^m$ where the subscript is $j = 1, \ldots, n$. Explicit indexing of individual entries in the matrix is given by two subscripts ij, denoting the ith row and jth column, i.e. a_{ij}.
The Kronecker matrix product is indicated by the operator $\otimes$.

Abbreviations

AC	Alternating Currents.
ACS	AC Susceptometry.
BLS	Biomagnetic Liver Susceptometry.
CC	Correlation Coefficient.
CRC	Collaborative Research Center.
DBS	Deep Brain Stimulation.
DC	Direct Current.
EFC	Electric Frequency Conversion.
EPR	Electron Paramagnetic Resonance.
FFL	Field Free Line.
FFP	Field Free Point.
FFT	Fast Fourier Transform.
FWHM	Full Width Half Maximum.
GD	Gradient Descent.
ISTA	Iterative Soft Thresholding.
LOD	Limit of Detection.
LTI	Linear Time-Invariant.
MAT	Magneto Acoustic Tomography.

ME	Magnetoelectric.
MFC	Magnetic Frequency Conversion.
MMOCT	Magnetomotive Optical Coherence Tomography.
MNP	Magnetic Nanoparticle.
MPI	Magnetic Particle Imaging.
MPM	Magnetic Particle Mapping.
MPS	Magnetic Particle Spectrometry.
MRI	Magnetic Resonace Imaging.
MRX	Magnetorelaxometry.
MRXI	Magnetorelaxometry Imaging.
MSI	Magnetic Susceptibility Imaging.
MSPM	Magnetic Susceptibility Particle Mapping.
NMR	Nuclear Magnetic Resonance.
NN	Nonnegativity.
NP-hard	Non-Deterministic Polynomial-Time hard.
nSMI	nonlinear Susceptibility Magnitude Imaging.
OCT	Optical Coherence Tomography.
PBS	Phosphate-Buffered Saline.
PMMA	Poly(methyl methacrylate).
PSF	Point-Spread-Function.
sASI	Spectroscopic AC Susceptibility Imaging.
SLNB	Sentinel Lymph Node Biopsy.
SMI	Susceptibility Magnitude Imaging.
SMPS	Scanning Magnetic Particle Spectrometry.
SNR	Signal-To-Noise Ratio.
SQUID	Superconduction Quantum Interference Device.
SVD	Singular Value Decomposition.
TSVD	Truncated Singular Value Decomposition.
TV	Total Variation.

Latin Symbols

a	Damping Term of Resonator.
a_i	Complex Prefactors that describe Particle Responses.
$\boldsymbol{A}$	Model Matrix.
$\boldsymbol{A}^{\dagger}$	Pseudoinverse of $\boldsymbol{A}$.
$\boldsymbol{A}_k^{\dagger}$	Approximate Pseudoinverse of $\boldsymbol{A}$.
$\boldsymbol{A}_c$	Concatenation of Model Matrices.
$\boldsymbol{A}_{\mathrm{B}}$	Block Matrix Containing all Model Matrices.
$\boldsymbol{A}_{\mathrm{D}}$	Magnetic Vector Potential.
b	Restoring Term of Resonator.
$\boldsymbol{b}$	Magnetic Field from MNP Distribution (Discrete).
B	Magnetic Flux Density.
B_{D}	Projected Magnetic Dipole Field.
B_{m}	Projected Magnetic Field at Measurement Position $\boldsymbol{r}_{\mathrm{m}}$.
$\boldsymbol{B}$	Magnetic Flux Density (Vector).
$\boldsymbol{B}_{\mathrm{D}}$	Magnetic Dipole Field.
$\boldsymbol{B}_{\mathrm{m}}$	Magnetic Field at Measurement Position $\boldsymbol{r}_{\mathrm{m}}$.
c_i	Weighting Factors.
C_{D}	Projected Magnetic Dipole Field.
$\boldsymbol{C}$	Linear Combination of Model Matrices.
d_{core}	Magnetic Core Diameter.
d_{hydro}	Hydrodynamic Diameter.
$\boldsymbol{D}$	Matrix Containing Magenetic Field of MNP Distribution for different Projections.

$\hat{\boldsymbol{e}}_i$	Unit Vector.
E	Electric Field.
f	Frequency [Hz].
f_r	Resonance Frequency.
f_1	First Resonance Frequency.
f_2	Second Resonance Frequency.
$f(\boldsymbol{r}_\mathrm{m})$	Background Voltage Signal at Measurement Position $\boldsymbol{r}_\mathrm{m}$.
$\boldsymbol{f}$	Function Values of Magnetic Dipole Field for Parameters $\boldsymbol{\beta}$.
$\boldsymbol{F}$	Concatenation of Criteria for Data Fitting.
h_{ij}	Dipole Field Geometry Functions.
H	Magnetic Field.
$\boldsymbol{H}$	Dipole Field Geometry Matrix.
$\boldsymbol{H}_\mathrm{P}$	Polar Part of the Dipole Field Geometry Matrix.
$\boldsymbol{H}_\mathrm{m}$	Magnetic Field (Vector).
i	Index.
$\boldsymbol{I}$	Identity Matrix.
j	Index, Imaginary Unit.
$\boldsymbol{J}$	Jacobian.
k	Iteration Index.
k_B	Boltzmann Constant.
K	Number of Iterations for Gradient Descent.
L	Langevin Function.
$\mathcal{L}$	Lagrangian.
$\boldsymbol{L}$	Matrix for Regularization.
m	Magnetic Moment.
$\boldsymbol{m}$	Magnetic Moment (Vector).
$\hat{\boldsymbol{m}}$	Unit Vector of $\boldsymbol{m}$.
M	Magnetization.

M_s	Saturation Magnetization.
$\boldsymbol{M}$	Magnetization (Vector), Matrix for the Deviation to the Mean of a Vector.
$\boldsymbol{M}_{ij}$	Matrix Containing Magenetic Field of MNP Distribution for different Projections.
n	Integer.
$\boldsymbol{n}$	Fixed Direction of MNP.
$\boldsymbol{q}_i$	Vectors Containing Particle Responses in $\boldsymbol{Q}$.
Q	Quality Factor, Periodic Function in Hill Differential Equation.
$\boldsymbol{Q}$	Matrix Containing Particle Responses.
r	Spatial Distance.
r_{eq}	Equisurface of the Magnetic Dipole Field.
$\boldsymbol{r}$	Spatial Position.
$\boldsymbol{r}_{\mathrm{m}}$	Measurement Position.
$\boldsymbol{R}_k$	Resolution Matrix for Iteration k.
$\boldsymbol{R}_{\mathrm{GD},k}$	Resolution Matrix for GD and Iteration k.
$\boldsymbol{R}_{\mathrm{SVD},k}$	Resolution Matrix for SVD and Iteration k.
$\boldsymbol{s}$	Sensitivity Axis of ME Sensor.
$\hat{\boldsymbol{s}}$	Unit Vector of $\boldsymbol{s}$.
S	Sensor Geometry PSF.
$\boldsymbol{S}$	Diagonal Matrix Containing Singular Values σ_i from SVD.
t	Time.
T	Temperature.
$\boldsymbol{u}_i$	Left Singular Vectors from SVD.
U	Substition Function for y.
$\boldsymbol{U}$	Unitary Matrix Containing Left Singular Vectors $\boldsymbol{u}_i$ from SVD.
v	Sensor Voltage at Measurement Position $\boldsymbol{r}_{\mathrm{m}}$, L^1-Norm Estimate of $\boldsymbol{x}$.
v_i	Sensor Voltage at Measurement ith Measurement Position.

$\boldsymbol{v}_i$	Right Singular Vectors from SVD.
V	Volume.
$\boldsymbol{V}$	Unitary Matrix Containing Right Singular Vectors $\boldsymbol{v}_i$ from SVD.
x	Spatial x-Coordinate.
$\boldsymbol{x}$	Magnetic Particle Distribution (Discrete).
$\boldsymbol{x}_{\text{true}}$	Ground Truth Magnetic Particle Distribution.
$\boldsymbol{x}_{\text{recon}}$	Reconstructed Magnetic Particle Distribution.
$\boldsymbol{x}_c$	Concatenation of MNP Distributions of Different Types.
$\boldsymbol{x}_{\text{P}_1}$	MNP Distributions of Particle Type 1.
$\boldsymbol{x}_{\text{P}_2}$	MNP Distributions of Particle Type 2.
$\boldsymbol{x}_{\boldsymbol{Q}}$	Nonnegative Projection of Magnetic Particle Distribution for Different Particle Types.
y	Spatial y-Coordinate, Amplitude of Resonator.
$\boldsymbol{y}$	Nonnnegative Weight Vector.
z	Spatial z-Coordinate.
Z	Substition Function for y.

Greek Symbols

α	Step Size for Gradient Descent.
α_{ME}	Magnetoelectric Coefficient.
β	Step Size for Gradient Descent.
$\boldsymbol{\beta}$	Parameters of Single Magnetic Dipole.
δ	Noise Standard Deviation.
$\boldsymbol{\delta}$	Optimal Update via Levenberg–Marquardt.
ϵ	Amplitude for Relative Change in Resonance Frequency.
η	Phase Scaling Factor, Parameter for Discepancy Principle.
θ_m	Polar Angle of Magnetic Moment $\boldsymbol{m}$.
θ_s	Polar Angle of Sensitive Axis $\boldsymbol{s}$.
$\boldsymbol{\theta}$	Parameters within Model Matrix $\boldsymbol{A}$.
λ	Magnetostrictive Strain, Regularization Parameter, Lagrange Multiplier.
$\boldsymbol{\lambda}$	Description of Supporting Hyperplane for Feasible Set in Multicriteria Problem.
μ_0	Vacuum Permeability.
ξ	Langevin Parameter.
ρ	Magnetic Particle Distribution (Continuous).

σ	Stress.
σ_i	ith Singular Value from SVD.
$\boldsymbol{\sigma}$	Vector Containing Singular Values σ_i from SVD.
τ	Relaxation Time.
τ_{eff}	Effective Relaxation Time.
τ_{B}	Brownian Relaxation Time.
τ_{N}	Néel Relaxation Time.
$\varphi_{\lambda,i}$	Filter Factors for Tikhonov Regularization.
φ_m	Elevation Angle of Magnetic Moment $\boldsymbol{m}$.
φ_s	Elevation Angle of Sensitive Axis $\boldsymbol{s}$.
Φ	Cost Function.
χ	Magnetic Susceptibility.
χ'	Real Part of Magnetic Susceptibility.
χ''	Imaginary Part of Magnetic Susceptibility.
χ_0	Static Magnetic Susceptibility.
Ψ	Magnetic Dipole PSF of Sensor with Geometry S.
ω	Frequency [rad/s], Radius of Euclidean Ball.
ω_0	Resonance Frequency of a Resonator.
Ω	Spatial Domain of MNP.

List of Figures

2.1 The interrelations for the magnetoelectric effect. The direct ME effect is indicated by a dashed line. The indirect effect is shown as the relationship of the magnetic field to the strain, which turns via mechanical coupling to stress in the piezoelectric material, where it induces a polarization. Redrawn from [6] 6

2.2 Left: Photo of ME sensor of the cantilever type used in this thesis (taken from [15]). Right: Simulated frequency response of a resonator for a Q factor of 1000 8

2.3 Magnetic frequency conversion shown for an input spectrum (left), that is fed through a nonlinear function. As a result, frequency mixing occurs and combinations of the input frequencies are present (right). The spectrum is shown for a quadratic nonlinearity. Redrawn from [5] 10

2.4 Magnetic nanoparticle with biocompatible coating. The MNP consists of a magnetic core, which is coated via a shell. The magnetic core has a diameter of d_{core}, while the whole particle has a hydrodynamic diameter of d_{hydro}. Image redrawn from [30] 11

2.5 Langevin function that shows the nonlinear magnetization behavior of MNP (solid blue line). The dashed line indicates the linear response around the origin. To visualize the effect of a larger magnetic field on the MNP ensembles, the reorientation of the magnetic moments is shown above the plot for different magnetic field strengths. The periodic arrangement of the MNP does not hold meaning. Redrawn from [2] 12

2.6 Brownian and Néel relaxation mechanisms. For Néel relaxation, the magnetization $\boldsymbol{M}$ in the MNP core rotates. For Brownian relaxation, the whole MNP rotates (indicated by a fixed directional vector $\boldsymbol{n}$ for the MNP), aligning with an external field $\boldsymbol{B}$. Redrawn from [36] 13

2.7 Debye relaxation of the MNP. As the frequency approaches the relaxation frequency τ^{-1}, the real part of the magnetic susceptiblity begins to decrease monotonically. At the relaxation frequency, the imaginary part has a maximum, indicating the largest energy dissipation. The reason is that the MNP cannot follow the magnetic fields direction anymore and lag behind 15
2.8 Generation of higher harmonic excitations due to magnetic nonlinearity . . . 16

3.1 Schematic concept for the MPM measurement approach 24
3.2 Equisurface of the magnetic dipole field for different moment directions . . . 27
3.3 Equisurfaces of the magnetic dipole field for different moment directions, cut at a distance z from the dipole 28
3.4 The magnetic dipole field projections for different magnetic moment orientations 29
3.5 Proximal gradient method schematic 40
3.6 Sparsification via L^1 norm compared to L^2 norm regularization 41
3.7 Phase responses of MNP types 44
3.8 Cone in the complex plane in which the coefficients x_i have to lie 45
3.9 Derivative of matrix $\boldsymbol{A}$ with respect to the vector $\boldsymbol{\theta}$ yields a 3D matrix (tensor) 47
3.10 Box constraint on the possible model parameters. The feasible set C is the shaded box 48
3.11 The individual model matrices corresponding to the different combinations of magnetic moment direction and sensitive axis direction refer to different PSFs for the imaging system 50
3.12 The measurement $\boldsymbol{b}$ is estimated to lie in a 3-dimensional subspace spanned by the estimates for the field projections in the x-, y- and z-directions, i.e. $\boldsymbol{A}_{31}\boldsymbol{x}$, $\boldsymbol{A}_{32}\boldsymbol{x}$ and $\boldsymbol{A}_{33}\boldsymbol{x}$. We thus need to find a point on a sphere of radius $\|\boldsymbol{b}\|$ 54
3.13 The matrix consisting of all quadratic forms shows the correlation between different magnetic field components for different moment directions 57
3.14 Estimating the correct distance z of the sensor to the sample involves the successive decrease of the z distance such that, at some distance, the measured data $\boldsymbol{b}$ can be closely approximated, thus yielding a lower residual norm $\|\boldsymbol{A}\boldsymbol{x} - \boldsymbol{b}\|$. This follows from allowing higher spatial frequencies (from the model $\boldsymbol{A}_z$) to be incorporated in the estimate $\boldsymbol{A}_z\boldsymbol{x}$ 59
3.15 Integration of the dipole field projection yields a nonnegative function with finite L_1 norm, which is proportional to the magnetic moment producing the field 61

3.16 The columns of the resolution matrix $\boldsymbol{R}_k$ tells about the spread of a delta-like input, which can be thought of as the Point-Spread-Function of the system. For the inverse operator for different iterations k, the resolution matrix attains a more delta-like response, which means that the spread is reduced and that the resolution is enhanced 66

4.1 MNP reference distribution used for simulations and reconstructions 71

4.2 Correlation coefficient (CC) and relative error of total magnetic moment of the reconstructions for gradient descent (GD) and gradient descent with nonnegativity constraint (GD+NN). Noise level is set to 30dB and error bars are given from the standard deviation from 30 repeats 72

4.3 Reconstruction of the simulated colored MPM signal from two different MNP types 74

4.4 Correlation coefficient for the reconstructions for different MNP phase responses for several SNRs. Top: Colored MPM is performed such that an additional projection $\mathcal{P}_+^{\boldsymbol{Q}}$ is used for the enforcement of a nonnegativity constraint. The colored images can be extracted from a transformation via $\boldsymbol{Q}^{-1}$ and taking the real and imaginary parts to distinguish both MNP types. Bottom: Reconstruction with no constraints 75

4.5 Quantification accuracy and correlation coefficient as a function of the choice of model for the reconstruction 78

4.6 Adaptive reconstruction to iterate the MNP distribution $\boldsymbol{x}$ and the sensitive axis $\boldsymbol{s}$ simultaneously. Shown are individual iterations as denoted in the upper left corner of each subplot. In the lower right corner of each subplot the estimated sensitive axis direction (polar) is shown. The ground truth for this axis has an angle of $\varphi_m = 0°$. The black color indicates MNPs and the red lines are level sets to guide the eye 80

4.7 Correlation coefficient for different initial sensitive axis directions. The true sensitive axis lies in the x direction. For the upper half space ($z \geq 0$), the correlation coefficients form a sphere, indicating that the algorithm converges to the true MNP distribution. For the lower half plane, there are regions where the right MNP distribution is not found via the algorithm 81

4.8 Top: Correlation coefficient of the reconstruction to the ground truth. Middle: Angle error of the magnetic dipole direction. Bottom: Angle error of the sensitive axis direction. All points in the graph are results for a different combination of an initial dipole field direction, indicated by angles θ_m (polar) and φ_m (elevation), and sensitive axis directions, indicated by angles θ_s (polar) and φ_s (elevation) 83

4.9 Achievable resolution for TSVD and GD techniques as a function of SNR for a 2D system with a) 1 mm sensor distance and b) 2 mm sensor distance . . 85

4.10 Schematic setup for a depth imaging system 87

4.11 Contribution strength of each point in the source domain for different sensor positions for homogeneous magnetic field H in x-direction. The sensor sensitive axis is in y-direction. a) Sensor (as shown in red) is at a 0° angle to the circular MNP domain, yielding an antisymmetric contribution from all points in the MNP domain. b) Sensor (as shown in red) is at a 45° angle to the circular MNP domain, yielding a symmetric contribution from all points in the MNP domain 88

4.12 Point-Spread-Functions for different SNR and radial parameters of the source domain for $\boldsymbol{x}$ for the 45° system 89

4.13 Point-Spread-Functions and the radial dimension along the peak value for different SNR and radial position of the source domain for $\boldsymbol{x}$ 90

5.1 Experimental setup for MPM measurements 95

5.2 Sensor resonance frequency response and noise density measurements 97

5.3 MPS measurements effective magnetic moments from the MNP, shown as hysteresis loops 100

5.4 MPS measurements of the effective magnetic moments from the MNP, shown as spectra 101

5.5 MPS measurements of the third harmonic of the effective magnetic moments from the MNP 102

5.6 MPM measurements of the magnetic fields of the cell droplet 104

5.7 a) MPM reconstruction of magnetically labeled cells and b) light microscopy image of same cell distribution. c) MPM reconstruction of magnetically labeled where the cell droplet has been smeared out. Comparing with the light microscopy image in c), the darker regions indicate higher densities of cells (enclosed red circle). The region containing bubbles (yellow circle) is of lower cell density. Because the cell densities are directly proportional to the strength of a measurable magnetic signal, an MPM reconstruction should reflect the regions mentioned here 107
5.8 Sample holder for colored MPM measurements 110
5.9 Field amplitude dependent phase response of measured signal 112
5.10 Measured voltage signals from the magnetic fields of the MNP distribution . 113
5.11 Reconstructions of MNP distributions for the colored MPM measurements . 114
5.12 Sample types for MPM measuerements 118
5.13 Determination of spatial resolution for a 2D MPM imaging system 119
5.14 Determination of temporal resolution for the MPM imaging system 120
5.15 MNP quantification measurements via MPM 121
5.16 Multiple MPM measurements of the same sample measured in succession . . 122

A.1 Multicriteria problem visualized via its feasible set. The optimal points are given by the supporting hyperplanes describe by nonnegative vectors $\boldsymbol{\lambda}$ . . . 132

B.1 AC susceptiblity measurement of the magnetoelectric sensor 140
B.2 Measured *harmonic* frequency response of the ME sensor 142
B.3 Parametric resonance for Mathieu's equation and a magnetoelectric sensor . 144
B.4 Cost function over a region containing a magnetic source measured by a set of sensors 147

List of Tables

3.1 List of different projection operators for the implementation of constrained optimization 42

5.1 Sensor parameters from sensitivity calibration 97
5.2 List of particle data and MPS values measured at 2.5 kHz for 10 mTμ_0^{-1} . . 101
5.3 Estimated directions of the sensor's sensitive axis $\hat{\boldsymbol{s}}$ and the excited magnetic moments direction $\hat{\boldsymbol{m}}$ from the sample 105
5.4 Estimated directions of the sensors sensitive axis $\hat{\boldsymbol{s}}$ and the excited magnetic moments direction $\hat{\boldsymbol{m}}$ for the colored MPM experiment 114

List of Algorithms

1 Nonnegative ISTA 42
2 Colored Magnetic Particle Mapping 45
3 ISTA and Model Estimation 49
4 Model Estimation For Sensitive Axis 51
5 Model Estimation 56

CHAPTER 1

Introduction

1.1 Motivation and Scope of the Thesis

Magnetic Nanoparticles (MNPs) are used in medical and biotechnological applications. The magnetic properties of the MNPs are exploited to detect their presence in various ways. Especially imaging of MNPs shows great potential in the medical context of therapeutics and diagnostics. They are used in magnetic resonance imaging as a contrast agent, for hyperthermia in cancer therapy, or in targeted drug delivery[1]. Another application is in Magnetic Particle Imaging (MPI) systems that are able to visualize blood flow using MNPs as tracers[2]. Additionally, MNPs can be used for Sentinel Lymph Node Biopsy (SLNB) for cancer detection. The localization and imaging of MNPs is paramount for the efficacy of the intended application.

Another possible direction for imaging MNPs is in tissue engineering of bioscaffolds. Three-dimensional bioscaffolds hold promise for generating implantable tissue replacement[3]. Homogeneous growth within the bioscaffold is important for this kind of application and has to be ensured. Conventional methods of investigating cell growth in such scaffold materials is highly time consuming and are destructive in nature. Furthermore, if the scaffold materials are non-transparent, light microscopy approaches are not able to image cell distributions. The use of MNP-labeled cells opens up the possibility to measure the magnetic response of the MNPs from which in turn the cell distribution can be inferred. For this, proper imaging is essential and the system description needs to be able to correctly infer the distribution from the data.

To be able to measure the magnetic signal of the MNPs, sensitive magnetometers have to be used. One possible choice is magnetoelectric (ME) sensors, which are based on composites containing piezoelectric and magnetostrictive materials. Depending on the structure of these sensors, they can exhibit mechanical resonances that amplify the sensitivity of the sensors. In this way, very small magnetic fields can be measured.

In this thesis a scanning-type MNP imaging system based on resonant magnetoelectric sensors is developed for a process called Magnetic Particle Mapping (MPM). The

MNPs are magnetically excited into the nonlinear regime, and a mechanical resonance of the sensor is used for frequency selective sensing of the MNP response. The MNP response is mapped in space using the ME sensor in a scanning apparatus and the underlying MNP distribution is imaged by using a model of the imaging system. The MPM system in this thesis is the first ME sensor-based MNP imaging system of its kind to be presented in the literature. The content of this thesis deals with the description and experimental investigation of the capabilities of such an imaging system.

1.2 Structure of the Thesis

The present thesis develops a model for the MPM imaging system is developed. Here, the reader is guided through the tools and considerations necessary for a proper understanding of the system description and data analyses. Subsequently, simulations of the imaging system are performed to derive fundamental limitations of the imaging system. The model is then experimentally validated and the capabilities of the imaging system are determined.

The contents of the individual chapters are given in the following.

The second chapter gives an overview of ME sensors, MNPs and imaging methods for MNPs. Also current literature of MNP sensing via ME sensors is highlighted.

The third chapter deals with developing a forward model for the MPM imaging system that relates the spatial MNP distribution to the measurable magnetic field. Using the forward model, an inversion algorithm will be developed to determine the MNP distribution from the measured data. The model will be generalized to account for additional parameters within the forward model. Important parameters such as resolution will be derived. General limitations of such an imaging system will also be shown. Additionally, colored MPM will be developed that permits the detection and imaging of different magnetic responses from the MNPs.

The fourth chapter deals with simulation of the developed model and estimation of the MNP distribution from the simulated data. The applicability of the derived algorithm will be shown. The resolution limitations of the imaging system will be simulated. Furthermore, the requirements for colored MPM will be explored.

In the fifth chapter, the MPM system will be experimentally investigated with respect to achievable resolution for two dimensional systems, minimum detectable amounts of MNPs, temporal resolutions, the ability for colored MPM imaging and the applicability

for the detection of magnetically labeled cells.

The thesis ends with a conclusion of the MPM imaging system and directions for future research.

CHAPTER 2

Theoretical Background and State of the Art

In this Chapter, the theoretical groundwork for magnetoelectric (ME) sensors and magnetic nanoparticles (MNPs) will be set. Furthermore, imaging of MNP will be discussed with respect to its numerous imaging systems and their respective signal acquisition schemes.

2.1 Magnetoelectric Sensors

Composite magnetoelectric sensors are able to measure magnetic fields by converting these to voltage signals via a mechanical coupling between magnetostrictive and piezoelectric materials. Interesting for the sensing application is the use of a mechanical resonator structure for such sensors, because it enables the amplification of signals near its resonance frequency. These sensors are able to measure magnetic fields with very high sensitivity and have limit of detections (LOD) in the pT range (tabulated overview given in [4] page 15). To enable frequency conversions of magnetic field signals to the resonance, modulation techniques are used. As such, ME sensors are promising to be used for biomagnetic sensing applications. This section deals with the description of ME sensors and gives an overview of the readout schemes for signal acquisition.

2.1.1 Magnetoelectric Effect

The ME effect describes the ability to convert magnetic field signals to voltage signals. Here, the effect can be categorized into the direct and indirect ME effect. The former describes an intrinsic ME effect of a single-phase material, whereas the latter describes the ME effect of a material compound. The difference between them is shown in Figure 2.1 [5], [6]. The direct ME effect is able to generate a polarization from a magnetic field as

a single phase material[7]. However, the direct ME effect is small due to impeding properties necessary for a large effect related to ferromagnetism and ferroelectricity[8]. To circumvent this, one can turn to composite materials where a mechanical effect is taken as an intermediary, i.e. a magnetostrictive response becomes coupled to a piezoelectric response via a mechanical coupling. Here, a magnetic field induces a magnetostrictive response, which in turn induces a polarization from a mechanical strain in a piezoelectric material. This way, an indirect ME effect can be much larger than the direct ME effect[9]. Especially if the mechanical coupling is enhanced from the mechanical resonance of the sensor. This is the case for cantilever type ME sensors, which are used throughout this thesis[10]. The magnetoelectric coefficient α_{ME} describes the conversion

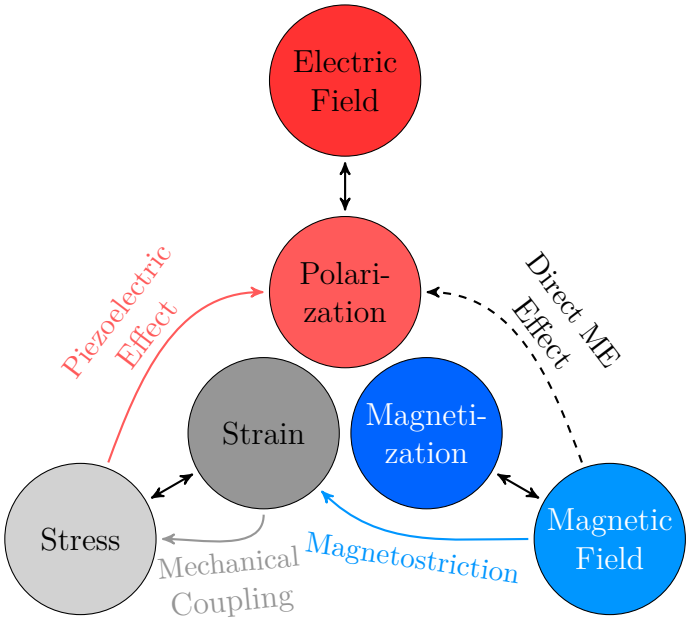


Figure 2.1: The interrelations for the magnetoelectric effect. The direct ME effect is indicated by a dashed line. The indirect effect is shown as the relationship of the magnetic field to the strain, which turns via mechanical coupling to stress in the piezoelectric material, where it induces a polarization. Redrawn from [6].

of the magnetic field H to the electric field E via the magnetostrictive strain λ and the induced stress σ[7], [11]:

$$\alpha_{\mathrm{ME}} = \frac{\partial E}{\partial \sigma}\frac{\partial \sigma}{\partial \lambda}\frac{\partial \lambda}{\partial H} \tag{2.1}$$

It is the proportionality between a supplied magnetic field to the resulting voltage. From the equation it can be seen that the ME coefficient is directly proportional to the slope of the $\lambda - H$ magnetostriction curve. The magnetostriction curve is directly proportional to the square of magnetization $\lambda \propto M^2$ (c.f. [12]) and hence, to yield a large ME coefficient, one needs to employ a magnetic bias field to shift the working point. This can be done via a supplied external magnetic field, or use the exchange bias effect to internalize this bias, as done in [13], [14].

2.1.2 Mechanical Resonance

The mechanical structure of the ME sensors enables the occurrences of resonances, which are able to store energy in form of oscillations at certain frequencies — the resonance frequencies. The limiting factor of the amount of energy that can be stored, is energy dissipation from damping within the system, e.g. viscous losses from air, clamping losses or heating losses within the substrate[15]. As a figure of merit, the quality factor Q determines the amount of damping for the resonator, as its inverse is related to the damping. The type of ME sensors used in this thesis exhibit large Q-factors of about 1000 in ambient conditions and more than 2-3 times that in vacuum[15]. The Q-factor in turn indicates the bandwidth of the resonator, and if the Q-factors are large, the bandwidth is small. This way, the ME sensors experience only a narrow bandwidth for the resonance, usually about 10 Hz for the type of sensors in this thesis. The bandwidth can be estimated from the resonance frequency and the Q-factor via

$$\Delta f = \frac{f_r}{Q}. \tag{2.2}$$

The sensors used in this thesis have a resonance frequency of about 7.5 kHz, and a Q factor of 1000 amounts to a bandwidth of 7.5 Hz. An exemplary image of the sensor and a resonance curve for a Q factor of 1000 can be seen in Figure 2.2. These ME sensors are extremely selective with respect to the frequency of signals. If the signal matches the resonance frequency, this signal becomes massively amplified, making it attractive to be able to exploit this resonance for sensing applications. This poses challenges on the operation of the sensors. To measure magnetic fields at low frequencies, one needs to perform frequency conversions such that these signals can be read within the resonance of the sensor. For this, one can employ frequency conversion techniques[5]. These approaches will be explained further below.

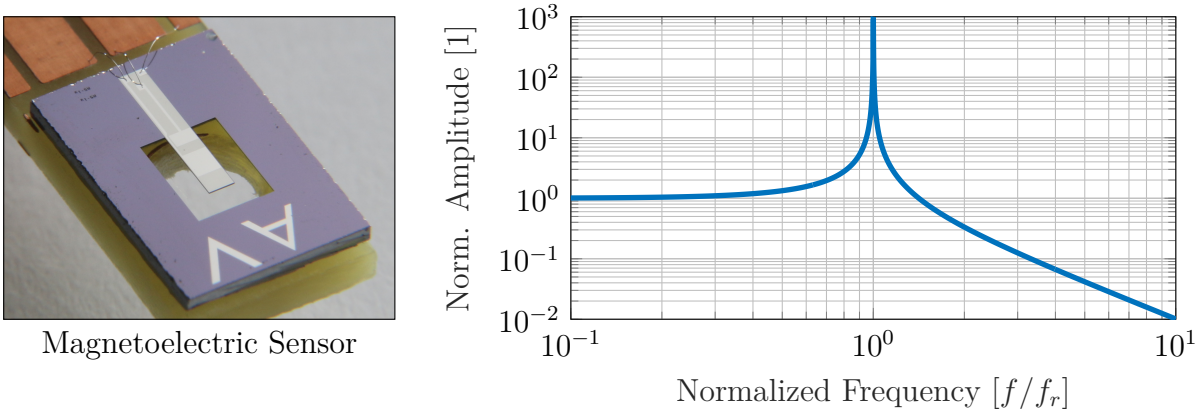


Figure 2.2: Left: Photo of ME sensor of the cantilever type used in this thesis (taken from [15]). Right: Simulated frequency response of a resonator for a Q factor of 1000.

2.1.3 Readout Schemes

This section is an overview of the readout schemes for cantilever ME sensors. The previously mentioned frequency conversions for ME sensors will be discussed as well as direct detection at the resonance frequency of the sensor. While the ME sensor offers a great variety in readout schemes, one has to consider that these are not exclusive of each other. This means that all effects can take place for a measurement. An elaborate source for a discussion on readout schemes can be found in [5].

2.1.3.1 Direct Measurement

The most straightforward way to use the ME sensor and its mechanical resonance is to measure magnetic fields whose frequencies are at the resonance frequency of the sensor. This way, the signal becomes directly amplified by the resonator. This can be beneficial for applications where the magnetic field frequencies can be chosen arbitrarily. Another example for direct detection is the localization of coils from sensor measurements, or the localization of sensors from a set of measurements [16]. Also, in the topic of this thesis, the frequency of signals can be adjusted to match the resonance of the sensor[17] for imaging applications for MNP.

2.1.3.2 Electric Frequency Conversion

To be able to measure low frequency magnetic fields, one needs to employ techniques that convert those low frequency signals to near resonance frequency. One way to achieve this is the electric frequency conversion (EFC). This is done via the application of a strong voltage pump signal. This causes a strain for the piezoelectric material, which in turn is coupled mechanically to the magnetostrictive layer. Due to the magnetoelastic effect, the magnetization of the magnetostrictive material changes as a function of strain[18], [19]. This can cause frequency mixing with low frequency magnetic fields, which can in turn couple into the resonance, given that the pump signal is of appropriate frequency.

2.1.3.3 Frequency Conversion via ΔE Effect

Another related frequency conversion method uses the so called ΔE effect[20], [21]. For this, one can employ the fact that the sensor itself is magnetic. The sensor changes its properties ever so slightly from the magnetic signal that one wishes to measure. This is expressed via a change in resonance frequency, because the magnetostrictive material either stiffens or softens mechanically, therefore detuning the sensor from its original resonance frequency. This detuning can then be used to modulate a supplied small voltage carrier via the electrodes. For this, the sensor is driven via a voltage signal near resonance. The detuning modulates this carrier and, as a result, side bands form around the carrier frequency, which can then couple into the resonance of the sensor. This way, low frequency magnetic fields can be detected.

2.1.3.4 Magnetic Frequency Conversion

A different way to measure low frequency magnetic fields is using a magnetic pump signal[22]–[24]. The pump signal is applied near resonance of the sensor and frequency mixing occurs due to the nonlinear magnetostriction curve. The working point changes periodically and is expressed via a nonlinear function of the magnetic input fields. This way, combinations of the pump signal frequency ω_2 and a signal to be measured with frequency ω_1 occur, as is shown exemplary in Figure 2.3 for a quadratic nonlinearity[5]. A low frequency magnetic field can thereby be measured via the resonance of the sensor. This readout scheme also highlights the inherent nonlinearity of the sensor due to the nonlinear magnetostriction for larger magnetic excitation. While the sensor shows a linear sensitivity for many orders of magnitude[25], the linear sensitivity does not show

the nonlinearity in terms of frequency conversion, because only a harmonic response is measured. Only at larger amplitudes it begins to deviate in the linear (harmonic) sensitivity, in [26] it was about 600 µT and in [27] in the range of a few µT for ambient conditions. Driving the sensor magnetically with large amplitudes shows the formation of higher harmonic excitations[26], [28], which in turn also implies the occurnence of parametric resonances. Furthermore, the sensors nonlinearity is then also expressed in nonlinear resonances, leading to softening and hardening frequency responses (see Appendix B.1.2). As a result, in circumstances where a frequency conversion is not wanted, one has to consider this effect and minimize it accordingly.

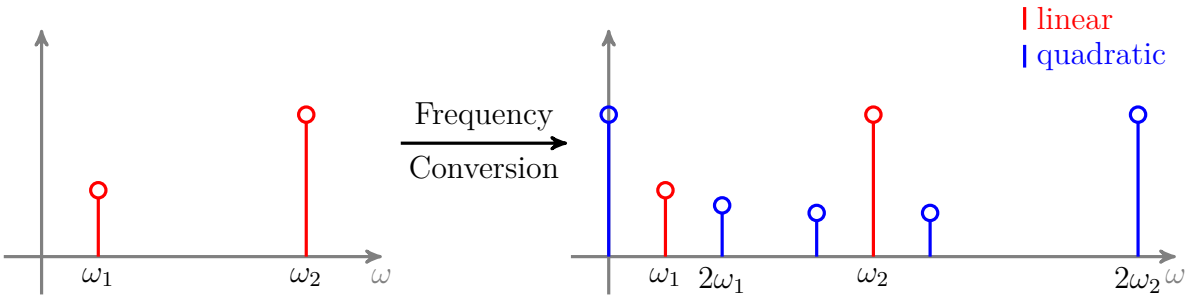


Figure 2.3: Magnetic frequency conversion shown for an input spectrum (left), that is fed through a nonlinear function. As a result, frequency mixing occurs and combinations of the input frequencies are present (right). The spectrum is shown for a quadratic nonlinearity. Redrawn from [5].

2.2 Magnetic Nanoparticles

Magnetic Nanoparticles (MNP), in particular iron oxide-based nanoparticles, offer the possibility to be used in clinical interventions, due to their biocompatibility[2]. MNP are based on a magnetic core, which is covered by a coating, which aims to functionalize the particle for various environments, while also preventing the agglomeration to other MNP by reducing particle-particle interactions. Figure 2.4 shows a schematic of such a MNP. It has to be noted that multi-core MNP are also available[29]. The size of the core of the particles is usually about 1-100 nm[2]. The magnetic core of the MNP possess a large magnetic moment, due to a single domain state. This way, MNP ensembles act paramagnetic with a very high magnetic susceptibility. The magnetic behavior can be described (in a static environment) via the Langevin theory of paramagnetism[12]. The

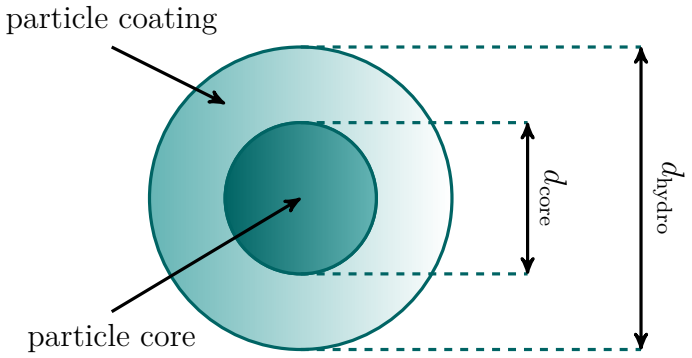


Figure 2.4: Magnetic nanoparticle with biocompatible coating. The MNP consists of a magnetic core, which is coated via a shell. The magnetic core has a diameter of d_{core}, while the whole particle has a hydrodynamic diameter of d_{hydro}. Image redrawn from [30].

magnetization is given by the Langevin function $L(\xi)$:

$$\frac{M}{M_s} = L(\xi) = \coth(\xi) - \frac{1}{\xi} \tag{2.3}$$

With ξ being the Langevin parameter related to the MNP (intrinsic and environmental) properties, such as magnetic moment m, temperature T and the applied magnetic field H:

$$\xi = \frac{\mu_0 m H}{k_{\text{B}} T} \tag{2.4}$$

Here, μ_0 denotes the vacuum permeability and k_{B} the Boltzmann constant. An exemplary plot of the Langevin function and the corresponding rearrangement of magnetic moments towards a magnetic field H is shown in Figure 2.5. The magnetic moment m is given by the total volume V (related to core diameter d_{core}) of the magnetic core and its saturation magnetization M_s:

$$m = V M_s \tag{2.5}$$

$$V = \frac{1}{6}\pi d_{core}^3 \tag{2.6}$$

The nonlinearity of the MNP behavior is used for many detection schemes, as will be described further below. The MNP ensembles show no remanent magnetization in a zero field environment. This means that if the MNPs experience a magnetic field,

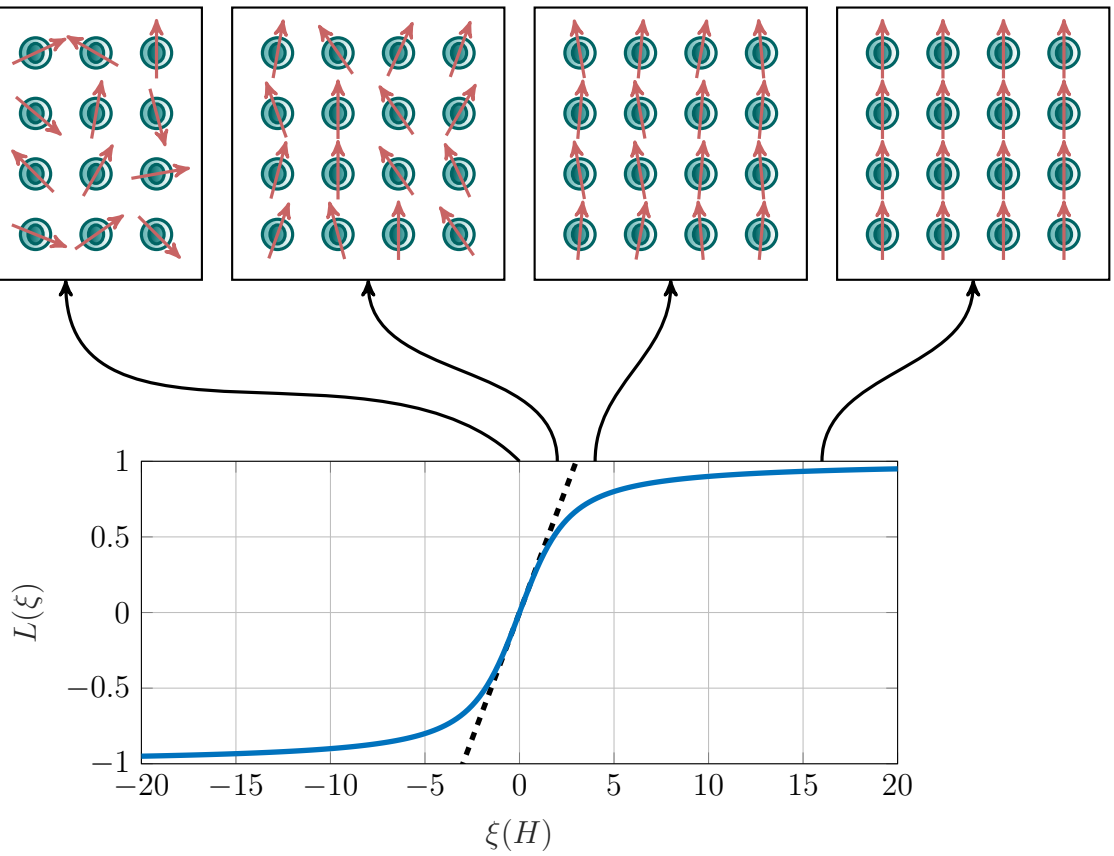


Figure 2.5: Langevin function that shows the nonlinear magnetization behavior of MNP (solid blue line). The dashed line indicates the linear response around the origin. To visualize the effect of a larger magnetic field on the MNP ensembles, the reorientation of the magnetic moments is shown above the plot for different magnetic field strengths. The periodic arrangement of the MNP does not hold meaning. Redrawn from [2].

which is subsequently switched off, the ensemble will lose all net magnetization. The time scale of this process is given by the *relaxation time* τ. There are two relaxation mechanisms responsible for this, the Brownian relaxation and Néel relaxation[31], [32]. The relaxation mechanisms are shown in Figure 2.6, where the Brownian relaxation is given by the timescale for rotation of the MNP to a magnetic field to yield an equilibrium. Néel relaxation is given by the timescale where the magnetization is rotating towards the field. If no field is applied, the magnetization may spontaneously flip. However, these relaxation mechanisms are themselves functions of the dynamic magnetic field (strength) and, to be able to describe this, one needs to employ, for example, solving the Fokker-Planck-Equation. Therefore, the description for such systems is much more

complex and demanding, see [33] for further information. The relaxation properties of the MNP can be used for imaging techniques, where MNP types are imaged separately from each other[34], [35].

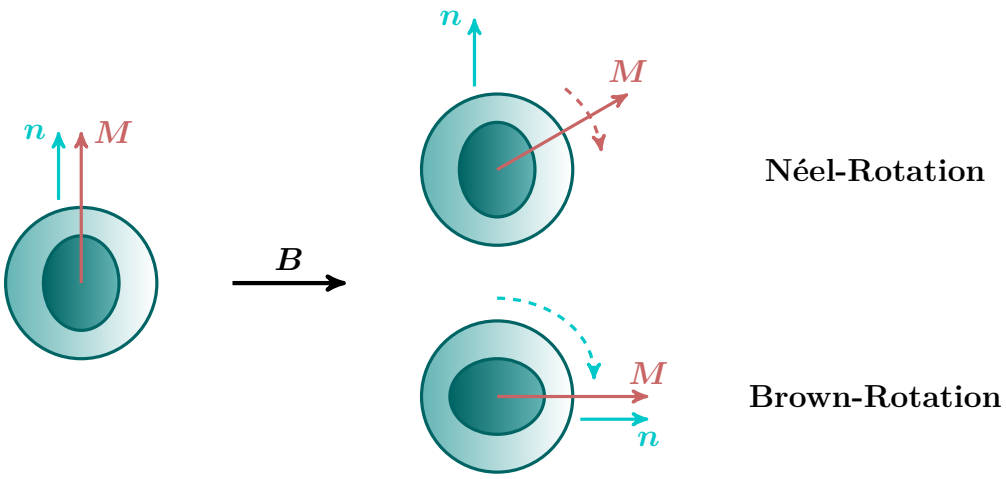


Figure 2.6: Brownian and Néel relaxation mechanisms. For Néel relaxation, the magnetization $\boldsymbol{M}$ in the MNP core rotates. For Brownian relaxation, the whole MNP rotates (indicated by a fixed directional vector $\boldsymbol{n}$ for the MNP), aligning with an external field $\boldsymbol{B}$. Redrawn from [36].

2.2.1 Applications of Magnetic Nanoparticles

Magnetic nanoparticles and their applications is a vast field of research. They offer great potential in respect to medical applications and life sciences[37]–[40].

Possible applications of MNP include biological and medical use in relation to drug delivery[41], [42], cell tracking[43], [44], tissue engineering[45], [46], hyperthermia for cancer therapy[47]–[51], or clinical use for sentinel lymph node biopsy (SLNB) for cancer detection. It was shown that SLNB with MNP tracers is not inferior to the conventional techniques using radioactive tracers[52]–[54]. Overall, imaging of MNP offers to be a great tool for medical and clinical applications. They can be used in magnetic resonance imaging for enhanced contrast[37]. They can be used as a tracer material for Magnetic Particle Imaging, which can be used for cardiovascular interventions[55], [56]. The previously mentioned SLNB could be facilitated via a handheld MPI device[57]–[59].

2.2.2 Characterization of Magnetic Nanoparticles

Magnetic nanoparticles can be characterized by a variety of techniques. Here, the focus lies on the frequency response of MNP to an AC magnetic field. In the following, two techniques will be explained, namely AC Susceptometry (ACS) and Magnetic Particle Spectrometry (MPS).

2.2.2.1 AC Susceptometry

AC Susceptometry measures the susceptibility of the MNP. For this, only a harmonic response of the MNP is measured, nonlinear magnetic behavior is not considered. The frequencies range for ACS from 10 Hz to 1 MHz[60]. The frequency response of the MNP susceptibility will show distinctive relaxation behaviors related to the Brownian and Néel relaxation, which can effectively be described via the Debye model[61], [62]:

$$\chi'(\omega) = \frac{\chi_0}{1 + (\omega\tau_{\text{eff}})^2} \quad \text{and} \quad \chi''(\omega) = \frac{\chi_0\omega\tau_{\text{eff}}}{1 + (\omega\tau_{\text{eff}})^2} \tag{2.7}$$

Here, χ' and χ'' denote the real and imaginary part of the susceptibility, ω is the frequency and τ_{eff} an effective relaxation constant. The effective relaxation constant is related to the Brownian and Néel relaxation time, τ_{B} and τ_{N} respectively:

$$\frac{1}{\tau_{\text{eff}}} = \frac{1}{\tau_{\text{B}}} + \frac{1}{\tau_{\text{N}}} \tag{2.8}$$

The parameter χ_0 describes the static susceptibility, which is given via the susceptiblity of the Langevin function around the origin (c.f. Figure 2.5 slope of dashed line). An exemplary plot of the relaxation behavior is given in Figure 2.7. It shows that the susceptibility decreases after passing the time constant τ, which corresponds to a lag in following the AC magnetic field. The peak in the imaginary part χ'' corresponds to the largest energy dissipation. From the spectrum, important parameters such as the relaxation time τ can be extracted, and with that, information about the MNP and its environment[63]. In reality, one has to consider the size distribution of the MNP to be able to correctly describe the ACS spectra. An excellent reference for the analysis of MNP ACS spectra is given by Ludwig et al.[60]. While the ACS spectra only give information about the linear response of MNP, they also yield information about the environment of the MNP, which was shown by Cabrera et al.[64] for magnetically labeled cells. Here, a change in properties due the uptake of MNP by the cells were observed.

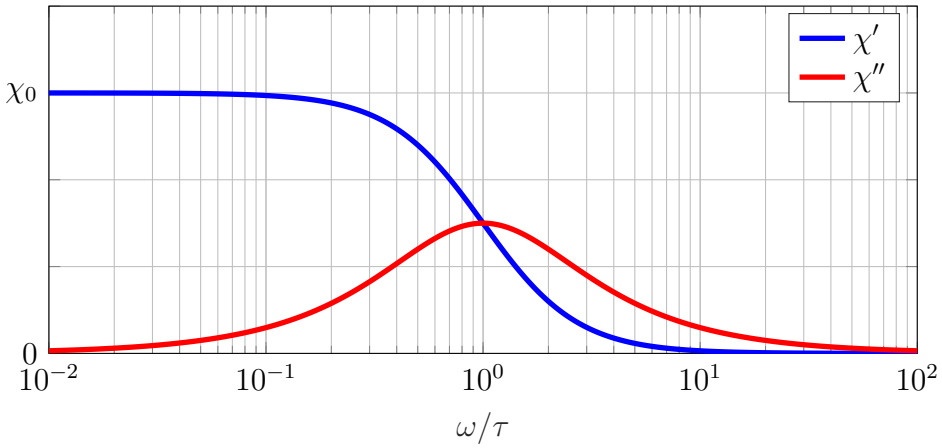


Figure 2.7: Debye relaxation of the MNP. As the frequency approaches the relaxation frequency τ^{-1}, the real part of the magnetic susceptiblity begins to decrease monotonically. At the relaxation frequency, the imaginary part has a maximum, indicating the largest energy dissipation. The reason is that the MNP cannot follow the magnetic fields direction anymore and lag behind.

2.2.2.2 Magnetic Particle Spectrometry

In Magnetic Particle Spectrometry (MPS), the monofrequent magnetic excitation amplitude for the MNP is much larger than in ACS, meaning that the MNP show nonlinear responses. Therefore, with MPS the dynamic magnetic response of the MNP are measured. This process can be seen in Figure 2.8 in a simplified view. A monofrequent magnetic field magnetizes the MNP, which in turn generate a magnetic field according to the achieved magnetization. Because the magnetization curve is nonlinear, higher harmonic excitations are present in the MNP magnetic response. These higher harmonic excitations of the MNP are detected by pick-up coils, yielding a MPS spectrum[65]. In MPS, the influence of the relaxation behavior of the MNP has major influences on the spectra[66]. Because these spectra are very hard to describe theoretically, MPS offers a great tool for deeper insight in MNP dynamics[33]. The requirements for a MPS system are much more demanding compared to ACS, because a clean excitation signal has to be ensured to drive the coils. As such, a MPS system can be thought of as a zero dimensional MPI system, because the measurement principle via the coils and much of the equipment is the same[65]. For an idea about the capabilities for a MPS system, Draack et al. custom built a MPS system with magnetic field amplitudes of $H < 30\ \mathrm{mT}/\mu_0$ in the frequency range of $100\ \mathrm{Hz} \leq f \leq 25\ \mathrm{kHz}$[67].

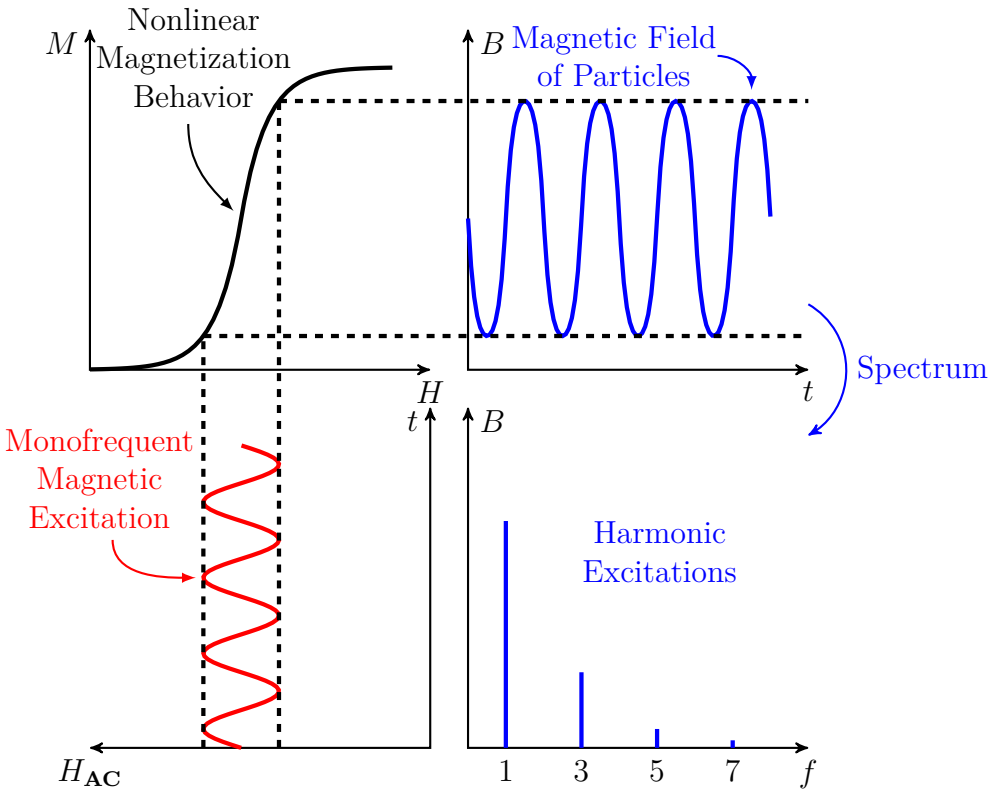


Figure 2.8: Generation of higher harmonic excitations due to magnetic nonlinearity: a monofrequent magnetic excitation of the MNPs results in a time-varying response, which contains frequencies of multiples of the excitation frequency.

2.3 Imaging Systems for Magnetic Nanoparticles

This section serves as an overview of some of the imaging techniques available for MNP. Imaging of MNP can be achieved in a variety of ways. For imaging, several tracer based techniques were developed to greater extent. These techniques are, among others, Magnetic Particle Imaging (MPI), Magnetorelaxometry Imaging (MRXI), Scanning Magnetic Particle Spectrometry (SMPS), Magnetic Susceptibility Imaging (MSI) and Magneto Acoustic Tomography (MAT). Furthermore Magnetic Resonance Imaging (MRI) and Magnetomotive Optical Coherence Tomography (MMOCT) can also be used for imaging the MNP, though these techniques can also work without MNP. In this thesis, another tracer based imaging system will be introduced and developed, a scanning type MNP imaging system via magnetoelectric sensors, called Magnetic Particle Mapping (MPM).

2.3.1 Magnetic Particle Imaging

Magnetic Particle Imaging (MPI) is based on the nonlinear magnetization of MNP. This nonlinearity is used in combination with strong inhomogeneous magnetic fields and AC magnetic fields to spatially select and gather the frequency response of the MNP. The spatial resolution of MPI can be below 1 mm, has rapid acquisition times of less than 0.1 s[68], shows very high sensitivity for even small amounts of tracer MNP and is inherently quantitative, meaning that the signal is directly proportional to the quantity of MNP present[69].

MPI is capable of in-vivo imaging, as was presented for a beating mouse heart and is therefore able to image blood flow via MNP tracers[70]. This is relevant for medical applications, e.g. related to cardiovascular interventions[55], [71]. Cell implant monitoring for cell tracking via MPI was also reported[44]. Another possibility is the detection of MNP in lymph nodes for sentinel lymph node biopsy for the detection of cancer cells[58], [72]–[74].

Signal acquisition is based on the induction voltage in receiving coils from a change in magnetization of the MNP from an applied AC field. Thereby, one gains a signal spectrum of the MNP. To gain spatial information of the MNP, inhomogeneous magnetic fields are used, such that only a selected region in the sample is able to show a MNP

response via the receive coils. For this, one can use Field-Free-Points (FFP) or Field-Free-Lines (FFL)[30], [68], [75]. FFPs can be created from Maxwell configurations of coils/magnets. FFLs can be created from different coil geometries[30], [59], but also arrays of permanent magnets can be used[76], [77]. Single-sided MPI systems are also being developed, which show the ability for hand-held devices[57]–[59].

2.3.2 Scanning Magnetic Particle Spectrometry

A Scanning Magnetic Particle Spectrometer (SMPS) uses a scanning device, on which a Magnetic Particle Spectrometer (MPS) was mounted. MPS systems are basically zero dimensional MPI systems and the use of a scanning device enables the spatial mapping of MNP and its associated properties/surroundings, e.g. temperature[66], [78], [79]. The underlying signals are the higher harmonic (and harmonic) generations of the MNP measured via coils. Using a scanning MPS system, the spatial resolution is lower compared to MPI (about 2 mm resolution, depending on the measurement), because no FFPs or FFLs are used to detect MNP selectively[78]. Instead, the MNP are detected in relation to the vicinity of the mounted MPS system. Furthermore, the acquisition time is much longer compared to MPI, ranging from 15 mins to several hours, depending on the type of measurement[78], [79]. It was recently shown that SMPS systems are able to detect biomolecule functionalized MNPs and image these spatially, which was not realized so far for MPI systems[80].

2.3.3 Magnetorelaxometry Imaging

In Magnetorelaxometry (MRX), the magnetic moments of MNP are aligned via an applied external magnetic field and a net magnetic moment is formed. The external field is then switched off and the relaxation of the MNPs' net magnetic moment is measured via magnetometers. Many types of magnetometers were used for MRX, such as superconducting quantum interference devices (SQUID), fluxgates or optically pumped magnetometers (OPM) [81]–[83]. From MRX measurements, one can extract information about the MNP relaxation behavior and even distinguish between different relaxation behaviors from MNP[35]. By using arrays of sensors or scanning setups, as well as sets of activation coils for spatially selective magnetic fields, one can perform imaging of the underlying MNP distributions[81], [82].

Elaborate imaging systems were developed that aim to enhance the imaging capabilities by adapting geometries[84] or activation coil sequences[85]. Sensor fusion approaches based on the combination with an Electron Paramagnetic Resonance (EPR) imaging system[86], [87] were also studied theoretically[88]. Acquisition times for MRXI depend on the particular system. For example, scanning MRXI systems need to approach each measurement position, magnetize the sample, turn off external field, measure the signal and maybe average a few measurements[82], [89]. For such systems, measurements can take hours[82]. The resolution in this 2D imaging system is reported to be about a few millimeters, which varied with the type of sensor use. To enhance the scanning speed for such systems, one can resort to an array of sensors. On the other hand, MRXI systems using a spatially fixed array of sensors, and using selective activation coils, can perform imaging on much smaller timescales, usually about a 30s-100s[85], though the proper choice of imaging system depends on the particular application.

2.3.4 Magnetic Susceptibility Imaging

Magnetic Susceptibility Imaging (MSI) is based on the MNP response to magnetic fields. Here, tomographic imaging can be performed by using sets of coils of varying strengths to expose a sample to[90]. Sensors are used to measure the resulting magnetic fields of the sample. Such a system was for example developed in [91], called Susceptibility Magnitude Imaging (SMI), where fluxgates are used for the detection and imaging of a MNP in a sample. Further developement on these systems were done using the nonlinear MNP response for Spectroscopic AC Susceptibility Imaging (sASI)[92] and nonlinear Susceptibility Magnitude Imaging (nSMI)[93]. Theoretical enhancements on the setup were proposed in [94] based on figure of merits for the inverse problem in imaging. The overall imaging abilities of the mentioned systems in terms of acquisition time were reported to be about a minute[92], [93], though further enhancements were mentioned. Resolution was about 5 mm, though this was limited due to the setups sample holder.

2.3.5 Magneto Acoustic Tomography

In Magneto Acoustic Tomography (MAT), MNPs are exposed to a pulsing magnetic field (1.0 μs/pulse) which leads to magnetomotive forces on the MNPs and therefore the surrounding tissue begins to vibrate at MHz frequencies. As a result, sound is generated, which can be picked up via ultrasonic transducers. By mapping these responses in space

from all directions, one can perform tomographic imaging of the MNP and resolve the MNP distribution with a resolution of a few millimeters in size[95]. Ultrasound-based MNP imaging was also used for detecting, monitoring and imaging intracellular accumulation of MNP[96], [97]. MAT is able for in-vivo imaging with high resolution (about 2 mm) which is primarily determined by the ultrasound bandwidth and its attenuation by the tissue[98].

2.3.6 Magnetomotive Optical Coherence Tomography

In [99], the authors used optical coherence tomography (OCT) in combination with magnetomotive forces on MNP from an applied magnetic field. The forces result in regional changes in optical scattering, which can then be imaged to create contrast for MNP. Therefore, the technique is not inherently tracer-based, which means that an image can be taken even without MNP — the MNP merely act as a way to enhance contrast. The magnetic field strength for the technique can be as low as 80-100 mT[100]–[102]. The authors in [103] imaged magnetically labeled cells in three-dimensional tissue scaffolds using magnetomotive OCT (MMOCT) under *in vivo* conditions. While OCT is rather unspecific in terms of the imaged tissue, MMOCT enhances the imaging technique to be specific to MNP, or rather, MNP labeled cells. This makes MMOCT a promising candidate for a cell tracking imaging modality with cellular resolution and overall an imaging modality for three dimensional scaffolds[102]–[105]. The sensitivity of the technique amounts to about 600 MNP per 10 μm diameter cell volume[101] and is hence highly sensitive in terms of MNP detection. Though OCT (and therefore MMOCT) is limited to optically translucent materials and a penetration depth of about 3 mm, it offers superior resolution (μm range) for three dimensional cell tracking to most other MNP imaging techniques listed here.

2.3.7 Magnetic Resonance Imaging

Magnetic Resonance Imaging (MRI) is based on Nuclear Magnetic Resonance (NMR) which describes the formation of an electromagnetic signal (radio wave) from atomic nuclei (most often a proton/hydrogen nucleus) due to a radio frequency perturbation while being suspended in a strong DC magnetic field. The nuclei have a spin associated with them which is aligned with the strong DC magnetic field. The perturbation disturbs this equilibrium and then, after removing the perturbation, the spin precession induces

a voltage in a receiving coil, which can be used for imaging, e.g. water density in the body. The amount of time it takes to return to equilibrium can be affected by MNP, which can hence be used as a contrast agent in MRI[37], [106].

2.4 Magnetoelectric Sensors for Detecting Magnetic Nanoparticles

Magnetoelectric sensors were recently used for detecting the magnetic response of MNPs. That this is possible was first shown by [107], where a laminate composite consisting of 500 µm thick PZT with 18 µm thick soft magnetic Ni-based Metglas ribbon. The research was performed in the context of clinical interventions. It was argued that ME sensors could be used for interventions such as sentinel lymph node biopsy (SLNB) for cancer detection, an application that is also argued for other imaging techniques, as mentioned earlier. With their setup, they performed a one dimensional measurement of the magnetic field, which can be thought of as a precursor for imaging MNP with ME sensors. To magnetize the MNPs, a permanent magnet was used, and the sensor was aligned such that no in plane magnetic field component affected the sensor. The smallest amount of MNP they were able to detect was 310 ng at a distance of 2 mm.

ME sensors were also used for the detection of tissue iron content for Biomagnetic Liver Susceptometry (BLS)[108]. In the study, permanent magnets were used to magnetize the sample and bias the sensor simultaneously. The sample is then moved periodically, such that a low frequency magnetic signal is created that can be detected via the ME sensor. The source of the magnetic signal was the protein ferritin, whose magnetic response is paramagnetic. This approach was reinvented in [109] for the imaging of MNP and is called Magnetic Susceptibiltiy Particle Mapping (MSPM). To generate a low frequency signal of the MNP, a motion modulated approach was taken, where the MNP distribution is mounted on a rotating disc, which is moved through a magnetic field of permanent magnets. The permanent magnets also bias the sensor for high sensitivity, while using the shape anisotropy of the sensor to adjust the extent if biasing.

In the context of this thesis, some of the just mentioned considerations were used as well[17]. The shape anisotropy of the sensors will be used for separation of externally applied field and the MNP field. Imaging of MNP is performed in 2D using AC fields for magnetic excitation and linear stages for translation. The measured data is then

analyzed for the spatial distribution of MNP via an elaborate model. The signal acquisition involves an AC field that magnetically excites the MNP to detect higher harmonic responses via the sensor, similar to MPI or sMPS. The imaging system developed in this thesis is called Magnetic Particle Mapping (MPM), which will be the topic of the next chapter.

CHAPTER 3

Magnetic Particle Mapping

Having introduced the applications of Magnetic Nanoparticles (MNPs) and their state-of-the-art imaging, we will now deal with the modeling of an imaging system using magnetoelectric sensors for MNPs.

In this chapter, a measurement approach called Magnetic Particle Mapping (MPM) will be proposed upon which a model will be developed, called the forward model for the imaging system. For this, magnetic properties of the MNPs and sensor characteristics will be considered and exploited, and a mathematical relationship for the imaging system will be derived. Using the forward model, a formulation to the inverse problem will be introduced in which we seek to reconstruct (i.e. to image) spatial particle distributions from measurements. Common metrics and figures of merit for the inverse problem will be introduced and solution approaches will be elucidated.

Furthermore, a generalization of the model will be developed which is able to remove uncertainties in the modeling and add it into the inverse problem. It will be shown that unique solutions can exist for such generalizations.

Additionally ”colored” magnetic particle mapping will be developed theoretically that uses differences in relaxation behaviors of MNPs to map the respective MNP types in space.

Finally, resolution limits of such imaging systems will be expressed mathematically for certain reconstruction methods that allow the evaluation of resolutions in imaging systems for given model/system geometries.

3.1 Introduction

To investigate the requirements of using magnetoelectric sensors for the detection and imaging of MNPs, a measurement approach will be proposed. With this proposal, we develop a forward model that maps a spatial particle distribution to the measurable signal. Using this model, we further show ways to infer an approximate spatial distribution

from measurements.

In this section, the concept for Magnetic Particle Mapping (MPM) will be explained. For this, we first introduce the properties of the individual parts for this imaging system, namely the sensor and the MNPs. The parts will be combined such that a favorable constellation with respect to positioning and orientation of the sensor to the MNPs can be found for measurability and signal strength. The proposed measurement approach can be seen in Figure 3.1. Here, an AC magnetic field perpendicular to the sensor plane

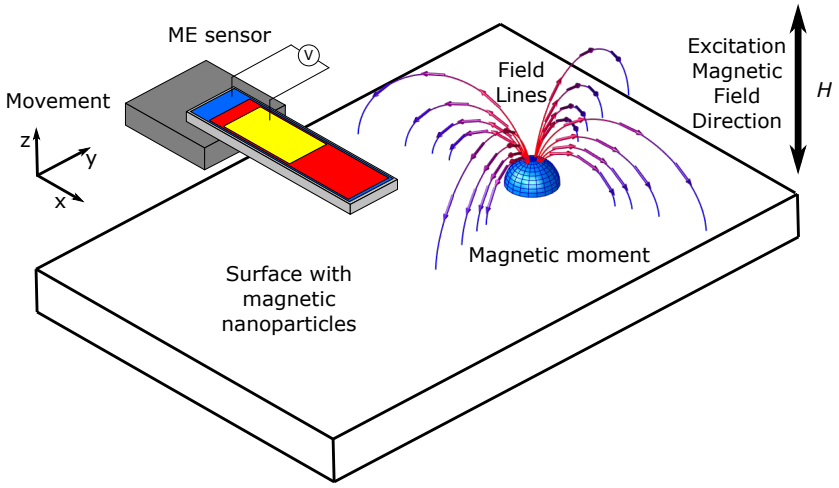


Figure 3.1: Schematic concept for the MPM measurement approach. A magnetic field is applied perpendicular to the plane of the sensor. Magnetic moments of the sample get aligned with the external field. This field is then measured with the sensor[17].

will be applied and magnetizes a sample which contains MNPs. The reorientation of the MNPs magnetic moments leads to a net magnetization of the sample, from which the magnetic field can be measured in space. As indicated, a magnetic moment creates a magnetic field, which in turn can be measured by the sensor.

The reason that the AC field is oriented perpendicular to the plane of the sensor is that we attempt to attenuate the influence of the AC field on the sensor's measurement by using the sensor's strong shape anisotropy - the perpendicular direction exhibits a large demagnetization factor and is thus able to attenuate the external field signal. Since the sensor only measures a single projection of the magnetic field, the above-mentioned direction is also non-sensitive, which also shows that attenuation is achieved in this direction. Furthermore, the measurement principle relies on the fact that ensembles of MNPs exhibit a nonlinear magnetization behavior (c.f. Figure 2.8). The external

excitation is adjusted such that one of the higher harmonic excitations coincides with the sensor's mechanical resonance frequency. In this way, we can distinguish between the signal from the external excitation and the signal from the MNPs. Furthermore, the magnetoelectric sensor is oriented such that the influence of the external magnetic field is minimized by using the strong demagnetization factor out of plane due to the geometry of the sensor.

This way, we achieve an attenuation of the external magnetic field in two ways, namely with respect to frequency and spatial orientation:

- the (off-resonance) external signal is not amplified by the sensor, and
- the external signal is attenuated by lying in a non-sensitive direction of the sensor.

We will thus use homogeneous magnetic fields for easy alignment of the sensor and further modeling. This will fix the direction of the magnetic dipoles as well as the possible measurable projections of the magnetic field. In the subsequent sections these aspects will be expanded on.

3.2 Forward Modeling

To model the imaging system, we have to develop a mathematical relationship between the sources (MNPs) and the measurement positions (sensor positions). The MNPs have a magnetic (vector)field associated with them due to their magnetic dipole moment $\boldsymbol{m}$ and the sensor ideally measures only a single projection of the magnetic field via the sensitivity axis $\boldsymbol{s}$. The next section will deal with the role of the magnetic dipole field and the sensor in context of an imaging system for MNPs. Furthermore, we can expect the system to be linear as the MNPs' magnetic fields simply superimpose.

3.2.1 The role of the magnetic point-dipole and the sensor

The magnetic field $\boldsymbol{B}_{\mathrm{D}}$ of a magnetic dipole moment $\boldsymbol{m}$ at a spatial position $\boldsymbol{r}$ can be calculated from the magnetic vector potential $\boldsymbol{A}$

$$\boldsymbol{A}(\boldsymbol{r}, \boldsymbol{m}) = \frac{\mu_0}{4\pi} \frac{(\boldsymbol{m} \times \boldsymbol{r})}{r^3}. \tag{3.1}$$

The magnetic field $\boldsymbol{B}_\mathrm{D}$ associated with a potential under the assumption of large distance from the dipole is given by

$$\begin{aligned}\nabla \times \boldsymbol{A} &= \boldsymbol{B}_\mathrm{D} \\ &= \begin{bmatrix} \frac{\partial A_z}{\partial y} - \frac{\partial A_y}{\partial z} \\ \frac{\partial A_x}{\partial z} - \frac{\partial A_z}{\partial x} \\ \frac{\partial A_y}{\partial x} - \frac{\partial A_x}{\partial y} \end{bmatrix} \\ &= \frac{\mu_0 \boldsymbol{m}^\intercal}{4\pi r^3} \left(3\hat{\boldsymbol{r}}\hat{\boldsymbol{r}}^\intercal - \boldsymbol{I}\right). \end{aligned} \tag{3.2}$$

If we measure only a single projection of the magnetic field via the sensor's sensitive axis $\boldsymbol{s}$, we have

$$\begin{aligned}\frac{4\pi}{\mu_0} B_\mathrm{D} &= \boldsymbol{m}^\intercal \frac{(3\hat{\boldsymbol{r}}\hat{\boldsymbol{r}}^\intercal - \boldsymbol{I})}{(\boldsymbol{r}^\intercal \boldsymbol{r})^{3/2}} \boldsymbol{s} \\ \frac{4\pi}{\mu_0 \left\|\boldsymbol{m}\right\| \left\|\boldsymbol{s}\right\|} B_\mathrm{D} &= \hat{\boldsymbol{m}}^\intercal \boldsymbol{H} \hat{\boldsymbol{s}}. \end{aligned} \tag{3.3}$$

The projected magnetic field can thus be written in a bilinear form with magnetic moment direction $\hat{\boldsymbol{m}}$, sensitive direction of the sensor $\hat{\boldsymbol{s}}$ and a symmetric matrix $\boldsymbol{H}$. Important to point out are the functions contained in $\boldsymbol{H}$ and their respective symmetries. The functions in the matrix are denoted as:

$$\boldsymbol{H} = \begin{pmatrix} h_{11} & h_{12} & h_{13} \\ h_{21} & h_{22} & h_{23} \\ h_{31} & h_{32} & h_{33} \end{pmatrix}$$

Due to the outer product $\hat{\boldsymbol{r}}\hat{\boldsymbol{r}}^\intercal$, the diagonal will yield symmetric functions while the off-diagonal elements exhibit antisymmetries with respect to the spatial coordinates. This fact will be important at a later stage, because they imply orthogonality of the measurable fields. Only a few correlated fields remain, making estimation of source distributions easier and allowing the possibility of adaptive models in the inverse problem, as will be shown in section 3.4.

To show the shape of the magnetic fields, we can plot the magnetic equisurfaces in

spherical coordinates. If we write the term $3\hat{\boldsymbol{r}}\hat{\boldsymbol{r}}^\intercal - \boldsymbol{I}$ in spherical coordinates, we get:

$$\boldsymbol{H} = \frac{3}{r^3}\boldsymbol{H}_P \tag{3.4}$$

with

$$\boldsymbol{H}_P = \begin{bmatrix} \sin^2(\phi)\cos^2(\varphi) - 1/3 & 1/2\sin^2(\phi)\sin(2\varphi) & \sin(\phi)\cos(\phi)\cos(\varphi) \\ 1/2\sin^2(\phi)\sin(2\varphi) & \sin^2(\phi)\sin^2(\varphi) - 1/3 & \sin(\phi)\cos(\phi)\sin(\varphi) \\ \sin(\phi)\cos(\phi)\cos(\varphi) & \sin(\phi)\cos(\phi)\sin(\varphi) & \cos^2(\phi) - 1/3 \end{bmatrix} \tag{3.5}$$

The entries of the matrix correspond to the polar components of the magnetic dipole field. They describe the overall shape of the dipole field with respect to spatial direction given its magnetic moment direction. The equisurfaces of the magnetic field are thus given by:

$$r_{\text{eq}} = \sqrt[3]{\frac{3}{B_{\text{D}}}\boldsymbol{m}^\intercal\boldsymbol{H}_P\boldsymbol{s}}. \tag{3.6}$$

The equisurfaces are shown in Figure 3.2. We can see that the functions on the diagonal (left to right in the image) are symmetric equisurfaces for all spatial orientations while the off-diagonal equisurfaces are antisymmetric with respect to two spatial axes. In order to relate this image to the proposed setup, we only look at a single plane at a

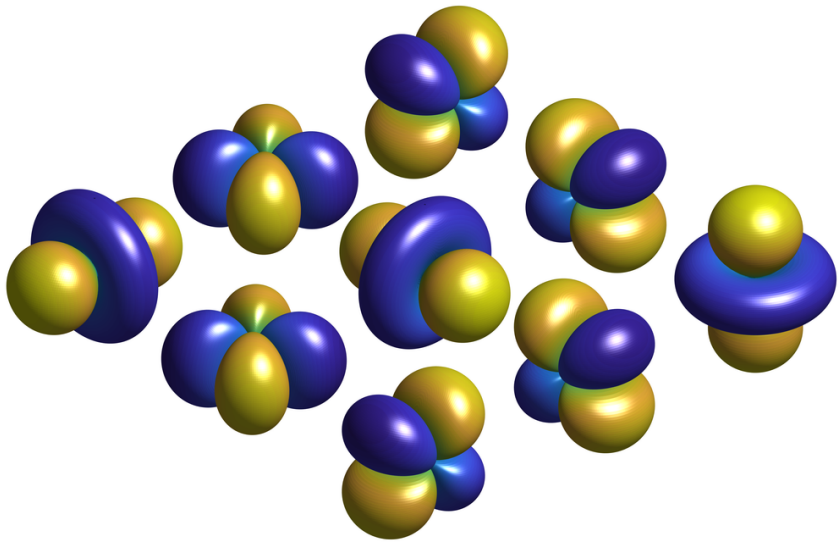


Figure 3.2: Equisurface of the magnetic dipole field for different moment directions.

distance z from the magnetic moment, as can be seen in Fig. 3.3. Here we measure in an $x-y$ plane for a fixed height z. The magnetic dipole field projections for the different orientations in this case are shown in Figure 3.4. Furthermore, it has to be stated that only certain projections of the magnetic moments magnetic field are measurable under the condition that the external field direction is perpendicular to the sensor plane. Under this condition, diagonal elements of the dipole field in $\boldsymbol{H}$ (Eq.3.3) have to be omitted because they violate the condition. The magnetic dipole field is key for the magnetic inverse problem for the estimation of particle distributions, because it enables us to appropriately model the system. We will thus measure some projection of superimposing magnetic fields of MNPs. The measurement procedure shall then be used for imaging applications.

3.2.2 Temporal Behavior of Magnetic Nanoparticles

For modeling the imaging system, we assume that the response of the particles remains the same for all positions in space. This way, spatially varying amplitudes in the magnetization (normalized to unit mass particles) from inhomogeneous fields are not considered in the further descriptions, though they can be implemented. To see why the description above is applicable, we note that the magnetic moment $\boldsymbol{m}$ is a function of the externally

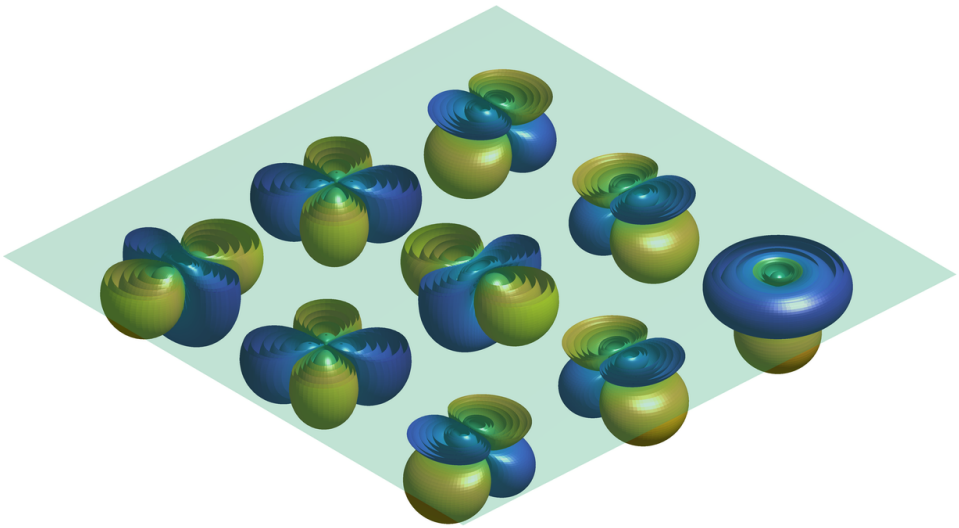


Figure 3.3: Equisurfaces of the magnetic dipole field for different moment directions, cut at a distance z from the dipole.

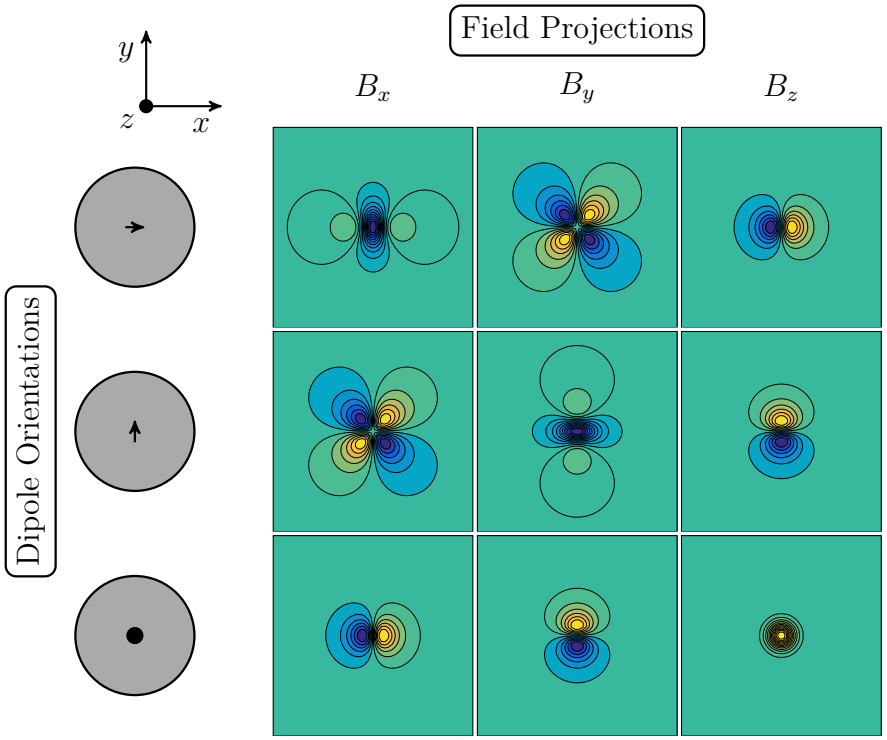


Figure 3.4: The magnetic dipole field projections for different magnetic moment orientations. The colors denote the magnetic field values with blue being negative and yellow being positive.

applied magnetic field direction and amplitude $\boldsymbol{H}_m$, i.e.

$$\boldsymbol{m} = m(\|\boldsymbol{H}_m\|)\frac{\boldsymbol{H}_m}{\|\boldsymbol{H}_m\|}. \tag{3.7}$$

The function for the magnetic moment strength, $m(\|\boldsymbol{H}_m\|)$, is a function of frequency and amplitude of the magnetic field $\boldsymbol{H}_m$. As a side note, the correct description for the magnetic moment can get arbitrarily complicated for rapid spatiotemporal changes of an external magnetic field, i.e. strong inhomogeneous fields that vary rapidly. This is a known problem in MPI research, as the computation of the response becomes expensive[33]. In our case this is not important, as the direction of the magnetic field stays the same (aside from a π change in phase for the polarity change in a period of an AC magnetic field). In our case, the MNPs magnetic behavior can be fully characterized by Magnetic Particle Spectrometry (MPS)[67], such that accurate responses can be used in the modeling.

Furthermore, because the MNPs will exhibit a phase response, the description for

the magnetic moment will be explicitly pointed out by an additional complex factor

$$\boldsymbol{m} = m(\|\boldsymbol{H}_m\|)e^{j\phi}\frac{\boldsymbol{H}_m}{\|\boldsymbol{H}_m\|}. \tag{3.8}$$

The main point is that the gained magnetization per unit mass of MNP is assumed to be the same for all positions in the sample. This way, all modeling of the MNPs magnetic field can be described via the dipole field equation with a scaled amplitude (depending on magnetic excitation field $\boldsymbol{H}_m$) which can be determined from MPS measurements.

3.2.3 Relationship of Particle Distribution to Measurable Fields

We now introduce the relationship of the spatial distribution of MNPs and the resulting magnetic fields in space (regions where we measure the field). We denote the spatial magnetic particle distribution as ρ, and the region where particles are present is the domain Ω over which will be integrated. The measurement positions are denoted as $\boldsymbol{r}_\mathrm{m}$. The resulting magnetic fields B_m at the measurement positions $\boldsymbol{r}_\mathrm{m}$ are then given by

$$\int_\Omega \rho(\boldsymbol{r})B_\mathrm{D}(\boldsymbol{r}_\mathrm{m},\boldsymbol{r})\mathrm{d}^3\boldsymbol{r} = B_\mathrm{m}(\boldsymbol{r}_\mathrm{m}) \tag{3.9}$$

The equation above is a Fredholm integral equation of the first kind[110]. In fact, in this case the integral equation is a convolution of the form

$$\int_\Omega \rho(\boldsymbol{r})B_\mathrm{D}(\boldsymbol{r}_\mathrm{m}-\boldsymbol{r})\mathrm{d}^3\boldsymbol{r} = B_\mathrm{m}(\boldsymbol{r}_\mathrm{m}) \tag{3.10}$$

The projected dipole field B_D is called the kernel of this equation and is, in this case, equivalent to an impulse response of the system or is also commonly known as the Point-Spread-Function (PSF) used in optics/imaging systems. The mapping from the spatial particle distribution to the measurable signal is the forward model. In this case, the system is linear and shift-invariant, assuming the Point-Spread-Function does not change depending on the sample position. The linearity stems from the assumption that the particles do not interact with each other (thus not altering the PSF depending on e.g. local concentrations) and that the magnetic fields linearly superimpose. This assumption can be assumed if homogeneous fields are used, which is to a sufficient degree the case. Therefore, one can describe this system, similar to linear time-invariant (LTI)

systems, as a *linear space-invariant* system.

Having introduced the relationship of the spatial particle distribution to the measurable signal, we can state the following objective:

Given measurements $B_m(\boldsymbol{r}_m)$,
how are the sources $\rho(\boldsymbol{r})$ *spatially distributed?*

This is the problem one needs to solve, i.e. the inverse problem.

3.2.4 Particle-Sensor Relationship to Measurable Signal

The previously introduced description for the imaging system was the Fredholm integral equation of the first kind:

$$\boldsymbol{B}_m(\boldsymbol{r}_m) = \int_\Omega \boldsymbol{B}_\mathrm{D}(\boldsymbol{r}_m, \boldsymbol{r})\rho(\boldsymbol{r})\mathrm{d}^3\boldsymbol{r} \tag{3.11}$$

with $\boldsymbol{B}_m$ being the magnetic field at the measurement position $\boldsymbol{r}_m$ from the domain Ω. The integral kernel $\boldsymbol{B}_\mathrm{D}$ describes the magnetic field of a point dipole and ρ is the spatial particle distribution.
It is important to distinguish between the magnetic field of the MNP distribution and the measurement signal of the sensor. The latter is a voltage signal generated from the magnetic field, and a transfer function is associated with the sensor, related to its sensitivity, frequency response, and spatial characteristics. Since the sensor only measures a single projection of the magnetic field, the magnetic field $\boldsymbol{B}_m$ is projected onto the sensitive axis $\boldsymbol{s}$ of the sensor. The magnitude of $\boldsymbol{s}$ denotes the sensitivity of the sensor in e.g. units of V/T. Furthermore, there may be additional background signals in the voltage signal which superimpose with the signal generated from the magnetic fields of the particles. Under these circumstances, the imaging system can be described by a Fredholm integral equation of the second kind:

$$v(\boldsymbol{r}_m) = f(\boldsymbol{r}_m) + \int_\Omega C_\mathrm{D}(\boldsymbol{r}_m, \boldsymbol{r})\rho(\boldsymbol{r})\mathrm{d}^3\boldsymbol{r} \tag{3.12}$$

with v being the sensors voltage signal and $C_\mathrm{D} = \boldsymbol{s}^\intercal \boldsymbol{B}_\mathrm{D}$. The function $f(\boldsymbol{r_m})$ is an unwanted background signal in the measurement. The total voltage signal v is then composed of the unwanted background signal and the voltage signal generated by the fields of the MNPs. Since the sensor itself is magnetic, the fields of the MNPs may change

the sensor properties, depending on the strength of the magnetic field. If this is the case, one can describe this via a field dependent kernel in the integral equation. Under these circumstances, the imaging system can be described via the integral equation:

$$v(\boldsymbol{r}_m) = f(\boldsymbol{r}_m) + \int_\Omega C_\mathrm{D}(\boldsymbol{r}_m, \boldsymbol{B}_m(\boldsymbol{r}_m), \boldsymbol{r})\rho(\boldsymbol{r})\mathrm{d}^3\boldsymbol{r}. \tag{3.13}$$

To describe a possible behavior of the system, one would have to know $f(\boldsymbol{r}_m)$ beforehand, or minimize it such that its influence in the imaging system can be neglected. Then, one can describe the imaging system in the more relaxed version

$$v(\boldsymbol{r}_m) = \int_\Omega C_\mathrm{D}(\boldsymbol{r}_m, \boldsymbol{B}_m(\boldsymbol{r}_m), \boldsymbol{r})\rho(\boldsymbol{r})\mathrm{d}^3\boldsymbol{r}. \tag{3.14}$$

For a more elaborate discussion on what the effect of $\boldsymbol{B}_m(\boldsymbol{r}_m)$ on the kernel C_D could be, one needs to consider the circumstances in which the measurements take place. The particle signal is generated such that it couples into the resonance of the sensor, which in turn means that the frequency response around its mechanical resonance is important. If the magnetic field of the particles changes the properties of the sensor, it would be expressed via, e.g. a shift in the resonance frequency. That a shift in resonance occurs for increasing magnetic excitation amplitudes is shown in Appendix B.1.3. This implies a shift in the measured phase response (as well as amplitude response). Since the phase shift is linear around the resonance frequency, one could describe this behavior in the sensitivity vector via

$$\boldsymbol{s} = \|\boldsymbol{s}\|_2 \, e^{j\eta|B_m(\boldsymbol{r}_m)|}\hat{\boldsymbol{s}}. \tag{3.15}$$

This new equation introduces an amplitude dependent phase shift $e^{j\eta|B_m(\boldsymbol{r}_m)|}$ depending on $B_m(\boldsymbol{r}_m)$ (which in turn is directly related to the voltage signal of the sensor) and a scaling factor η, which would be related to the rate of change for the phase response of the sensor around the resonance, i.e. the quality factor of the resonator. As a result, the integral equation that describes the imaging system can be written as

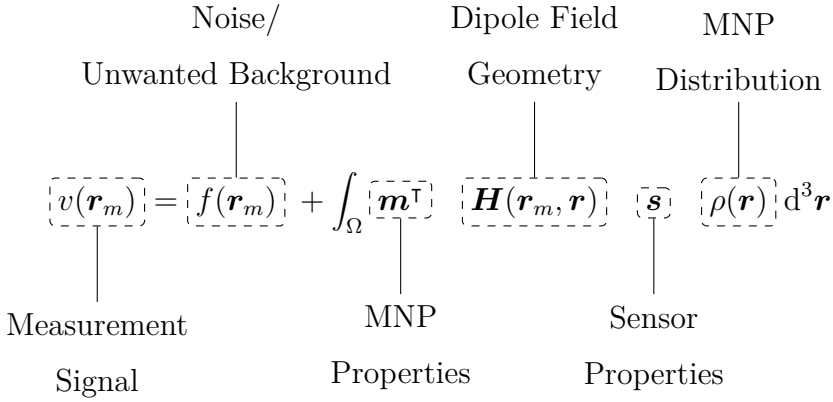
$$\begin{aligned} v(\boldsymbol{r}_m) &= \int_\Omega C_\mathrm{D}(\boldsymbol{r}_m, \boldsymbol{r}) e^{j\eta|\boldsymbol{B}_m(\boldsymbol{r}_m)|}\rho(\boldsymbol{r})\mathrm{d}^3\boldsymbol{r} \\ \Rightarrow \frac{v(\boldsymbol{r}_m)}{\|\boldsymbol{s}\|_2} &= \boldsymbol{B}_m(\boldsymbol{r}_m) = e^{j\eta|\boldsymbol{B}_m(\boldsymbol{r}_m)|} \int_\Omega \hat{\boldsymbol{s}}^\intercal \boldsymbol{B}_\mathrm{D}(\boldsymbol{r}_m, \boldsymbol{r})\rho(\boldsymbol{r})\mathrm{d}^3\boldsymbol{r} \end{aligned} \tag{3.16}$$

Throughout this thesis, it will be assumed that the MNPs do not interact. However, it is worth mentioning for the avid reader how the imaging system would be formulated if

the MNPs interacted to a large extent. Then the particle response would be a function of the spatial MNP distribution as well. In this case, the imaging system would be described by a nonlinear Urysohn integral equation of the form [111], [112]:

$$\begin{aligned} v(\boldsymbol{r}_m) &= f(\boldsymbol{r}_m) + \|\boldsymbol{s}\|_2 \, e^{j\eta|\boldsymbol{B}_m(\boldsymbol{r}_m)|} \int_\Omega \hat{\boldsymbol{s}}^\intercal \boldsymbol{B}_\mathrm{D}(\boldsymbol{r}_m, \boldsymbol{r}, \boldsymbol{B}_m(\boldsymbol{r}))\rho(\boldsymbol{r})\mathrm{d}^3\boldsymbol{r} \\ &= f(\boldsymbol{r}_m) + \|\boldsymbol{s}\|_2 \, e^{j\eta|\boldsymbol{B}_m(\boldsymbol{r}_m)|} \int_\Omega \hat{\boldsymbol{s}}^\intercal \boldsymbol{H}(\boldsymbol{r}_m, \boldsymbol{r})\boldsymbol{m}(\boldsymbol{B}_m(\boldsymbol{r}))\rho(\boldsymbol{r})\mathrm{d}^3\boldsymbol{r}. \end{aligned} \tag{3.17}$$

In summary, the relationship to the signal measured by the sensor can be written in the form shown in Eq. 3.18, where the properties of the sensor and the MNPs are encoded in the sensitivity $\boldsymbol{s}$ and magnetic moment $\boldsymbol{m}$, respectively.



(3.18)

3.2.5 Discretization

The next step involves discretizing the continuous forward model in Eq. 3.9 for a discrete amount of measurement positions, such that we can solve the discrete problem computationally. For the discretization, we choose a cartesian grid with equal step sizes in x- and y-directions. At this point, one can reasonably proceed in two way: integrating on pixels of (pixelwise) constant MNP concentrations, or choosing point sources to be the contributors to the measurement signal. The former method refers to the Galerkin method, whereas the latter is called the quadrature method. Even though the former is more accurate, if one wishes to choose very fine spatial discretizations, the latter is not much different from the former. Since we wish to do imaging on a small scale, we choose the latter method, because it is very easy to implement computationally. An exhaustive source for the discretizations can be found in [113]. For a detailed explanation of the Galerkin method for the magnetic inverse problem, see [114], [115].

Due to the linearity of the integral equation (Eq. 3.9), the discrete problem can be

represented as a system of linear equations of the form:

$$\boldsymbol{A}\boldsymbol{x} = \boldsymbol{b} \tag{3.19}$$

Here, $\boldsymbol{A} \in \mathbb{R}^{m \times n}$ is encoding the dipole field, $\boldsymbol{x} \in \mathbb{R}^n$ represents the spatial MNP distribution and $\boldsymbol{b} \in \mathbb{R}^m$ is the resulting superposition of all magnetic fields of the particles. Depending on the data $\boldsymbol{b}$, the set of numbers could also be $\mathbb{C}$ instead of $\mathbb{R}$, though it will be explicitly pointed out when necessary.

3.2.6 Model generalizations

Because the PSF B_D is dependent on the orientation of the magnetic dipole $\boldsymbol{m}$ with respect to the sensitive axis of the sensor $\boldsymbol{s}$, one can explicitly include these parameters in the model. Then, substituting the expression from Eq. 3.3, we yield the forward model:

$$\begin{aligned} \int_\Omega \rho(\boldsymbol{r}) B_\mathrm{D}(\boldsymbol{r}_\mathrm{m} - \boldsymbol{r}) \mathrm{d}^3\boldsymbol{r} &= B_\mathrm{m}(\boldsymbol{r}_\mathrm{m}) \\ \Rightarrow \int_\Omega \rho(\boldsymbol{r}) \boldsymbol{m}^\intercal \boldsymbol{H}(\boldsymbol{r}_\mathrm{m} - \boldsymbol{r}) \boldsymbol{s} \mathrm{d}^3\boldsymbol{r} &= B_\mathrm{m}(\boldsymbol{r}_\mathrm{m}). \end{aligned} \tag{3.20}$$

The bilinear form, which forms the PSF, i.e. $B_\mathrm{D} = \boldsymbol{m}^\intercal \boldsymbol{H} \boldsymbol{s}$, can be written as

$$\begin{aligned} B_\mathrm{D} =& m_1(s_1 h_{11} + s_2 h_{12} + s_3 h_{13}) \\ &+ m_2(s_1 h_{21} + s_2 h_{22} + s_3 h_{23}) \\ &+ m_3(s_1 h_{31} + s_2 h_{32} + s_3 h_{33}). \end{aligned} \tag{3.21}$$

Here, h_{ij} denotes the individual functions contained in $\boldsymbol{H}$. Similarly, the matrix for the discrete model is then a weighted superposition of the matrices corresponding to all combinations of magnetic moment directions and sensitive axis directions (i.e. h_{ij}),

$$\begin{aligned} \boldsymbol{A} =& m_1(s_1 \boldsymbol{A}_{11} + s_2 \boldsymbol{A}_{12} + s_3 \boldsymbol{A}_{13}) \\ &+ m_2(s_1 \boldsymbol{A}_{21} + s_2 \boldsymbol{A}_{22} + s_3 \boldsymbol{A}_{23}) \\ &+ m_3(s_1 \boldsymbol{A}_{31} + s_2 \boldsymbol{A}_{32} + s_3 \boldsymbol{A}_{33}). \end{aligned} \tag{3.22}$$

The model matrix can be more compactly represented using the Kronecker matrix product (denoted by $\otimes$)

$$\boldsymbol{A} = \left(\boldsymbol{m}^T \otimes \boldsymbol{I}_{m\times m}\right) \boldsymbol{A}_{\mathrm{B}} \left(\boldsymbol{s} \otimes \boldsymbol{I}_{n\times n}\right) \tag{3.23}$$

where $\boldsymbol{A}_{\mathrm{B}}$ is the blockmatrix containing all models

$$\boldsymbol{A}_{\mathrm{B}} = \begin{pmatrix} \boldsymbol{A}_{11} & \boldsymbol{A}_{12} & \boldsymbol{A}_{13} \\ \boldsymbol{A}_{21} & \boldsymbol{A}_{22} & \boldsymbol{A}_{23} \\ \boldsymbol{A}_{31} & \boldsymbol{A}_{32} & \boldsymbol{A}_{33} \end{pmatrix} \tag{3.24}$$

We can thus think of the model matrix $\boldsymbol{A}$ as a function of the magnetic moment direction $\boldsymbol{m}$ and the sensitive axis of the sensor $\boldsymbol{s}$.

3.3 Inverse Problem

3.3.1 Objective

Using the forward model we have developed, we now wish to infer the spatial particle distribution from the measured magnetic fields - we are looking for ways to invert the forward model — i.e. we wish to solve the inverse problem. Assuming that the model is accurate, the solution involves computing an estimate that is closely related to the data. For this, we need to minimize the difference between the estimate $\boldsymbol{Ax}$ and the data $\boldsymbol{b}$ via some form of metric. Commonly chosen is the L^2 norm (Euclidean norm) as the distance measure between the two vectors $\boldsymbol{Ax}$ and $\boldsymbol{b}$. This choice stems from the differentiability of this distance, because the norm is induced by the inner product, such that an analytic expression can be found. The differentiability is useful because the solutions can be iterated via gradient descent procedures. However, because we are dealing with an inverse problem, the least square minimum is not the ideal choice, because of numerical instabilities and amplification of noise in the measurements[113], [116], [117]. The cost function we start out with is:

$$\Phi(\boldsymbol{x}) = \|\boldsymbol{Ax} - \boldsymbol{b}\|_2^2 \,. \tag{3.25}$$

To combat the issues mentioned above, one needs to regularize the solution. Regularization refers to the addition of constraints to the original problem - we are looking

to both be close to the data $\boldsymbol{b}$ and still have physically meaningful results. For this we add another term to the cost function called the regularizer $\mathcal{R}$.

$$\Phi(\boldsymbol{x}) = \|\boldsymbol{A}\boldsymbol{x} - \boldsymbol{b}\|_2^2 + \lambda\mathcal{R}(\boldsymbol{x}) \tag{3.26}$$

The parameter λ is called the regularization parameter. The regularizer $\mathcal{R}$ can be written as

$$\mathcal{R}(\boldsymbol{x}) = \|\boldsymbol{L}\boldsymbol{x}\|_p^{c_p} \tag{3.27}$$

where $\boldsymbol{L}$ is a matrix, p is the value for the norm used and c_p is exponent for the regularizer. For different $\boldsymbol{L}$, p, and c_p, the problems have different names, such as Tikhonov regularization, LASSO, or Total variation regularization, just to name a few. Combinations of different regularizers are also possible, see e.g. elastic net regularization[118]. The choices are manifold and solution algorithms are numerous and therefore only a few will be discussed in this thesis that give insight into the problem of imaging MNPs.

A possible geometric meaning of the regularizer can be imagined as the description of a set in which the solution has to lie. The easiest way to see this is by using the Euclidean norm of the solution as the regularizer, i.e.

$$\Phi(\boldsymbol{x}) = \|\boldsymbol{A}\boldsymbol{x} - \boldsymbol{b}\|_2^2 + \lambda \|\boldsymbol{x}\|_2^2 . \tag{3.28}$$

An equivalent description is

$$\Phi(\boldsymbol{x}) = \|\boldsymbol{A}\boldsymbol{x} - \boldsymbol{b}\|_2^2 + \lambda \left(\|\boldsymbol{x}\|_2^2 - w\right) \tag{3.29}$$

because the minimizer is still the same. But we see here that this description is the same as for constrained optimization via the Lagrange multiplier λ. Thus, the role of the regularization parameter λ is to set the solution size (the Euclidean norm in this case). This type of regularization is also referred to as Tikhonov regularization. The advantage of this regularizer is that it is also differentiable, and thus a closed-form solution can also be found.

The question one then needs to consider is how large the solution $\boldsymbol{x}$ should be when setting the regularization parameter λ. For this, there are heuristics one can apply to gain physically meaningful results and can be expected to lie close to the real spatial particle distribution. For a discussion of this, see reference [113]. We will use the discrepancy principle, which uses the standard deviation of the noise to indicate whether

the residual norm $\|\boldsymbol{A}\boldsymbol{x} - \boldsymbol{b}\|$ is dominated by noise for a given estimate of $\boldsymbol{x}$.

We furthermore need to impose the constraint that the particle distribution is non-negative, i.e. $\boldsymbol{x} \geq 0$, because negative particle amounts do not make physical sense. If the particles domain is complex, then it has to lie on a line in the complex plane (in order to consider relaxation behavior). The implementation of this constraint will be covered in the upcoming section. To summarize, we need to solve the following objective:

$$\min_{\boldsymbol{x}} \left\{ \|\boldsymbol{A}\boldsymbol{x} - \boldsymbol{b}\|_2^2 + \lambda \mathcal{R}(\boldsymbol{x}) \right\} \quad \text{s.t.} \quad \boldsymbol{x} \geq 0. \tag{3.30}$$

3.3.1.1 Figure of merit

To evaluate the possible solutions of the spatial particle distribution, we will use the correlation coefficient. The correlation coefficient (CC) between the reconstruction $\boldsymbol{x}_{\text{recon}}$ and exact particle distribution $\boldsymbol{x}_{\text{true}}$ is a measure of the (spatial) accuracy of the reconstruction. It is given by:

$$\begin{aligned} CC &= \frac{\boldsymbol{x}_{\text{recon}}^T \boldsymbol{M}\boldsymbol{M}^T \boldsymbol{x}_{\text{true}}}{\sqrt{\boldsymbol{x}_{\text{recon}}^T \boldsymbol{M}\boldsymbol{M}^T \boldsymbol{x}_{\text{recon}}} \sqrt{\boldsymbol{x}_{\text{true}}^T \boldsymbol{M}\boldsymbol{M}^T \boldsymbol{x}_{\text{true}}}} \\ &= \frac{(\boldsymbol{x}_{\text{recon}}, \boldsymbol{x}_{\text{true}})_{\boldsymbol{D}}}{||\boldsymbol{x}_{\text{recon}}||_{\boldsymbol{D}} ||\boldsymbol{x}_{\text{true}}||_{\boldsymbol{D}}} \end{aligned} \tag{3.31}$$

with $\mathbf{1} \in \mathbb{R}^N$ being the all-one vector, $\boldsymbol{I}$ being the identity matrix, $\boldsymbol{D} = \boldsymbol{M}\boldsymbol{M}^T$ and $\boldsymbol{M} = \left(\boldsymbol{I} - \frac{\mathbf{1}}{N}\right)$.

3.3.2 Solution Methods

Having identified the inverse problem and its constraints, we now need to solve for an optimal solution. The algorithms for solving the inverse problem are plentiful and an exhaustive discussion on this is beyond the scope of this thesis. We will introduce solution methods that give insight to the problem and whether they are readily applicable in our case. The standard procedures to solve the inverse problem are truncated singular value decomposition (TSVD) and Tikhonov regularization. To generalize the solution approach via regularization, the proximal gradient descent approach will be introduced.

3.3.2.1 Truncated Singular Value Decomposition

A standard way to solve linear inverse problems is the use of truncated singular value decomposition (TSVD) [113]. Here, the forward operator $\boldsymbol{A}$ is decomposed via the singular value decomposition (SVD) into a product of three matrices, i.e.

$$\boldsymbol{A} = \boldsymbol{U}\boldsymbol{S}\boldsymbol{V}^{\intercal} \tag{3.32}$$

with

$$\boldsymbol{U}^{\intercal}\boldsymbol{U} = \boldsymbol{I} \tag{3.33}$$

$$\boldsymbol{V}^{\intercal}\boldsymbol{V} = \boldsymbol{I} \tag{3.34}$$

$$\boldsymbol{S} = \operatorname{diag}(\boldsymbol{\sigma}) \tag{3.35}$$

Here, $\boldsymbol{\sigma}$ is the vector consisting of the singular values of $\boldsymbol{A}$. From the forward equation we can see that

$$\begin{aligned} \boldsymbol{A}\boldsymbol{x} &= \boldsymbol{b} \\ \boldsymbol{U}\boldsymbol{S}\boldsymbol{V}^{\intercal}\boldsymbol{x} &= \boldsymbol{b} \\ \Rightarrow \boldsymbol{x} &= \boldsymbol{V}\boldsymbol{S}^{-1}\boldsymbol{U}^{\intercal}\boldsymbol{b} \\ &= \sum_i \frac{\boldsymbol{u}_i^{\intercal}\boldsymbol{b}}{\sigma_i}\boldsymbol{v}_i \end{aligned} \tag{3.36}$$

The left and right singular vectors, $\boldsymbol{u}_i$ and $\boldsymbol{v}_i$ respectively, can be understood as being related to spatial frequencies that make up the measured signal and the particle distribution. With increasing index i, the spatial frequencies also increase, which means more detail can be expected in the particle distribution given that the projection $\boldsymbol{u}_i^{\intercal}\boldsymbol{b}$ is not dominated by the noise. Given the limitation to not fit the noise, one truncates the summation and an index k, which gives the best approximation to the spatial particle distribution for a given amount of noise in the measurement. One can thus understand the TSVD as a perfect lowpass filter.

3.3.2.2 Tikhonov Regularization

Another commonly used technique is Tikhonov regularization. It is the introduction of a regularizer to the cost function, which is the square of the Euclidean norm of the

particle distribution $\|\boldsymbol{x}\|_2^2$.

$$\Phi(\boldsymbol{x}) = \|\boldsymbol{A}\boldsymbol{x} - \boldsymbol{b}\|_2^2 + \lambda \|\boldsymbol{x}\|_2^2 \tag{3.37}$$

Minimizing this function using the singular value decomposition, we get the expression[113]:

$$\boldsymbol{x} = \sum_i \varphi_{\lambda,i} \frac{\boldsymbol{u}_i^\intercal \boldsymbol{b}}{\sigma_i} \boldsymbol{v}_i \tag{3.38}$$

with $\varphi_{\lambda,i}$ being filter factors depending on the value of the regularization parameter

$$\varphi_{\lambda,i} = \frac{\sigma_i^2}{\sigma_i^2 + \lambda^2}. \tag{3.39}$$

The Tikhonov regularization acts as a suppressant of high frequency components where we have the condition $\lambda \gg \sigma_i^2$, i.e. it acts as a low pass filter. As a side note, the filter factors φ_i can be altered and tailored for particular inverse problems to gain certain behaviors of the reconstruction, see [119], [120] for references.

3.3.2.3 Proximal Gradient Descent

The last method to be introduced and exhaustively used in this thesis is the proximal gradient method. Using this method, one seeks to find solutions to the inverse problems when the regularizer is convex but not differentiable. This method is especially useful when trying to enforce constraints in the solution. We can think of this method as using a projection step in addition to a gradient descent step[113]. The method can be visualized as shown in Fig. 3.5. We start with the gradient descent step:

$$\boldsymbol{x}_{k+1} = \boldsymbol{x}_k - \alpha \boldsymbol{A}^\intercal \left(\boldsymbol{A}\boldsymbol{x}_k - \boldsymbol{b}\right). \tag{3.40}$$

In the proximal gradient method, one instead projects the updated particle distribution via the projection operator $\mathcal{P}$, i.e. we can write

$$\boldsymbol{x}_{k+1} = \mathcal{P}\left(\boldsymbol{x}_k - \alpha \boldsymbol{A}^\intercal \left(\boldsymbol{A}\boldsymbol{x}_k - \boldsymbol{b}\right)\right). \tag{3.41}$$

Now we can choose the projection operator for our problem. Since regularization is not explicitly in the form above, we describe the regularization via the projection operator.

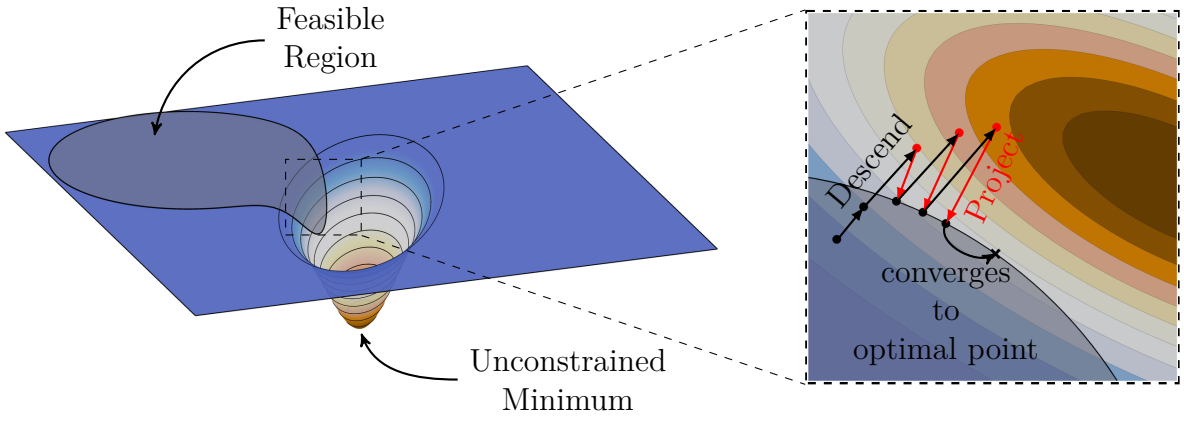


Figure 3.5: Proximal gradient method. Each gradient descent step is projected back into a feasible set. In this way, the solution becomes regularized, as the solution size can not lie outside the feasible set. If the feasible set is convex, the solution will converge to an optimal point within the set. Image recreated from [121].

The operator is often also called *prox* operator and is defined as:

Definition 1: Proximal Mapping

Given a convex function f, the proximal mapping of f is the operator given by

$$\text{prox}_f(\boldsymbol{x}) = \min_{\boldsymbol{u}} \{ f(\boldsymbol{u}) + \frac{1}{2} \|\boldsymbol{u} - \boldsymbol{x}\|_2^2 \}. \tag{3.42}$$

If the projection operator describes the projection onto the Euclidean ball (L^2 ball), (see Appendix A.2) the proximal gradient descent optimal point is the same as for the Tikhonov regularization. In addition to the projection onto the Euclidean ball, another projection into the nonnegative orthant (i.e. all parameters are nonnegative) is necessary to include the nonnegativity constraint (see Appendix A.4). This way one enforces the solution size while also being nonnegative, in order to be physically meaningful.

Another projection operator that is useful in our application is the projection onto the nonnegative L^1 norm ball with radius r (also called the scaled standard simplex, or scaled probability simplex). This has been demonstrated , e.g., in magnetorelaxometry imaging [85]. Because the L^1 norm of the spatial particle distribution is the total amount of particles in the domain, L^1 is a natural choice for the regularizer in our problem. This way, the regularized solution will set the total amount of particles that has to explain

the measurement $\boldsymbol{b}$. In addition to that, the projection also enforces sparsity in the solution, such that a higher resolution could be achieved, contrary to L^2 regularization. The sparsification can be seen in Fig. 3.6, where the feasible set is shown in blue for both the L^1 and L^2 ball. The minimum level set of the cost function that lies in the feasible set are likely to lie on the corners of the L^1 ball, leading to a shrinkage of the other parameters, i.e. sparsification. The projection onto the L^1 ball is also called soft-thresholding, which is why the iterative methods can be called the iterative soft-thresholding algorithm (ISTA)[122]. Using an additional nonnegativity constraint, we can call it an iterative nonnegative soft-thresholding algorithm. See Algorithm 1 for the algorithm with discrepancy principle stopping criterion. The projections necessary for the L^1 regularization can be found in the Appendix A.3.

3.3.2.4 List of Projection Operators for Description of Constraints

At this point, it is useful to have an overview of possible projection operators that can be used for the implementation of constraints. The projection operators used in this thesis are listed in Table 3.1. An implementation within Matlab for the different projection operators can be found in Appendix A. Some of the projection operators listed here will be introduced in the next sections.

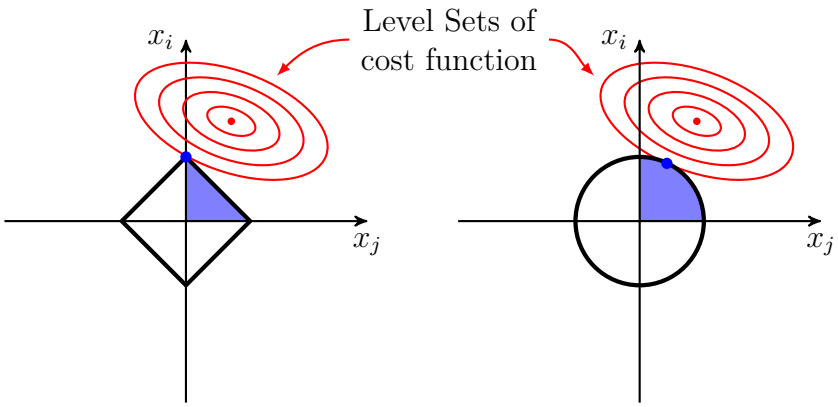


Figure 3.6: Given an optimization problem where the solution lies in the set of the unit ball in L^1 or L^2, the solution parameters are shrunk in the L^1-case, because the corners of the L^1 ball lie in the parameter axes. This enforces sparsity. This is not the case for the L^2 ball. We furthermore demand that the solution lies in the nonnegative orthant, as indicated by the blue region.

Algorithm 1 Nonnegative ISTA

Given: iterations K, data $\boldsymbol{b}$, L^1 norm estimate v, estimate of noise standard deviation δ, stopping term for discrepancy principle η, nonnegative soft-thresholding operator $\mathcal{P}_+^{\mathrm{L1},v}$.
Initialize forward operator $\boldsymbol{A}$, particle distribution $\boldsymbol{x}$.
for $k = 1$ to K **do**
    $\boldsymbol{x}_{k+1} = \mathcal{P}_+^{\mathrm{L1},v}\left(\boldsymbol{x}_k + \|\boldsymbol{A}\|_2^{-2}\,\boldsymbol{A}^\intercal(\boldsymbol{b} - \boldsymbol{A}\boldsymbol{x}_k)\right)$
    if $\|\boldsymbol{A}\boldsymbol{x}_{k+1} - \boldsymbol{b}\|_2 / \delta \leq \eta$ **then**
        return $\boldsymbol{x}_{k+1}$
    end if
end for
return $\boldsymbol{x}_{k+1}$

Proj. Operator	**Name**	**Parameters**
$\mathcal{P}$	Any Projection operator	-
$\mathcal{P}_C$	Projection into a Box	Box set C
$\mathcal{P}_+$	Projection into nonnegative orthant	-
$\mathcal{P}_+^{\boldsymbol{Q}}$	$\mathcal{P}_+$ Projection under the mapping $\boldsymbol{Q}$	Matrix $\boldsymbol{Q}$
$\mathcal{P}^{\mathrm{L1},v}$	Projection onto the scaled L1 ball	Radius of ball v
$\mathcal{P}^{\mathrm{L2},w}$	Projection onto the scaled L2 ball	Radius of ball w
$\mathcal{P}_+^{\mathrm{L1},v}$	Combined $\mathcal{P}^{\mathrm{L1},v}$ and $\mathcal{P}_+$	Radius of ball v
$\mathcal{P}_+^{\mathrm{L2},w}$	Combined $\mathcal{P}^{\mathrm{L2},w}$ and $\mathcal{P}_+$	Radius of ball w

Table 3.1: List of different projection operators for the implementation of constrained optimization.

3.3.3 Colored Magnetic Particle Mapping

In this section we will introduce colored Magnetic Particle Mapping. This expression is taken out of the magnetic particle imaging (MPI) community (see e.g. [34]), where differences in magnetic particles responses are used for distinctive imaging of the involved particles, e.g. imaging two particle types denoted by P_1 and P_2. To do this, we can go two ways:

- incorporate the amplitude and phase responses of the particles into the model

matrices $\boldsymbol{A}_{\mathrm{P}_1}$ and $\boldsymbol{A}_{\mathrm{P}_2}$ (by concatenation of two matrices), or

- use the same model matrix and subsequent computation of the respective local amounts via a linear mapping using the amplitude and phase responses.

The first method can be implemented by concatenation of the respective model matrices. The model matrices in our case only differ in a complex scalar value, i.e.

$$\boldsymbol{A}_c = \begin{pmatrix} a_1\boldsymbol{A} & a_2\boldsymbol{A} \end{pmatrix} \tag{3.43}$$

with $a_j = |a_j| \exp(i\phi_j)$ being the complex prefactors. These factors account for the relaxation behaviors of the MNPs. The spatial particle distribution is then also concatenated for both particle types $\boldsymbol{x}_{\mathrm{P}_1}$ and $\boldsymbol{x}_{\mathrm{P}_2}$, i.e.

$$\boldsymbol{x}_c = \begin{pmatrix} \boldsymbol{x}_{\mathrm{P}_1} \\ \boldsymbol{x}_{\mathrm{P}_2} \end{pmatrix}. \tag{3.44}$$

The second method can only be applied if the model matrices are equal except for a complex scalar difference. Under these circumstances, it is favorable to use the second approach, since it involves fewer computations and uses less memory than concatenating the matrix as listed in the first approach.

We thus use the latter approach. To implement this approach, we need to redefine the projection operator for the nonnegativity constraint. The constraint that the solution lies in the nonnegative orthant, i.e. $\boldsymbol{x} \geq 0$, needs to be extended to incorporate the phases in the entries of $\boldsymbol{x}$, i.e. x_i. As a result, the entries x_i need to lie in a cone in the complex plane, as depicted in Figure 3.8.

To compute the respective concentrations, we note that the entries x_i can be written as a superposition of the responses of types P_1 and P_2, i.e.

$$x_i = x_{i,\mathrm{P}_1} + x_{i,\mathrm{P}_2} \tag{3.45}$$

$$\begin{pmatrix} \mathrm{Re}(x_i) \\ \mathrm{Im}(x_i) \end{pmatrix} = \begin{pmatrix} 1 \\ i \end{pmatrix}^{\mathsf{T}} \begin{pmatrix} |a_1|\cos(\phi_{\mathrm{P}_1}) & |a_2|\cos(\phi_{\mathrm{P}_2}) \\ |a_1|\sin(\phi_{\mathrm{P}_1}) & |a_2|\sin(\phi_{\mathrm{P}_2}) \end{pmatrix} \begin{pmatrix} |x_{i,\mathrm{P}_1}| \\ |x_{i,\mathrm{P}_2}| \end{pmatrix} \tag{3.46}$$

$$= \begin{pmatrix} 1 \\ i \end{pmatrix}^{\mathsf{T}} \boldsymbol{Q} \begin{pmatrix} |x_{i,\mathrm{P}_1}| \\ |x_{i,\mathrm{P}_2}| \end{pmatrix}. \tag{3.47}$$

The associated matrix $\boldsymbol{Q}$ is composed of the different particle behaviors and needs to be inverted to compute the respective particle concentrations. Figure 3.7 shows the mapping of the matrix $\boldsymbol{Q}$ in the complex plane that comprises the reconstructed values for x_i. Considering the real and imaginary parts of the reconstruction, we can compute the respective concentrations of types P_1 and P_2 via

$$\begin{pmatrix} |x_{i,\mathrm{P}_1}| \\ |x_{i,\mathrm{P}_2}| \end{pmatrix} = \frac{1}{|a_1||a_2|\sin(\phi_{\mathrm{P}_2} - \phi_{\mathrm{P}_1})} \begin{pmatrix} |a_2|\sin(\phi_{\mathrm{P}_2}) & -|a_2|\cos(\phi_{\mathrm{P}_2}) \\ -|a_1|\sin(\phi_{\mathrm{P}_1}) & |a_1|\cos(\phi_{\mathrm{P}_1}) \end{pmatrix} \begin{pmatrix} \mathrm{Re}(x_i) \\ \mathrm{Im}(x_i) \end{pmatrix} \tag{3.48}$$

$$= \boldsymbol{Q}^{-1} \begin{pmatrix} \mathrm{Re}(x_i) \\ \mathrm{Im}(x_i) \end{pmatrix} \tag{3.49}$$

Here, we also see that phase differences need to be present, otherwise the determinant would be zero and the matrix not invertible. Using this approach, one can distinguish between different particle types. Colored MPM is limited to two particle types if only a single frequency can be measured. If more harmonics were measured, one could use these to distinguish more types/states of particles, see [34]. To use colored MPM, one needs to employ a new projection operator $\mathcal{P}_+^{\boldsymbol{Q}}$ based on the considerations outlined above. The projection operator $\mathcal{P}_+^{\boldsymbol{Q}}$ is given by using the inverse of $\boldsymbol{Q}$, then projecting the parameters into the nonnegative orthant (see Appendix A.4) and mapping back by $\boldsymbol{Q}$, see Appendix A.6 for more insight. Additionally, one needs to distinguish be-

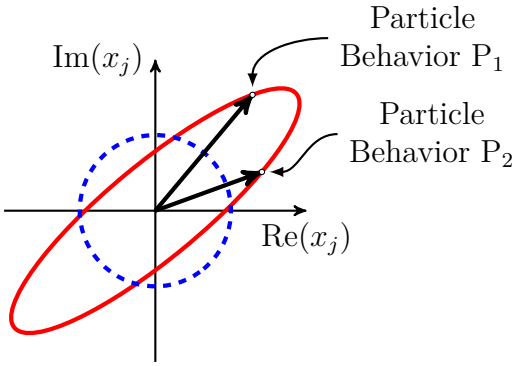


Figure 3.7: The complex magnetic response of the MNPs contains information about their respective relaxation behavior. Knowing the amplitude and phase response of these particles, one can construct a matrix containing the responses, such that one can use the inverse to separate different particle behavior in the signal and reconstruction via the real and imaginary axes. The dashed circle indicates the transformation via $\boldsymbol{Q}^{-1}$.

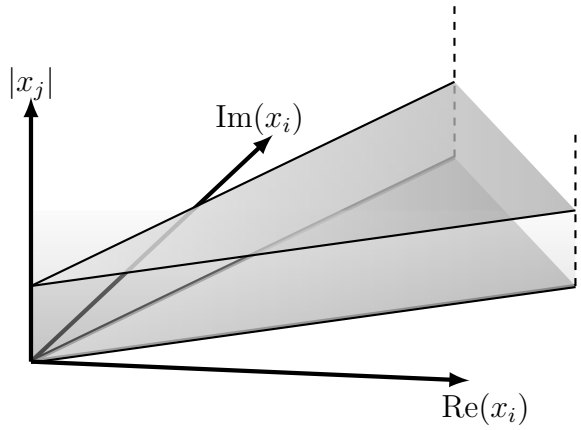


Figure 3.8: Cone in the complex plane in which the coefficients x_i have to lie. This is because a nonnegative superposition of complex numbers with fixed angles have to lie within this cone.

tween the reconstructed "uncolored" particle distribution $\boldsymbol{x}$ and the "colored" particle distribution $\boldsymbol{y}$, which means that the parameters in $\boldsymbol{x}$ need to be associated with the particular particle behaviors described by $\boldsymbol{Q}$ to constitute $\boldsymbol{y}$. The algorithm can be seen in Algorithm 2

Algorithm 2 Colored Magnetic Particle Mapping

Given: iterations K, data $\boldsymbol{b}$, estimate of noise standard deviation δ, stopping term for discrepancy principle η, particle type matrix $\boldsymbol{Q}$, cone projection operator for particle types $\mathcal{P}_+^{\boldsymbol{Q}}$.
Initialize forward operator $\boldsymbol{A}$, particle distribution $\boldsymbol{x}$.
for $k = 1$ to K **do**
    $[\boldsymbol{x}_{k+1}, \boldsymbol{y}_{k+1}] = \mathcal{P}_+^{\boldsymbol{Q}} \left(\boldsymbol{x}_k + \|\boldsymbol{A}\|_2^{-2} \boldsymbol{A}^\intercal (\boldsymbol{b} - \boldsymbol{A}\boldsymbol{x}_k) \right)$
    if $\|\boldsymbol{A}\boldsymbol{x}_{k+1} - \boldsymbol{b}\|_2 / \delta \leq \eta$ **then**
        return $\boldsymbol{y}_{k+1}$
    end if
end for
return $\boldsymbol{y}_{k+1}$

3.4 Model Estimation

While it is useful to use as much gathered information in the inverse problem as possible, we cannot guarantee the accuracy of that information. This can lead to errors in the forward model, which will result in an incorrect reconstruction, see e.g. [123]. For

example, because the sensitive axis of the sensor is dependent on the magnetic state, the correct angle of the sensitive axis may be altered without our knowledge (i.e. application of external field). To accommodate for that, one needs to incorporate the ability for a different sensitive axis within the model matrix. In chapter 3.2.6 we introduced a generalized model for the description of the imaging system. The model matrix was expanded to be dependent on the sensitive axis of the sensor and the orientation of the magnetic dipoles. The forward model introduced was:

$$\begin{aligned} \boldsymbol{b} &= \boldsymbol{A}\boldsymbol{x} \\ &= \left(\boldsymbol{m}^T \otimes \boldsymbol{I}_{m\times m}\right) \boldsymbol{A}_{\mathrm{B}} \left(\boldsymbol{s} \otimes \boldsymbol{I}_{n\times n}\right) \boldsymbol{x} \end{aligned} \tag{3.50}$$

In this chapter, we will deal with the estimation of these parameters within the model matrix. We will furthermore discuss whether it is possible to estimate other parameters such as sensor positioning or the averaging of the magnetic field over the geometry of the sensor.

3.4.1 General description

For the estimation of model parameters, we first introduce the description for the cost function and its gradients on a general basis. To do this, we recall the cost function for our fitting procedure:

$$\Phi\left(\boldsymbol{x}\right) = \frac{1}{2} \left\|\boldsymbol{A}\boldsymbol{x} - \boldsymbol{b}\right\|_2^2 \tag{3.51}$$

We now include parameters $\boldsymbol{\theta}$ within the model in $\boldsymbol{A}$, i.e.

$$\Phi\left(\boldsymbol{x}, \boldsymbol{\theta}\right) = \frac{1}{2} \left\|\boldsymbol{A}\left(\boldsymbol{\theta}\right)\boldsymbol{x} - \boldsymbol{b}\right\|_2^2 . \tag{3.52}$$

Now, the model matrix $\boldsymbol{A}\left(\boldsymbol{\theta}\right)$ itself is a function of parameters $\boldsymbol{\theta}$ that is related to the sensor projection axis of the magnetic field, positioning (e.g. distance to sample) and the averaging effect of the sensors geometry.

The aim is thus to successively estimate the particle distribution $\boldsymbol{x}$ while updating the model $\boldsymbol{A}$ via a gradient descent procedure. For this, we use the derivative of the matrix $\boldsymbol{A}$ with respect to a vector $\boldsymbol{\theta}$, which is a 3D matrix (tensor), as illustrated in Figure 3.9. The partial derivatives of the cost function Φ with respect to the particle distribution $\boldsymbol{x}$ and the model parameters $\boldsymbol{\theta}$ are given by

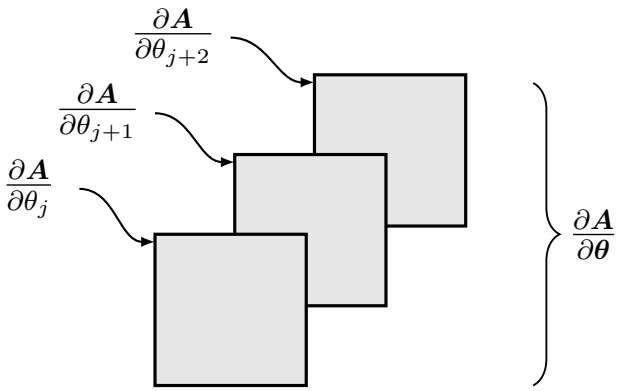


Figure 3.9: Derivative of matrix $\boldsymbol{A}$ with respect to the vector $\boldsymbol{\theta}$ yields a 3D matrix (tensor).

$$\nabla_{\boldsymbol{x}} \Phi = \boldsymbol{A}^{\intercal} (\boldsymbol{A}\boldsymbol{x} - \boldsymbol{b}) \tag{3.53}$$

$$\nabla_{\theta_j} \Phi = \boldsymbol{x}^{\intercal} \frac{\partial \boldsymbol{A}^{\intercal}}{\partial \theta_j} (\boldsymbol{A}\boldsymbol{x} - \boldsymbol{b}) \tag{3.54}$$

We can thus propose a two-step procedure for solving the inverse problem. The update procedure for the particle distribution $\boldsymbol{x}$ and the model parameters $\boldsymbol{\theta}$ is then

$$\boldsymbol{x}_{k+1} = \boldsymbol{x}_k - \alpha \nabla_{\boldsymbol{x}} \Phi(\boldsymbol{x}_k, \boldsymbol{\theta}_h) \tag{3.55}$$

$$\boldsymbol{\theta}_{h+1} = \boldsymbol{\theta}_h - \beta \nabla_{\boldsymbol{\theta}} \Phi(\boldsymbol{x}_{k+1}, \boldsymbol{\theta}_h). \tag{3.56}$$

Here, α and β are appropriate step sizes. In addition, we can use estimates of reasonable ranges of the model parameters $\boldsymbol{\theta}$. We thus define the set of possible parameters:

Definition 2: Set of possible model parameters

Reasonable model parameters are defined as the convex set C.

$$C \coloneqq \{ \operatorname{diag}(\boldsymbol{a})(\boldsymbol{\theta}_{min} - \boldsymbol{\theta}_{max}) + \boldsymbol{\theta}_{max} \mid \boldsymbol{a} \in [0,1]^n, \boldsymbol{\theta}_{min}, \boldsymbol{\theta}_{max} \in \mathbb{R}^n \} \tag{3.57}$$

Using this set, we project the model parameters into this set for each iteration using the projection operator $\mathcal{P}_C$. This projection describes a box constraint on the parameters as illustrated in Figure 3.10 and can easily be implemented via a min/max function, see Appendix A.5 for code.

As discussed in chapter 3.3.2.3, we use the projection onto the nonnegative L^1 ball for the update of the particle distribution $\boldsymbol{x}$, such that the solution vector has the

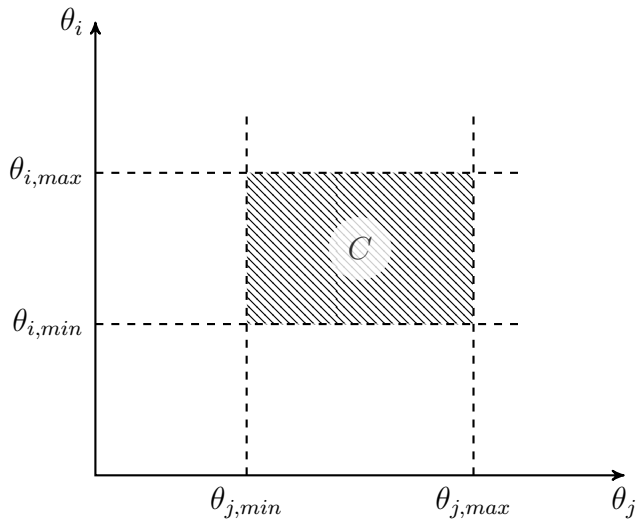


Figure 3.10: Box constraint on the possible model parameters. The feasible set C is the shaded box.

appropriate norm, corresponding to the overall particle amount in the system. The associated projection operator is denoted as $\mathcal{P}_v$, with v being an estimate of the L^1 norm of the particle distribution $\boldsymbol{x}$, i.e. $v \approx \|\boldsymbol{x}\|_1$.
The overall update of the model and distribution estimate can be written as:

$$\boldsymbol{x}_{k+1} = \mathcal{P}_v \left(\boldsymbol{x}_k - \alpha \nabla_{\boldsymbol{x}} \Phi(\boldsymbol{x}_k) \right) \tag{3.58}$$

$$\boldsymbol{\theta}_{h+1} = \mathcal{P}_C \left(\boldsymbol{\theta}_h - \beta \nabla_{\boldsymbol{\theta}} \Phi(\boldsymbol{x}_{k+1}, \boldsymbol{\theta}_h) \right). \tag{3.59}$$

We furthermore introduce an allowed incremental change p of the estimate of the total particle concentration v by:

$$p = \min \left(\left\| 1 - \frac{\|\boldsymbol{A}\boldsymbol{x}\|_1}{\|\boldsymbol{b}\|_1} \right\|, q \right). \tag{3.60}$$

Here, q is the maximum allowed incremental change of the estimate v. The intuition behind this approach is that if the computed $\|\boldsymbol{A}\boldsymbol{x}\|$ is smaller than $\|\boldsymbol{b}\|$, we need to increase the estimate v. The algorithm can then be written as shown in Algorithm 3.

3.4.2 Sensitive Axis or Dipole Orientation

Here the system for a fixed magnetic moment direction $\hat{\boldsymbol{m}}$ with unknown projection axis $\hat{\boldsymbol{s}}$ from the sensor will be described.

Algorithm 3 ISTA and Model Estimation

Given: iterations K, data $\boldsymbol{b}$, set of possible model parameters C, L^1 norm estimate v, maximum relative change of estimate q, estimate of noise standard deviation δ, stopping term for discrepancy principle η, projection operator $\mathcal{P}_C$, $\mathcal{P}_v$.
Initialize estimate of model parameters $\boldsymbol{\theta}$, particle distribution $\boldsymbol{x}$.
for $k = 1$ to K **do**
    $\boldsymbol{A} = \boldsymbol{A}(\boldsymbol{\theta}_k)$
    $\boldsymbol{x}_{k+1} = \mathcal{P}_v\left(\boldsymbol{x}_k + \|\boldsymbol{A}\|_2^{-2}\,\boldsymbol{A}^\intercal(\boldsymbol{b} - \boldsymbol{A}\boldsymbol{x}_k)\right)$
    $\boldsymbol{\theta}_{k+1} = \mathcal{P}_C\left(\boldsymbol{\theta}_k - \beta\nabla_{\boldsymbol{\theta}}\Phi(\boldsymbol{x}_{k+1}, \boldsymbol{\theta}_k)\right)$
    $p = \min\left(\left|1 - \frac{\|\boldsymbol{A}\boldsymbol{x}_{k+1}\|_1}{\|\boldsymbol{b}\|_1}\right|, q\right)$
    if $\|\boldsymbol{A}\boldsymbol{x}_{k+1}\|_1 \leq \|\boldsymbol{b}\|_1$ **then** ▷ Update the L^1 norm estimate of $\boldsymbol{x}$.
        $v = v(1+p)$
    else
        $v = v(1-p)$
    end if
    if $\|\boldsymbol{A}\boldsymbol{x}_{k+1} - \boldsymbol{b}\|_2 / \delta \leq \eta$ **then**
        return $\boldsymbol{x}_{k+1}, \boldsymbol{\theta}_k$
    end if
end for

We proceed by creating a model matrix that can be described as a superposition of the forward operator in the corresponding axes x, y, z for a fixed magnetic moment direction $\boldsymbol{m}$ in the z axis direction, i.e. as shown in Figure 3.11. We could take any row or column of the block matrix $\boldsymbol{A}_{\mathrm{B}}$ to construct a forward operator for the subsequent discussion.

The chosen case was taken because it is the projection axis and magnetic moment direction which will be investigated experimentally. The model matrix $\boldsymbol{A}$ can be written for an unknown projection axis as:

$$\boldsymbol{A} = s_1\boldsymbol{A}_{31} + s_2\boldsymbol{A}_{32} + s_3\boldsymbol{A}_{33} \tag{3.61}$$

Under these circumstances, the gradient in Eq.(3.54) can be rewritten as

$$\begin{aligned}\nabla_s\Phi &= \boldsymbol{x}^\intercal\frac{\partial\boldsymbol{A}^\intercal}{\partial\boldsymbol{s}}\left(\boldsymbol{A}\boldsymbol{x} - \boldsymbol{b}\right)\\ &= \boldsymbol{D}^\intercal\left(\boldsymbol{D}\boldsymbol{s} - \boldsymbol{b}\right)\end{aligned} \tag{3.62}$$

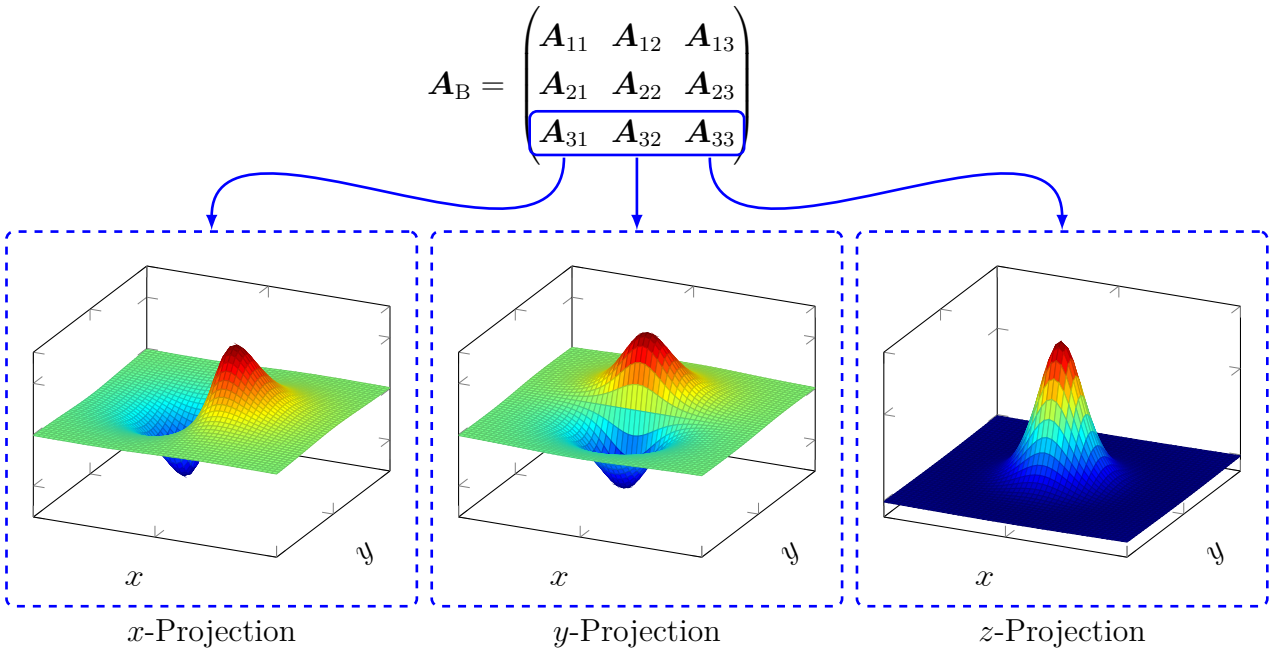


Figure 3.11: The individual model matrices corresponding to the different combinations of magnetic moment direction and sensitive axis direction refer to different PSFs for the imaging system. In this section we take the projections for the magnetic moment in the z direction, which is indicated by the model matrices enclosed by the blue borders. The dashed boxes show the corresponding PSFs for the model matrices.

with

$$\boldsymbol{D} = [\boldsymbol{A}_{31}\boldsymbol{x}, \boldsymbol{A}_{32}\boldsymbol{x}, \boldsymbol{A}_{33}\boldsymbol{x}] \tag{3.63}$$

$$\boldsymbol{s} = [s_1; s_2; s_3]\,. \tag{3.64}$$

As a result, the algorithm to compute the particle distribution $\boldsymbol{x}$ and the model parameters $\boldsymbol{s}$ can be written as shown in Algorithm 4. Under the condition that the correct model can be expressed as the linear combination of model matrices corresponding to the x, y and z-projection of the magnetic field, we write for the cost function:

$$\Phi\left(\boldsymbol{x}\right) = \frac{1}{2}\left\|\left(\sum_{i}^{N} s_i \boldsymbol{A}_{3i}\right)\boldsymbol{x} - \boldsymbol{b}\right\|_2^2. \tag{3.65}$$

In this case, we would have $N = 3$ matrices for the projections in the x, y and z-direction. Recall the dipole functions as depicted in Figure 3.11. Take e.g. the orientation of the

Algorithm 4 Model Estimation For Sensitive Axis

Given: iterations K, data $\boldsymbol{b}$, set of possible model parameters C, L^1 norm estimate v, maximum relative change of estimate q, estimate of noise standard deviation δ, stopping term for discrepancy principle η, projection operator $\mathcal{P}_C$, $\mathcal{P}_v$.
Initialize $\boldsymbol{A}_{31}$, $\boldsymbol{A}_{32}$, $\boldsymbol{A}_{33}$ possible forward operators, particle distribution $\boldsymbol{x}$, projection estimate $\boldsymbol{s}$.
for $k = 1$ to K **do**
    $\boldsymbol{A} = s_{1,k}\boldsymbol{A}_{31} + s_{2,k}\boldsymbol{A}_{32} + s_{3,k}\boldsymbol{A}_{33}$.
    $\boldsymbol{x}_{k+1} = \mathcal{P}_v\left(\boldsymbol{x}_k + \|\boldsymbol{A}\|_2^{-2}\,\boldsymbol{A}^\intercal(\boldsymbol{b} - \boldsymbol{A}\boldsymbol{x}_k)\right)$
    $\boldsymbol{D} = [\boldsymbol{A}_{31}\boldsymbol{x}_{k+1}, \boldsymbol{A}_{32}\boldsymbol{x}_{k+1}, \boldsymbol{A}_{33}\boldsymbol{x}_{k+1}]$
    $\boldsymbol{s}_{k+1} = \mathcal{P}_C\left(\boldsymbol{s}_k + \|\boldsymbol{D}\|_2^{-2}\,\boldsymbol{D}^\intercal\,(\boldsymbol{b} - \boldsymbol{D}\boldsymbol{s}_k)\right)$
    $p = \min\left(\left\|1 - \frac{\|\boldsymbol{A}\boldsymbol{x}_{k+1}\|_1}{\|\boldsymbol{b}\|_1}\right\|, q\right)$
    if $\|\boldsymbol{A}\boldsymbol{x}_{k+1}\|_1 \leq \|\boldsymbol{b}\|_1$ **then** ▷ Update the L^1 norm estimate of $\boldsymbol{x}$.
        $v = v(1+p)$
    else
        $v = v(1-p)$
    end if
    if $\|\boldsymbol{A}\boldsymbol{x}_{k+1} - \boldsymbol{b}\|_2 / \delta \leq \eta$ **then**
        return $\boldsymbol{x}_{k+1}, \boldsymbol{s}_{k+1}$
    end if
end for

dipole in z-direction and take the product of any two different projections of the dipole fields, which correspond to the PSFs in Figure 3.11. The result will yield equal positive and negative parts (given that we have a fine Cartesian discretization and a spatially large enough domain). This will be important in the following step. If we expand the expression above, we have

$$\Phi(\boldsymbol{x}) = \frac{1}{2}\left(\boldsymbol{x}^\intercal\boldsymbol{C}^\intercal\boldsymbol{C}\boldsymbol{x} + \boldsymbol{b}^\intercal\boldsymbol{b} - \boldsymbol{b}^\intercal\boldsymbol{C}\boldsymbol{x} - \boldsymbol{x}^\intercal\boldsymbol{C}^\intercal\boldsymbol{b}\right) \tag{3.66}$$

with $\boldsymbol{C} = \sum_i^N s_i\boldsymbol{A}_{3i}$. Now, the cross terms (i.e. $i \neq j$) in the quadratic forms are equal to zero

$$\boldsymbol{x}^\intercal\boldsymbol{A}_{3i}^\intercal\boldsymbol{A}_{3j}\boldsymbol{x} = 0 \tag{3.67}$$

which means that the matrix $\boldsymbol{D}$ is orthogonal

$$\begin{aligned} \boldsymbol{D} &= [\boldsymbol{A}_{31}\boldsymbol{x}, \boldsymbol{A}_{32}\boldsymbol{x}, \boldsymbol{A}_{33}\boldsymbol{x}] \\ \boldsymbol{D}^\intercal\boldsymbol{D} &= \operatorname{diag}(\boldsymbol{a}) . \end{aligned} \tag{3.68}$$

This follows from the fact that the inner product of the two dipole field projections is zero, since it contains equal amounts of positive and negative parts. We can thus write

$$\Phi(\boldsymbol{x}) = \frac{1}{2}(1-N)\|\boldsymbol{b}\|_2^2 + \frac{1}{2}\sum_i^N \|s_i\boldsymbol{A}_{3i}\boldsymbol{x} - \boldsymbol{b}\|_2^2 . \tag{3.69}$$

Because all terms correspond to strictly convex functions, the problem is uniquely solvable. Yet, because the number of parameters suffices for any of the matrices A_{ji} to express the data $\boldsymbol{b}$, one will still need to enforce a nonnegativity constraint, which will lead to the correct estimation in the end. The derivative with respect to the parameters for the projection $\boldsymbol{s}$ is

$$\nabla_i\Phi = \boldsymbol{d}_i^\intercal(\boldsymbol{d}_i s_i - \boldsymbol{b}) \tag{3.70}$$

$$\Rightarrow s_i = \frac{\boldsymbol{d}_i^\intercal\boldsymbol{b}}{\boldsymbol{d}_i^\intercal\boldsymbol{d}_i}$$

$$s_i = \frac{\boldsymbol{x}^\intercal\boldsymbol{A}_{3i}^\intercal\boldsymbol{b}}{\boldsymbol{x}^\intercal\boldsymbol{A}_{3i}^\intercal\boldsymbol{A}_{3i}\boldsymbol{x}} \tag{3.71}$$

which means it can be calculated from the projection of the estimate $\boldsymbol{A}_{3i}\boldsymbol{x}$ onto the data $\boldsymbol{b}$. The vector $\boldsymbol{b}$ can thus be expanded by an N-dimensional subspace that is constructed from the estimated particle distribution $\boldsymbol{x}$:

$$\boldsymbol{b} = \sum_i^N \frac{\boldsymbol{b}^\intercal\boldsymbol{A}_{3i}\boldsymbol{x}}{\|\boldsymbol{A}_{3i}\boldsymbol{x}\|}\frac{\boldsymbol{A}_{3i}\boldsymbol{x}}{\|\boldsymbol{A}_{3i}\boldsymbol{x}\|}. \tag{3.72}$$

Combining the results, we get

$$\begin{aligned}
\Phi(\boldsymbol{x}) &= \frac{1}{2}(1-N)\|\boldsymbol{b}\|_2^2 + \frac{1}{2}\sum_i^N \left\| \left(\frac{\boldsymbol{A}_{3i}\boldsymbol{x}\boldsymbol{x}^\intercal \boldsymbol{A}_{3i}^\intercal}{\boldsymbol{x}^\intercal \boldsymbol{A}_{3i}^\intercal \boldsymbol{A}_{3i}\boldsymbol{x}} - \boldsymbol{I} \right) \boldsymbol{b} \right\|_2^2 \\
&= \frac{1}{2}(1-N)\|\boldsymbol{b}\|_2^2 + \frac{N}{2}\|\boldsymbol{b}\|_2^2 - \frac{1}{2}\sum_i^N \frac{(\boldsymbol{b}^\intercal \boldsymbol{A}_{3i}\boldsymbol{x})^2}{\boldsymbol{x}^\intercal \boldsymbol{A}_{3i}^\intercal \boldsymbol{A}_{3i}\boldsymbol{x}} \\
&= \frac{1}{2}\|\boldsymbol{b}\|_2^2 - \frac{1}{2}\sum_i^N \left(\boldsymbol{b}^\intercal \frac{\boldsymbol{A}_{3i}\boldsymbol{x}}{\|\boldsymbol{A}_{3i}\boldsymbol{x}\|} \right)^2 \\
\frac{2}{\|\boldsymbol{b}\|_2^2}\Phi(\boldsymbol{x}) &= 1 - \sum_i^N \left(\frac{\boldsymbol{b}^\intercal}{\|\boldsymbol{b}\|} \frac{\boldsymbol{A}_{3i}\boldsymbol{x}}{\|\boldsymbol{A}_{3i}\boldsymbol{x}\|} \right)^2 \\
\frac{2}{\|\boldsymbol{b}\|_2^2}\Phi(\boldsymbol{x}) &= 1 - \sum_i^N \cos(\theta_i)^2
\end{aligned} \tag{3.73}$$

Here, we see that the cost function is minimized if the projection of the estimate $\boldsymbol{A}_{3i}\boldsymbol{x}$ onto the data $\boldsymbol{b}$ is maximized (or that the angle θ_i between the data $\boldsymbol{b}$ and the estimate $\boldsymbol{A}_{3i}\boldsymbol{x}$ is minimized). The direction cosines thus add up to 1 if we find the minimum of the cost function. This can be imagined as finding a point on a unit sphere, i.e. the decomposition of $\boldsymbol{b}/\|\boldsymbol{b}\|$ into orthogonal components related to the projection of the magnetic field (see Figure 3.12). Our task is thus finding the very specific subspace that is able to describe the data $\boldsymbol{b}$ completely. The derivative of this cost function is then given by

$$\begin{aligned}
\frac{1}{\|\boldsymbol{b}\|_2^2}\nabla\Phi(\boldsymbol{x}) &= \frac{1}{\|\boldsymbol{b}\|_2^2}\sum_i^N \frac{\boldsymbol{x}^\intercal \boldsymbol{A}_{3i}^\intercal \boldsymbol{b}}{\boldsymbol{x}^\intercal \boldsymbol{A}_{3i}^\intercal \boldsymbol{A}_{3i}\boldsymbol{x}} \boldsymbol{A}_{3i}^\intercal \left(\frac{\boldsymbol{x}^\intercal \boldsymbol{A}_{3i}^\intercal \boldsymbol{b}}{\boldsymbol{x}^\intercal \boldsymbol{A}_{3i}^\intercal \boldsymbol{A}_{3i}\boldsymbol{x}} \boldsymbol{A}_{3i}\boldsymbol{x} - \boldsymbol{b} \right) \\
&= \sum_i^N \cos(\theta_i) \frac{\boldsymbol{A}_{3i}^\intercal}{\|\boldsymbol{A}_{3i}\boldsymbol{x}\|} \left(\cos(\theta_i) \frac{\boldsymbol{A}_{3i}\boldsymbol{x}}{\|\boldsymbol{A}_{3i}\boldsymbol{x}\|} - \frac{\boldsymbol{b}}{\|\boldsymbol{b}\|} \right)
\end{aligned} \tag{3.74}$$

which is simply a scaled direction in comparison to the conventional gradient descent. The direction is altered depending on the value of the projection in $\cos(\theta_i)$ and yields the correct direction to describe the data $\boldsymbol{b}$.

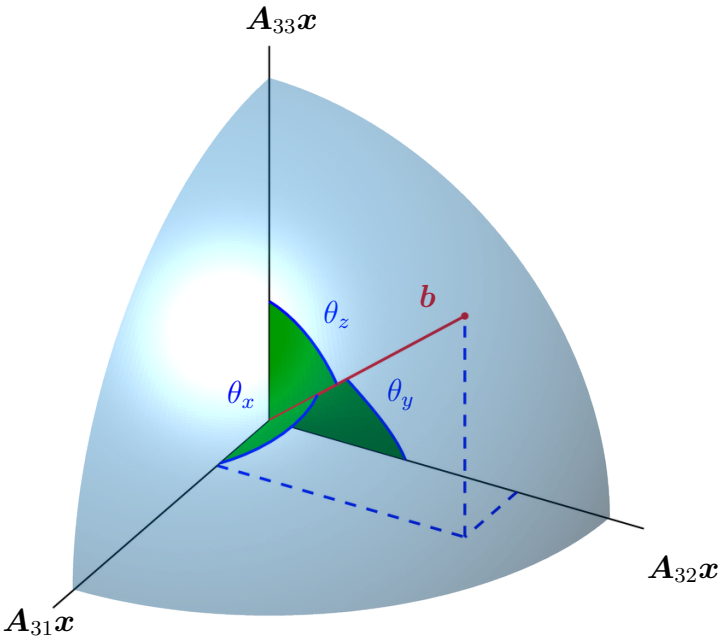


Figure 3.12: The measurement $\boldsymbol{b}$ is estimated to lie in a 3-dimensional subspace spanned by the estimates for the field projections in the x-, y- and z-directions, i.e. $\boldsymbol{A}_{31}\boldsymbol{x}$, $\boldsymbol{A}_{32}\boldsymbol{x}$ and $\boldsymbol{A}_{33}\boldsymbol{x}$. We thus need to find a point on a sphere of radius $\|\boldsymbol{b}\|$.

3.4.3 Sensitive Axis and Dipole Orientation

In this section, we will describe how to estimate the sensitive axis $\boldsymbol{s}$ and magnetic dipole direction $\boldsymbol{m}$ simultaneously. In this case, the model matrix can be written as

$$\begin{aligned}\boldsymbol{A} = \quad & m_1 \left(s_1\boldsymbol{A}_{11} + s_2\boldsymbol{A}_{12} + s_3\boldsymbol{A}_{13}\right) \\ & + m_2 \left(s_1\boldsymbol{A}_{21} + s_2\boldsymbol{A}_{22} + s_3\boldsymbol{A}_{23}\right) \\ & + m_3 \left(s_1\boldsymbol{A}_{31} + s_2\boldsymbol{A}_{32} + s_3\boldsymbol{A}_{33}\right). \end{aligned} \tag{3.75}$$

We can thus write for the cost function

$$\begin{aligned}\Phi\left(\boldsymbol{m}, \boldsymbol{s}, \boldsymbol{x}\right) &= \frac{1}{2}\left\|\boldsymbol{A}\boldsymbol{x} - \boldsymbol{b}\right\|_2^2 \\ &= \frac{1}{2}\left\|\left(\boldsymbol{m}^\intercal \otimes \boldsymbol{I}_{m\times m}\right)\boldsymbol{A}_\mathrm{B}\left(\boldsymbol{s} \otimes \boldsymbol{I}_{n\times n}\right)\boldsymbol{x} - \boldsymbol{b}\right\|_2^2. \end{aligned} \tag{3.76}$$

Here, $\boldsymbol{A}_{\mathrm{B}}$ is the block matrix

$$\boldsymbol{A}_{\mathrm{B}} = \begin{pmatrix} \boldsymbol{A}_{11} & \boldsymbol{A}_{12} & \boldsymbol{A}_{13} \\ \boldsymbol{A}_{21} & \boldsymbol{A}_{22} & \boldsymbol{A}_{23} \\ \boldsymbol{A}_{31} & \boldsymbol{A}_{32} & \boldsymbol{A}_{33} \end{pmatrix}_{3m \times 3n} . \tag{3.77}$$

The derivative of the cost function with respect to $\boldsymbol{m}$ can be written as

$$\frac{\partial \Phi}{\partial m_i} = \boldsymbol{x}^{\mathsf{T}} \left(\boldsymbol{s}^{\mathsf{T}} \otimes \boldsymbol{I}_{n\times n}\right) \boldsymbol{A}_{\mathrm{B}}^{\mathsf{T}} \left(\hat{\boldsymbol{e}}_i \otimes \boldsymbol{I}_{m\times m}\right) \left(\left(\boldsymbol{m}^{\mathsf{T}} \otimes \boldsymbol{I}_{m\times m}\right) \boldsymbol{A}_{\mathrm{B}} \left(\boldsymbol{s} \otimes \boldsymbol{I}_{n\times n}\right) \boldsymbol{x} - \boldsymbol{b}\right). \tag{3.78}$$

This can be rewritten in the form of

$$\begin{aligned} \frac{\partial \Phi}{\partial \boldsymbol{m}} =& \boldsymbol{M}_{\boldsymbol{m}}^{\mathsf{T}} \left(\boldsymbol{M}_{\boldsymbol{m}} \boldsymbol{m} - \boldsymbol{b}\right) \\ =& \left(\boldsymbol{I}_{3\times 3} \otimes \boldsymbol{s}^{\mathsf{T}}\right) \begin{pmatrix} \boldsymbol{M}_{1j}^{\mathsf{T}} \\ \boldsymbol{M}_{2j}^{\mathsf{T}} \\ \boldsymbol{M}_{3j}^{\mathsf{T}} \end{pmatrix} \left[\left(\left(\boldsymbol{I}_{3\times 3} \otimes \boldsymbol{s}^{\mathsf{T}}\right) \begin{pmatrix} \boldsymbol{M}_{1j}^{\mathsf{T}} \\ \boldsymbol{M}_{2j}^{\mathsf{T}} \\ \boldsymbol{M}_{3j}^{\mathsf{T}} \end{pmatrix} \right)^{\mathsf{T}} \boldsymbol{m} - \boldsymbol{b} \right] \end{aligned} \tag{3.79}$$

with

$$\begin{aligned} \boldsymbol{M}_{ij} =& \begin{pmatrix} \boldsymbol{A}_{i1} & \boldsymbol{A}_{i2} & \boldsymbol{A}_{i3} \end{pmatrix} \left(\boldsymbol{I}_{3\times 3} \otimes \boldsymbol{x}\right) \\ =& \begin{pmatrix} \boldsymbol{A}_{i1}\boldsymbol{x} & \boldsymbol{A}_{i2}\boldsymbol{x} & \boldsymbol{A}_{i3}\boldsymbol{x} \end{pmatrix}. \end{aligned} \tag{3.80}$$

The derivative with respect to $\boldsymbol{s}$ can intuitively be written by swapping the indices as

$$\begin{aligned} \frac{\partial \Phi}{\partial \boldsymbol{s}} =& \boldsymbol{M}_{\boldsymbol{s}}^{\mathsf{T}} \left(\boldsymbol{M}_{\boldsymbol{s}} \boldsymbol{s} - \boldsymbol{b}\right) \\ =& \left(\boldsymbol{I}_{3\times 3} \otimes \boldsymbol{m}^{\mathsf{T}}\right) \begin{pmatrix} \boldsymbol{M}_{i1}^{\mathsf{T}} \\ \boldsymbol{M}_{i2}^{\mathsf{T}} \\ \boldsymbol{M}_{i3}^{\mathsf{T}} \end{pmatrix} \left[\left(\left(\boldsymbol{I}_{3\times 3} \otimes \boldsymbol{m}^{\mathsf{T}}\right) \begin{pmatrix} \boldsymbol{M}_{i1}^{\mathsf{T}} \\ \boldsymbol{M}_{i2}^{\mathsf{T}} \\ \boldsymbol{M}_{i3}^{\mathsf{T}} \end{pmatrix} \right)^{\mathsf{T}} \boldsymbol{s} - \boldsymbol{b} \right]. \end{aligned} \tag{3.81}$$

To sum it up, the derivatives are

$$\frac{\partial \Phi}{\partial \boldsymbol{x}} = \boldsymbol{A}^\intercal \left(\boldsymbol{A}\boldsymbol{x} - \boldsymbol{b}\right) \tag{3.82}$$

$$\frac{\partial \Phi}{\partial \boldsymbol{s}} = \boldsymbol{M}_{\boldsymbol{s}}^\intercal \left(\boldsymbol{M}_{\boldsymbol{s}}\boldsymbol{s} - \boldsymbol{b}\right) \tag{3.83}$$

$$\frac{\partial \Phi}{\partial \boldsymbol{m}} = \boldsymbol{M}_{\boldsymbol{m}}^\intercal \left(\boldsymbol{M}_{\boldsymbol{m}}\boldsymbol{m} - \boldsymbol{b}\right). \tag{3.84}$$

Important to note in the gradients is the matrix containing all quadratic forms, i.e.

$$\begin{pmatrix} \boldsymbol{M}_{1j}^\intercal \\ \boldsymbol{M}_{2j}^\intercal \\ \boldsymbol{M}_{3j}^\intercal \end{pmatrix} \begin{pmatrix} \boldsymbol{M}_{1j}^\intercal \\ \boldsymbol{M}_{2j}^\intercal \\ \boldsymbol{M}_{3j}^\intercal \end{pmatrix}^T = \begin{pmatrix} \boldsymbol{M}_{1j}^\intercal \boldsymbol{M}_{1j} & \boldsymbol{M}_{1j}^\intercal \boldsymbol{M}_{2j} & \boldsymbol{M}_{1j}^\intercal \boldsymbol{M}_{3j} \\ \boldsymbol{M}_{2j}^\intercal \boldsymbol{M}_{1j} & \boldsymbol{M}_{2j}^\intercal \boldsymbol{M}_{2j} & \boldsymbol{M}_{2j}^\intercal \boldsymbol{M}_{3j} \\ \boldsymbol{M}_{3j}^\intercal \boldsymbol{M}_{1j} & \boldsymbol{M}_{3j}^\intercal \boldsymbol{M}_{2j} & \boldsymbol{M}_{3j}^\intercal \boldsymbol{M}_{3j} \end{pmatrix}. \tag{3.85}$$

By plotting this matrix one can gain an idea about the correlation between possible magnetic field components for different dipole orientations, see Figure 3.13. We see that because we have off-diagonal elements not equal to zero, the fields for different dipole orientations are correlated. On the other hand, we see that the block diagonal elements are diagonal sub-matrices, implying that the magnetic dipole fields are orthogonal if the orientation of the dipole lies on the (orthogonal) coordinate system axes. We saw this in the approach before where we said that the dipole moment lies in the z-direction, see chapter 3.4.2. An algorithm that estimates the MNP distribution $\boldsymbol{x}$, sensitive sensor axis $\boldsymbol{s}$ and magnetic dipole direction $\boldsymbol{m}$ can be seen in Algorithm 5.

Algorithm 5 Model Estimation

Given: iterations K, data $\boldsymbol{b}$, estimate of noise standard deviation δ, stopping term for discrepancy principle η, projection operator $\mathcal{P}_+$.
Initialize estimate of model parameters $\boldsymbol{s}$, $\boldsymbol{m}$, MNP distribution $\boldsymbol{x}$.
for $k = 1$ to K **do**
  $\boldsymbol{A} = \left(\boldsymbol{m}^T \otimes \boldsymbol{I}_{m\times m}\right) \boldsymbol{A}_{\mathrm{B}} \left(\boldsymbol{s} \otimes \boldsymbol{I}_{n\times n}\right)$
  $\boldsymbol{x}_{k+1} = \mathcal{P}_+ \left(\boldsymbol{x}_k - \|\boldsymbol{A}\|_2^{-2} \boldsymbol{A}^\intercal(\boldsymbol{A}\boldsymbol{x}_k - \boldsymbol{b})\right)$
  $\boldsymbol{m}_{k+1} = \boldsymbol{m}_k - \|\boldsymbol{M}_{\boldsymbol{m}}\|_2^{-2} \boldsymbol{M}_{\boldsymbol{m}}^\intercal \left(\boldsymbol{M}_{\boldsymbol{m}}\boldsymbol{m}_k - \boldsymbol{b}\right)$
  $\boldsymbol{s}_{k+1} = \boldsymbol{s}_k - \|\boldsymbol{M}_{\boldsymbol{s}}\|_2^{-2} \boldsymbol{M}_{\boldsymbol{s}}^\intercal \left(\boldsymbol{M}_{\boldsymbol{s}}\boldsymbol{s}_k - \boldsymbol{b}\right)$
  if $\|\boldsymbol{A}\boldsymbol{x}_{k+1} - \boldsymbol{b}\|_2 / \delta \leq \eta$ **then**
    return $\boldsymbol{x}_{k+1}, \boldsymbol{\theta}_k$
  end if
end for

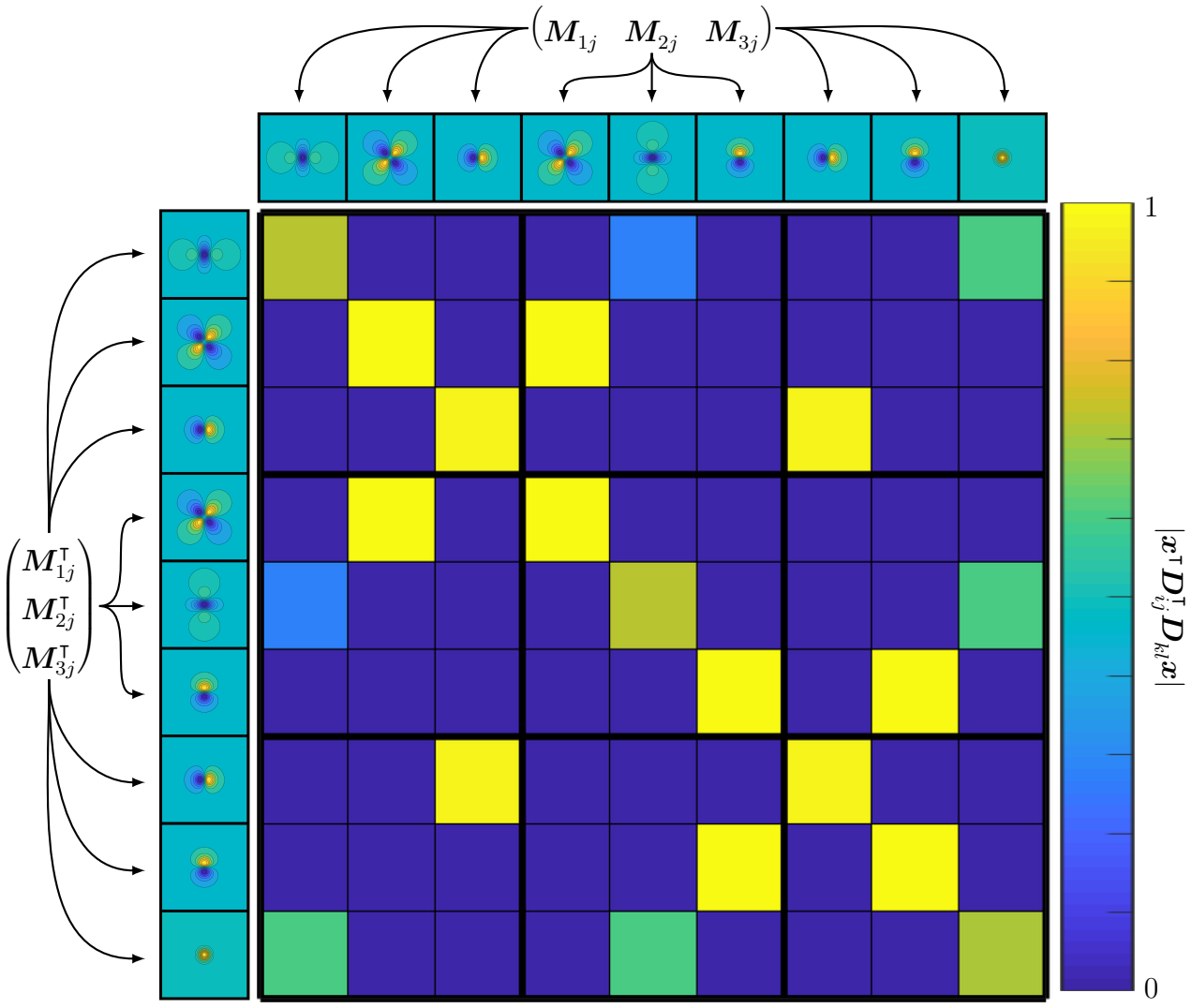


Figure 3.13: The matrix consisting of all quadratic forms shows the correlation between different magnetic field components for different moment directions. We see that most of the field components are orthogonal to each other, while there are some off-diagonal elements, meaning that there exists a correlation between the corresponding fields. However, they are still linearly independent.

3.4.4 Sensor Positioning and Geometry Influence

As explained in the last section, most of the projections of the magnetic dipole field are orthogonal to each other and few correlated, but linearly independent, fields remain. The reason the above method works is because of these orthogonalities.

Up to this point, we only considered the sensor to be a point-like sensor, which means that the actual size of the sensor did not play a role. To incorporate the size, one needs to extend the model and describe the influence of the sensor size/geometry via an additional spatial filter (another PSF function denoted by S). The sensor is thereby described as made up of small segments that contribute to the overall signal via some weights/coefficients.The PSF of the imaging system Ψ can then be described as the convolution of the dipole field PSF B_D and the geometry PSF S

$$\Psi = B_\mathrm{D} * S. \tag{3.86}$$

Alternatively, one can also think of the expanded problem as being a weighted sum of matrices $\boldsymbol{A}_i$, where the weights are given by the coefficients for the spatial filter of the sensor, i.e.

$$\boldsymbol{A} = \sum_i^N c_i \boldsymbol{A}_i. \tag{3.87}$$

However, the individual matrices $\boldsymbol{A}_i$ are very much similar to each other as the only differences stem from a slightly different spatial position. This way, they correlate highly and the underlying spectral decomposition is also similar, which means there exists an ambiguity about the correct basis in which the solution is expanded. In other words, one could choose from a linear combination of different bases corresponding to the matrices $\boldsymbol{A}_i$ and the coefficients c_i. One is thus unlikely to correctly estimate the correct filter coefficients c_i from MPM measurements. One would need to expose the sensor to highly inhomogeneous fields and measure the sensor response, such that one could assign these coefficients correctly.

The same argumentation basically goes for fitting sensor positioning, i.e. fitting the correct height. The reason is that the matrices are closely correlated, and thus one is able to fit the data appropriately without using the correct model matrix, i.e. there is an ambiguity left and one would need more information to infer the parameters correctly. For sensor positioning, the most important parameter to be estimated is the height, whereas the x and y position is not as important, since one can model the system as a

linear space invariant system (see chapter 3.2.3) such that the result would only yield an x/y shift and the PSF remains unaltered. The only statement one can make with respect to the z positioning is that there must exist a minimum distance such that all spatial frequencies in $\boldsymbol{b}$ could be expressed reliably (as depicted in Figure 3.14). However, this does not mean that the minimum distance is correct, so there still exists some ambiguity.

A possible way to combat these shortcomings may be knowing the norm of $\boldsymbol{x}$ beforehand and demanding the solution lies on some ball in a given metric via regularization. This, however, only reduces the possible parameters that explain the data, but does not definitely define them. To summarize, they cannot be estimated correctly via MPM measurements. Other means for estimating these parameters are needed.

3.4.5 Estimation of Magnetic Content

In this section, it will be shown how to estimate the magnetic content via the measurement itself. This is especially useful for regularization, because there one sets the norm of the spatial particle distribution. Thus, if the norm is known beforehand, the correct amount of regularization can be chosen. To introduce this, consider a plane in

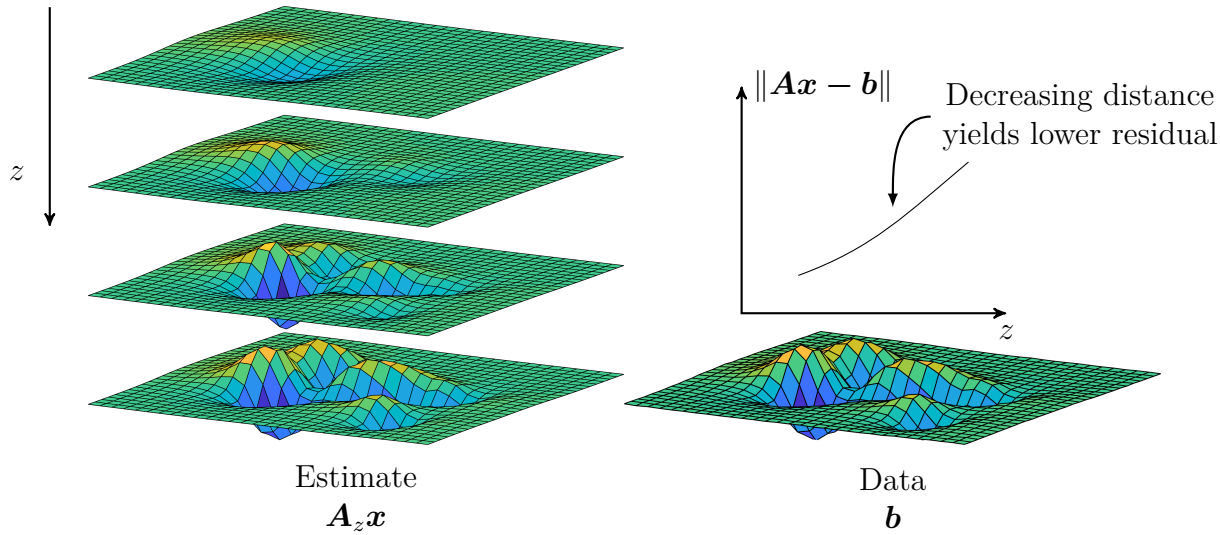


Figure 3.14: Estimating the correct distance z of the sensor to the sample involves the successive decrease of the z distance such that, at some distance, the measured data $\boldsymbol{b}$ can be closely approximated, thus yielding a lower residual norm $\|\boldsymbol{Ax} - \boldsymbol{b}\|$. This follows from allowing higher spatial frequencies (from the model $\boldsymbol{A}_z$) to be incorporated in the estimate $\boldsymbol{A}_z\boldsymbol{x}$.

the $x-y$ directions at a distance z from a dipole. Here, one can draw the magnetic field projections with respect to that coordinate system for different orientations of the dipole moment. For this recall Figure 3.4. Here the coordinate axes for the directions is used. The antisymmetric fields with respect to one spatial coordinate are interesting for the following reason: The magnetic field can be used to calculate the overall magnetic moment associated with that field.

For this, we do the following: We assume that the magnetic moment $\boldsymbol{m}$ is oriented in the z-direction, i.e.

$$\boldsymbol{m} = \|\boldsymbol{m}\| \begin{pmatrix} 0 \\ 0 \\ 1 \end{pmatrix} \tag{3.88}$$

and we measure the x-projection of the magnetic field, i.e. the sensitive axis $\boldsymbol{s}$ is:

$$\boldsymbol{s} = \|\boldsymbol{s}\| \begin{pmatrix} 1 \\ 0 \\ 0 \end{pmatrix} \tag{3.89}$$

then we can write

$$B_x = \frac{\mu_0 \|\boldsymbol{m}\| \|\boldsymbol{s}\|}{4\pi} \frac{3xz}{\left(x^2+y^2+z^2\right)^{5/2}}. \tag{3.90}$$

The projection above is antisymmetric with respect to the x-direction. We then integrate this projection in the x-direction. The result is

$$\int_{-\infty}^{x} B_x \mathrm{d}x = -\frac{\mu_0 \|\boldsymbol{m}\| \|\boldsymbol{s}\|}{4\pi} \frac{z}{\left(x^2+y^2+z^2\right)^{3/2}}. \tag{3.91}$$

We see that the function is of equal sign from $-\infty$ to $+\infty$ for the x and y variables. The next step involves integrating over the whole $x-y$ plane. The result is

$$\int_{-\infty}^{\infty}\int_{-\infty}^{\infty} -\frac{\mu_0 \|\boldsymbol{m}\| \|\boldsymbol{s}\|}{4\pi} \frac{z}{\left(x^2+y^2+z^2\right)^{3/2}} \mathrm{d}x\mathrm{d}y = -\frac{\mu_0 \|\boldsymbol{m}\| \|\boldsymbol{s}\|}{2}. \tag{3.92}$$

Thus, the given procedure is proportional to the magnetic moment, which is, mathematically speaking, the L_1 norm of the negative integrated dipole field projection. A

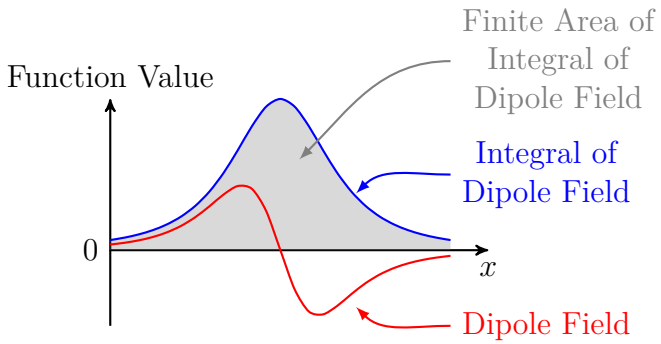


Figure 3.15: Integration of the dipole field projection yields a nonnegative function with finite L_1 norm, which is proportional to the magnetic moment producing the field.

visual guide for the procedure can be seen in Figure 3.15. It enables us to calculate the magnetic moment directly from the data, given that a sufficiently large region of the magnetic field is measured to approximate the procedure given above. It is important to point out that the result is independent of the z-distance. On one hand, this means that we can estimate the magnetic moment without knowing the z-distance, while on the other hand it means that there is no depth information from this procedure.

To generalize this approach, one can use an arbitrary distribution of magnetic moments, given that the measured projection is equal to the example given above. We here denote the field of a magnetic moment as B_D. We can write the magnetic field associated with a moment distribution, given as B_L, as

$$B_L(\boldsymbol{r}) = \int_\Omega B_D(\boldsymbol{r} - \boldsymbol{r}', \boldsymbol{m})\, \rho(\boldsymbol{r}')\, \mathrm{d}^3\boldsymbol{r}'. \tag{3.93}$$

As above, we assume the same direction of the magnetic moment $\boldsymbol{m}$, and integrate in the x-direction and then integrate over the $x - y$ plane. Because the integral is not dependent on the z-distance (as explained above), one gets the result

$$-\frac{2}{\mu_0 \|\boldsymbol{m}\| \|\boldsymbol{s}\|} \int_{-\infty}^{\infty}\int_{-\infty}^{\infty}\int_{-\infty}^{x} B_L(\boldsymbol{r})\, \mathrm{d}x\mathrm{d}x\mathrm{d}y = \int_\Omega \rho(\boldsymbol{r}')\, \mathrm{d}^3\boldsymbol{r}'. \tag{3.94}$$

Because the moment distribution ρ is nonnegative (i.e. $\rho \geq 0$), the following statement is obvious

$$\|\rho\|_1 = \int_\Omega \rho(\boldsymbol{r}')\, \mathrm{d}^3\boldsymbol{r}'. \tag{3.95}$$

Thus, the total amount of magnetic content can be computed from the magnetic field if the measured projection is the same as in the form above. It would also work for the projection in the y direction. This way, one can infer the total amount of particles from the measurement itself and can use this for the regularization via the projection onto the scaled L_1 ball in the proximal gradient method. One has to point out that, because the result is independent on the z-distance, any reconstruction from *any* height that is able to construct the vector $\boldsymbol{b}$ via its estimate $\boldsymbol{Ax}$ yields the same amount of MNP content.

3.5 Resolution Limits

Resolution in an imaging system refers to its ability to resolve features that are close together. The resolution for an imaging system such as a microscope normally uses the Point-Spread-Function as a figure of merit. This quantity tells about the spatial spread of a point source input to the imaging system. With the use of deconvolution techniques, the resolution can be enhanced, and the spread of the Point-Spread-Function can be reduced.

The proper assessment of the enhancement of a linear imaging system can be done via the so-called resolution matrix $\boldsymbol{R}$[124], [125]. The meaning of this operator is that no features can be reconstructed that are sharper than given by the columns, which in turn makes using *inverse operators intrinsically resolution limited* [126], [127]. To introduce this matrix, we start off with the system of equations that relate the particle distribution $\boldsymbol{x}$ with the magnetic field $\boldsymbol{b}$ via the model matrix $\boldsymbol{A}$

$$\boldsymbol{Ax} = \boldsymbol{b}. \tag{3.96}$$

The approach for solving this system of equations uses an inverse operator that, when applied to the left hand side of the equation, yields just the particle distribution $\boldsymbol{x}$, i.e.

$$\boldsymbol{A}^{\dagger}\boldsymbol{Ax} = \boldsymbol{x}. \tag{3.97}$$

Here, $\boldsymbol{A}^{\dagger}$ denotes the pseudoinverse of the model matrix $\boldsymbol{A}$. However, under normal circumstances, only an approximate inverse operator is used, which we will denote as $\boldsymbol{A}_k^{\dagger}$. The subscript k refers to an iteration number for different approaches of computing the pseudoinverse, which will be shown further below. The reason that only an approximate inverse operator is used is that, otherwise, noise would be amplified in the measurement

vector $\boldsymbol{b}$, which would yield unreliable/unphysical results for the particle distribution $\boldsymbol{x}$. We can thus write

$$\begin{aligned} \boldsymbol{A}_k^\dagger \boldsymbol{A}\boldsymbol{x} &= \boldsymbol{A}_k^\dagger \boldsymbol{b} \\ \boldsymbol{R}_k \boldsymbol{x} &= \boldsymbol{A}_k^\dagger \boldsymbol{b}. \end{aligned} \tag{3.98}$$

The operator $\boldsymbol{R}_k = \boldsymbol{A}_k^\dagger \boldsymbol{A}$ refers to the resolution matrix for a given approximate pseudoinverse. To compute the resolution matrix, we choose two different approaches: the singular value decomposition and gradient descent.

3.5.1 Resolution Matrix using SVD

We first make a singular value decomposition (SVD) of the matrix $\boldsymbol{A}$.

$$\boldsymbol{A} = \boldsymbol{U}\boldsymbol{S}\boldsymbol{V}^\intercal \tag{3.99}$$

One can use the truncated SVD. For this, one only uses the first k singular values, for the approximation of the operator $\boldsymbol{A}$. This will be denoted by the subscript k. One can use the SVD to explicitly write down an inverse operator $\boldsymbol{A}^\dagger$ as

$$\begin{aligned} \boldsymbol{A}^\dagger \boldsymbol{A} &= \boldsymbol{I} \\ \boldsymbol{A}^\dagger \boldsymbol{U}\boldsymbol{S}\boldsymbol{V}^\intercal &= \boldsymbol{I} \\ \Rightarrow \boldsymbol{A}^\dagger &= \boldsymbol{V}\boldsymbol{S}^{-1}\boldsymbol{U}^\intercal. \end{aligned} \tag{3.100}$$

If we only include the first k singular values/vectors, thereby only approximating the inverse operator, we write down the resolution matrix for the SVD $\boldsymbol{R}_{\mathrm{SVD},k}$

$$\begin{aligned} \boldsymbol{R}_{\mathrm{SVD},k} =& \boldsymbol{A}_k^\dagger \boldsymbol{A} \\ =& \boldsymbol{V}_k \boldsymbol{S}_k^{-1} \boldsymbol{U}_k^\intercal \boldsymbol{A}. \end{aligned} \tag{3.101}$$

The off-diagonal elements of the matrix describe the spatial spread of a single parameter in $\boldsymbol{x}$ or, more correctly, the columns of the resolution matrix $\boldsymbol{R}_k$. The more singular values are included, the more the resolution matrix becomes the identity matrix.

3.5.2 Resolution Matrix using Gradient Descent

We can also create a resolution matrix from gradient descent iterations, i.e.

$$\boldsymbol{x}_{k+1} = \boldsymbol{x}_k + \alpha \boldsymbol{A}^\intercal (\boldsymbol{b} - \boldsymbol{A}\boldsymbol{x}_k) \tag{3.102}$$

$$\boldsymbol{x}_{k+1} = \alpha \left(\sum_{n=0}^{k} (\boldsymbol{I} - \alpha \boldsymbol{A}^\intercal \boldsymbol{A})^n \right) \boldsymbol{A}^\intercal \boldsymbol{b}. \tag{3.103}$$

Here, α is the step size and is commonly given by

$$\alpha = \|\boldsymbol{A}^\intercal \boldsymbol{A}\|^{-1} \tag{3.104}$$

The optimal point $\boldsymbol{x}$ is given as the limit $\lim_{k\to\infty}$. Using the SVD of the matrix $\boldsymbol{A}$, we see that

$$\boldsymbol{x}_k = \alpha \boldsymbol{V} \left(\sum_{n=0}^{k-1} \left(\boldsymbol{I} - \alpha \boldsymbol{S}^2 \right)^n \right) \boldsymbol{S}\boldsymbol{U}^\intercal \boldsymbol{b} \tag{3.105}$$

and thus the resolution matrix for the gradient descent procedure $\boldsymbol{R}_{\mathrm{GD}}$ for the kth iteration is

$$\boldsymbol{R}_{\mathrm{GD},k} = \alpha \boldsymbol{V} \left(\sum_{n=0}^{k-1} \left(\boldsymbol{I} - \alpha \boldsymbol{S}^2 \right)^n \right) \boldsymbol{S}^2 \boldsymbol{V}^\intercal. \tag{3.106}$$

Since the sum is a geometric series, the result converges as long as $\alpha \boldsymbol{S}^2 < 1$ (i.e. all eigenvalues have an absolute value below 1), which also dictates the step size for the gradient descent procedure, since the matrices have to be normalized by their Euclidean norm. Thus, in the limit the resolution matrix would also converge to the identity matrix, i.e.

$$\lim_{k\to\infty} \boldsymbol{R}_{\mathrm{GD},k} = \alpha \boldsymbol{V} \left(\sum_{n=0}^{\infty} \left(\boldsymbol{I} - \alpha \boldsymbol{S}^2 \right)^n \right) \boldsymbol{S}^2 \boldsymbol{V}^\intercal \tag{3.107}$$

$$= \boldsymbol{V} \boldsymbol{S}^{-2} \boldsymbol{S}^2 \boldsymbol{V}^\intercal \tag{3.108}$$

$$= \boldsymbol{I}. \tag{3.109}$$

3.5.3 Assessing the Resolution of an Imaging System

We have introduced two resolution matrices based on different procedures to solve for the particle distribution $\boldsymbol{x}$, which are

$$\boldsymbol{R}_{\mathrm{GD},k} = \alpha \boldsymbol{V} \left(\sum_{n=0}^{k-1} \left(\boldsymbol{I} - \alpha \boldsymbol{S}^2 \right)^n \right) \boldsymbol{S}^2 \boldsymbol{V}^\intercal \tag{3.110}$$

$$\boldsymbol{R}_{\mathrm{SVD},k} = \boldsymbol{V}_k \boldsymbol{S}_k^{-1} \boldsymbol{U}_k^\intercal \boldsymbol{A} \tag{3.111}$$

Lets look into their meaning of these matrices in more detail. The resolution matrix can be thought of in two ways:

- The columns can be understood as the spatial spread of a delta-like input, i.e. the Point-Spread-Function
- The rows can be understood as the convolution of the MNP distribution with the Point-Spread-Function. It is the (scaled) averaging function of the system.

As can be seen in Fig. 3.16, the columns (blue enclosure of the matrix) represent the spatial spread of a delta-like input at particle position j. The red enclosure in the matrix refers to the weighted (the weights can be negative) sum of all field contributions from all MNP, such that it refers to an *averaging function* of the MNP responses. Because the system is a linear space-invariant system, the resolution is the same for all positions.

The peaks as shown in Fig. 3.16 become narrower with increasing iteration number. This means that the resulting overall resolution is given by the last iteration we are able to perform without fitting noise. For this, there are several criteria that can be used for the termination of the reconstruction [113]. It has to be emphasized that the resolution matrix relies on the analytic expressions presented here such that procedures like the proximal gradient algorithm for the L^1 projection cannot meaningfully produce a resolution matrix. The only cases where an analytic expression can be found is if the regularizer is differentiable (e.g. Tikhonov regularization), or semiconvergent properties of gradient descent are used[113], or truncation via a singular value decomposition is applied.

3.5.4 General Remark on the Notion of Resolution

A more general perspective on the resolution matrix (or rather, resolution map) is that it can be viewed as the effect of a single input on the vector $\boldsymbol{b}$, which subsequently needs

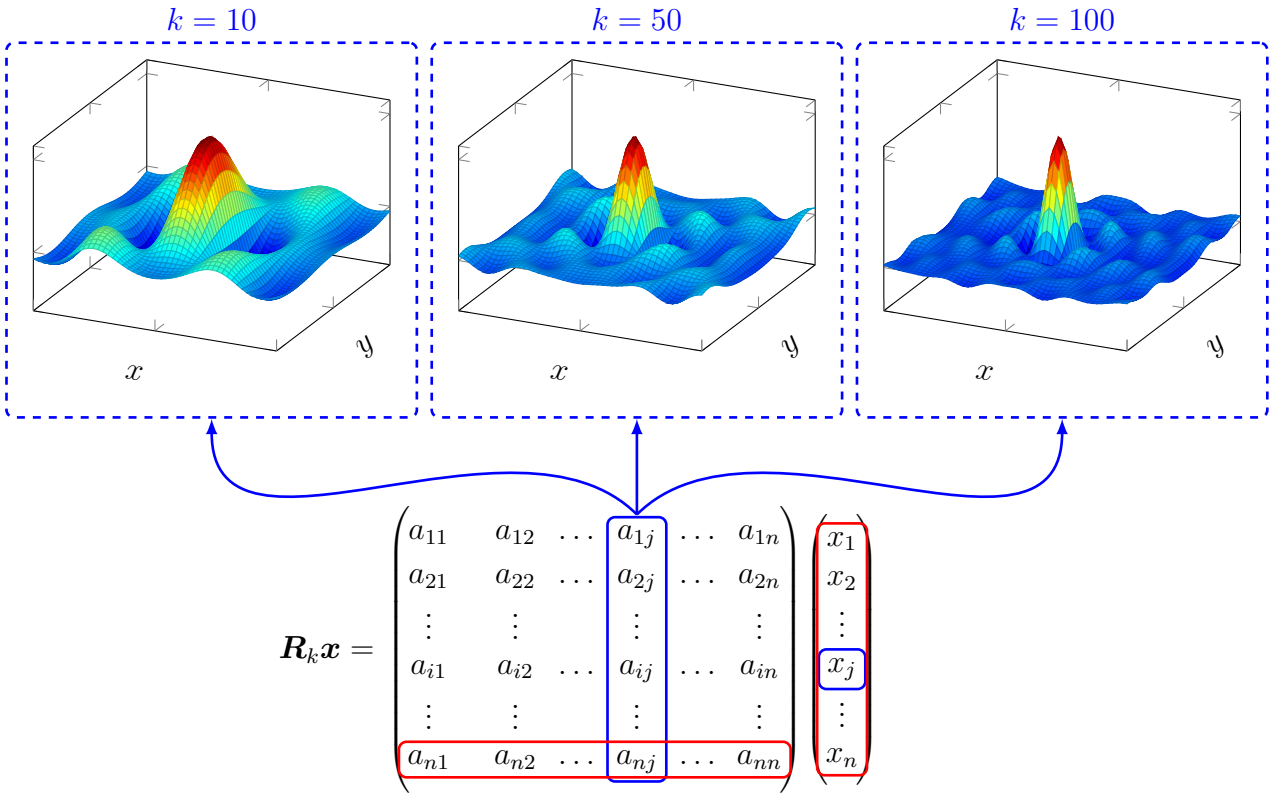


Figure 3.16: The columns of the resolution matrix $\boldsymbol{R}_k$ tells about the spread of a delta-like input, which can be thought of as the Point-Spread-Function of the system. For the inverse operator for different iterations k, the resolution matrix attains a more delta-like response, which means that the spread is reduced and that the resolution is enhanced.

to be inverted[128]. For this, we look at the change of the reconstruction $\delta\boldsymbol{x}_i$ from a unit change $\hat{\boldsymbol{e}}_i$ in $\boldsymbol{x}$ via the inversion operation $\mathcal{G}$, i.e.

$$\delta\boldsymbol{x}_i = \mathcal{G}(\boldsymbol{A}(\boldsymbol{x} + \hat{\boldsymbol{e}}_i)) - \mathcal{G}(\boldsymbol{A}\boldsymbol{x}) \tag{3.112}$$

In case of linearity, that is, if an analytic expression is found via an approximate (generalized) inverse $A_k^\dagger$, then we have:

$$\begin{aligned}\delta\boldsymbol{x}_i &= \mathcal{G}(\boldsymbol{A}(\boldsymbol{x} + \hat{\boldsymbol{e}}_i)) - \mathcal{G}(\boldsymbol{A}\boldsymbol{x}) \\ &= \boldsymbol{A}_k^\dagger\boldsymbol{A}\hat{\boldsymbol{e}}_i + \boldsymbol{A}_k^\dagger\boldsymbol{A}\boldsymbol{x} - \boldsymbol{A}_k^\dagger\boldsymbol{A}\boldsymbol{x} \\ &= \boldsymbol{R}_k\hat{\boldsymbol{e}}_i.\end{aligned} \tag{3.113}$$

Thus, in the linear case, the output $\delta\boldsymbol{x}_i$ from a unit change directly yields a column

of the resolution matrix, which tells us about the Point-Spread-Function / spatial spread of the parameter x_i of the particle distribution $\boldsymbol{x}$. Important to point out is that this inversion process is only dependent on the model itself and not on the particle distribution. This is a direct result of the linearity of the inversion process.
On the other hand, if the inverse map does not obey linearity, which is the case for e.g. L^1 regularization, we have:

$$\mathcal{G}\left(\boldsymbol{A}(\boldsymbol{x}+\hat{\boldsymbol{e}}_i)\right) \neq \mathcal{G}\left(\boldsymbol{A}\boldsymbol{x}\right) + \mathcal{G}\left(\boldsymbol{A}\hat{\boldsymbol{e}}_i\right). \tag{3.114}$$

As a result, the spatial spread $\delta\boldsymbol{x}_i$ of parameter x_i depends on the particle distribution $\boldsymbol{x}$ itself and a general statement of the resolution for a model inversion procedure, when the inverse map is not linear, cannot be given. Therefore, assessment of resolution is in this case is only beneficial if a standard reference is used, such that the results can be comparable.

3.6 Summary

In this chapter, all necessary models, criteria and tools to investigate an imaging system for MNPs using magnetoelectric sensors were introduced. A measurement approach, called Magnetic Particle Mapping, was proposed for measuring and mapping signals of MNPs using magnetoelectric sensors. Furthermore, a model that is able to describe the forward mapping of the spatial particle distribution $\boldsymbol{x}$ to the magnetic field $\boldsymbol{b}$ was derived.

Generalizations of the model were developed and their behavior for inversions were predicted on a mathematical basis. It was shown that, under some circumstances, parameters such as sensor projection axes $\hat{\boldsymbol{s}}$ and dipole orientations $\hat{\boldsymbol{m}}$ can be simultaneously estimated while solving for the magnetic particle distribution $\boldsymbol{x}$.

Colored MPM was developed based on the phase responses of MNPs, and appropriate inversion schemes for imaging different particle types under a nonnegativity constraint was outlined.

A technique was introduced that allows for the estimation of total magnetic content from measurements alone, which can be used for L^1 regularization. Other parameters, such as positioning and geometry influence of the sensor can not be predicted reliably via MPM measurements.

Furthermore, techniques for the estimation of resolution of imaging systems was

discussed for linear and nonlinear inversion maps, which will aid the determination of resolution for a given imaging system.

In the next chapter about simulations of the imaging system, we will verify the different models with their parameters in more detail. In the experimental chapter, an experimental investigation of the MPM system will be done.

CHAPTER 4

Simulation

4.1 Introduction

In this chapter, simulation studies will be performed based on the models introduced in the previous chapter.

First, the MPM model will be implemented for a planar 2D system, as depicted in Chapter 3.1. To give expectations about the reconstruction, inversion schemes will be implemented and results will be shown for visual inspection. The forward model will be implemented and the inversion schemes will be applied using different constraints. The importance of constraints will be highlighted by contrasting between unconstrained and constrained reconstructions. From this, the general applicability of the inversion scheme as well as general expectations for the reconstructions can be established.

Afterwards, colored MPM will be investigated and discussed using the approach developed in Chapter 3.3.3. The necessities for colored MPM will be found based on simulations and signal to noise ratios. The circumstances under which colored MPM is possible will be determined.

Furthermore, the model estimation techniques as developed in Chapter 3.4 will be implemented. The ability for the simultaneous reconstruction and model estimation will be elucidated and the necessities for the correct estimation will be highlighted.

Then, resolution limitations for MPM will be simulated and discussed with respect to signal-to-noise ratios and distances to the sample plane. This will set the expectations for the imaging system proposed in this thesis. Further enhancement possibilities and directions will be developed for better imaging.

The last part of this chapter deals with the ability for depth imaging as a precursor for 3D imaging in MPM. Limitations of the approach and resolution expectations will be set using a circular 2D system, whose measurement positions lie outside the perimeter of the sample domain. From this, an outlook and directions for 3D imaging will be set.

4.2 Magnetic Particle Mapping

4.2.1 Objectives

Prior to detailed simulations, general simulation steps will be performed for the Magnetic Particle Mapping (MPM) approach. In this section, the MPM model will be implemented by solving the inverse problem. The inverse solution will be investigated with respect to parameters such as distance to the sample and projections used. Furthermore, comparability of estimation and ground truth will be shown using the correlation coefficient. The method used will be the proximal gradient method (see section 3.3.2.3). A Signal-to-Noise ratio (SNR) of 30 dB will be used. For the denotation of a SNR, the average signal amplitude to standard deviation of the signal amplitudes will be used. For this, a standard distribution with the letters "B7" is used. It must be emphasized that this SNR depends on the sample used.

4.2.2 Methods

4.2.2.1 Simulation

For the simulation of the data, a reference MNP distribution is taken (see Figure 4.1). The source domain is chosen to be 20×20 mm^2 with an equidistant discretization of 50×50 points. The measurement domain is taken to be of the same dimensions. The distance between measurement domain and source domain varies from 0.1 mm to 5 mm.

4.2.2.2 Reconstruction

For the reconstruction, two procedures are taken. A gradient descent procedure (GD) with and without a projection step into the nonnegative orthant (GD+NN) are used. As a stopping criterion, the discrepancy principle is used and set to be $\eta = 1.1$ (c.f. [113]). For each finished reconstruction, the correlation coefficient (CC) and the total magnetic content is computed and compared to the reference distribution.

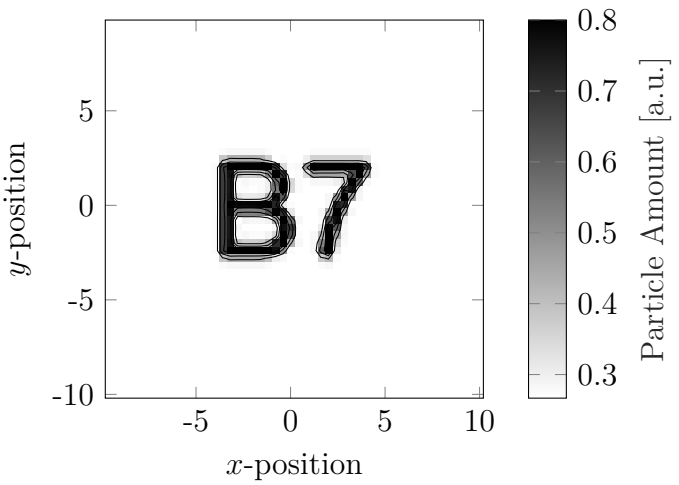


Figure 4.1: MNP reference distribution used for simulations and reconstructions.

4.2.3 Results and Discussion

The results of the simulations are shown in Figure 4.2. It can be seen that the correlation coefficient decreases for increasing z-distance for both inversion schemes. The GD+NN procedure lies above the GD procedure for all distances. The relative error of the total magnetic content to the reference distribution ranges from 26% to 61% for the GD procedure and from 10% to 24% for the GD+NN procedure. A peak of the error can be seen at a distance of about 0.8 mm for both inversion schemes. From the results, it can be seen that the use of a projection step into the nonnegative orthant yields better results, both with respect to quantification and the correlation coefficient. For the quantification, the L^1 norm of the reconstruction was taken. Thus, it also includes negative parts in the reconstruction of the GD inversion. The peak in the relative error to the magnetic content could be due to the discretization of the source domain, because its discretization step amounts to 0.4 mm. Furthermore, the noise may also play a role, because here it is set by the maximum amplitude of the magnetic field. The correlation coefficient, which is a measure of the spatial accuracy of the reconstruction, is high for small z-distances. This implies that a small distance is better for imaging. This is expected, since more features (i.e. higher spatial frequencies) are present in the magnetic field, such that more information in the reconstruction can be used. Therefore, small distances will be used and nonnegativity constraints will be enforced for the experimental investigation.

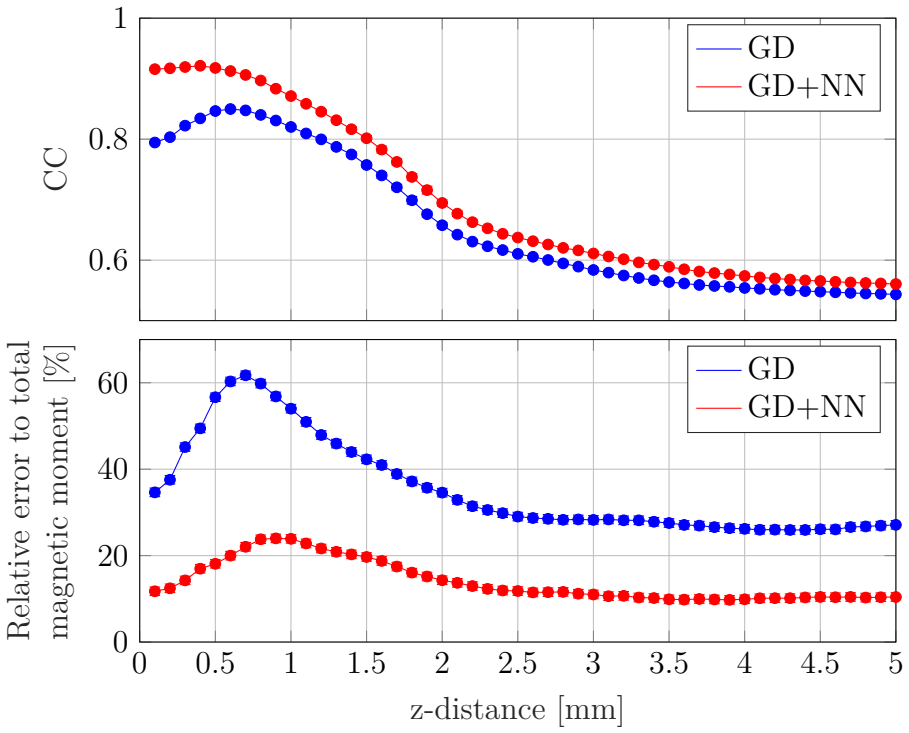


Figure 4.2: Correlation coefficient (CC) and relative error of total magnetic moment of the reconstructions for gradient descent (GD) and gradient descent with nonnegativity constraint (GD+NN). Noise level is set to 30 dB and error bars are given from the standard deviation from 30 repeats. The error bars are within the symbol size.

4.3 Colored Magnetic Particle Mapping

4.3.1 Objectives

Distinctions between the behaviors of MNPs can be important in a biomedical context, because changes in the behavior may indicate that the particle is bound to some entity, indicating biological activity. Colored MPM permits imaging different magnetic behaviors explicitly.

In this chapter, the ability of an MPM system to distinguish different particle behaviors will be investigated. Different MNP types will be shown with different colors, hence the common name ”colored” MPM. The effect of noise on the reconstruction will be investigated via the correlation coefficient. The simulation study will give information about the bare necessities for proper reconstructions in colored Magnetic Particle Mapping. Dependencies of the spatial accuracy of the reconstruction will be investigated

with respect to angle differences of the MNP responses for different signal-to-noise ratios.

4.3.2 Methods

The methods used will involve the proximal gradient descent technique using a new projection operator $\mathcal{P}_+^{\boldsymbol{Q}}$ (see Appendix A.6) for the inclusion of a nonnegativity constraint for complex reconstructions in $\boldsymbol{x}$ to give proper (real) particle distributions.

The underlying distribution $\boldsymbol{x}_{true}$ will be split into two parts consisting of a single symbol of the expression "B7" (i.e. "B" and "7"). Each part will get an associated phase, corresponding to the phase of the particles response. Here, it is assumed that the particles generate the same amplitude per unit mass. Furthermore, the noise level is adjusted from 5 dB up to 30 dB in 5 dB increments. Each reconstruction is run 25 times and the average is shown with the associated errorbar based on the standard deviation. As a stopping criterion for the iterations, the discrepancy principle was taken for $\eta = 1.1$. Since the projection operator enforces a nonnegativity constraint for each step, this stopping criterion is not necessarily reached, such that a maximum iteration number of 500 was taken.

4.3.3 Results and Discussion

The results for a (noiseless) reconstruction of the particle distribution is shown in Figure 4.3. As can be seen from the Figure, both the "B" and "7", shown in red and blue respectively, can be reconstructed reliably and resolve the overall distribution "B7". Under these circumstances, the phase differences between the two MNP types is irrelevant as long as the particle type matrix $\boldsymbol{Q}$ (see Appendix A.6 and section 3.3.3) is invertible (i.e. a phase difference exists) and are not limited by machine precision. Figure 4.4 shows the effect of the angle difference of the particle types on the correlation coefficient for different SNRs. The top plot includes the usage of the projection operator, whereas the bottom plot does not distinguish between the particle types, i.e. it does not include a nonnegativity constraint and hence the reconstruction amplitude of the complex values are shown. The top plot shows that as the angle difference approaches zero, the correlation coefficient decreases steadily. The behavior of the decrease is steeper with increasing SNR, though the onset of the decrease is lowered in comparison to small SNRs.

As a comparison, the bottom plot shows the correlation coefficient as a function of the angle difference when no projection operator is applied, i.e. nonnegativity is

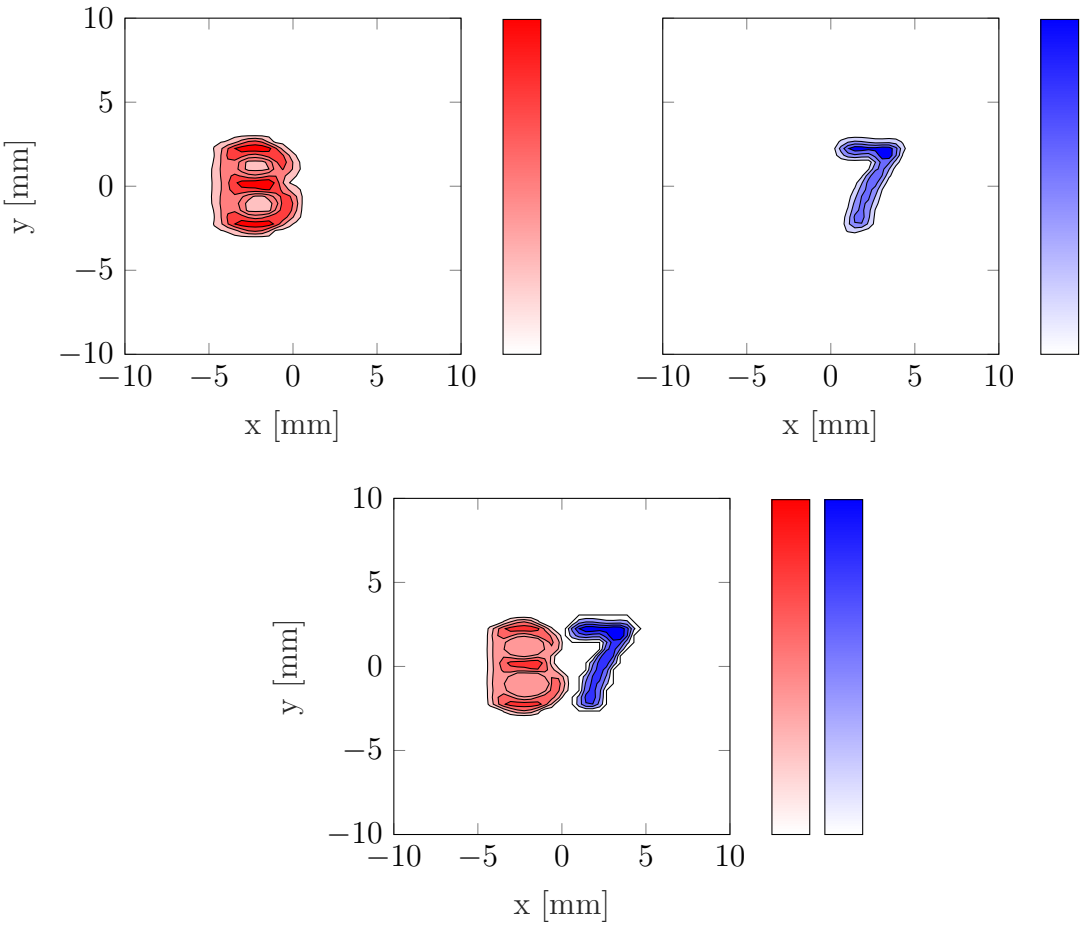


Figure 4.3: Reconstruction of the simulated colored MPM signal from two different MNP types. Red indicates MNP type I and blue indicates MNP type II.

not imposed. Here, the reconstruction is constant for all values of angle difference, as opposed to the case when the projection operator is applied. For colored MPM, the phase difference between the particle types/responses is necessary for proper reconstruction using a nonnegativity constraint. Ideally, the phase difference is at least $\Delta\phi \geq 10°$ to compute reconstructions with high spatial accuracy. The spatial accuracy of the reconstruction is increased with increasing SNR, which is to be expected, because more information from the data $\boldsymbol{b}$ is available for the reconstruction that is not dominated by noise.

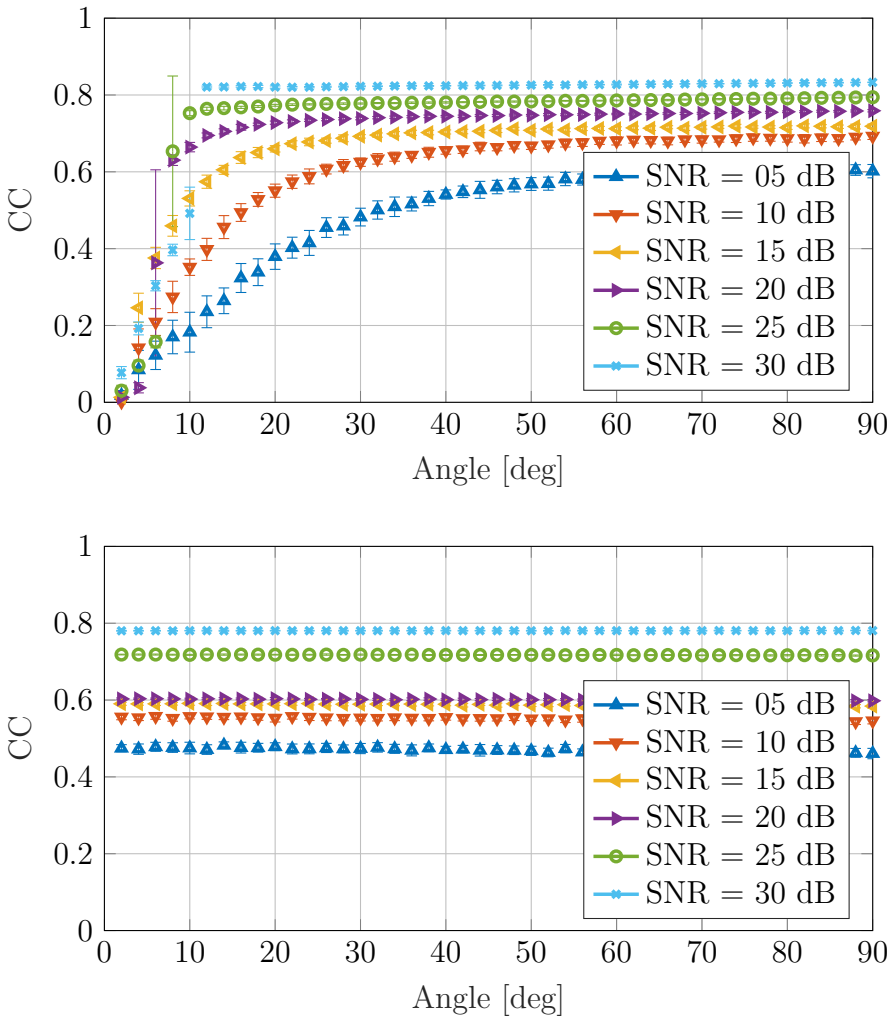


Figure 4.4: Correlation coefficient for the reconstructions for different MNP phase responses for several SNRs. Top: Colored MPM is performed such that an additional projection $\mathcal{P}_+^{\boldsymbol{Q}}$ is used for the enforcement of a nonnegativity constraint. The colored images can be extracted from a transformation via $\boldsymbol{Q}^{-1}$ and taking the real and imaginary parts to distinguish both MNP types. Bottom: Reconstruction with no constraints.

4.3.4 Conclusion

The implication for the usefulness of colored MPM is that it could be used in a biological context. For example, if MNP behavior changes due to incorporation in a cell as compared to a free MNP, this change in behavior can be used for distinct imaging of the MNP. It has been shown that the MNP dynamics change in a cellular environment [64], [129]. This may be an issue in the sense that supplying particles to the cells may lead

to a saturated uptake, such that both free MNP and MNP in cells are present. From the approach outlined here, necessary angle differences in the particle behaviors were pointed out.

4.4 Model Estimation

4.4.1 Objectives

The correct reconstruction of the particle distribution is paramount for any imaging application for MNPs. Since the model itself depends on parameters related to the sensor or external magnetic fields, knowing these beforehand is of major importance. If some of these parameters are only approximately known, they can cause the formation of artifacts in the reconstruction, which thus shows erroneous MNP distributions. Therefore, the adaptive model, described in Chapter 3.4, that includes these parameters is simulated and investigated.

For this, an expectation of the reconstruction errors using incorrect model parameters will be set to see the parameters influence on the reconstructions. Then, adaptive models will be used to both estimate the MNP distribution and the parameters, such as projection axis and magnetic moment direction. As a figure of merit, the correlation coefficient and the angle difference between the estimations and ground truths (particle distribution $\boldsymbol{x}$, projection axis $\boldsymbol{s}$, magnetic moment direction $\boldsymbol{m}$) will be used.

4.4.2 Methods

A set of different approaches with respect to the constraints will be used such that one can show the necessity of giving constraints for the correct estimation of the parameters. The reconstructions will be done via the GD with and without nonnegativity constraints. The following cases will be investigated:

1. Projection axis $\boldsymbol{s}$ is fixed to arbitrary directions and magnetic moment direction $\boldsymbol{m}$ is known.
2. Projection axis $\boldsymbol{s}$ is unknown and magnetic moment direction $\boldsymbol{m}$ is known.
3. Projection axis $\boldsymbol{s}$ is unknown and magnetic moment direction $\boldsymbol{m}$ is unknown.

4.4.2.1 Simulation

The source domain of the MNP distribution $\boldsymbol{x}$ and the simulated data $\boldsymbol{b}$ is set to be of dimensions 50×50 and is distributed equidistant over 20×20 mm^2. The distance between sensor and sample is set to 1 mm.

4.4.2.2 Reconstruction

For the simulations, the proximal gradient descent procedure will be used. Additional update steps on the model parameters $\boldsymbol{s}$ and $\boldsymbol{m}$ will be used for the respective cases. For the reconstructions $\boldsymbol{x}_{recon}$, the correlation coefficients to ground truth distribution $\boldsymbol{x}_{true}$ and the reconstruction are computed. Furthermore, the quantification accuracy via $\frac{\|\boldsymbol{x}_{recon}\|_1}{\|\boldsymbol{x}_{truth}\|_1}$ is computed as well. The stopping criteria are either the discrepancy principle with $\eta = 1.1$ if noise is present, or a maximum number of 500 iterations if the result aims to show it's applicability for correct estimation.

4.4.3 Results and Discussion

4.4.3.1 Case 1

Figure 4.5 shows the quantification and correlation coefficients in terms of the direction of the sensitive axis for the inversion process. The correct model lies in the x-axis, as is denoted by the blue lines. It can be seen that the correlation coefficient is highest in this axis for both the gradient descent and gradient descent with nonnegativity constraint. The quantification for the gradient descent with nonnegativity constraint has its largest value in the direction of the sensitive axis (x direction). On the other hand, for the gradient descent procedure, there is no clear directionality given for the proper quantification, although the only reliable quantification should be achieved when the model for the correct direction is used. Thus, there can be a quantification error if the wrong model is used, as well as a decreased correlation coefficient. For this reason it is necessary to find the correct model for the measurement $\boldsymbol{b}$.

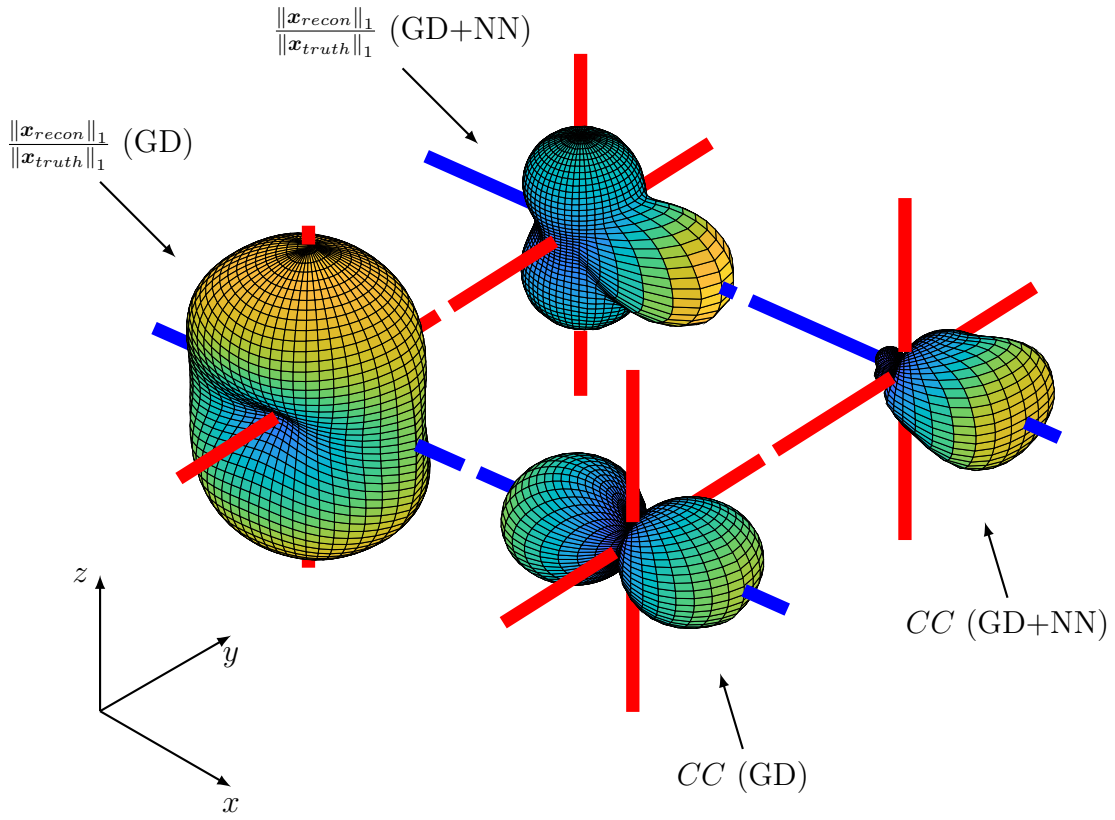


Figure 4.5: Quantification accuracy and correlation coefficient as a function of the choice of model for the reconstruction. The blue direction denotes the x direction for the sensitive sensor axis, the red ones the y and z axes, respectively. The true model has a sensitive axis in the positive x direction, as indicated by the coordinate system drawn.

4.4.3.2 Case 2

As was shown for the previous case, a nonnegativity constraint enhances the reconstruction. Even though the cost function is strictly convex (c.f. 3.4.2), the reconstruction for any model could explain the data. Important is then the nonnegativity constraint, such that it acts as a guide to find the correct model. For the case where the magnetic moment direction is known and the sensitive axis has to be estimated while computing the MNP distribution, Algorithm 4 will be used. For each MNP distribution update, the estimated sensitive axis is updated. An overview of the iterations of the inversion can be seen in Figure 4.6. The data for the reconstruction was computed via a sensitive axis that lies in the x-y plane at an angle of 0° (x-direction). The algorithm is initiated via a sensitive axis direction of 90°. It can be seen that the angle approaches a value of 1° for the 50th iteration, and that the MNP reconstruction yields the letters "B7", which indicates that the algorithm is able to simultaneously find the MNP distribution and the sensitive axis direction.

To further investigate the algorithm, a true projection axis for the data is chosen in the x-direction. The algorithm is initiated using a projection axis for all spatial directions which lie on the unit sphere. To quantify the ability to correctly estimate the MNP distribution, the correlation coefficient is taken of the final iteration. Then, the correlation coefficient from the MNP reconstruction for the initial direction are used as a radius for that direction. In the case of correct estimation of the projection axis for all initial directions, the result would be a sphere. Figure 4.7 shows the results. It can be seen that for the initial sensitive axes in the upper half plane ($z \geq 0$), the algorithm converges to the correct MNP distribution, indicated by the large correlation coefficient. For some regions in the lower half plane, the algorithm fails to converge to the correct MNP distribution. However, if a good guess is taken for the true sensitive axis, the algorithm will simultaneously find the sensitive axis and the MNP distribution.

4.4.3.3 Case 3

Next, the case when both the projection axis and the magnetic moment orientation are unknown is considered. In this case, the estimation procedure involves updating the particle distribution, followed by an update of the projection axis of the sensor, followed by an update on the magnetic moment direction. Whether the projection axis or the magnetic moment direction is updated first is irrelevant, because there exists an ambiguity between the magnetic moment direction and the projection axis, as is

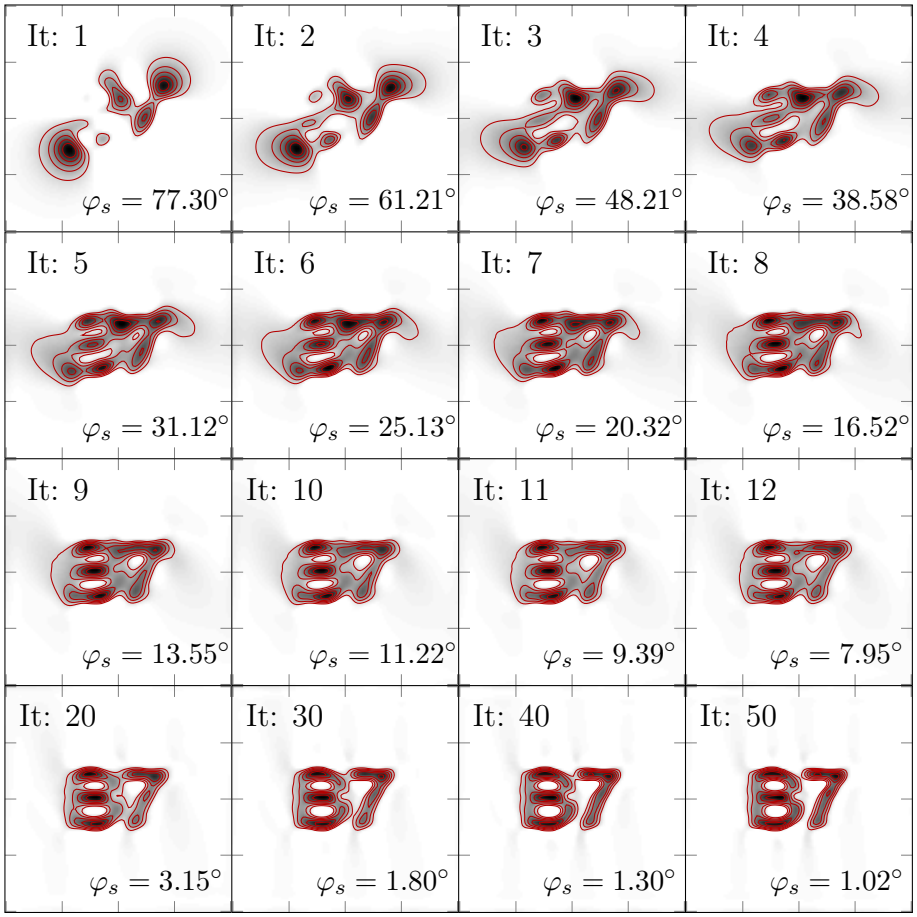


Figure 4.6: Adaptive reconstruction to iterate the MNP distribution $\boldsymbol{x}$ and the sensitive axis $\boldsymbol{s}$ simultaneously. Shown are individual iterations as denoted in the upper left corner of each subplot. In the lower right corner of each subplot the estimated sensitive axis direction (polar) is shown. The ground truth for this axis has an angle of $\varphi_m = 0°$. The black color indicates MNPs and the red lines are level sets to guide the eye.

apparent from the bilinear form that dictates the impulse response of the system and the fact that the matrix of the bilinear form is symmetric (c.f. Eq. 3.3).

To investigate the reliability of the proposed algorithm (see Algorithm 5), one sweeps the parameter space for all orientations of the projection axis and magnetic moment direction. We choose the correct (i.e. to be estimated) projection axis and magnetic moment direction in the x- and z-direction, respectively. In addition, a box constraint on the projection axis $\boldsymbol{s}$ and magnetic moment direction $\boldsymbol{m}$ in the form of a predetermined half-space is imposed. That is, the x component of the projection axis cannot be negative and the z component of the magnetic moment direction cannot be negative.

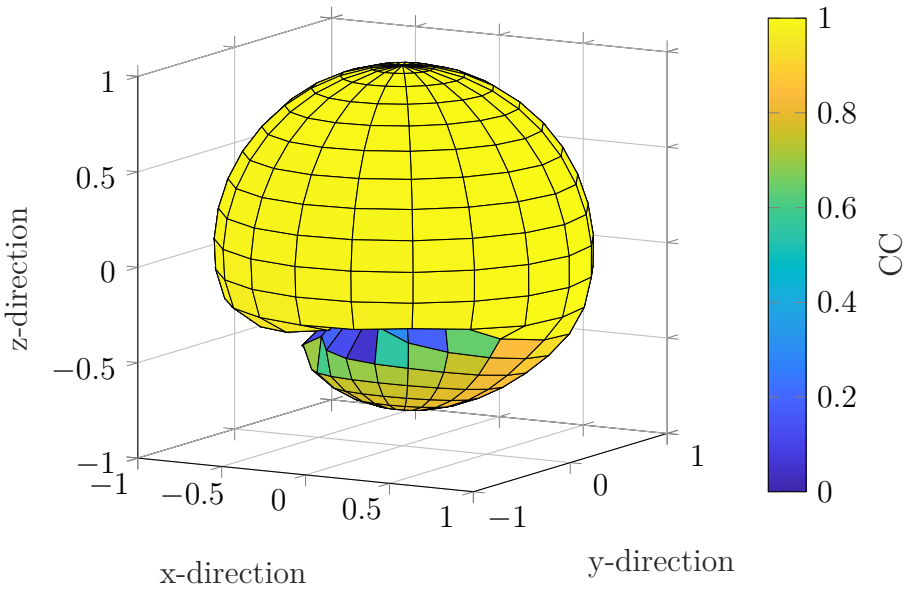


Figure 4.7: Correlation coefficient for different initial sensitive axis directions. The true sensitive axis lies in the x direction. For the upper half space ($z \geq 0$), the correlation coefficients form a sphere, indicating that the algorithm converges to the true MNP distribution. For the lower half plane, there are regions where the right MNP distribution is not found via the algorithm.

It is furthermore imposed that the projection axis and magnetic moment direction is of unit length. A nonnegativity constraint on the particle distribution $\boldsymbol{x}$ is imposed as well. In Figure 4.8 one can see the correlation coefficient of the estimated MNP distribution to the ground truth as well as the angle differences of the estimated projection axis of the sensor and the angle difference of the estimated magnetic moment direction (with respect to the ground truths, respectively). It can be seen that the correlation coefficient CC is high for most parameter combinations of the directions of the sensitive axis $\boldsymbol{s}$ and dipole orientation $\boldsymbol{m}$, as indicated by their direction angles in spherical coordinates. For the dipole moment $\boldsymbol{m}$, the angles θ_m (polar) and φ_m (elevation) describe the direction, and for the sensitive axis $\boldsymbol{s}$ the angles θ_s (polar) and φ_s (elevation). Furthermore, it can also be seen that for initial parameter combinations where to correlation coefficient is large, the angle between the true and estimated directions of $\boldsymbol{s}$ and $\boldsymbol{m}$ are also small. This indicates that the algorithm is capable of finding the correct MNP distribution while also estimating the directions of $\boldsymbol{s}$ and $\boldsymbol{m}$ correctly.

4.4.4 Conclusion

It was shown that the proposed adaptive inversion scheme is able to estimate both the model parameters and MNP distribution simultaneously. The approach shown is able to overcome unknown initial information, such as sensor sensitivity direction, and estimate it correctly. Thus, the generalized model can be used in circumstances where the sensor sensitive axis is not known exactly or incorrectly measured, and thereby reduces sources of error in the model for better reconstructions, which ultimately improves the imaging application.

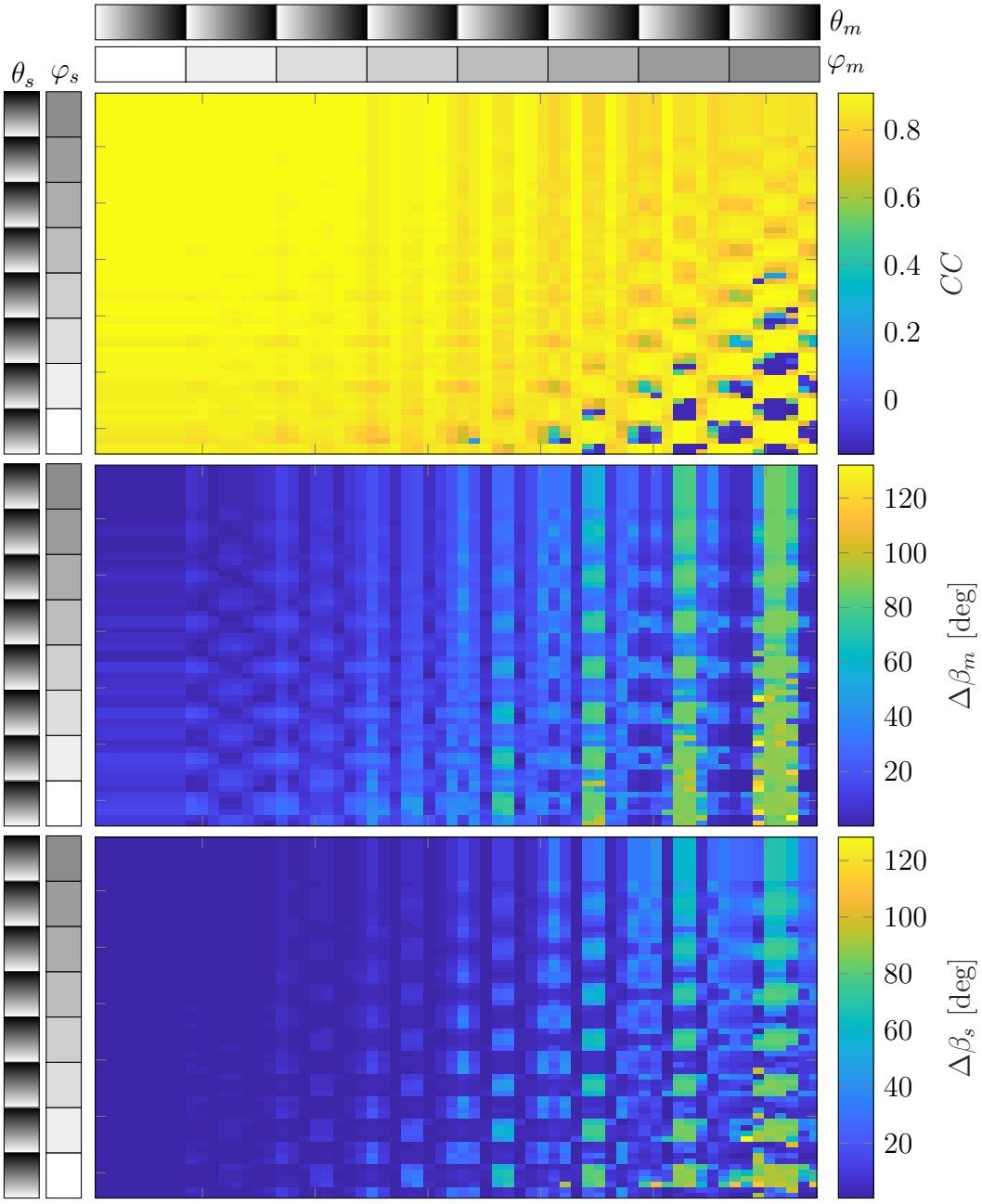


Figure 4.8: Top: Correlation coefficient of the reconstruction to the ground truth. Middle: Angle error of the magnetic dipole direction. Bottom: Angle error of the sensitive axis direction. All points in the graph are results for a different combination of an initial dipole field direction, indicated by angles θ_m (polar) and φ_m (elevation), and sensitive axis directions, indicated by angles θ_s (polar) and φ_s (elevation).

4.5 Resolution

4.5.1 Objectives

Resolution in imaging is a figure of merit that sets the expectations and capabilities for an imaging technique. A definite description for resolution is tricky and an elaborate assessment is needed. This section deals with the evaluation of resolution for the planar 2D MPM system. Dependencies of resolution on SNR and distance to the measurement plane will be investigated. From this, general limits of the imaging system can be derived. These limits are then expanded on in the discussion and put into the context of this thesis.

4.5.2 Methods

For the evaluation of the resolution, linear inversion schemes for the inverse problem are used. This way, the statements made on resolution are independent of the particle distribution (c.f. 3.5.4). For the denotation of an SNR, the average signal amplitude to standard deviation of the signal amplitudes will be used. For this a standard distribution with the letters "B7" is used. It must be emphasized that this SNR is dependent on the sample used. For the computation of a resolution matrix $\boldsymbol{R}_k$ (cf. 3.5.3), the gradient descent (GD) procedure and truncated singular value decomposition (TSVD) will be used. Here, the associated SNR will be computed from the ratio of the maximum (and absolute) value in $\boldsymbol{b}$ to the residuals $\boldsymbol{Ax} - \boldsymbol{b}$ standard deviation. Computations are done on a 50×50 grid for a total dimension of 20×20 mm^2 for different z-distances. As a resolution measure, the Full-Width-Half-Maximum (FWHM) of the corresponding Point-Spread-Functions (PSF) will be used.

4.5.3 Results and Discussion

The results of achievable resolution are shown in Figure 4.9 for two different z-distances (top: 1mm and bottom: 2mm) for two different spatial directions in x and y directions. The dashed and solid lines distinguish between the resolutions for the x and y directions, which implies that the achievable resolution is *spatially anisotropic*. The achievable FWHM as a measure of resolution decreases with increasing SNR, meaning that the overall resolution is better with increasing SNR. It can be seen that the two procedures

for the assessment of resolution, GD and TSVD, converge to the same values for high SNR, which is to be expected, since they ultimately should converge to the same optimal solution. The curves shown for the TSVD approach are more jagged since they can only be added in increments related to the singular vectors. The GD curves are smoother, because the step size can be chosen arbitrarily (as long as the step size is below a maximum value, cf. 3.5.2). For both distances, it can be noted that the approximate

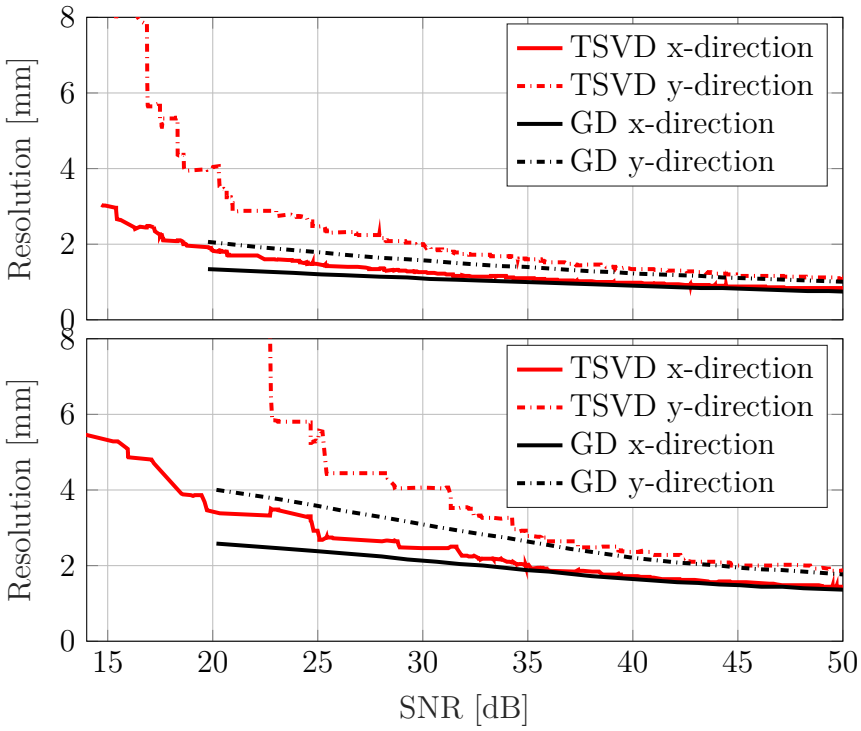


Figure 4.9: Achievable resolution for TSVD and GD techniques as a function of SNR for a 2D system with Top: 1 mm sensor distance and Bottom: 2 mm sensor distance.

converging resolution is slightly below the distance to the sample. This implies that it is difficult to have a resolution that is better than the distance to the sample with the outlined MPM setup. Since the model used involved a point-like sensor, the resolution may be worse if one considers a spatially extended sensor, since it averages the magnetic field over its dimension to constitute the magnetic field signal.

4.5.4 Conclusion

From the results it can be concluded that the achievable resolution for a 2D system as outlined here is about the same as the z-distance to the sample. Further enhancement of the imaging system would need to employ inhomogeneous fields such that measurements are more distinct from each other. The results shown here are done for a point-like sensor and perfect model, and thus can only be worse in reality. The anisotropic resolution also implies preferential directions for imaging the sample. If any structure on the MNP distribution is known beforehand, the resolution could be increased by using specific inversion schemes, though no qualitative assessment can be done, instead merely heuristics and direct visual comparisons. For instance, the "B7" sample used in these simulation studies is sparse and piece-wise constant, which would best be reconstructed using Total-Variation (TV) regularized techniques [130], because it is perfectly applicable for these kinds of distributions. Another example would be if only very few sources are present, one would need an $\|\boldsymbol{x}\|_0$ regularized approach (which would be NP-hard and non convex), which fixes the number of free parameters [126]. These approaches could explain the data just as well as the conventional approach. Yet, if nothing is known about a spatial structure of the particle distribution beforehand, one is limited to the resolutions as were shown here.

4.6 Resolution in Depth Imaging

4.6.1 Objectives

A demand for 3D imaging arises in the context of MPM if one aims to image cell distributions within a 3D scaffold. As such, one needs to be able to resolve sources reliably that are furthest away from the sensors, i.e. deeper lying sources. As we direct our attention to the 3D imaging case for MPM, the imaging problem becomes much harder. The description of the data $\boldsymbol{b}$ via the estimate $\boldsymbol{Ax}$ can be ambiguous due to the lack of distinct features in $\boldsymbol{b}$ from the inner sources. This lack of features stems from the fact that inner sources can only contribute low frequency components to the data, which can hence also be described by near-surface MNP distributions. In this chapter, an approach is discussed that aims to give insight into 3D imaging for MPM and gives directions for enhancements in this context. For this a 2D depth imaging system will be proposed, which could easily be extended to a 3D system. A circular setup will be

proposed, where measurements are simulated on the outside the perimeter of the circular sample. The aim is to evaluate imaging the MNP distribution inside the circular sample, especially for deeper lying sources. The system will be investigated on simulations with respect to achievable resolution for different signal to noise ratios.

4.6.2 Methods and Propositions

A circular sample is taken where the measurements are simulated from near the perimeter of the sample, as can be seen in Figure 4.10. For this approach all measurements

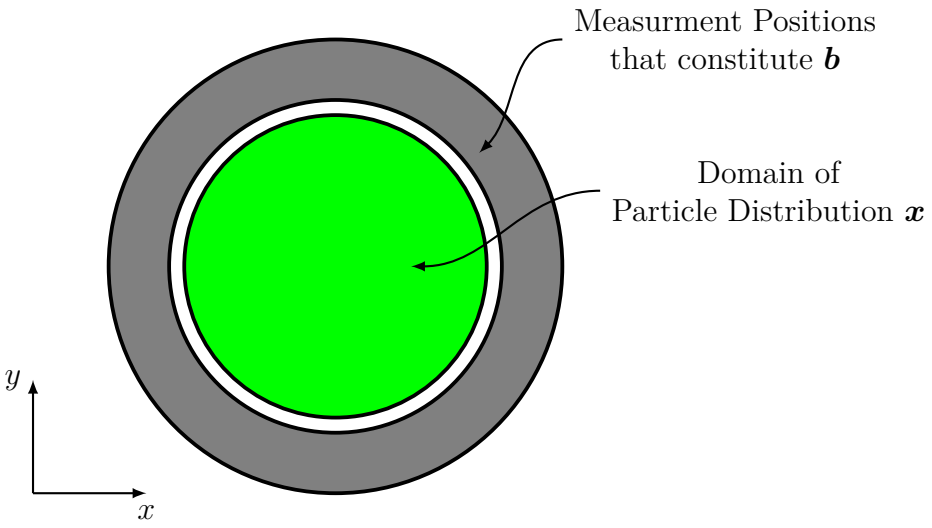


Figure 4.10: Schematic setup for a depth imaging system. The green circle describes the domain of the MNP distribution $\boldsymbol{x}$ and the gray area describes the measurement positions for $\boldsymbol{b}$.

for a single radius can be measured by rotating the sample and keeping the sensor position fixed. This way, one can expect the systems impulse response to be *rotationally invariant*. Furthermore, the initial orientation of the sensors sensitive axis can be chosen and thereby gives different possibilities for the response of the imaging system, which could yield better resolution for deeper lying sources and hence enhance the imaging in that respect. Here, two distinct possibilities will be considered and compared. These possibilities refer to two different sensor orientations, yielding different projections of the magnetic field. The associated averaging functions (c.f. 3.5.3) to these cases are shown in Figure 4.11. The averaging function gives insight into the contribution strength for each point in the MNP distribution $\boldsymbol{x}$ (e.g. in units of Tesla per unit mass MNP). It

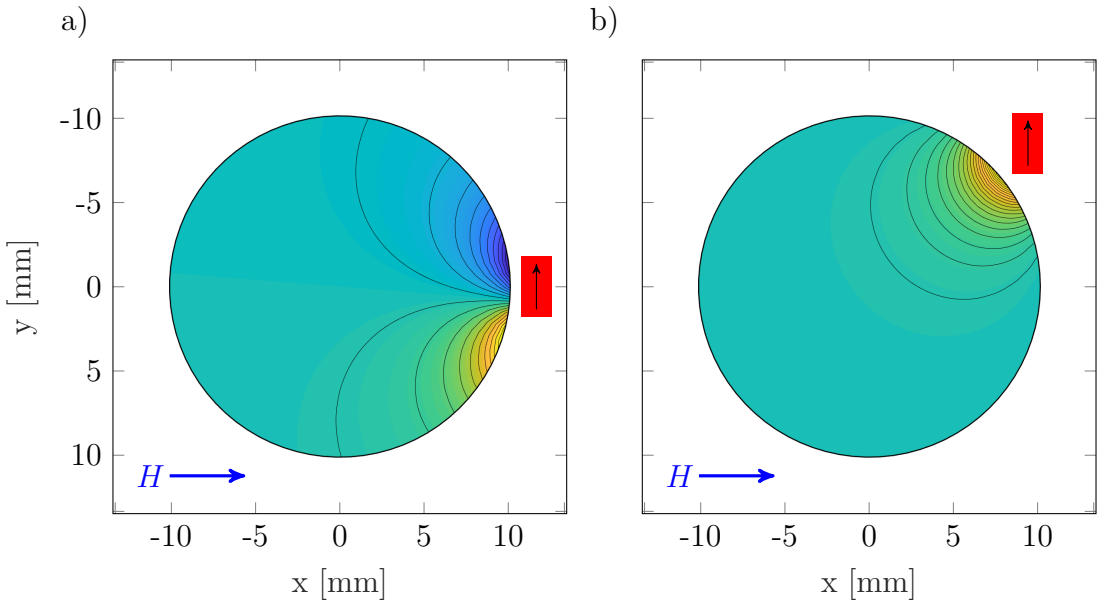


Figure 4.11: Contribution strength of each point in the source domain for different sensor positions for homogeneous magnetic field H in x-direction. The sensor sensitive axis is in y-direction. a) Sensor (as shown in red) is at a 0° angle to the circular MNP domain, yielding an antisymmetric contribution from all points in the MNP domain. b) Sensor (as shown in red) is at a 45° angle to the circular MNP domain, yielding a symmetric contribution from all points in the MNP domain.

can be seen in Figure 4.11 a) the contributions show an antisymmetry along the radial dimension and have, as such, no MNP response along this dimension. Therefore, it can be considered to have low resolution in that dimension. On the other hand, in Figure 4.11 b) the averaging function shows a symmetry along the radial dimension and can reach deeper lying sources. For this case, one can expect a better resolution in that dimension. These propositions will be investigated by using a polar grid for the MNP distribution. Different SNRs will be considered and the resolution matrix $\boldsymbol{R}_k$ will be computed. From the resolution matrix, the spatial spread of a single parameter along the radial dimension will be investigated, because it gives insight about the ability to resolve deeper lying sources of the MNP distribution.

4.6.3 Results and Discussion

Figure 4.12 shows the shape of the spatial spread for different radial positions and SNR. It can be seen that for increasing SNR, the PSF becomes more localized. Also, for

radial parameters that lie deeper, the PSF becomes more localized at deeper levels. Furthermore, the PSF is more localized for larger radial positions, indicating that near surface sources can be resolved better. Deeper lying sources show a large spatial spread for the corresponding radial parameter. As such, the statement can be made that deeper lying sources show worse resolution. For the radial parameter $r = 0$ mm, the resulting PSF is symmetric, which can be expected because the contribution to $\boldsymbol{b}$ is equal for all rotation positions.

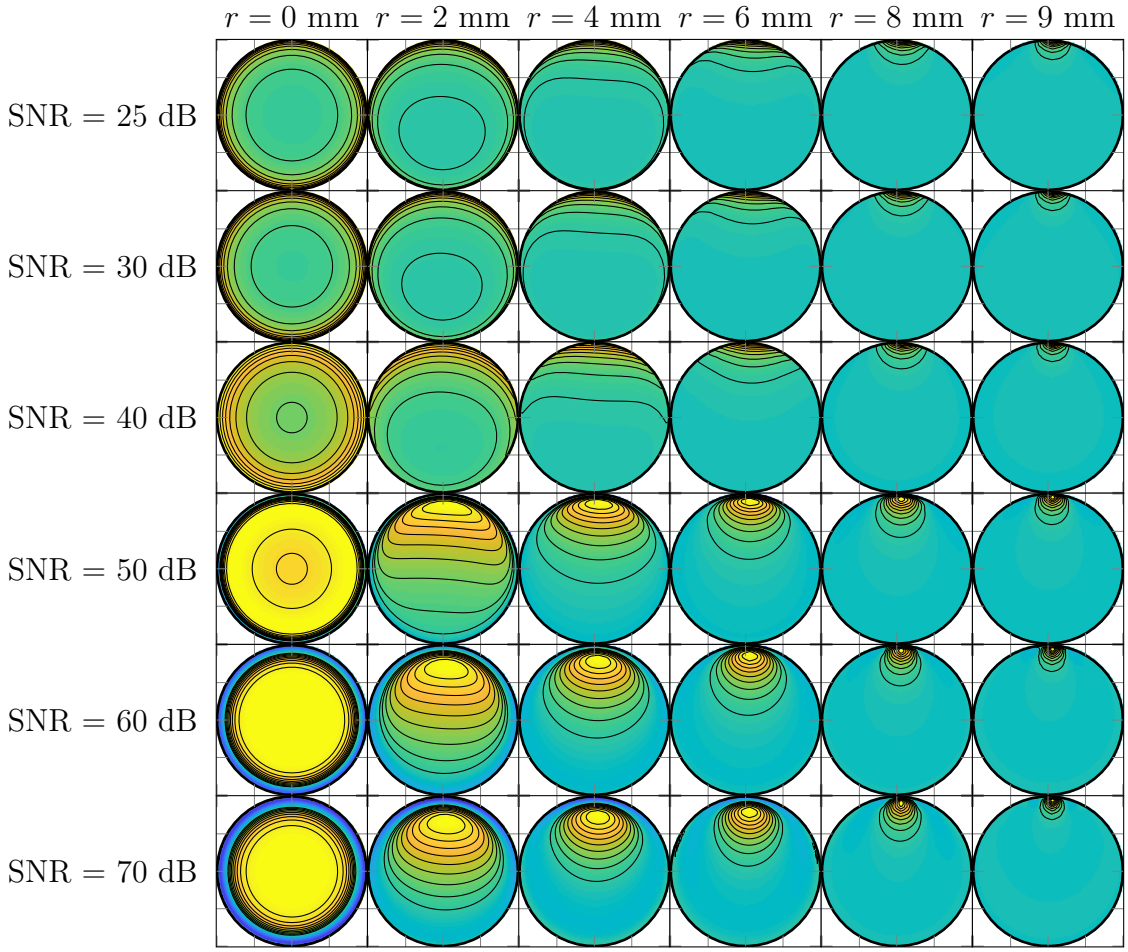


Figure 4.12: Point-Spread-Functions for different SNR and radial parameters of the source domain for $\boldsymbol{x}$ for the 45° system.

To compare both cases shown in Figure 4.11, the PSFs for these cases for different SNR are computed. To visualize these, only the curve from the center to the perimeter of the source domain along the maximum PSF value is taken. Each curve is normalized to its maximum value. These curves are shown for every radial parameter and several

SNRs in Figure 4.13. The left and right graph columns refer to a system where the sensor is positioned 0° and 45° (cases a) and b) from Figure 4.11). The lines in the figures refer to level sets to guide the eye.

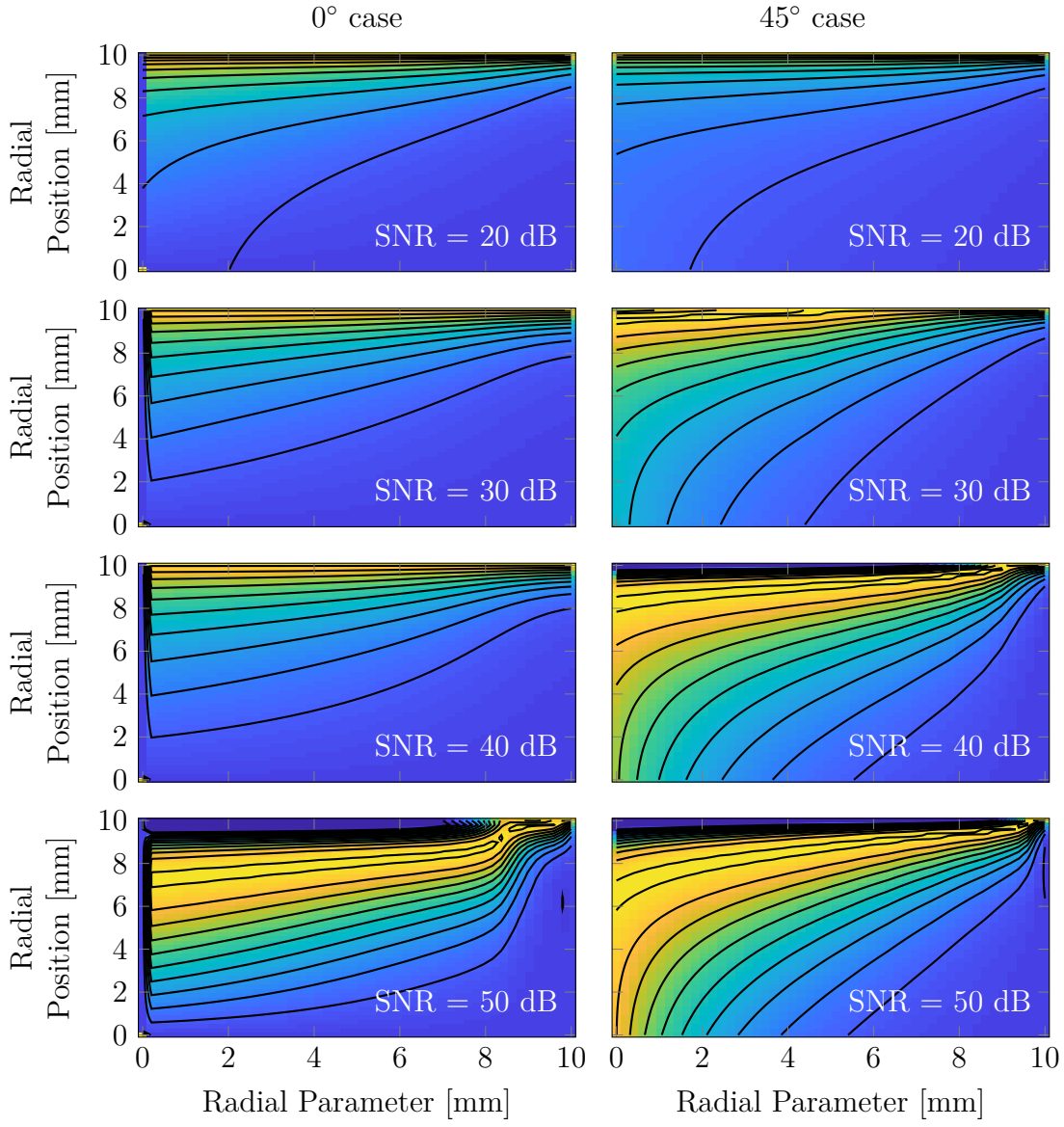


Figure 4.13: Point-Spread-Functions for different SNR and radial position of the source domain for $\boldsymbol{x}$.

As can be seen from Figure 4.13, with increasing SNR the maximum of the PSF reaches further into the source domain of the particle distribution, meaning that deeper lying sources can be better resolved. Comparing the cases for the 0° and 45° (left and right columns) shows that the 45° system yields higher PSF amplitudes for deeper

sources, implying a better reconstruction for such a system. However, it can also be seen that, even for high SNR, the PSF is mostly spread out for deeper sources, which means that these sources cannot be imaged for high resolution (in either case). This is a general limitation for such a system. However, the 45° points in a worthwhile direction, as it is able to yield a higher signal for deeper sources. The reason for this lies in the shape of the initial PSF of the system (see Figure 4.11). Its spatial sensitivities reach deeper into the sample volume, whereas the 0° case does not. The simulations suggest that a better resolution can be achieved in such a 45° system, though the resolution is still rather poor.

The reason for the poor resolution for deeper sources lies in the fact that these sources contribute only little and with low spatial frequencies to the measurement $\boldsymbol{b}$. With that, a bias to near surface sources can be experienced. To combat this, one could use a depth weight for the parameters. However, this only means that a heuristic measure is taken, which has no grounds in a rigorous mathematical sense. It can also be thought of as an "equalization" of the individual sources for their contribution to the measurement $\boldsymbol{b}$. Yet it would bias the reconstruction such that it may have no resemblance to the real distribution. There would have to be a trade-off with respect to the surface bias that is intrinsically present and the artificial bias that a depth weight would introduce. That something like this can work as a heuristic measure is, for example, shown in [85]. Yet, to be able to reconstruct the correct MNP distribution, one needs to consider things beyond such heuristics and change the imaging system such that good depth imaging can be done. This could be possible, for example, by inhomogeneous magnetic fields (c.f. [85]).

4.6.4 Conclusion

Overall, the circular system can be expected to have rather low resolution compared to the planar 2D system discussed before. The reason lies in the lack of features in the measurements from deeper lying sources. Enhancements to such a system can only be achieved if measurements are more selective for the parameters. Possibilities for such enhancements are inhomogeneous magnetic fields to selective magnetic excitation. For example, in MPI usage of Field Free Points/Lines are fundamental for imaging [2], [131], or in MRX imaging, selective activation coils [81], [85], [132]. However, at the same time one needs to consider cross sensitivities of the sensor, meaning that using inhomogeneous excitation fields may affect the sensor's sensitivity, resonance frequency and/or its spatial characteristics, because it would be much more difficult to position the

sensor accordingly. Any of these effects would need to be incorporated in the modeling for the reconstructions such that imaging can be successful.

CHAPTER 5

Experimental Investigation

After simulating the imaging system in Chapter 4, which was modeled in Chapter 3, we turn our attention to the experimental investigation of a 2D MPM imaging system. For this, objectives will be formulated which aim to determine the abilities of the imaging system. Approaches and results will be highlighted in the context of the previous simulations and the current literature and state of the art of MNP imaging systems.

5.1 Objectives

This chapter is split into several parts. First, overall objectives will be formulated and the experimental setup will be discussed. System calibration will be explained and different measurements for the system aspects will be performed.

The particles will be characterized with respect to their magnetic properties at different amplitudes for relevant frequencies using a Magnetic Particle Spectrometer (MPS). The inversion schemes developed in Chapter 3 will be used for the reconstruction of the particle distribution from the MPM data. Biological samples of magnetically labeled cells will be used for the MPM system to show its ability to image cells. Measurements for colored MPM will be carried out based on prior MNP characterization measurements via MPS (c.f. 2.2.2.2). General limitations of the imaging system will be shown with respect to spatial resolution, temporal resolution, and minimum particle amount.

5.2 Experimental Setup, Sensor and Calibration

5.2.1 Experimental Design

The measurement concept, as explained in Chapter 3.1, relies on the exploitation of the spatial characteristics of the sensor and the applied magnetic field direction. Since the sensor measures only a projection of the magnetic field, the applied magnetic field direction is applied perpendicular to the sensitive direction. Furthermore, the direction perpendicular to the plane of the sensor is chosen because of higher attenuation due to the sensors large demagnetization factor in that direction.

Measurement signals from MNP can be gathered by choosing an excitation frequency that lies at an integer fraction of the sensor's resonance frequency, i.e. $f_{\mathrm{ex,n}} = 1/n$ with $n = 2, 3, 4 \ldots$. This way, the external magnetic excitation is further attenuated, since it is not amplified by the sensor's resonance (**Note**: only true if the equations of motion for the sensor have constant parameters, see Appendix B.1 for a discussion on this). An ensemble of MNPs exhibit the formation of higher harmonic excitation, which couple into the resonance of the sensor, allowing for the measurement of MNPs while suppressing the external magnetic excitation. The setup for Magnetic Particle Mapping is shown in Figure 5.1. It consists of several pairs of Helmholtz coils, intended for different uses. The coils (denoted as excitation coils) create the excitation magnetic field that magnetizes the MNPs into the nonlinear regime. The compensation coils can be used to minimize a background signal at the resonance frequency of the sensor.

A sample holder, attached to motorized x-y stages, is used to position the sample in the magnetic field of the excitation field. The x-y stages are able to cover a region of $20 \times 20\,\mathrm{mm}^2$. A general assumption used for modeling the system is that the sample is exposed to a homogeneous magnetic field, which is still justified in this case because this assumption only needs to be true in the vicinity of the sensor. The sensor itself is fixed to a position in between the excitation coils using a sensor holder. Only minor positional adjustments are done using the manual x-y-z stages. An additional tip, tilt, and rotation stage is used to align the sensor correctly.

The excitation coils and the compensation coils are connected to an amplifier (2002 PAS or AE Techron 7224). Since the compensation coils only need to create a rather small magnetic field, impedance matching is not necessary. For the excitation coils,

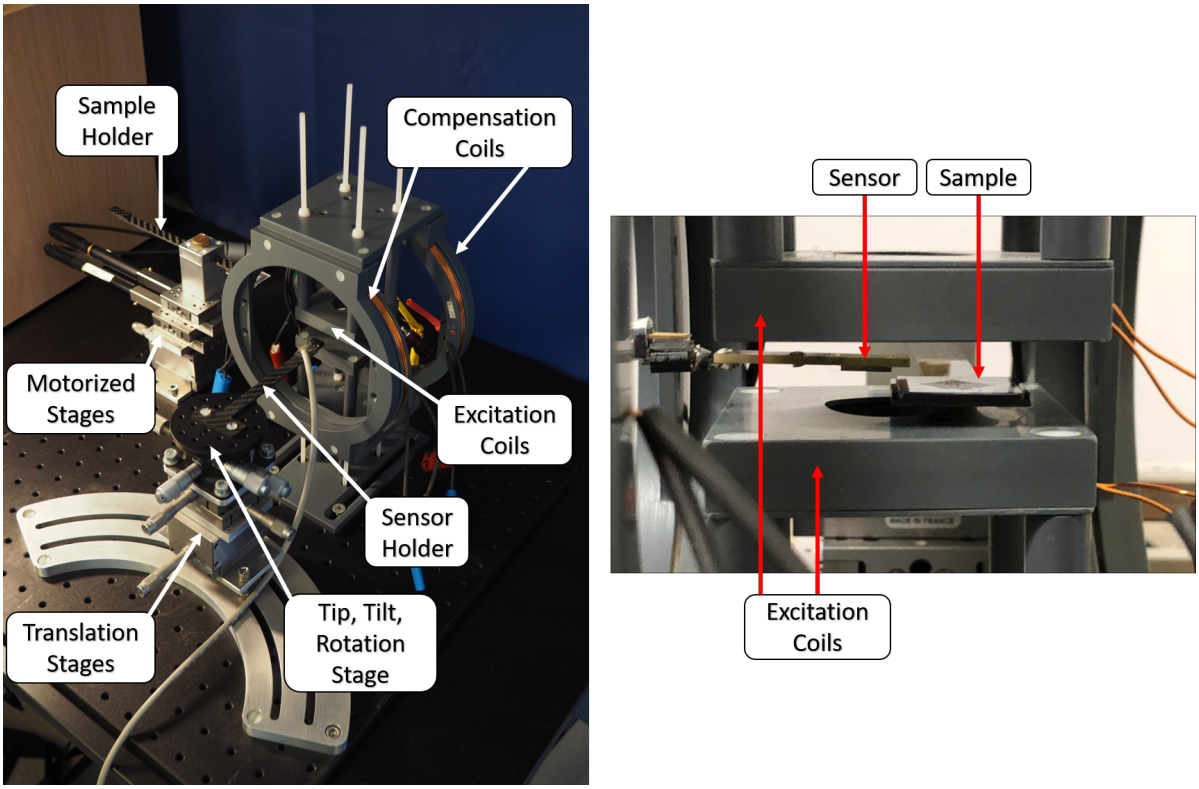


Figure 5.1: Left: experimental setup for MPM measurements with important components. Right: close-up of sensor to sample distance in between the excitation coils.

impedance matching for the excitation frequency is achieved via a set of capacitors (Arcotronics MKP) to drive the inductive load efficiently at 1/3 the resonance frequency.

For the signal generation and sensor readout, an RME Fireface UC external audio interface is used. The sensor signal is furthermore enhanced by a charge amplifier (AD745), as used in various publications (see [17], [133], [134]). Important to point out is the necessity for linear amplification such that no higher harmonics due to the amplifier can couple into the resonance.

5.2.2 Sensor

5.2.2.1 Fabrication

The sensor fabrication was carried out by Dr.-Ing. Christine Kirchhof. The ME-sensor has the shape of a cantilever with 3 mm length and 1 mm width and consists of 50 μm poly-silicon with the magnetostrictive and piezoelectric phase on top. It is fabricated by MEMS technology from an oxidized silicon/poly-silicon wafer. Effectively 1 μm of the magnetostrictive alloy $Fe_70.2Co_7.8Si_12B_10$ (FeCoSiB) is sputtered in the form of an exchange bias stack with (Ta-5nm/Cu-3nm/MnIr-8nm/ FeCoSiB-200nm) $\times$ 5. . On top of this, 2 μm highly piezoelectric aluminium nitride is sputtered using a low temperature deposition process as described in [135] with 5 nm Ta and 100 nm Pt as seed. The cantilever is released using wet and dry etching technologies. Details of the process can be found in [10].

The piezoelectric voltage generated by the magnetostrictive-induced bending of the cantilever is read out by a plate capacitor with the Pt seed and a golden top electrode. A silicon frame of 7.5 $\times$ 11 mm^2 surrounds the sensor for easy handling. The sensor is annealed in an oil bath for 30 min at 250 °C with a magnetic field of 1 kG applied 60° to the long axis of the cantilever. By this, the exchange bias effect is imposed, which shifts the magnetostriction curve in such a way that the highest slope is at zero external magnetic field. Details of this process can be found in [13].

5.2.2.2 Calibration

Sensor calibration was carried out by Dr.-Ing. Phillip Durdaut using a magnetically shielded chamber[136]. Two ME sensors were used in this thesis. Here, a sinusoidal magnetic signal of known amplitude was generated and a frequency sweep was performed to measure the sensor's frequency response. From the known amplitude and the voltage response from the sensor, the magnetoelectric α_{ME} coefficient for each frequency was calculated. As can be seen in Figure 5.2 (a), the (measured and fitted) frequency response for two different sensor's shows a characteristic peak at about 7639 Hz and 7569 Hz, indicating each sensor's resonance frequency. Additionally, the sensor's noise spectra are shown in Figure 5.2 (b).

The sensors are exchange biased to eliminate the need of an external magnetic bias field and to operate at large sensitivities. The maximum sensitivities at resonance are 93 kV/T and 19.4 kV/T, using a charge amplifier (AD745). The associated limits of detec-

tion (LOD) at the resonance frequency are 4 pT/$\sqrt{\text{Hz}}$ and 15 pT/$\sqrt{\text{Hz}}$. All parameters are listed in Table 5.1. Both sensors are used for experiments. Sensor WV3#5 is used for the cell experiments. Sensors C2 is used for all other experiments because it is more sensitive and has a lower LOD.

Sensor	Resonance f_r [Hz]	Sensitivity α_{ME} [kV/T]	Noise Density [nV/$\sqrt{\text{Hz}}$]	LOD@f_r [pT/$\sqrt{\text{Hz}}$]
C2	7639	93.0	385	4
WV3#5	7569	19.4	290	15

Table 5.1: Sensor parameters from sensitivity calibration.

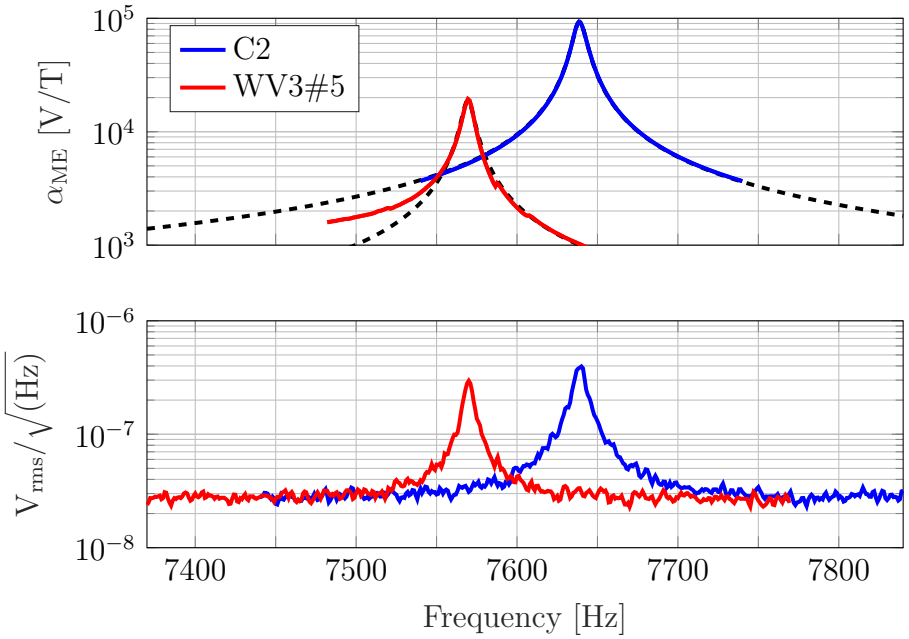


Figure 5.2: Top: amplitude frequency response of the sensor's resonance used in this thesis. Measurement is shown in solid lines, a fit on the data is shown as the dashed lines. Bottom: noise density of the sensors.

5.2.3 Setup Calibration

Calibration prior to measurements needs to be done to ensure repeatability and clean measurement signals. First, the excitation signal is applied to the system, which is

about 10 mT/μ_0. The frequency of the signal is matched with an integer fraction of the resonance frequency f_r of the sensor. Due to the antisymmetric, nonlinear magnetic behavior of the MNPs (in the absence of DC fields), the excitation frequency is chosen as $\frac{1}{3}f_r$. Beforehand, a frequency sweep is done to determine the resonance frequency in order to use the maximum sensitivity of the sensor.

Second, since most power dissipates at the coils, a warm-up time for the coils of about 30 min to an hour is used. This way, thermal variation and drift is reduced, which could otherwise change the magnetic field amplitude over time.

Thirdly, the sensor is aligned such that any third harmonic peak (not from MNPs) which couples into the sensor's resonance is minimized. Since no sample containing MNP are present yet, one needs to ensure that the signal at the resonance frequency is minimized as much as possible such that an MNP signal is strong compared to any residual signal from the system. The signal at the resonance frequency of the sensor may be have different causes. The amplifier for the magnetic field generation may show harmonic distortions, which then couple into the resonance. Another, more important reason is that the sensor behaves as a parametric resonator which can show higher harmonics due to parametric resonances. This can be understood by simply seeing that the excitation at $\frac{1}{3}f_r$ acts as a signal carrier and that the excitation signal modulates itself due to a periodic change in the resonance frequency (ΔE effect). Then the side peaks of the carrier couple into the resonance of the sensor. Thus, a background signal at resonance can be expected even if a perfect monofrequent magnetic signal is applied. The exact description of that effect and the influences on the sensitivity is elusive and beyond the scope of this thesis. Here, this background signal is simply minimized as much as possible via proper aligning of the sensor and usage of the compensation coils to destructively interfere with the signal. A more elaborate discussion on the role of the sensor in this context can be found in Appendix B.1.

In the last step, the sample is inserted into the system directly beneath the sensor with a minimal air gap in between. This ensures the largest sample signals possible. The sample is moved in an x-y plane and for each measurement position, the signal at the resonance frequency is measured via an Fast Fourier Transform (FFT) of the measured time signal.

5.3 Particle Characterization

In the context of MPM, particle characterization needs to be done via Magnetic Particle Spectrometry (MPS). MPS measurements give information on the magnetic response of MNPs for different frequencies and magnetic field amplitudes. The MNPs show a dynamic relaxation effect that results in a certain amplitude and phase response. The MPS measurements were carried out by M. Sc. Sebastian Draack from TU Braunschweig in the group of Prof. Dr. Meinhard Schilling and apl. Prof. Dr. Frank Ludwig. The MPS system used is explained in [67]. For each measurement, a reference measurement without a sample was performed, which was subsequently subtracted from the measurement with a sample. This way, any background stemming from the setup was reduced.

5.3.1 Objectives

Varying magnetic field amplitudes and frequencies were used to measure the magnetic response of several commercially available MNP. The objective is to assess the best particles for MPM measurements with respect for cells and colored MPM measurements. For this, the measured MPS spectra will be analyzed with respect to the harmonic responses that are used for MPM measurements. The particles with the largest third harmonic response will be used for imaging and cell experiments. Furthermore, the particles which show the largest phase difference in their response will be used for colored MPM measurements. For these assessments, the MPS spectra at 2.5 kHz will be used as they most closely match 1/3 the resonance frequency of the sensor. The characterization of MNPs allows for the proper choice of particles for MPM measurements, i.e. gaining the largest response possible for better imaging.

5.3.1.1 Magnetic Particle Spectrometry

Several MNPs from Chemicell were used. For all measurements, an amount of 150 μl were used. The MNPs were characterized at different frequencies as well as different magnetic field amplitudes. A list of the MNPs will be given with important values further below (see Table 5.2). The MNPs differ in size (hydrodynamic) and coatings. As an example, Figure 5.3 shows the measured magnetic response from MNPs CT100 fluidMAG (Chemicell, Berlin). It can be seen that for low magnetic field amplitudes, the magnetic response behaves basically linearly and that no hysteresis is present. For

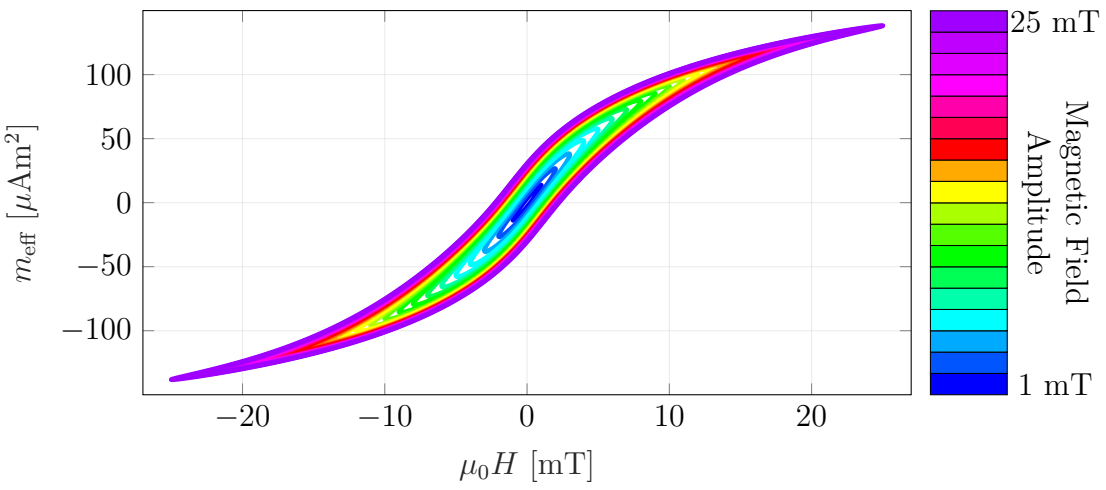


Figure 5.3: MPS measurements effective magnetic moments from the MNP, shown as hysteresis loops. The excitation frequency was 2.5 kHz with varying magnetic field amplitudes up to 25 mT. The total amount of MNP was 150 μl CT100 from Chemicell.

larger magnetic field excitations, one can see a deviation from a linear response for the particles, while also the formation of a strong hysteresis is seen. This also indicates the formation of higher harmonic excitations in the magnetization behavior. A different representation of the hysteresis curve in a spectrum can be seen in Figure 5.4. Important for MPM measurements is having only a single higher harmonic response of the particles, since it is the higher harmonic that couples into the resonance of the sensor. A list of important values will be discussed further below and can be seen in Table 5.2.

The third harmonic response of the particles as a function of magnetic field amplitude at a frequency of 2.5 kHz can be seen in Figure 5.5. It can be seen that with increasing magnetic field amplitude, the effective magnetic moment increases as well. The phase responses of CT100, CT50, and D100 show a minimum in phase for about 7 mT excitation amplitudes. ARA100 shows an increase in the phase response for increasing magnetic field amplitudes. From the graph we can list the characterized MNPs with respect to their response strength: CT50, CT100, D100, ARA100. Experiments will be performed for excitation amplitudes of 10 mTμ_0^{-1}. Thus, the particle parameters for that excitation amplitude will be compared. A list of the parameters can be seen in Table 5.2. We choose CT100 for further experiments, as it gives large amplitudes as well as a large phase difference to ARA100. For colored MPM measurements, one needs large differences in phase in the response of the particles. D100 will not be used, even though it has slightly larger phase difference to ARA100 than CT100, because the signal

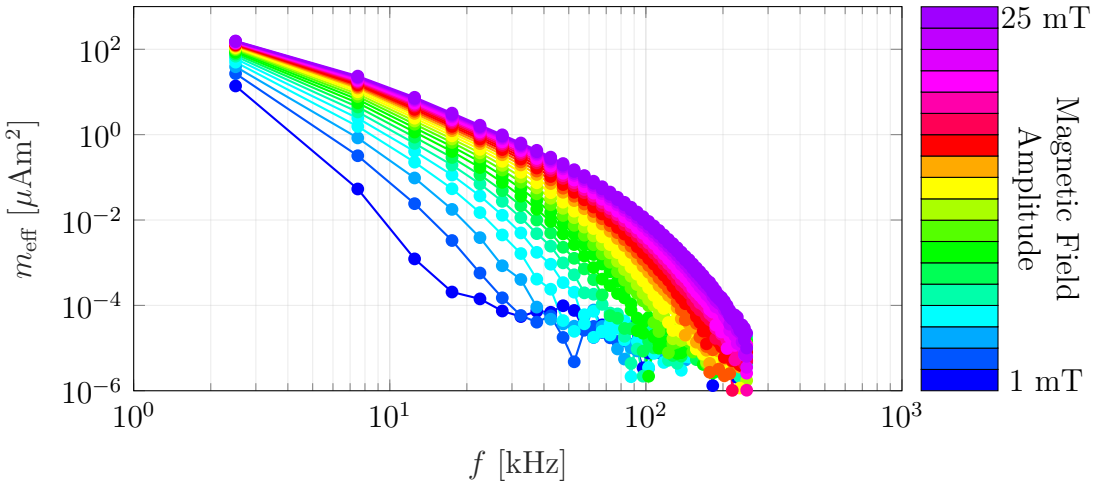


Figure 5.4: MPS measurements of the effective magnetic moments from the MNPs, shown as spectra. The excitation frequency was 2.5 kHz with varying magnetic field amplitudes up to 25 mT. The total amount of MNPs was 150 μl CT100 from Chemicell.

amplitude would be smaller.

Particles	Producer	weight volume [mg/ml]	Particle density [1/g]	Amplitude [nAm^2/μl]	Phase [Deg]
CT100	Chemicell	25	$1.8 \cdot 10^{15}$	52.13	-115.81
CT50	Chemicell	25	$1.3 \cdot 10^{16}$	57.4	-104.31
D100	Chemicell	25	$1.8 \cdot 10^{15}$	33.13	-116.08
ARA100	Chemicell	25	$1.8 \cdot 10^{15}$	30.67	-101.81

Table 5.2: List of particle data and MPS values measured at 2.5 kHz for 10 mTμ_0^{-1}.

5.4 Imaging Cell Distributions

5.4.1 Objective

To see the feasibility of the MPM approach to measure cell distributions, measurements of magnetically labeled cells have to be performed. For this, cells are magnetically labeled and deposited into a matrix, which are then placed into the MPM setup. Then,

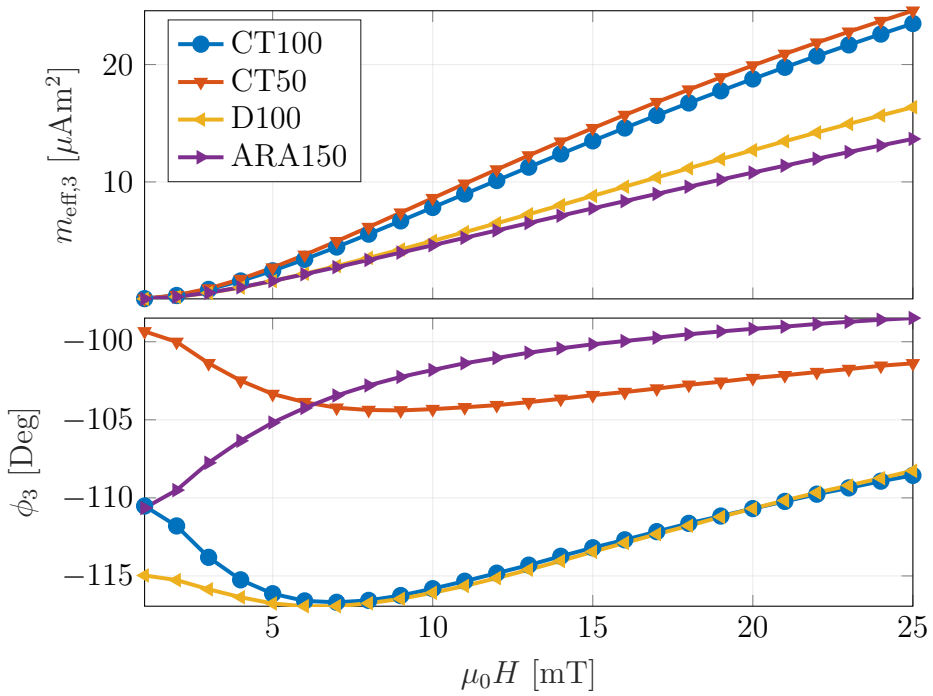


Figure 5.5: MPS measurements of the third harmonic of the effective magnetic moments from the MNP. The total amount of MNP was 150 μl of different MNP from Chemicell. Shown are the amplitude $m_{\mathrm{eff},3}$ and phase (ϕ_3) responses of the third harmonic of different MNP types.

the signal strength was compared with the amount of cells (and their iron content) to deduct the minimum amount detectable with this approach.

5.4.2 Materials and Methods

5.4.2.1 Sample Preparation

The cell sample preparation was carried out by Dr. Nils Lukat from the group for Biocompatible Nanomaterials under the supervision of Prof. Dr. Christine Selhuber-Unkel. Rat embryonic fibroblasts (Ref52 wt) were grown in 6-well plates (Sarstedt AG & Co.) using Dulbecco's modified Eagle's medium (DMEM, Biochrom) supplemented with 10% fetal bovine serum (Biochrom) at 37°C, 5% CO_2, and about 90% humidity. Once confluent, superparamagnetic MNPs (50 µg/ml) were added to 3 ml medium for 24 h. The MNPs have a hydrodynamic diameter of 50 nm (in water) and the magnetic core is embedded in a polymer matrix consisting of citric acid (fluidMAG-CT50, Chemicell,

Berlin). Previous magnetic measurements of cells (magnetophoresis measurement conducted by Dr. Nils Lukat) suggest about 10 pg of iron per cell. After 24 h, the adherent cells are washed with phosphate-buffered saline (PBS) three times to remove all MNPs from the supernatant. Subsequently, the cells are trypsinised and spinned down. The supernatant is removed carefully and the cells are resuspended into 100 μl of Matrigel (Matrigel Matrix Phenol Red Free 10 ml, Corning). In the experiments, two sample holders were used that consist of a 1 mm thick PMMA slice, each with a cavity of 8 mm diameter in the center. Into each of these cavities a droplet of 30 μl cell-Matrigel solution is added. To stabilize the droplet, the remaining volume of the hole is filled with pure Matrigel. In one of the two samples the cell droplet is mixed with the surrounding Matrigel, so that the cells are distributed over a much larger area. Both samples contain approximately 8×10^5 cells.

5.4.2.2 Measurement

For the experiment, the sensor WV3#5 was taken (c.f. Table 5.1). A magnetic field amplitude of 10 mTμ_0^{-1} was used. The frequency was adjusted to be 1/3 of the resonance frequency of the sensor. Prior to inserting the sample, the sensor was adjusted (via, e.g., tilting) such that the peak at the resonance frequency was minimized (c.f. 5.2.3). Additionally, a compensation signal was used to further suppress the signal at the peak. Then the sample was inserted into the MPM system. The sensor-to-sample distance was adjusted to be around 1 mm. Furthermore, the measurement is done by moving the sample with respect to the sensor. A Cartesian grid was used for the measurement positions. For each measurement position, the voltage signal of the sensor was measured and an FFT was computed using a Blackman window. The time length was set to be 4096 samples with a sampling frequency of 32 kHz to yield a spectral resolution of 7.8 Hz. The signal amplitude and phase at the resonance frequency was recorded for each position. Subsequently, data analysis can be performed. The measured magnetic fields from the magnetically labeled cells can be seen in Figure 5.6. Here, two samples are used, a localized cell droplet and a smeared-out cell droplet. This is done to simply see that a different spatial arrangement will lead to a different measurement of the magnetic field of the labeled cells.

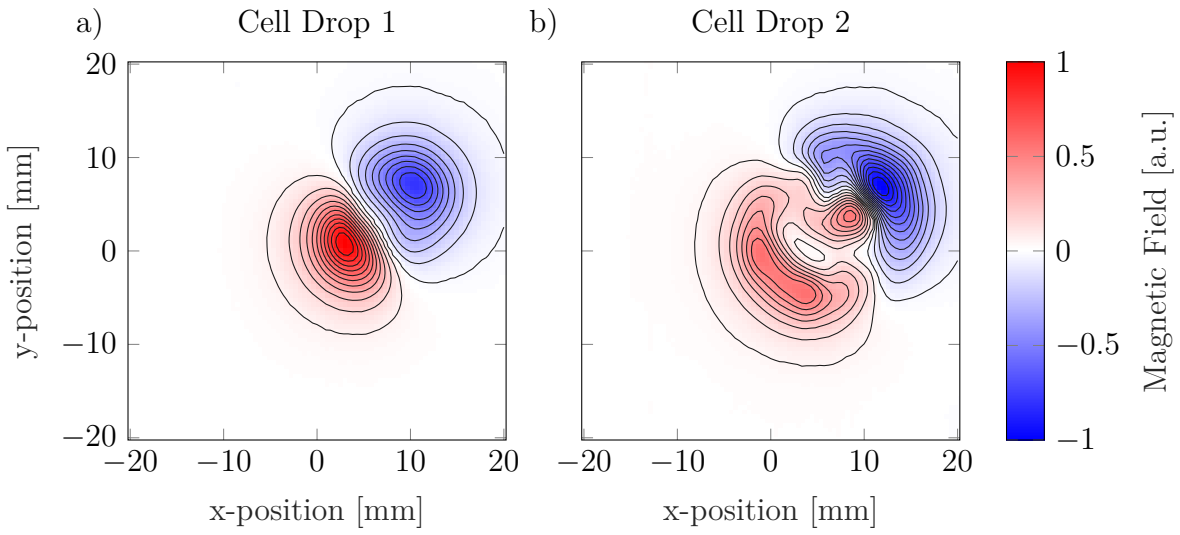


Figure 5.6: MPM measurements of the magnetic fields of the cell droplet: a) shows the measurement of a cell droplet, and b) measurement of cell droplet that has been spatially smeared out.

5.4.2.3 Data Analysis

Data analysis of the measured data is done by solving the inverse problem. Here, the adaptive algorithm as developed in Chapter 3.4 is used, because it allows for the proper sensitive axis and dipole directions to be estimated based on the data alone. The final iteration was based on visual inspection of the reconstruction, though more elaborate stopping criteria can be used, such as the discrepancy principle[113] in combination with defining the total amount of MNPs from the measurement via the procedure outlined in Section 3.4.5 via projecting into this set. For each iteration, the particle reconstruction was projected into the nonnegative orthant to account for a nonnegative particle distribution. The source domain for the reconstruction was set to be a 2D Cartesian plane with the same dimensions as the number of measurement points and a total area of 20×20 mm^2. A wider reconstruction domain is not necessary as it was made sure that the particle distribution lies within the chosen dimensions. The total number of measurement points and hence source distribution points are 85×85. Initial directions of the sensor's sensitive axis and the dipole direction are the y and z directions, respectively.

5.4.3 Results

The reconstruction of the cell distribution can be seen in Figure 5.7. For a direct comparison to the real distribution of the cells, a light microscopy image of the sample is placed next to it. The maximum magnetic field values of the droplets are 84 nT and 58 nT, respectively. The total estimated magnetic moments are 15.3 nAm^2 and 14.9 nAm^2. The estimated directions of the sensitive axis of the sensor as well as the dipole directions for both measurements can be seen in Table 5.3.

5.4.4 Discussion

For both measurements, the direction of the sensitive axis and magnetic dipole direction remains basically the same, indicating the usability of the adaptive algorithm, because sensor arrangement was not changed between the measurements. This is reflected in the estimated directions given in Table 5.3. In fact, the same direction for the sensitive direction was found.

The reconstruction results of the unsmeared and smeared-out cell droplets can be

Spatial	Sensor $\hat{\boldsymbol{s}}$		Dipole $\hat{\boldsymbol{m}}$	
Component	Drop 1	Drop 2	Drop 1	Drop 2
x	0.6457	0.6457	−0.0148	−0.0564
y	0.7636	0.7636	−0.0208	−0.0063
z	0.0013	−0.0034	0.9997	0.9984

Table 5.3: Estimated directions of the sensor's sensitive axis $\hat{\boldsymbol{s}}$ and the excited magnetic moments direction $\hat{\boldsymbol{m}}$ from the sample. For both measurements, the estimated directions are very close to each other, further indicating the usability of the adaptive model for MPM.

seen in Figure 5.7. Each MPM reconstruction is compared to a light microscopy image of the same sample. As a heuristic, it can be estimated that the cell density is related to the darker areas of the light microscope image, because the cells are labeled with MNPs, which are dark in color. As for the unsmeared cell droplet, one would expect to have a round shape in the reconstruction as well. However, the reconstruction is elongated in the direction of the sensitive axis of the sensor. This may be due to the anisotropic Point-Spread-Function, as discussed in Chapter 4.5. For the smeared-out cell droplet,

regions of high cell densities can be seen as well as regions where air bubbles dominate the region. Comparing the MPM reconstruction with the light microscopy image, one can see that the dark region of the microscopy image coincides with a region of high particle concentration according to the MPM reconstruction. Additionally, the region of low cell density, indicated by the presence of air bubbles, corresponds to a region of low particle concentration in the MPM reconstruction. The direct overlay of both images may not be perfect as one has to manually compare the images, because no spatial reference point is given between MPM setup positioning and the light microscope. Either way, one can see that the MPM reconstruction for the smeared-out cell droplet shows many more features than the unsmeared droplet. Because the structure of the reconstruction can be found in the light microscope image, one can safely say that the cell distribution can be imaged using the MPM system. However, smaller structures are likely to be impossible to image, because of general limitations for the imaging system, as discussed in Chapter 3.5.

From the magnetic moment estimated from the MPM measurements (15.3 nAm^2 and 14.9 nAm^2), and the amount of cells in the droplets (about $10 \cdot 8^5$ cells), in combination with the MPS measurements from section 5.3, one can estimate the average iron content in the cells. This can then be compared with the estimated amounts from magnetophoresis measurements (done by Nils Lukat), which was about 10 pg. To calculate the iron content per cell c_{Fe}, the MPS values from Table 5.2 are taken. From the MPS measurements, the magnetic moments per μl is denoted as m_{MPS}, the iron content of the MNP solution as $\rho_{Fe} = 25\,\mu\mathrm{g}/\mu\mathrm{l}$ and the cell amount as $N_c = 10 \cdot 8^5$. The estimated magnetic moments of the cell droplets from the MPM measurements are denoted as m_{MPM}. The iron content per cell can the be computed by:

$$c_{\mathrm{Fe}} = \frac{\rho_{Fe}}{N_c} \frac{m_{\mathrm{MPM}}}{m_{\mathrm{MPS}}} \tag{5.1}$$

The estimated iron content per cell amounts to 8.33 pg/cell and 8.11 pg/cell, respectively. This is in close correspondence with the magnetophoresis measurements. This also lies in the range of commonly reported iron content in cells from MNP, which ranges from 4-50 $\mathrm{pg}_{\mathrm{Fe}}$/cell [129], [137]–[140]. In [129], the quantification of MNP in cells was performed using MPS. In [50], a maximal amount of 250 $\mathrm{pg}_{\mathrm{Fe}}$/cell was measured for the same type of MNP (CT50). One still has to consider that MNP inside cells show different magnetic responses, as reported in [129], which also suggests that the quantification via MPS measurements may be inaccurate for this purpose.

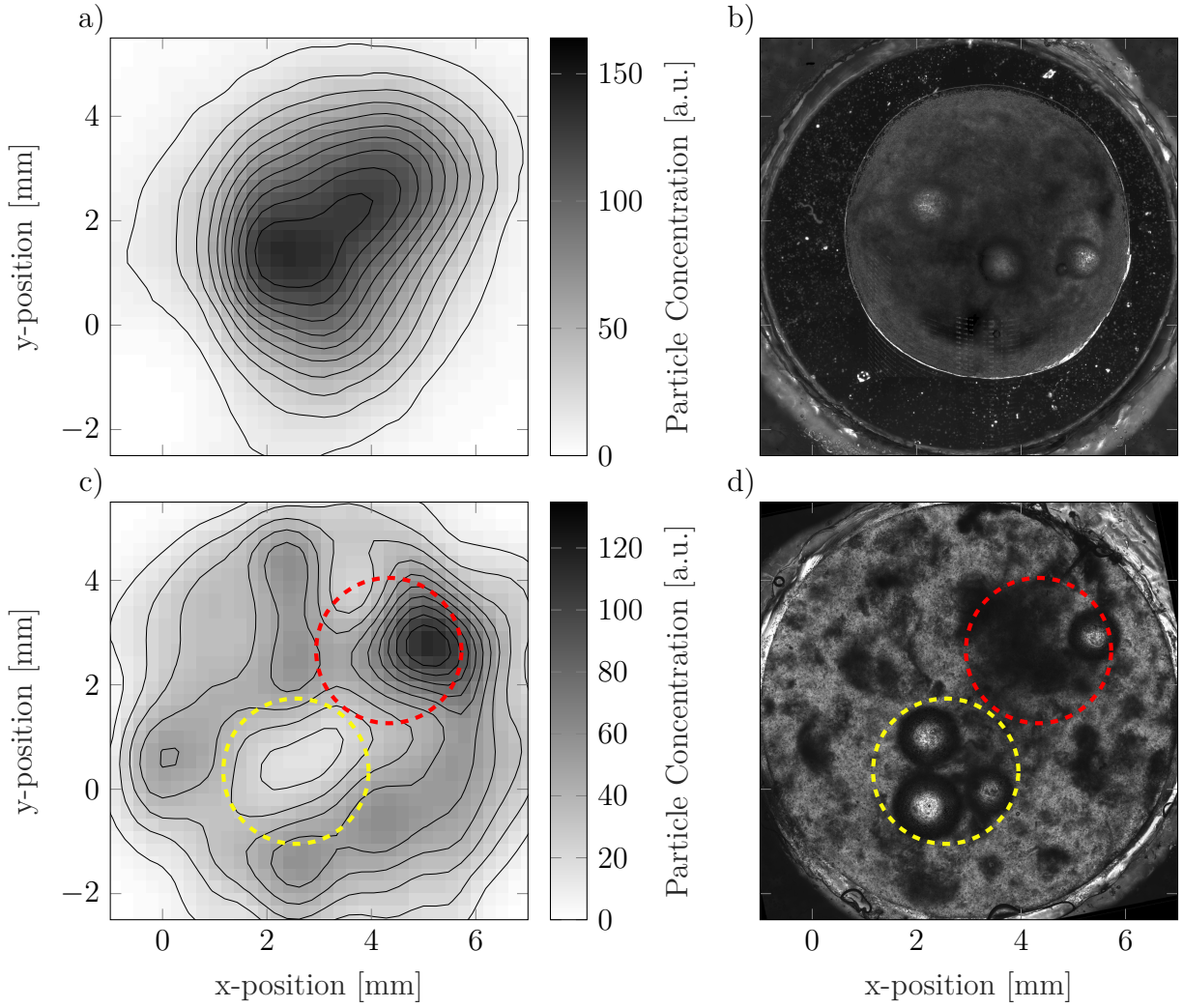


Figure 5.7: a) MPM reconstruction of magnetically labeled cells and b) light microscopy image of same cell distribution. c) MPM reconstruction of magnetically labeled where the cell droplet has been smeared out. Comparing with the light microscopy image in c), the darker regions indicate higher densities of cells (enclosed red circle). The region containing bubbles (yellow circle) is of lower cell density. Because the cell densities are directly proportional to the strength of a measurable magnetic signal, an MPM reconstruction should reflect the regions mentioned here.

5.4.5 Conclusion

It was shown that for a 2D MPM system, imaging of about $8 \cdot 10^5$ magnetically labeled cells using CT50 MNP from Chemicell could be performed. For the MPM measurements, the amount of cells that can be measured this way can be expected to lie around 200 cells,

given a limit of detection for the sensor of 15 pT/$\sqrt{\text{Hz}}$ and that the maximum magnetic fields were 58-84 nT for an estimated amount of $5 \cdot 10^5$ cells. However, *imaging* would not be possible, because no features can be extracted from data near the noise level. Thus, one would be limited to a minimum of several thousands (or tens of thousands) of cells for imaging. In addition to that, an unwanted background signal due to magnetic frequency conversion can worsen imaging due to an unclean MNP signal (c.f. Chapter 2.1.3.4, Eq. 3.18 and Appendix B.1.3). Furthermore, 3D imaging would face more problems as the distance to the sensor can be much higher and a lack of features in the measurement signal prohibits proper depth imaging (c.f. Chapter 4.6). Nevertheless, for a 2D system, cell imaging could be performed using magnetoelectric sensors with the MPM technique.

5.5 Colored Magnetic Particle Mapping

5.5.1 Objective

Imaging of different types of MNPs simultaneously has been shown to be possible for other imaging techniques such as MPI [34] or MRX [35] (c.f. Chapter 2.3). The possible benefits of such an ability can be, for example, that the environment of the MNP can be monitored (viscosity/temperature) [141], [142]. In the context of MPM for cell imaging, this can be beneficial because it has been shown that the incorporation of particles into the cells can change the magnetic response of the MNPs. If the change is large enough, one would be able to distinguish MNPs that are free or incorporated into cells.

After imaging cell distributions using the MPM system, one can now try to image different particle behaviors. Since for the MPM system only a single frequency is measured, only two different particle types can be distinguished from each other (as was discussed in Chapter 3.3.3), based on their phase relationship in their magnetic response. The ability for colored MPM will be investigated in this chapter.

5.5.2 Materials and Methods

5.5.2.1 Sample Preparation

The choice for MNPs were given in chapter 5.3, where CT100 and ARA100 were chosen for the experiment for colored MPM, because the phase differences were largest between the particles. The particles were deposited in spatially separated containers of a sample holder (see Figure 5.8). The thickness of the sample holder is 4 mm. The amount of MNPs was 14 μl for each type. The containers were sealed with adhesive tape to prevent evaporation.

5.5.2.2 Measurement

Colored MPM measurements were performed using the MPM setup and liquid MNP samples. A magnetic excitation field amplitude of 10 mTμ_0^{-1} was used. The frequency was adjusted to be 1/3 of the resonance frequency of the sensor. Prior to inserting the sample, the sensor was adjusted (via e.g. tilting) such that the peak at the resonance fre-

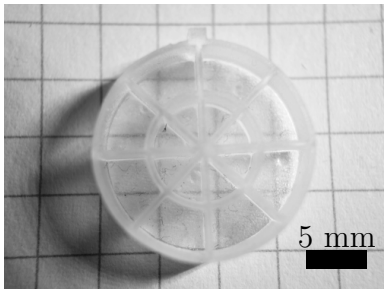


Figure 5.8: Sample holder for colored MPM measurements. The MNPs were filled in the volumes on the outer ring, opposite to each other. Only a single volume was filled for each type of MNP.

quency was minimized. Additionally, a compensation signal was used to further suppress the signal at the peak.

The sample was inserted into the MPM system. The sensor to sample distance was adjusted to be around 1 mm. It is important to point out the thickness of the sample, which is 4 mm. Thus, the measured signal is composed from MNPs from different heights. Furthermore, the measurement is done via moving the sample with respect to the sensor. An equidistant Cartesian grid was used for the measurement positions. The number of measurement points are 53×53 and the total measured dimensions are 20×20 mm^2. For each measurement position, the voltage signal of the sensor was measured and an FFT was computed using a Blackman window. The time length was set to be 4096 samples with a sampling frequency of 32 kHz, to yield a spectral resolution of 7.8 Hz. The complex peak signal at the resonance frequency was recorded and used for the data analysis.

5.5.2.3 Data Analysis

Prior to a reconstruction, possible outliers in the measured data are addressed. These outliers can stem from exterior circumstances (e.g. sound, vibration) that can couple into the sensor's resonance. For this, a visual inspection of the raw data is done and is removed from the data set. This is necessary because outliers can cause the formation of artifacts in the reconstruction.

Additionally, the data set was adjusted in its phase response to account for the influence of the MNP field on the sensor properties. See Chapter 3.2.4 for the derivation on this.

The reconstruction is done using the adaptive algorithm employed in Chapter 3.4. Additionally, to incorporate a nonnegativity constraint for the reconstructed particle distribution, the projection operator $\mathcal{P}_+^{\boldsymbol{Q}}$ is used (c.f. Chapter 3.3.3 and Appendix A.6), based on the particle phase response encoded in $\boldsymbol{Q}$. For the construction of the MNP response matrix $\boldsymbol{Q}$, the phases of the measured signals near the region of the different particles types are taken as a guide. Ideally, the phases of the MPS spectra are also retrieved in the measurement, but several phase delays can stem from, e.g., the fact that the signal is measured at the resonance which would yield an additional phase of 90° and that there is a delay. If the measurement is done only near the resonance, this additional phase may differ.

As a source domain for the reconstruction, a 2D Cartesian plane was used. The dimensions were the same as the measurement positions, with a difference in z height of 2.5 mm to roughly accommodate for the thickness of the sample. We thus use a 2D model for a 3D sample. A model that reflects the thickness of the sample is not necessary to show the ability for colored MPM, since the phase responses are not affected for homogeneous magnetic fields from the excitation. The reconstruction instead is spatially more spread out. This would even be true for a model that reflects the thickness of the sample, since there is a surface bias involved (see Chapter 4.6). An additional projection onto the scaled L^1 ball (see Appendix A.3) was used to counteract this spatial spread and visual inspection was used for the reconstruction. However, it was made sure that no important features were lost.

5.5.3 Results

5.5.3.1 Amplitude Dependent Phase

MPM measurement of a single type of MNP implies that the phase of the measured signal is constant (except for a π change due to polarity). Only the amplitude would show a variation, which ultimately gives information about the spatial distribution. If one measures two types of MNPs, which have two different phase responses, one can make the prediction that the (majority of the) phases of the measured data lie in between these two phases. A simulated example is seen in Figure 5.9 a) with the dashed line indicating the phase response of the particles.

However, not only the MNP response is important, but also the response of the sensor. If the sensor response is affected by the magnetic field of the particles, one can expect a phase shift (as well as amplitude) in the measured voltage data due to a shift in working point for the sensor. A phase shift depending on the field amplitude is

introduced in Figure 5.9 b) via a complex scalar $\exp(-j\eta|v_i|)$ with $|v_i|$ being the voltage amplitude and η a free parameter. It can be seen that the dashed lines are transformed from straight to curved lines, indicating the amplitude dependent phase.

Figure 5.9 c) shows the measurement data and it seems that the phases are dependent on the field amplitude. For a reconstruction, it would be necessary to transform the data beforehand such that the phase is again independent of the amplitude. Therefore, a complex scalar $\exp(j\eta|v_i|)$ is used to transform the data. For this, the aim is to transform the data such that two straight lines can enclose the data appropriately.

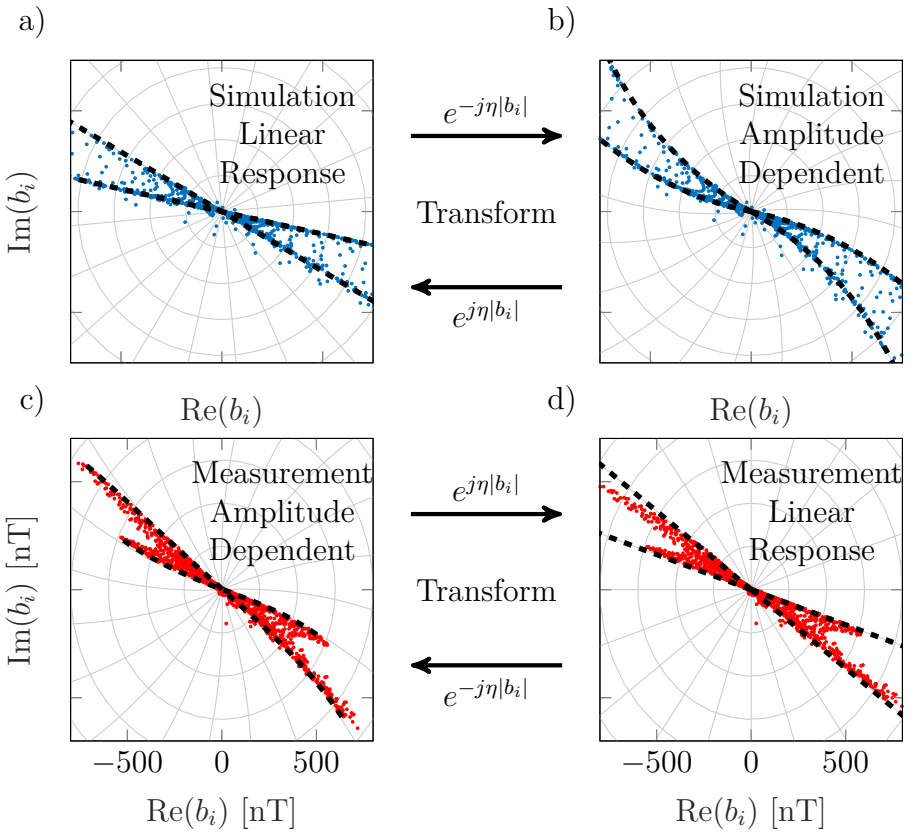


Figure 5.9: Real and imaginary part of measured/simulated magnetic field response of two different MNP types. a) Simulated magnetic response gained from two different MNP with different phase responses. b) Simulated magnetic field response in which the phase is dependent on the amplitude of the field. Linear response and amplitude dependent response can be transformed to each other via a complex scalar. c) Measured magnetic field response from the MNP using a ME sensor. d) Transformed data that yields a constant phase response, independent of the magnetic field amplitude.

5.5.3.2 Measurement and Reconstruction

The measured voltages from the magnetic fields can be seen in Figure 5.10, split into amplitude and phase plots. Some outliers in the measurement are present, as indicated by the dashed circle, which where subsequently omitted for the reconstruction. Furthermore, the absolute value of the phase mod π is shown for better visualization. The left region corresponds to particle type CT100 and the right to ARA100. An average phase for the corresponding regions can be extracted from the phase plot of about 23° (left) and 37° (right).

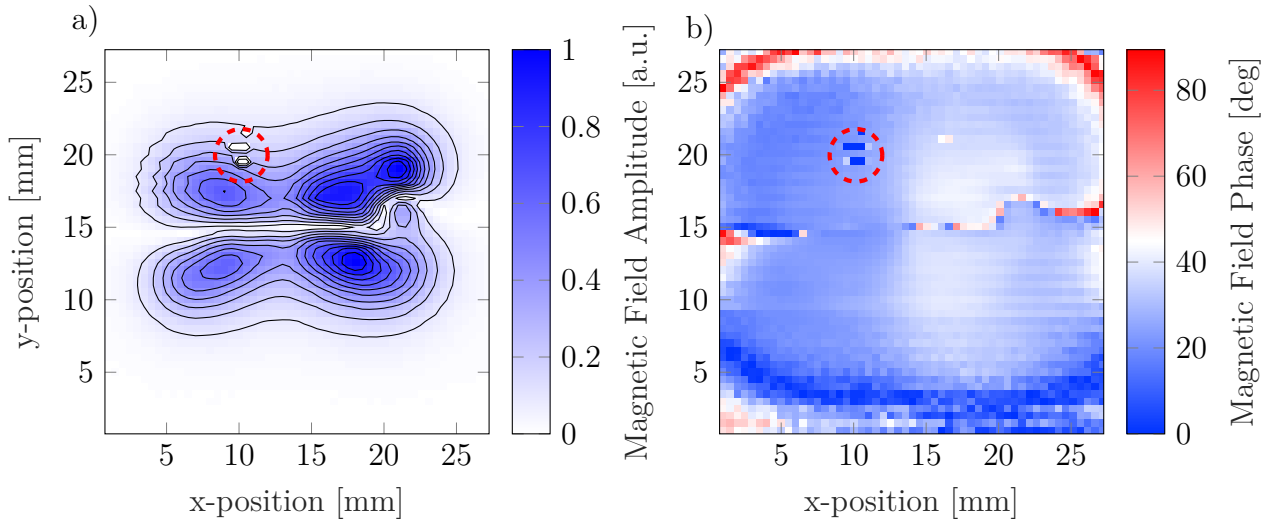


Figure 5.10: Measured voltage signals from the magnetic fields of the MNP distribution. Outliers in the data are shown within the dashed circle. These data points have been excluded for the reconstruction. a) Shows the voltage amplitudes, and b) shows the absolute value of the phase mod 180°.

For the reconstruction, the adaptive algorithm developed in Chapter 3.4 was used and the estimated directions for the sensitive axis of the sensor and the directions of the magnetic dipoles are listed in Table 5.4. The reconstruction from the data in Figure 5.10 is shown in Figure 5.11. It shows two plots for each particle type: Particle type CT100 is shown in red and ARA100 is shown in blue. An additional plot of both particle types simultaneously is included as well.

Spatial Component	Sensor $\hat{\boldsymbol{s}}$	Dipole $\hat{\boldsymbol{m}}$
x	0.0110	0.0588
y	0.9958	0.0950
z	0.0904	0.9937

Table 5.4: Estimated directions of the sensor's sensitive axis $\hat{\boldsymbol{s}}$ and the excited magnetic moments direction $\hat{\boldsymbol{m}}$ for the colored MPM experiment.

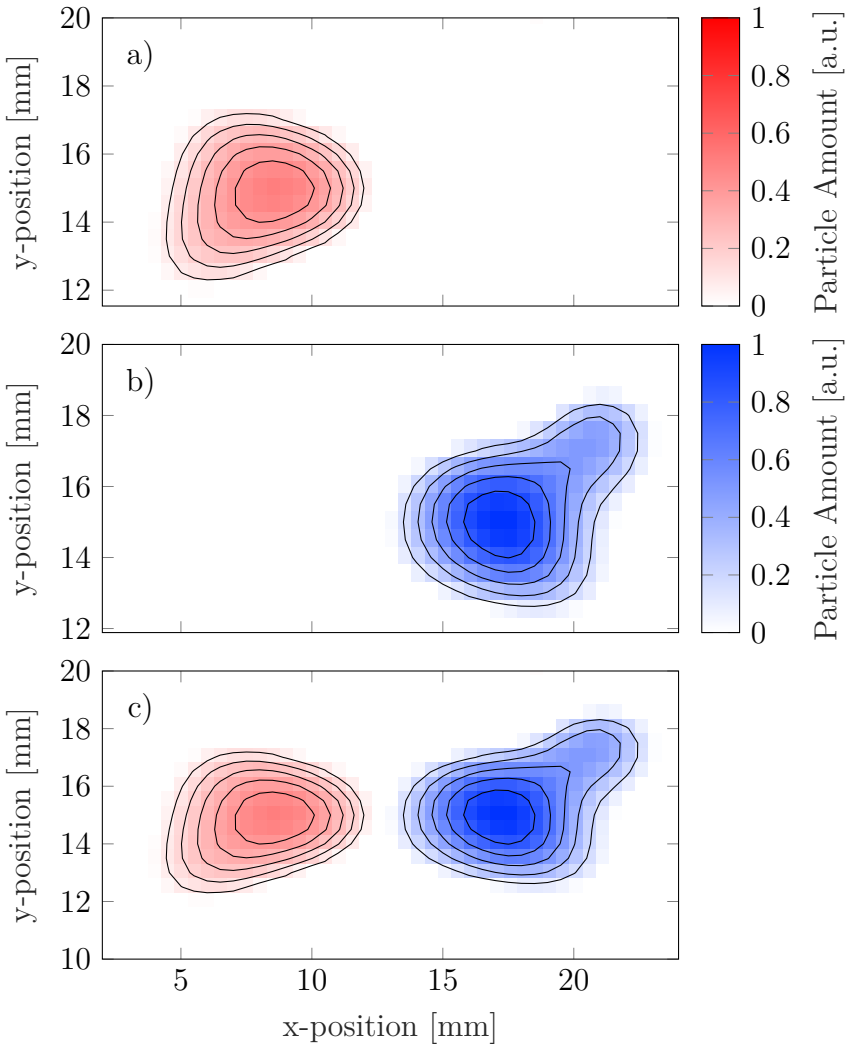


Figure 5.11: Reconstructions of MNP distributions for the colored MPM measurements. a) CT100 MNP are shown in red. b) ARA100 MNP are shown in blue. c) Both MNP types at the same time. Level sets of the reconstructions are shown to guide the eye.

5.5.4 Discussion

Prior to the reconstruction of the spatial particle distribution, the data was analyzed as it seemed that the magnetic fields of the particles were affecting the sensor's operating point. This resulted in amplitude dependent phase shifts. The fields associated with such behavior can already be in the range of a few hundred nT, as is indicated in the investigation shown in Appendix B.1.3, where a shift in the resonance is observed. Thus, one can say that the measurement itself affects the measurement results because the sensor changes its properties due to the effect of the magnetic field of the MNPs. This would be an influence of the ΔE effect. Most often for experiments using ME sensors, one would like to measure very small magnetic fields, such that an effect on the sensor properties as shown here is not noticed because it is negligible. However, if one wants to do imaging with the ME sensors, this effect can be detrimental as one needs to be able to model its effect accurately. One could argue that one just needs to use fewer particles, but if fields of larger volume need to be measured with larger distances to the sensor, then the sources closer to the surface of the volume may still cause this effect. If one does not account for the change in sensor properties, the reconstruction shows the formation of artifacts.

For MPM using single types of particles, the change of phase depending on the amplitude inhibit the proper use of a nonnegativity constraint on the MNP distribution. Furthermore, this can also be a resolution limiting factor for colored MPM, because to form the colored MNP image, the reconstruction is segmented into parts of different phase responses. If the data is affected by an amplitude dependent phase shift, this can not be done appropriately and artifacts form in the MNP distribution.

The reconstruction of the MNP distribution shown in Figure 5.11 shows that it is possible to image different particle behaviors. The reconstructions show a clear spatial separation of the particle types. The phase difference between the particle types was determined to be around 14°. The minimum phase response for proper colored reconstruction was shown to be around 10° (c.f. Chapter 4.3), which is met in this case. This was also supported by the MPS measurements shown in Chapter 5.3.

5.5.5 Conclusion

It was shown that the MPM imaging system is able to perform colored imaging for distinguishing particle types. It was furthermore shown that the magnetic fields of the MNPs can influence the sensor properties and an amplitude dependent phase shift was

observed in the measured signal, which needs to be accounted for in the computation of the reconstruction. This can be detrimental for imaging applications, but for this to be true the magnetic field values have to be rather large, as was the case here (about 500 nT). However, this effect probably persists even for low magnetic field values, though the influence on the reconstruction can then probably be neglected. The MPM system is only capable of imaging two different particles types. More particle types would only be possible if the sensor measured more than at a single frequency. A possible way to overcome this is measuring successively with two different excitation frequencies, i.e. 1/3 and 1/5 of the resonance frequency, such that one measures the 3rd and 5th harmonic in resonance. This way, one would be able to distinguish more MNP types, or possibly perform temperature imaging, as done in [78], [79]. In the future it may be possible to determine whether the MNP are inside of cells because cellular uptake of MNPs changes the MNP magnetic response, as shown in [129]. However, the authors did not report the phases associated with their findings, such that a statement on the viability cannot be made based on the simulations on the necessary phase changes as done in Chapter 4.3.

5.6 Resolution and Limitations

5.6.1 Objectives

In this section, experimental investigations of limitations of the imaging system such as spatial resolution, temporal resolution and minimum MNP amount for detection will be performed. To find the resolution of the 2D system, a set of experiments is performed on samples with trenches filled with MNPs, that successively get closer to each other. When the reconstruction fails to reliably resolve the MNPs in the trenches, this denotes the resolution of the imaging system for a chosen distance. Furthermore, to determine the minimum particle amount detectable with the MPM system, another set of experiments will be performed, in which point-like samples of a known amount of dried MNPs is used. Difficulties in the measurements to determine these tasks will be highlighted. Temporal resolution will be enhanced using a continuously moving sample instead of moving to a target location, stopping, measuring and moving to the next location.

5.6.2 Materials and Methods

5.6.2.1 Sample Preparation

The samples for the resolution measurements and for the limitations with respect to minimum resolvable amounts are schematically shown in Figure 5.12, labeled as a "Groove type" and "Dot type" samples, respectively. The "Dot type" sample has dimensions of 20×20 mm^2, a thickness of 1.5 mm, a hole of 1 mm diameter and a depth of 1 mm. The "Groove type" samples have a dimension of 20×20 mm^2, a thickness of 1.5 mm, and a grooves/trenches with a depth 1 mm embedded. These grooves are parallel and 1 mm apart. Certain amounts of MNPs are embedded into the dot or grooves and MPM measurements are performed on these samples. The MNPs used for these experiments are CT100, as characterized in Chapter 5.3. For the temporal resolution measurements, liquid CT100 particles in a flask were taken (Figure 5.12 bottom), because no reconstruction needs to be done for such measurements as the measurements only need to be reproducible for different measurement speeds. Multiple measurements of the same sample will be performed in succession to assess the reproducibility of the measurements.

5.6.2.2 Measurement

Colored MPM measurements were performed using the MPM setup and liquid MNP samples. A magnetic excitation field amplitude of 10 mTμ_0^{-1} was used. The frequency was adjusted to be 1/3 of the resonance frequency of the sensor. Prior to inserting the sample, the sensor was adjusted (via e.g. tilting) such that the peak at the resonance frequency was minimized. Additionally, a compensation signal was used to further suppress the signal at the peak.

The sample was inserted into the MPM system. The sensor-to-sample distance was adjusted to be around 2 mm. Furthermore, the measurement is done by moving the sample with respect to the sensor. A Cartesian grid was used for the measurement positions. The number of measurement points are 80×80 and the total measured dimensions are 20×20 mm^2. For each measurement position, the voltage signal of the sensor was measured and an FFT was computed using a Blackman window. The time length was set to be 4096 samples with a sampling frequency of 32 kHz, to yield a spectral resolution of 7.8 Hz. The complex peak signal at the resonance frequency is recorded and used for the data analysis.

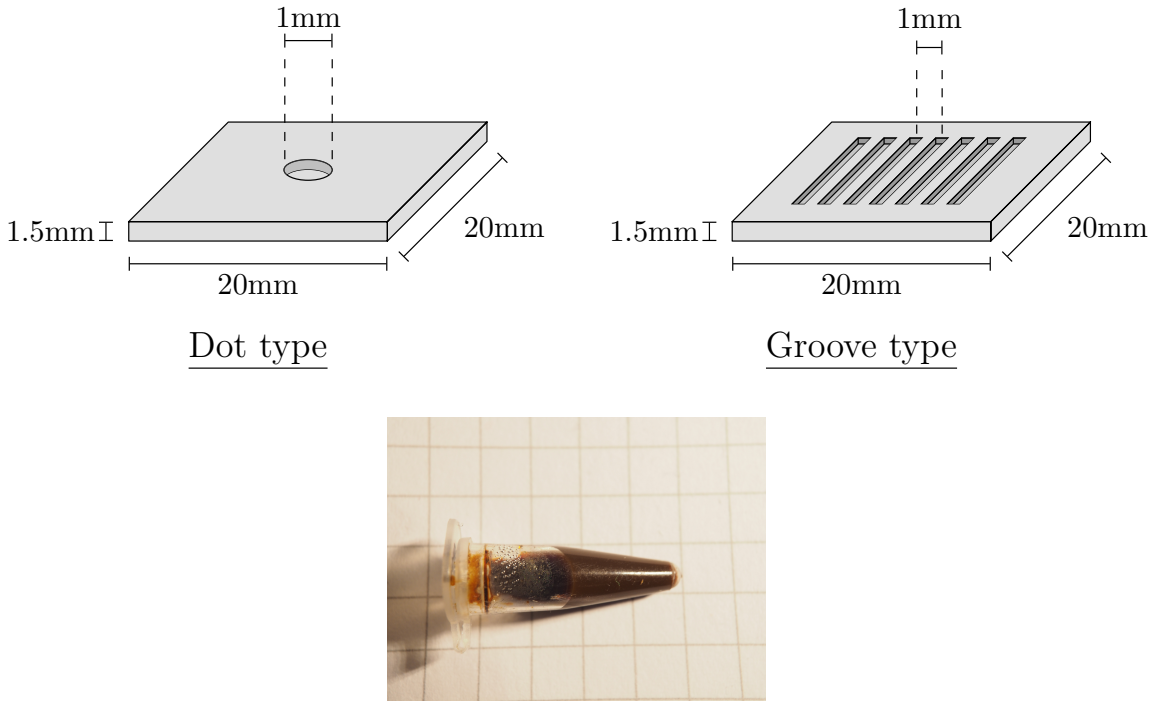


Figure 5.12: Sample types used in all investigations. (Left) Dot type, used for magnetic moment LOD. (Right) Groove type, used for spatial and temporal resolution tests. Taken from [143]. (Bottom) Flask with MNP for temporal measurements.

Furthermore, measurements were performed using different scanning speeds. Instead of individually measuring for a set position, the sample is continuously moved and the measurement signal is recorded. Depending on the speed, this would ensure a spatial averaging of the correct magnetic field value.

5.6.2.3 Data Analysis

For the reconstructions and quantification of the samples, it is necessary to analyze the data with respect to the phase response of the sensor. The phases where determined from a scatter plot and a subsequent linear interpolation is used to find the phase. In this case, contrary to the phases that were used for the colored MPM, which were liquid MNP samples, the phases where not exactly a line in the scatter plot. This may be due to changes in phase from a partially dried sample. However, for the data analysis, the data is projected onto a single phase, such that nonnegativity constraints can be

enforced. This may result in a worsening resolution. However, the constraints cannot be enforced otherwise. The reconstruction was done using the adaptive algorithm developed in Chapter 3.4.

The quantification from the "Dot type" samples is done via reconstructing the particle distribution under a nonnegativity constraint and taking the L^1-norm of the distribution, yielding the total amount of particles for the samples, based on the measured data.

The reconstruction iterations of the resolution "Groove type" samples was stopped based on visual inspection. An additional projection onto the scaled L^1 ball for each iteration was performed to promote sparsity in the reconstruction, yielding better resolution.

Furthermore, temporal resolution measurement are done with respect to repeatable experiments; that is, measuring the same sample multiple times for different measurement speeds and checking the similarity between the measurements. If different line shapes are a result, one needs to reduce the speed such that the data gathered is not limited by the sensor's transient motion during vibration.

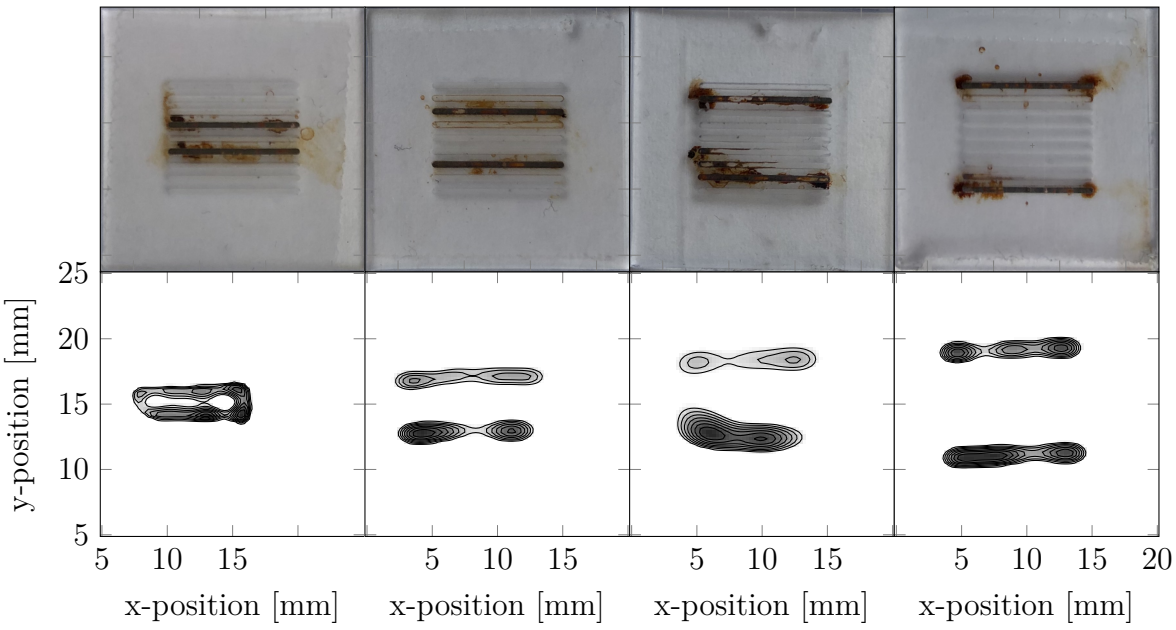


Figure 5.13: Determination of resolution for the 2D MPM system at a sample-to-sensor distance of about 2 mm. The reconstructions are shown below the sample photographs, on which MNPs were deposited, for visual comparison. Particle type CT100 from Chemicell were used.

5.6.3 Results

5.6.3.1 Spatial Resolution

The results for the resolution measurements are shown in Figure 5.13. For visual comparison, a photograph of the sample is shown above the reconstruction from the MPM measurements of shown sample. The dark regions of the photographs show the presence of MNPs, which were embedded in the grooves of the sample. Because the samples were initially sealed with tape to prevent evaporation of the water of the MNP solution, there is some spillage into other regions within the sample, as is most pronounced for the sample with 6 mm distance. However, even with tape, the liquid evaporated after some time, leaving dried MNPs in the grooves.

5.6.3.2 Temporal Resolution

Temporal resolution measurements are shown in Figure 5.14. Here, the same sample is measured 5 times with different speeds. The image shows the measured signals, each separated by an added 1 nT for better visualization. The direct comparison shows that the signal is essentially the same for all measurement speeds. Important to point out is the bump at about 120°. This stems from an impediment in the movement during measurement.

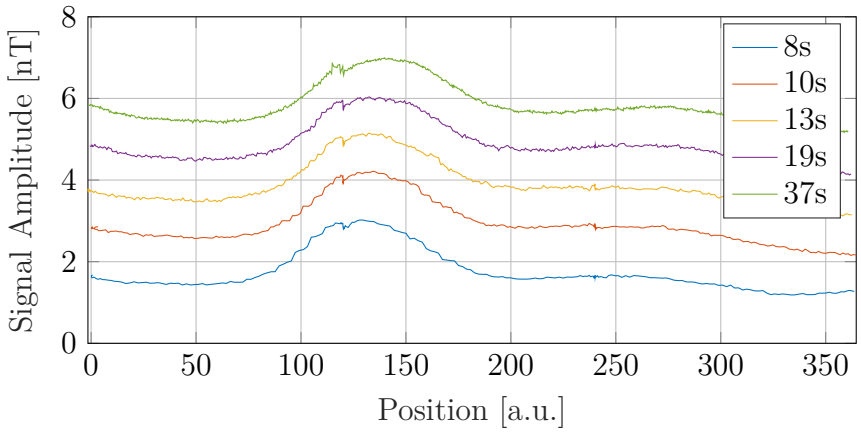


Figure 5.14: Measurements for the determination of temporal resolution. Each measurement is done for the same sample at different speeds. For visualization, each measurement is separated by an added 1 nT.

5.6.3.3 Limitation

The quantification and the maximum magnetic field values of the "Dot type" samples can be seen in Figure 5.15. For comparison, the response of CT100 MNPs based on MPS measurements are shown in the red line. The scattered data points seem to show a linear relationship, as is to be expected from the linearity of the integral equation for the imaging system (see Chapter 3.2.3). The blue line denotes a fitted line on the data, which are shown as the scattered blue dots. It can be seen that the MPM and MPS lines are separated by a factor of 5, indicating that the dried MNP of the "Dot type" samples may show a different response than the liquid samples. The maximum magnetic fields that can be resolved before a background signal starts to deteriorate the measurements is shown in Figure 5.15 b) and amounts to a few nT. A fitted line is shown for visual aid as well.

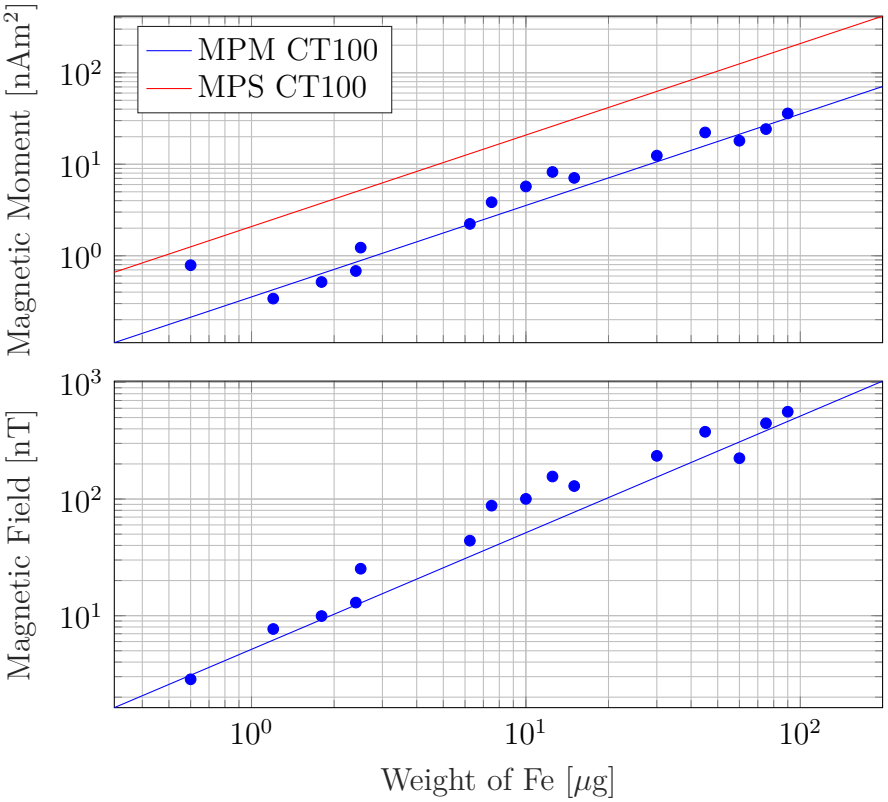


Figure 5.15: Measurement of the quantification of the MNP amount and the detected peak magnetic field amplitudes associated with different amounts of MNPs using the "Dot type" samples.

Furthermore, to assess the reproducibility of measurements, several MPM measure-

ments of the same sample were performed in succession. The result can be seen in Figure 5.16. The Figure shows the amplitude of the measured signal (converted to nT via the ME coefficient) for all measurement.

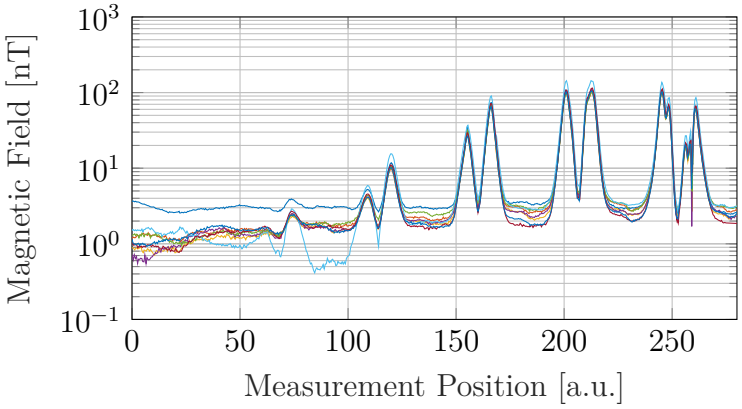


Figure 5.16: Multiple MPM measurements of the same sample measured in succession.

5.6.4 Discussion

5.6.4.1 Spatial Resolution

From the reconstructions shown in Figure 5.13, it can be seen that the samples with filled grooves that are 8 mm, 6 mm and 4 mm apart are clearly separated in the reconstructions. The sample in which the filled grooves are 2 mm apart show an overlap in the computed reconstructions. It is clear that if they are any closer to each other, the reconstructions would start to overlap, taking the resolution for a 2 mm sensor-to-sample distance to be about 2 mm. This is in accordance with the theoretical predictions as described in Chapter 4.5, maybe even a bit worse, because the geometry of the sensor over which the measured magnetic field is averaged needs to be considered as well.

Also for the sample with the grooves 6 mm apart, there is a spillage of MNPs into the neighboring grooves, which is also reflected in a more spread out MNP reconstruction from the MPM measurement (depicted via the dashed circle). Furthermore, because the MNPs inside the grooves dried out inhomogeneously, the MNPs show higher concentration especially at the ends of the grooves. At the same time, there are more MNPs depleted regions in between.

Spatial resolution for 2D is about the same as the distance to the sample. Possible enhancements can only be achieved if inhomogeneous magnetic fields are used, such that

regions can be selectively excitated. However, at the same time, the sensor's response to the inhomogeneous excitation fields have to be considered, because the sensor experiences parametric resonances (Appendix B.1.3). Background signal suppression for MPM with homogeneous excitation fields was achieved due to positioning of the sensor and using compensation coils. However, if one uses inhomogeneous magnetic fields, the sensor cannot be positioned in such a way that all inhomogeneous fields can be attenuated. The extent to which compensation coils can be used in this context is an open question and beyond the scope of this thesis. The compensation could be similar to the approach taken in [91]. Then, one also needs to consider effects on the sensitivity or resonance, because that is also affected by the excitation field (again Appendix B.1.3) and the compensation field. As a result, 3D imaging using the MPM approach will be exceedingly difficult to achieve, because many factors have to be considered for proper imaging.

Comparing the MPM system to other MNP imaging systems, one can say that scanning type imaging systems, such as the scanning type magnetorelaxometry imaging (MRXI) system described in [82], [89], or the scanning magnetic particle spectrometer (SMPS) described in [78], [79], have basically the same resolution. These are 2D imaging systems with a resolution of about 2 mm. The MPM system has a slightly better resolution due to the small size of the ME sensor, but the measurement procedure via homogeneous magnetic fields is fundamentally limited to resolutions that are roughly the distance to the sample.

5.6.4.2 Temporal Resolution

The results of the temporal resolution measurements show that for all measurement speeds (37s-8s), no major differences for the measurements can be seen. Only minor differences are present which can most likely be attributed to an unwanted background signal, as discussed in Chapter 3.2.4. The major features stay the same, which indicates the usefulness of a faster measurement speed. Thus in this case, the measurement speed could be increase by a factor of $\sim$5, which corresponds to about 1 $\frac{\text{mm}}{\text{s}}$, but can probably be even faster. The limiting factor will be the transient motion of the sensor, which is related to its quality factor. At the same time, there will be a trade-off between the temporal resolution and the spatial resolution, because the faster one measures, the fewer samples of the time signal can be used for the computation of data points for a reconstruction. There will be an averaging of the data with respect to the position in space during the movement.

5.6.4.3 Limitation

The measurements in Figure 5.15 show linear behavior with respect to the quantification of MNPs and the associated magnetic field based on the sensitivity of the sensor. It is shown in a log-log scale and it must be emphasized that, even if the linear trend is clearly visible, the measurement points scatter by a factor of 2-3 with regards to the trend line.

However, one would have to be careful to blindly associated the sensor signal with the magnetic field, because a background signal could be of different origins. For example, it could originate from the sensor itself due to external magnetic excitation, as is explored in Appendix B.1.3. This means that an assignment of a magnetic field to the voltage signal is inappropriate, because the background signal is caused by parametric amplification, and hence is a result of cross sensitivities of the sensor. The origin could be related to a changing working point on the magnetostriction curve of the sensor. The magnetic excitation field at $1/3f_r$ would then induce a frequency conversion into the resonance of the sensor, which interferes with the MNP signal. This statement is also supported in reference [5], where readout schemes and especially magnetic frequency conversions for magnetoelectric sensors are discussed. In reference [5] it is also discussed that the sensor shows different magnetic responses over time, indicating cross sensitivities of the sensor that need to be considered for imaging.

It can be seen that the quantification for the smallest amount of MNPs is way off compared to the other data points, by almost a factor of 5. This is due to a strong unwanted background, which was fitted during the data analysis. Because the background would not originate from the MNPs, the reconstruction gives the wrong results. The minimum value of the voltage signal, described in a magnetic field value via the sensor's sensitivity, is shown to be around 3 nT (for a spectral resolution of 7.8 Hz), whereas the limit of detection for the sensors is 3 orders of magnitude lower at 4 pt/$\sqrt{\text{Hz}}$. This implies that the cross sensitivity of the sensor to the external magnetic excitation limits its ability to be used for imaging applications. One would need to be able to describe the origin of the background signal to alleviate its effect on the measurement and thereby reconstruction for imaging. Due to that, the minimum amount that is reliably detectable is about 1 μg iron, or 0.3 nAm^2 for the magnetic moment.

The reproducibility measurements in Figure 5.16 show multiple MPM meaurements done in succession. The general shape of the curve is similar, especially for the peaks. However, one can see that for smaller amplitudes (a few nT), the curves differ substantially from each other. The reason for this is the background signal at the resonance, where the reasons for it are suggested to be due to magnetic frequency conversion (see

Chapter 2.1.3.4) and, with it, parametric resonances (c.f. Appendix B.1.3). One could only use the larger magnetic field values for imaging, because these values are most similar between measurements, but then one would lose information about the detail in the MNP distribution, thereby worsening the resolution.

Comparing the MPM system with the MSPM technique based on the ΔE effect developed in [109], the MSPM is much more robust, because an unwanted background due to magnetic frequency conversion does not occur and hence does not impede the measurement. The MSPM approach, unlike MPM, may not be able to perform colored imaging, because the timescales involved could be too small. This implies that the motion modulation would have to be high frequency, where the transient motion of the sensor affects the signal. In principle it would still be possible, though one would need to make use of higher order resonance modes, such that a larger bandwidth can be used for measurements, because MSPM essentially needs to describe an arbitrarily periodic function for each rotation, such that higher frequency terms need to be estimated correctly. For this, a larger bandwidth allows for more sensitivity, such that it can be resolved more correctly.

5.7 Summary

In this section, the MPM imaging systems figures of merit were experimentally investigated. This included spatial resolution, temporal resolution and the quantity limitations that can be detected via the system. The spatial resolution was determined to be around 2 mm for a 2 mm sensor-to-sample distance in a 2D system, which coincides with the theoretical estimate made earlier. The temporal resolution was enhanced via a continuous measurement scheme and amounts to about 1 $\frac{\text{mm}}{\text{s}}$. The limitations in terms of quantifying the MNP amount were found to be about 1 μg iron (or 0.3 nAm^2). The reproducibility of the MPM measurements was investigated by successive measurements of the same sample, which shows deviations at lower magnetic field values.

CHAPTER 6

Conclusion and Outlook

6.1 Conclusion

In this thesis, Magnetic Particle Mapping (MPM), a new imaging modality for magnetic nanoparticles using magnetoelectric sensors was developed and investigated. The technique exploits the nonlinear magnetic response of nanoparticles to enable higher harmonic detection in the mechanical resonance of the magnetoelectric sensor. A single highly sensitive magnetoelectric sensor is used in a scanning device. The magnetic response of the nanoparticles is mapped in space and from the measurement of the magnetic field, the spatial distribution of the MNPs is inferred. For this, the MPM imaging system was modeled and algorithms for the reconstruction and resolution of the spatial distribution were developed and verified using simulation and measurements. By solving the inverse problem from a forward model, MNP distributions were computed from measurement data.

Using the MPM technique, distributions of magnetically labeled cells were successfully imaged for 2D systems. This was done in the context of developing a possible technique for determining cell growth within scaffolds used in tissue engineering. Furthermore, colored imaging of different magnetic responses of the nanoparticles was performed, opening up possible applications with respect to immunoassays for the detection of molecular biomarkers. Another prospect may be imaging MNPs within cells and free MNPs. The algorithm developed for the reconstruction of the nanoparticle distribution is able to infer additional parameters related to sensor properties and magnetic nanoparticle orientations, such that these parameters and the nanoparticle distribution are estimated simultaneously. The algorithm was shown to work theoretically and in simulations and may be generalized to even predict parameters in other MNP imaging systems which also use a priori information that may be erroneous.

The evaluation of the MPM technique revealed the possible resolutions within such an imaging system and its current limitations. The resolution was shown to be limited to 1-2 mm in 2D and the imaging system is able to measure a magnetic moment of

$0.3\,\mathrm{nAm}^2$ in magnetic moment. These values are similar to other scanning MNP imaging techniques.

The MPM technique is restricted with respect to the measurable projections of the magnetic field because the sensor properties are exploited to attenuate an external excitation field that drives the MNPs into the magnetic nonlinear regime.

A drawback of the MPM imaging system is the sensor's response to strong AC magnetic excitation. This excitation shifts the working point of the sensor periodically, which thereby results in a modulation (magnetic frequency conversion) that couples into the resonance, even for monofrequent magnetic excitations. This signal then superimposes with the MNP response, yielding an unclean signal that interferes with proper imaging of the MNPs. As a result, a minimum MNP amount was experimentally found to be 1 µg iron detectable via MPM, which corresponded to a field strength of about 8 nT, which is far off the capabilities of the sensor (about $4\,\mathrm{pT}/\sqrt{\mathrm{Hz}}$).

The MPM technique was the first ME sensor-based imaging technique for MNP. ME sensors are attractive in this context because they are small, highly sensitive, have very low limit of detection and are fabricated via MEMS technology, which enables cheap production. Possibly large arrays of ME sensors can be used for imaging. Overcoming the shortcomings mentioned above is the subject of future research.

6.2 Outlook

6.2.1 Future Development

In the future, the capabilities of the imaging system can be further enhanced. With respect to measurement speed, faster motors for translation can be used. However, under these circumstances, one would need to consider the sensor's transient motion due to changing strengths of magnetic field from the MNP distribution, similarly considered in Magnetic Susceptibility Particle Mapping (MSPM) [109], [144].

To alleviate the background signal in resonance due to the sensor's magnetic frequency conversion, one would need to describe the sensor for the imaging system in detail, including nonlinear magnetic behaviors due to magnetostriction. At the same time, an in situ characterization of the sensor yields additional information that can be used for the reconstruction of the MNP distribution. However, these considerations only deal with the current MPM system, for which fundamental limitations in terms of

resolution were already derived and described. Hence, a different measurement approach needs to be invented to yield better resolution for 3D systems. For this, one would need to use inhomogeneous fields and clever combinations of the strengths of inhomogeneous fields, as done in [85]. However, at the same time one needs to ensure that the effect of the inhomogeneous field on the sensor is minimized. For all MNP sensing techniques where ME sensors are used, the placement of the sensor to an external magnetic field is paramount, i.e. in MPM, MSPM, [95] and [108]; in MPM to reduce frequency conversion effects from shifting working points, in MSPM, [95] and [108] for proper biasing of the sensor. The techniques MPM, MSPM and the research done in [95] use explicitly the shape anisotropy of the sensor to be able to perform measurements correctly. The use of inhomogeneous fields and the positioning of the sensor for proper MNP imaging becomes much more complicated. In MSPM, a permanent magnet arrangement was proposed that yields a Point-Spread-Function that changes depending on the depth in the sample[144]. While this is advantageous in the inverse problem, because the contribution of MNP at various positions in the sample is different, it does not necessarily guarantee good results for 3D imaging. What is needed are arrangements of coils/magnets that allow for spatially selective measurements, i.e. several measurements where different regions in the sample are excited. At the same time, proper compensation of unwanted sensor signals from the setup (coils/magnets) has to be performed, maybe similar to approaches such as the tomographic imaging setup developed in [91]–[93]. The choice of geometry of the inhomogeneous fields from coils/magnets comes into question. For this, one needs to optimize figure of merits (e.g. the matrix condition number) for the imaging system, as done in [84], [85], [87], [94]. Whether MPM, MSPM, or other scanning type MNP imaging systems, the 3D imaging of MNP distributions is far from trivial and the correct approach remains to be developed.

6.2.2 Potential Applications

6.2.2.1 Tissue Engineering

One application for MPM could be in tissue engineering, where cell distributions within scaffolds are imaged over time. While other native imaging techniques, such as Magnetomotive Optical Coherence Tomography (MMOCT), use MNPs as a contrast agent to yield an image of MNPs within a scaffold, the scaffolds need to be optically transparent/translucent to image the MNPs. Here, the MPM technique could prove to be useful, since ME sensors are rather small, although resolution will be limited to the mm scale

for 2D systems.

6.2.2.2 Sentinel Lymph Node Biopsy

A medical application for MPM could be Sentinel Lymph Node Biopsy (SLNB). SLNB has not yet been performed using ME sensors to this day. Perhaps a hand-held device is possible for detecting MNPs in lymph nodes, which would correspond to basically finding a (or a few) dipole(s) with ME sensor measurements. Finding single magnetic sources has essentially been performed several times in different contexts within the CRC 1261, in particular in the context of Deep Brain Stimulation (DBS) [145], [146] and ME sensor localization [16]. For this, a measurement approach and device geometry must be chosen carefully. This can be of interest in the future.

APPENDIX A

Appendix A

A.1 Multicriteria Problem

Tikhonov regularization can also be understood as a multicriteria optimization problem. Instead of having a single minimizer for the cost function, we have a set of possible solutions, which is also sometimes called the set of Pareto optimal points (given that the cost function is convex) [147]. We consider the cost function as the weighted superposition of the data-fidelity term $F_1 = \|\boldsymbol{A}\boldsymbol{x} - \boldsymbol{b}\|_2^2$ and the regularizer $F_2 = \|\boldsymbol{x}\|_2^2$ via a weight vector $\boldsymbol{\lambda}$, i.e.

$$\begin{aligned}
\boldsymbol{\lambda}^\intercal \boldsymbol{F} &= \begin{pmatrix} \lambda_1 & \lambda_2 \end{pmatrix} \begin{pmatrix} F_1(\boldsymbol{x}) \\ F_2(\boldsymbol{x}) \end{pmatrix} \\
&= \lambda_1 F_1(\boldsymbol{x}) + \lambda_2 F_2(\boldsymbol{x}) && \text{(A.1)} \\
&\Rightarrow \min_{\boldsymbol{x}} \left(F_1(\boldsymbol{x}) + \frac{\lambda_2}{\lambda_1} F_2(\boldsymbol{x}) \right) \\
&\Rightarrow \min_{\boldsymbol{x}} \left(\|\boldsymbol{A}\boldsymbol{x} - \boldsymbol{b}\|_2^2 + \lambda \|\boldsymbol{x}\|_2^2 \right). && \text{(A.2)}
\end{aligned}$$

Thus all combinations of $\boldsymbol{\lambda} \geq 0$ define the orientation of the supporting hyperplanes for the set of optimal points, as can be seen in Fig: A.1. It is interesting to point out that the line created by the optimal points is, if plotted on a log-log scale, the L-curve, which is used as a heuristic for the choice of regularization parameter for solving inverse problems [113].

A.2 Projection onto L2 ball

The projection onto the L2 ball is intuitivly clear, i.e. that the vector is just rescaled to the desired size while keeping its direction. To prove that, we start out by writing down

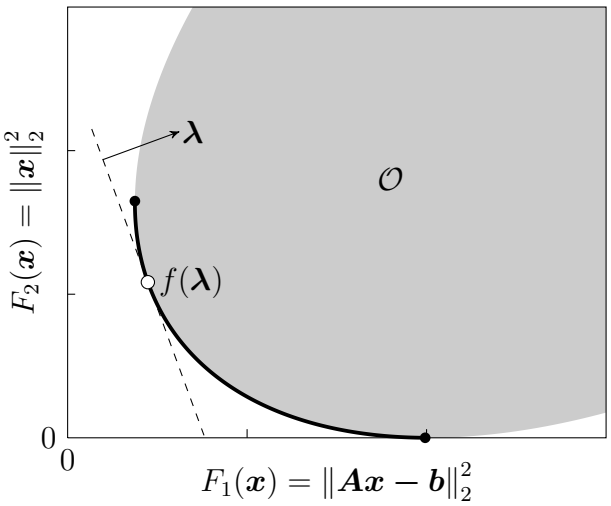


Figure A.1: The multicriteria problem, in this case regularized least squares, does not have a single optimal (i.e. minimal) point, but a set of optimal points, depending on the trade-off between regularization term $\|\boldsymbol{x}\|_2^2$ and the data fidelity term $\|\boldsymbol{A}\boldsymbol{x} - \boldsymbol{b}\|_2^2$. These solutions are defined by supporting hyperplanes given by $\boldsymbol{\lambda}$ of the set of feasible points $\mathcal{O}$. Inspired from [147] Page 58.

the Lagrangian

$$\mathcal{L}(\boldsymbol{u}, \lambda) = \frac{1}{2}\|\boldsymbol{u} - \boldsymbol{x}\|_2^2 + \lambda\frac{1}{2}\left(\|\boldsymbol{u}\|_2^2 - w\right). \tag{A.3}$$

The derivative with respect to $\boldsymbol{u}$ gives

$$\begin{aligned} \boldsymbol{u} - \boldsymbol{x} + \lambda\boldsymbol{u} &= \boldsymbol{0} \\ \boldsymbol{u} &= \frac{\boldsymbol{x}}{1+\lambda}. \end{aligned} \tag{A.4}$$

Plugging the result into the condition that $\|\boldsymbol{u}\|_2^2 = w$ yields

$$\lambda = \frac{\|\boldsymbol{x}\|}{w} - 1 \tag{A.5}$$

which means that

$$\boldsymbol{u} = \frac{\boldsymbol{x}}{\|\boldsymbol{x}\|}w \tag{A.6}$$

which was the expected result.

The Matlab code for the projection onto the L2 ball can be seen in the code snippet A.1.

```
function x = projection_L2_ball(x,xnrm)
  x = x/norm(x)*xnrm;
end
```

Listing A.1: Projection onto L2 Ball.

A.3 Projection onto L1 ball

The projection onto the L1 ball can be computed by minimizing the Lagrangian

$$\mathcal{L}(\boldsymbol{u}, \lambda) = \frac{1}{2} \|\boldsymbol{u} - \boldsymbol{x}\|_2^2 + \lambda (\mathbf{1}^\intercal \boldsymbol{u} - v). \tag{A.7}$$

Here we assume that $\boldsymbol{u} \in \mathbb{R}_+$. Differentiation with respect to $\boldsymbol{u}$ yields

$$\boldsymbol{u} = \max(\boldsymbol{x} - \lambda \mathbf{1}, \mathbf{0}) \tag{A.8}$$

where the max is applied component-wise. Under the condition that $\mathbf{1}^\intercal \boldsymbol{u} = v$, we get

$$\begin{aligned} \mathbf{1}^\intercal \max(\boldsymbol{x} - \lambda \mathbf{1}, \mathbf{0}) - v &= 0 \\ \sum_i^N \max(x_i - \lambda, 0) - v &= 0. \end{aligned} \tag{A.9}$$

We now need to find the λ for which this equation holds. The derivative of this equation is a piecewise linear function in λ, which can be solved efficiently via a few Newton iterations. An efficient implementation can be found in the IR Tools package *gdnnf_projection* function [148].

A.4 Projection into Nonnegative Orthant

The projection into the nonnegative orthant is simply imposing a box constraint on the parameters with minimum value 0 and maximum value ∞. The projection is thus given

by:

$$\mathcal{P}_{+}(\boldsymbol{x}) = \max(\boldsymbol{x}, 0) \tag{A.10}$$

where the max is applied component-wise. The Matlab code for the projection onto the L2 ball can be seen in the code snippet A.2.

```
function x = projection_nonnegative_orthant(x)
  x = max(x,0);
end
```

Listing A.2: Projection into the nonnegative orthant.

A.5 Projection into a Box

The projection into a box is simply imposing a box constraint on the parameters with minimum value $x_{\min}$ and maximum value $x_{\max}$ using min and max functions. The projection is thus given by:

$$\mathcal{P}_{C}(\boldsymbol{x}) = \min(\max(\boldsymbol{x}, x_{\min}), x_{\max}) \tag{A.11}$$

where the max and min is applied component-wise. The Matlab code for the projection onto the L2 ball can be seen in the code snippet A.3

```
function x = projection_box(x,xmin,xmax)
  x = min(max(x,xmin),xmax);
end
```

Listing A.3: Projection into a box.

A.6 Projection into a Cone

A cone can be understood as the set of points given by the linear combination of the linearly independent vectors $\boldsymbol{q}_i \in \mathbb{R}^n$ with $i = 1, 2, ..., k$, which constitute the matrix $\boldsymbol{Q}$, via nonnegative weights $\boldsymbol{y} \in \mathbb{R}^k_{\geq 0}$, i.e.

$$\boldsymbol{Q}\boldsymbol{y} = \boldsymbol{c}. \tag{A.12}$$

Projection of a point $\boldsymbol{x}$ into the cone ($\boldsymbol{x}_{\boldsymbol{Q}} = \mathcal{P}_+^{\boldsymbol{Q}}(\boldsymbol{x})$) is done via the projection of the mapping $\boldsymbol{Q}^{-1}\boldsymbol{x}$ into the nonnegative orthant, and mapping back via $\boldsymbol{Q}$, i.e.

$$\boldsymbol{x}_{\boldsymbol{Q}} = \boldsymbol{Q}\mathcal{P}_+\left(\boldsymbol{Q}^{-1}\boldsymbol{x}\right). \tag{A.13}$$

For a cone in the complex plane, given a complex vector $\boldsymbol{x}$, the projection would be done as shown in the code snippet A.4.

```
function [x,y] = projection_cone(x,Q)
  y = max(Q\[real(x),imag(x)]',0);

  x = [1,1i]*Q*h;
  x = x(:);
end
```

Listing A.4: Cone projection operator $\mathcal{P}_+^{\boldsymbol{Q}}$ for colored Magnetic Particle Mapping. The matrix $\boldsymbol{Q}$ incorporates magnetic particle behavior with respect to amplitude and phase responses. The magnetic particle distribution $\boldsymbol{x}$ has to lie in the cone spanned in the complex plane due to the different particle behaviors.

APPENDIX B

Appendix B

B.1 Sensor Behavior

The sensor's response to magnetic fields is often modeled as a resonator with low damping, indicating its high quality factor. This section serves as a discussion on the sensor behavior in general, pointing out basic behaviors that relate to the sensor's modes of signal aquisition. These are related to the modulation methods for the measurement of low frequency fields as well as the direction measurement of magnetic fields.

The main feature that allows the ME-sensors to be of high sensitivity is the mechanical resonance, because it amplifies the magnetoelectric coefficient due to a higher oscillation amplitude at the resonance. The sensor's mechanical resonance is described by the following equation of motion:

$$\ddot{y} + a\dot{y} + by = 0. \tag{B.1}$$

The important parameters, such as resonance frequency and quality factor, can be estimated using the coefficients a and b. While this model is very simple, it captures the most important behavior of the sensor. Electrical measurement will also exhibit this resonance behavior as a result of mechanical coupling into the piezoelectric material.

One has to emphasize that the properties of the resonance, i.e. resonance frequency and quality factor, are also related to the magnetic properties of the sensor. This is due to the relationship of the mechanical properties and the magnetic properties from its magnetostrictive material. As a result, additional sensitivities can be exploited for measurement of magnetic fields. One such technique uses the so called ΔE effect, where an external AC magnetic field changes the resonance frequency of the sensor, which modulates a supplied carrier signal. In other words, the external magnetic AC field detunes the sensor periodically. The carrier is supplied near the resonance of the sensor, such that the resulting modulation side bands exploit the large sensitivity at the resonance.

The effect of the external magnetic field can be described by a time dependent reso-

nance frequency via:

$$\ddot{y} + a\dot{y} + b(t)y = 0 \tag{B.2}$$

where $b(t)$ changes periodically with the external magnetic field's frequency. In fact, for small magnetic field amplitudes, the system can be described via a linearization about the resonance frequency at zero external magnetic field, i.e.

$$\ddot{y} + a\dot{y} + \omega_0^2(1 + \epsilon\cos(\omega_{ex}t))y = 0 \tag{B.3}$$

with $\epsilon \ll 1$. This is a type of Mathieu's differential equation. This also suggests the occurrence of parametric resonances, which has also been observed in magnetoelectric sensors in the past[149], [150]. This claim will be validated in the upcoming sections. Additional generalization also involves a periodic damping term, such that

$$\ddot{y} + a(t)\dot{y} + b(t)y = 0 \tag{B.4}$$

describes the sensor response. It has to be noted that because the coefficients are periodic with respect to the external magnetic field frequency, the eigensolutions to the differential equation are Bloch waves.

Thus, the differential equation can be rewritten as a Schrödinger Equation by using the substitution $y = U(t)Z(t)$ and choose the function $U(t)$ such that the damping in term of $\dot{Z}$ vanishes. As a result, the equation of motion becomes

$$\ddot{U}Z + \ddot{Z}U + 2\dot{U}\dot{Z} + a\dot{U}Z + a\dot{Z}U + bUZ = 0. \tag{B.5}$$

Next the condidtion on $U(t)$ mentioned above is imposed which leads to

$$2\dot{U} + aU = 0 \tag{B.6}$$

$$\Rightarrow U(t) = \exp\left(-\frac{1}{2}\int^t a(s)\mathrm{d}s\right) \tag{B.7}$$

and thereby

$$\ddot{Z} + Q(t)Z = 0 \tag{B.8}$$

$$\begin{aligned} Q(t) &= \frac{\ddot{U} + a\dot{U} + bU}{U} \\ &= -\frac{1}{4}a^2 - \frac{1}{2}\dot{a} + b \end{aligned} \tag{B.9}$$

which is often called a Hill differential equation due to the periodic $Q(t)$. This is equivalent to a Schrödinger Equation for a periodic potential, and hence due to Bloch's theorem, the solution to this differential equation are Bloch waves.

Since Bloch waves are plane waves modulated by a periodic function with a periodicity dictated by the function $a(t)$ and $b(t)$ (and hence by the external AC field), the solution spectra exhibit additional peaks around the main resonance frequency of the system. This will also be true for a driven oscillator.

B.1.1 Asymmetric Resonance

On the topic of measuring the susceptibility of the sensor as a function of frequency, the frequency response shows an asymmetric resonance, which suggest the interference with a background χ_0, which may be a complex value. For the measurement, an AC susceptometer was used (see Figure B.1). A possible reason could be that there is an interference between a background susceptibility from the magnetostrictive material and a change in susceptiblity from the mechanical resonance due to a magnetoelastic coupling during oscillations of the sensor. Though this is mere speculation and a more elaborate investigation is needed for a definite answer. Either way, the susceptility $\chi(\omega)$ can readily be described via the equation:

$$\chi(\omega) = \chi_0 + \frac{A}{1 - \left(\frac{\omega}{\omega_0}\right)^2 + iQ^{-1}\frac{\omega}{\omega_0}}. \tag{B.10}$$

Here, Q is the quality factor of the resonator and ω_0 the resonance frequency. Such an asymmetric resonance can also be observed for electrical measurements of the magnetoelectric coefficient, as shown in [5], [151], which also suggests that the reason is related to the magnetostrictive material[152]. Optical measurements of the cantilever deflection does not exhibit an asymmetric resonance.

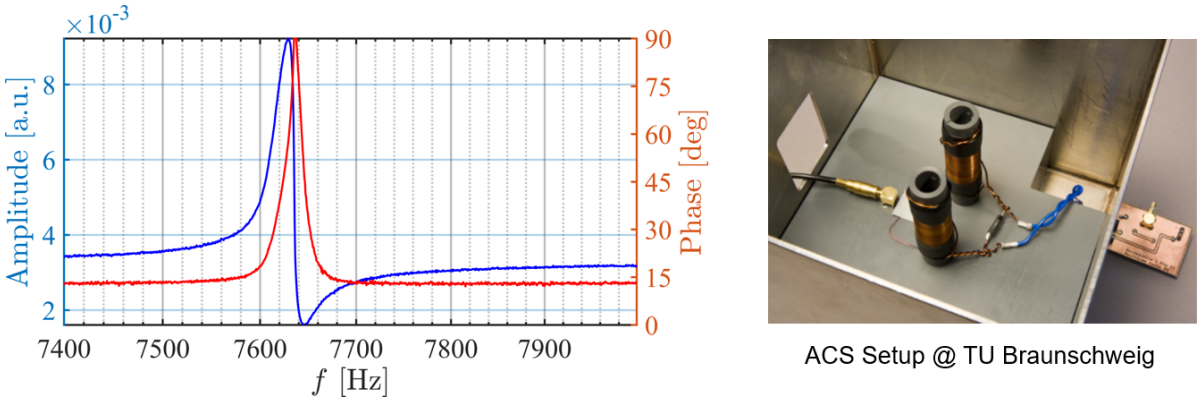


Figure B.1: AC susceptiblity measurment of the magnetoelectric sensor. An asymmetric resonance can be observed, which can be attributed to an interference with a background. The amplitude is directly proportional to the susceptiblity of the sensor. The calibration factor was lost due to a faulty calibration.

B.1.2 Nonlinearities

Additionally, the sensor can exhibit nonlinearities if the excitation amplitude becomes too large. Under these circumstances, the sensor detunes (either hardening or softening) and the frequency response "tilts" to either side. This can be described, e.g., by a Duffing oscillator. The resonators response is thereby dependent on the amplitude of oscillation itself. It was shown on several occasions that magnetoelectric sensors exhibit tilted resonance behaviors, as shown in [153], [154] and [155].

The correct description of a nonlinear oscillator can get arbitrarily complicated if one additionally considers the resonators parameters to be variable (as done for parametric resonators). Then, parameter estimation to describe the system from measurements becomes a daunting task. A possibly efficient approach to estimate these parameters would be state space modeling. This section does not serve as a guide on how to achieve this, because it lies beyond the scope of this thesis. This section merely acts as a pointer to important aspects to consider when using the sensor under a general set of circumstances. Furthermore, in the following sections, some claims of sensor properties based on theoretical considerations will be shown experimentally. A thorough description of the underlying mechanisms on a physical basis will not be the discussed. The reader may take this as an invitation to take up this task. The sections will only show the existence of certain sensor properties and how such properties might interfere

with measurements done for imaging applications in the context of MPM.

Figure B.2 shows the harmonic frequency response of the sensor for increasing magnetic excitation amplitudes. As can be seen for low excitation amplitudes, the frequency response shows a minimum, indicating an interference of a background signal and the resonance of the sensor. With increasing magnetic excitation amplitudes, the resonance frequency shifts to lower frequency, until it reverses to higher frequencies. The shift of the resonance frequency is due to an increased nonlinear contribution to the oscillator. When the symmetric frequency response's maximum tilts to lower frequencies, the nonlinear contribution leads to a "softening" of the resonator, i.e. the resonance frequency is reduced. If the frequency response tilts to high frequencies, the resonator shows a "hardening" behavior, which implies an increased resonance frequency. The transition regime between a softening and hardening resonator seems to nullify the nonlinearity.

It can furthermore be seen from Figure B.2 that for high magnetic excitation amplitudes, the maximum achievable amplitude decreases. The frequency response from about 450µT also shows no discontinuities, unlike the frequency reponses shown for excitation amplitudes of 25 µT-250 µT. The discontinuity implies an unstable regime for the resonator. Thus, the frequency response for excitation amplitudes above 450 µT were stable again.

B.1.2.1 Parameter Extraction

When measuring the harmonic frequency response (i.e. the frequency response for the excitation frequency) of the sensor, one may need to extract parameters described in the equations of motion. To extract parameters for a measured resonance frequency response, in this case for a Duffing Oscillator, one needs to employ numerical optimization techniques. For this Matlab's *lsqnonlin* function is used. As a necessary condition to use this function efficiently, one needs to compute the frequency response of a Duffing Oscillator for a given set of parameters efficiently. To do this, the approach used in [156] is employed, which computes the associated frequencies for a given amplitude. Other approaches often compute the current amplitudes from given frequencies. The latter involves solving systems of nonlinear equations and takes up more computation time than the former approach. Using the latter approach and Matlab's nonlinear optimization function *lsqnonlin*, one can extract the parameters for a Duffing oscillator for the sensor. However, the model was merely based on the (cubic) Duffing Oscillator, and any higher order nonlinear contribution is not considered.

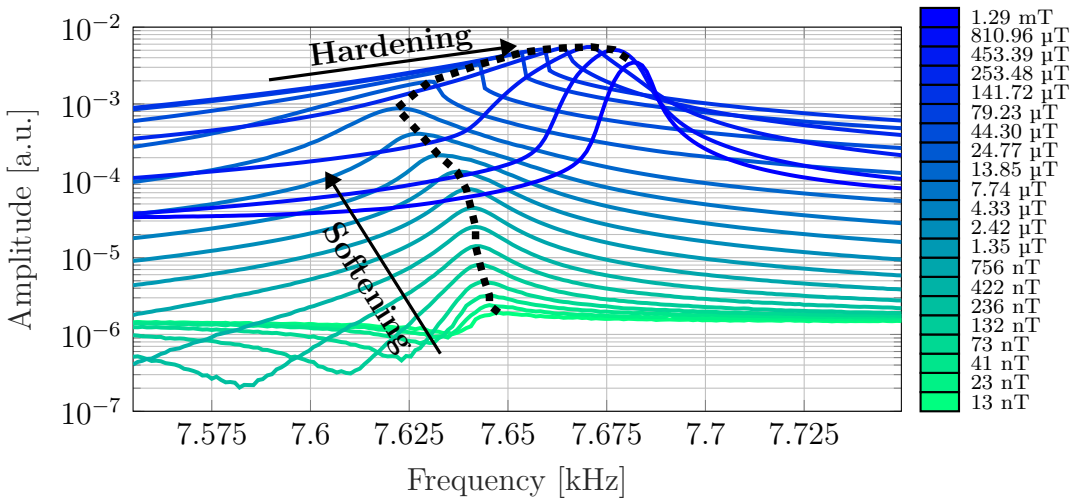


Figure B.2: Measured *harmonic* frequency response of the ME sensor. A minimum is seen for low excitation amplitudes, which is due to a background interfering with the resonator. With increasing excitation amplitude, the sensor shows nonlinear behavior by first a softening frequency response, followed by a hardening for even higher excitation amplitudes, which is indicated by a resonance frequency shift to lower values (softening) and shift to higher frequencies (hardening). This is furthermore indicated by a tilted resonance curve. The dashed line shows the course of the peak amplitudes of the frequency response with increasing excitation amplitudes.

Using this fitting approach, the data of B.2 can only be fitted (no fits shown) in the regions for low magnetic excitation and a softening resonator. It fails to fit the hardening frequency response of the resonator. One reason may be that nonlinear higher order contributions must be considered, as the resonator potential may be strongly asymmetric for these high excitation amplitudes.

B.1.3 Relationship to MPM

In MPM, magnetic nanoparticles are excited at 1/3 of the resonance frequency of the sensor, such that higher harmonic excitations are detected in resonance. The argument is then that the applied magnetic AC field has to be very clean, i.e. just a single frequency, such that only the MNP signal is measured at resonance. However, even if a perfectly clean signal is applied, higher harmonic excitations will still be generated because of the sensors detuning due to the external magnetic field. This effect may be alleviated through proper aligning of the sensor, though some effect would always be present.

If an external magnetic field is applied, it does not only change the properties of the sensor, but also drives the sensor to oscillation. Now, the combination of both can lead to the formation of higher harmonic excitations. This can most easily be imagined by first looking at a non-detuning sensor. In that case, the system behaves linear, and a single frequency input (forced oscillation) generates a single frequency output. However, if the sensor detunes during the oscillation cycle, amplitude and phase will shift, resulting in a multifrequency output. It can be considered as a modulation of the excitation. If the modulation is facilitated by the excitation itself, i.e. the signal that drives the sensor also detunes the sensor, then the modulation infers basically the formation of higher harmonic excitations. In the context of MPM, where one excites the system at 1/3 the resonance frequency, this detuning characteristic would also be a cross sensitivity that interferes with the measurement of magnetic nanoparticles.

Figure B.3 shows the occurence of parametric resonances for a theoretical system using a driven Mathieu's equation (Eq. B.3) (Parameters: Quality factor $Q = 100$, $a = \frac{Q^{-1}}{\omega_0}$, $\omega_0 = 1$ and $\epsilon = 0.1$) and measured for the ME sensor for strong magnetic excitation.

Both plots show the maximum oscillatory amplitudes of the spectra for each excitation frequency. It has to be emphasized that for every excitation frequency, a spectrum is associated with the data point, not only a single frequency. Hence, higher harmonic excitations are present that couple into the mechanical resonance of the sensor for fundamental excitations at fractions of the resonance frequency f_1. Additionally, a resonance is seen at $2f_1$, such that we can make the statement that resonances can be observed for $2f_1/n$ with n being a positive integer. This is characteristic for parametric resonances, as can be read here [157].

The frequency response from Mathieu's Equation (Figure B.3 Top) shows that already a simple description of the sensors behavior can roughly describe the occurrences of parametric resonances for the measurements. To yield a better description for the sensor behavior, one would need to describe the the modulation of the parameters of the resonators more correctly, and need to consider nonlinear terms, like for the Duffing equation. The parametric resonance at $2f_1$ is unstable and therefore grows exponentially. In reality, loss mechanisms would limit this behavior.

The Figure B.3 Bottom shows the ME frequency response for strong magnetic field excitations. Besides the apparent parametric resonances for $2f_1/n$, with $n = 1, 2, 3, 4, 5$, additional resonances are depicted in red, which are parametric resonances for the second bending mode at $\sim 6.2f_1$.

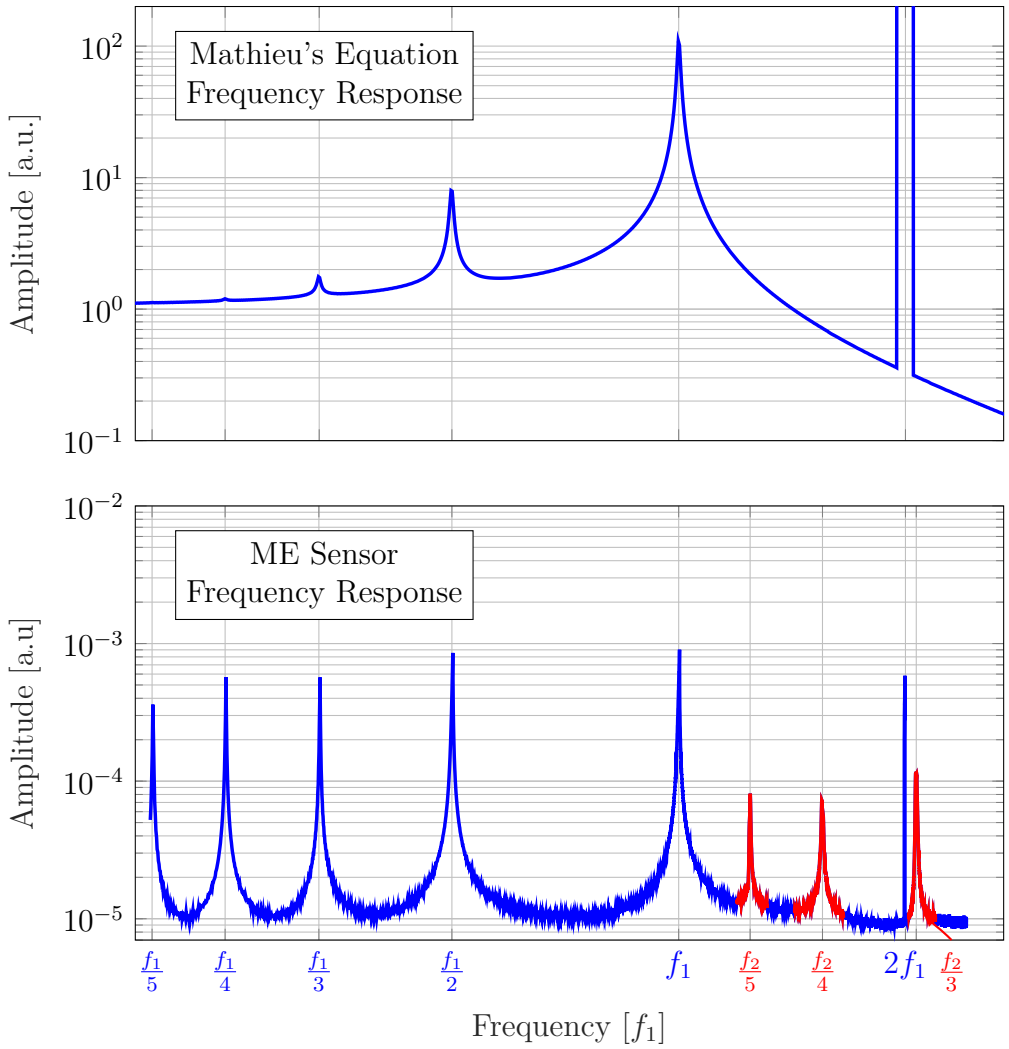


Figure B.3: Top: Simulated Frequency response of a driven Mathieu's equation. Bottom: Frequency response of a magnetoelectric sensor that shows parametric resonances. Note that for each excitation frequency (abscissa), the amplitude (ordinate) is given by the square root of the total power of the resulting response of the sensor. The blue curve corresponds to the measurement of the resonance in a harmonic manner, meaning the frequency with which the resonator is excited is the frequency at which the amplitude is measured.

B.2 Fitting a Single Dipole

This section deals with the estimation of parameters such as position and orientation of a single dipole. Under the circumstance that only one or few sources of magnetic dipoles have to be found, one can resort to nonlinear optimization techniques that only involve solving for the parameters one needs to describe the signal. This can, e.g., be position and magnetic dipole orientation. For this, some derivatives of the dipole field have to be introduced first. Then the Levenberg–Marquardt algorithm is used to estimate the parameters from simulated data. Results suggest that this method is highly effective and efficient to solve for unknown parameters of only a few dipoles.

B.2.1 Derivatives of Magnetic Dipole Field

The projected dipole field is given by

$$\begin{aligned} b &= \boldsymbol{m}^\intercal \boldsymbol{H} \boldsymbol{s} \\ &= \boldsymbol{m}^\intercal \frac{3\boldsymbol{r}\boldsymbol{r}^\intercal - \boldsymbol{r}^\intercal \boldsymbol{r} \boldsymbol{I}}{\left(\boldsymbol{r}^\intercal \boldsymbol{r}\right)^{5/2}} \boldsymbol{s}. \end{aligned} \tag{B.11}$$

Here, $\boldsymbol{m}$ denotes the magnetic dipole, $\boldsymbol{s}$ denotes the sensitivity axis of the sensor and $\boldsymbol{H}$ describes the dipole geometry. We now ask for the derivative w.r.t. $\boldsymbol{r}$. Since we are taking the gradient of the projected dipole field, the result will yield a vector:

$$\begin{aligned} \frac{1}{\|\boldsymbol{m}\| \, \|\boldsymbol{s}\|} \frac{\partial b}{\partial \boldsymbol{r}} =& \hat{\boldsymbol{m}}^\intercal \frac{\partial \boldsymbol{H}}{\partial \boldsymbol{r}} \hat{\boldsymbol{s}} \\ =& \frac{3}{\left(\boldsymbol{r}^\intercal \boldsymbol{r}\right)^2} \left(\left[\boldsymbol{I} - 5\hat{\boldsymbol{r}}\hat{\boldsymbol{r}}^\intercal \right] \hat{\boldsymbol{m}}\hat{\boldsymbol{r}}^\intercal + \hat{\boldsymbol{m}}^\intercal \hat{\boldsymbol{r}} + \hat{\boldsymbol{r}}\hat{\boldsymbol{m}}^\intercal \right) \hat{\boldsymbol{s}}. \end{aligned} \tag{B.12}$$

The derivatives with respect to the sensitivity $\boldsymbol{s}$ and $\boldsymbol{m}$ are given by (Note that $\boldsymbol{H} = \boldsymbol{H}^\intercal$)

$$\frac{1}{\|\boldsymbol{m}\|} \frac{\partial b}{\partial \boldsymbol{s}} = \boldsymbol{H} \hat{\boldsymbol{m}} \tag{B.13}$$

$$\frac{1}{\|\boldsymbol{s}\|} \frac{\partial b}{\partial \boldsymbol{m}} = \boldsymbol{H} \hat{\boldsymbol{s}}. \tag{B.14}$$

Using these derivatives, one can fit the unknown parameters to measurement data. The procedure on how to do this will be shown in the next section.

B.2.2 Iterative Estimation of Dipole Parameters

Given some measurement data $\boldsymbol{b}$, we now want to estimate the position and orientation of a single dipole. In the previous section, analytical expressions were introduced, which can be used to solve the nonlinear estimation problem. First, the problem to solve is

$$\min_{\boldsymbol{\beta}} \left\{ \| \boldsymbol{f}(\boldsymbol{\beta}) - \boldsymbol{b} \|_2^2 \right\} \tag{B.15}$$

The parameters $\boldsymbol{\beta}$ can consist of e.g. the position $\boldsymbol{r}$ and the sensitivity axis $\boldsymbol{s}$ (or the magnetic dipole $\boldsymbol{m}$). For iterative procedures we will use the Jacobian $\boldsymbol{J}$, which is defined as:

$$\boldsymbol{J} = \frac{\partial \boldsymbol{f}}{\partial \boldsymbol{\beta}}. \tag{B.16}$$

We can then use the Levenberg–Marquardt algorithm to solve iteratively. Here, we use a local linearization for the objective function using the Jacobian to find an expression to update the parameters $\boldsymbol{\beta}$ optimally. The optimal update $\boldsymbol{\delta}$ on the parameters $\boldsymbol{\beta}$ is then given by:

$$\boldsymbol{\delta} = \left(\boldsymbol{J}^\mathsf{T} \boldsymbol{J} + \lambda \boldsymbol{I} \right)^{-1} \boldsymbol{J}^\mathsf{T} \left(\boldsymbol{b} - \boldsymbol{f}(\boldsymbol{\beta}) \right) \tag{B.17}$$

with λ acting as a damping parameter to allow invertibility of the associated matrix. Few iterations are necessary to converge to a (local) minimum. An example cost function surface is shown in Figure B.4. The Figure shows the positions of magnetic sensors indicated as blue dots; the position of the dipole is indicated as the red dot after few iterations using the Levenberg–Marquardt algorithm. The level sets of the cost functions are drawn and the color indicates the (logarithmic) values, with blue being the smallest error and yellow the largest.

It is also **noteworthy** to point out that the relationship between dipole and sensor in this context can be swapped with respect to each other. That is: at blue positions, dipoles (e.g. coils creating a magnetic field) can be located and at red positions can be a sensor.

Thus, if one aims to locate a sensor with respect to measurements done by some spatial arrangement of coils, one can do so efficiently using this approach. The analytical expression of the Jacobian means that local derivatives can be computed cheaply and, additionally, the algorithm converges fast.

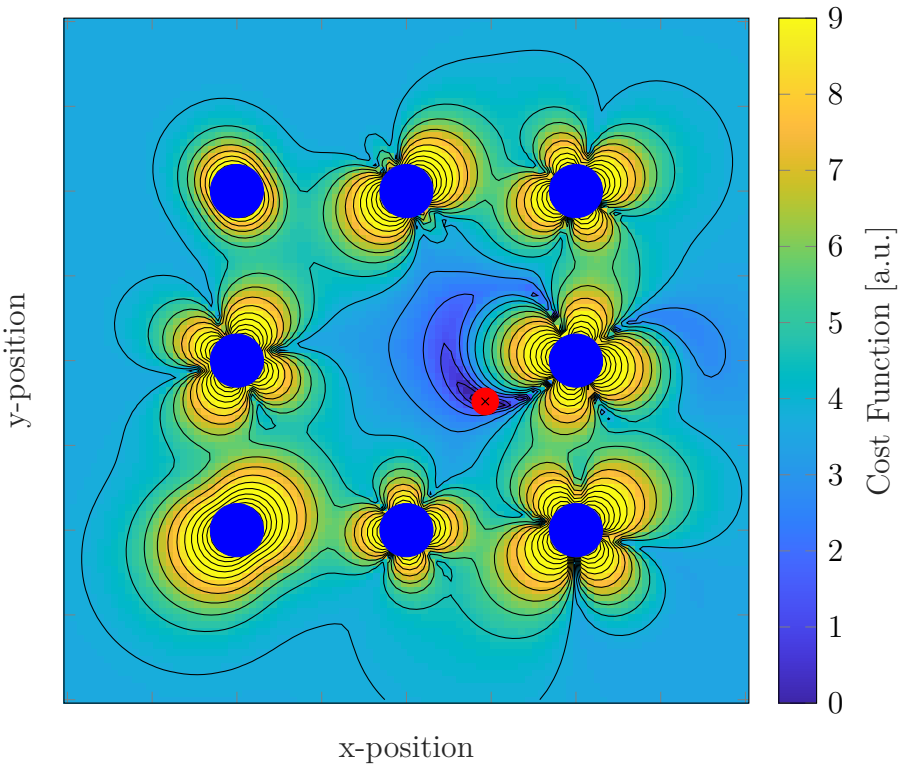


Figure B.4: Cost function over a region containing a magnetic source (RED) measured by a set of sensors (BLUE). The converse is also true, i.e. RED could be a sensor and BLUE the magnetic sources. The black cross denotes the estimated position.

List of Publications

Friedrich, R. M., Zabel, S., Galka, A., Lukat, N., Wagner, J. M., Kirchhof, C., Quandt, E., McCord, J., Selhuber-Unkel, C., Siniatchkin, M., Faupel, F. (2019). Magnetic particle mapping using magnetoelectric sensors as an imaging modality. Scientific Reports, 9(1). https://doi.org/10.1038/s41598-018-38451-0

Lukat, N., **Friedrich**, R. M., Spetzler, B., Kirchhof, C., Arndt, C., Thormählen, L., Faupel, F., Selhuber-Unkel, C. (2020). Mapping of magnetic nanoparticles and cells using thin film magnetoelectric sensors based on the delta-E effect. Sensors and Actuators, A: Physical, 309. https://doi.org/10.1016/j.sna.2020.112023

Spetzler, B., Golubeva, E. V., **Friedrich**, R. M., Zabel, S., Kirchhof, C., Meyners, D., McCord, J., Faupel, F. (2021). Magnetoelastic coupling and delta-e effect in magnetoelectric torsion mode resonators. Sensors, 21(6), 1–18. https://doi.org/10.3390/s21062022

Spetzler, B., Su, J., **Friedrich**, R. M., Niekiel, F., Fichtner, S., Lofink, F., & Faupel, F. (2021). Influence of the piezoelectric material on the signal and noise of magnetoelectric magnetic field sensors based on the delta-E effect. APL Materials, 9(3). https://doi.org/10.1063/5.0042448

Friedrich, R. M., & Faupel, F. (2022). Adaptive Model for Magnetic Particle Mapping Using Magnetoelectric Sensors. Sensors, 22(3). https://doi.org/10.3390/s22030894

Bibliography

[1] D. Yoo, J. H. Lee, T. H. Shin, and J. Cheon, "Theranostic magnetic nanoparticles," *Accounts of Chemical Research*, volume 44, number 10, pages 863–874, 2011, ISSN: 15204898. DOI: 10.1021/ar200085c (cited on page 1).

[2] T. M. Buzug, G. Bringout, M. Erbe, K. Gräfe, M. Graeser, M. Grüttner, A. Halkola, T. F. Sattel, W. Tenner, H. Wojtczyk, J. Haegele, F. M. Vogt, J. Barkhausen, and K. Lüdtke-Buzug, "Magnetic Particle Imaging: Introduction to imaging and hardware realization," *Zeitschrift fur Medizinische Physik*, volume 22, number 4, pages 323–334, 2012, ISSN: 09393889. DOI: 10.1016/j.zemedi.2012.07.004 (cited on pages 1, 10, 12, 91).

[3] V. Marx, "Tissue engineering: Organs from the lab," *Nature*, volume 522, number 7556, pages 373–377, 2015, ISSN: 14764687. DOI: 10.1038/522373a (cited on page 1).

[4] P. Hayes, "Converse magnetoelectric resonators for biomagnetic field sensing," en, PhD thesis, 2020. [Online]. Available: https://macau.uni-kiel.de/receive/macau_mods_00001263 (cited on page 5).

[5] S. D. Salzer, "Readout methods for magnetoelectric sensors," en, PhD thesis, 2018. [Online]. Available: https://macau.uni-kiel.de/receive/diss_mods_00023562 (cited on pages 5, 7–10, 124, 139).

[6] N. A. Spaldin and M. Fiebig, *The renaissance of magnetoelectric multiferroics*, 2005. DOI: 10.1126/science.1113357 (cited on pages 5, 6).

[7] M. Fiebig, *Revival of the magnetoelectric effect*, 2005. DOI: 10.1088/0022-3727/38/8/R01 (cited on page 6).

[8] N. A. Hill, "Why are there so few magnetic ferroelectrics?" *Journal of Physical Chemistry B*, volume 104, number 29, pages 6694–6709, 2000, ISSN: 15206106. DOI: 10.1021/jp000114x (cited on page 6).

[9] G. Lawes and G. Srinivasan, *Introduction to magnetoelectric coupling and multiferroic films*, 2011. DOI: 10.1088/0022-3727/44/24/243001 (cited on page 6).

[10] S. Zabel, C. Kirchhof, E. Yarar, D. Meyners, E. Quandt, and F. Faupel, "Phase modulated magnetoelectric delta-E effect sensor for sub-nano tesla magnetic fields," *Applied Physics Letters*, volume 107, number 15, 2015, ISSN: 00036951. DOI: 10.1063/1.4932575 (cited on pages 6, 96).

[11] C. W. Nan, "Magnetoelectric effect in composites of piezoelectric and piezomagnetic phases," *Physical Review B*, volume 50, number 9, pages 6082–6088, 1994, ISSN: 01631829. DOI: 10.1103/PhysRevB.50.6082 (cited on page 6).

[12] B. D. Cullity and C. D. Graham, *Introduction to Magnetic Materials*. 2008. DOI: 10.1002/9780470386323 (cited on pages 7, 10).

[13] E. Lage, C. Kirchhof, V. Hrkac, L. Kienle, R. Jahns, R. Knöchel, E. Quandt, and D. Meyners, "Biasing of magnetoelectric composites," *Nature Materials*, volume 11, number 6, pages 523–529, 2012, ISSN: 14764660. DOI: 10.1038/nmat3306 (cited on pages 7, 96).

[14] E. Lage, "Magnetoelektrische dünnschichtkomposite mit integriertem exchange bias," de, PhD thesis, 2014. [Online]. Available: https://macau.uni-kiel.de/receive/diss_mods_00014315 (cited on page 7).

[15] C. Kirchhof, "Resonante magnetoelektrische sensoren zurdetektion niederfrequenter magnetfelder," de, PhD thesis, 2017. [Online]. Available: https://macau.uni-kiel.de/receive/diss_mods_00022603 (cited on pages 7, 8).

[16] B. Spetzler, C. Bald, P. Durdaut, J. Reermann, C. Kirchhof, A. Teplyuk, D. Meyners, E. Quandt, M. Höft, G. Schmidt, and F. Faupel, "Exchange biased delta-E effect enables the detection of low frequency pT magnetic fields with simultaneous localization," *Scientific Reports*, volume 11, number 1, 2021, ISSN: 20452322. DOI: 10.1038/s41598-021-84415-2 (cited on pages 8, 130).

[17] R. M. Friedrich, S. Zabel, A. Galka, N. Lukat, J. M. Wagner, C. Kirchhof, E. Quandt, J. McCord, C. Selhuber-Unkel, M. Siniatchkin, and F. Faupel, "Magnetic particle mapping using magnetoelectric sensors as an imaging modality," *Scientific Reports*, 2019, ISSN: 20452322. DOI: 10.1038/s41598-018-38451-0 (cited on pages 8, 21, 24, 95).

[18] S. Salzer, M. Höft, R. Knöchel, P. Hayes, E. Yarar, A. Piorra, and E. Quandt, "Comparison of frequency conversion techniques for magnetoelectric sensors," in *Procedia Engineering*, volume 120, 2015, pages 940–943. DOI: 10.1016/j.proeng.2015.08.809 (cited on page 9).

[19] P. Hayes, S. Salzer, J. Reermann, E. Yarar, V. Röbisch, A. Piorra, D. Meyners, M. Höft, R. Knöchel, G. Schmidt, and E. Quandt, "Electrically modulated magnetoelectric sensors," *Applied Physics Letters*, volume 108, number 18, 2016, ISSN: 00036951. DOI: 10.1063/1.4948470 (cited on page 9).

[20] B. Gojdka, R. Jahns, K. Meurisch, H. Greve, R. Adelung, E. Quandt, R. Knöchel, and F. Faupel, "Fully integrable magnetic field sensor based on delta-E effect," *Applied Physics Letters*, volume 99, number 22, 2011, ISSN: 00036951. DOI: 10.1063/1.3664135 (cited on page 9).

[21] R. Jahns, S. Zabel, S. Marauska, B. Gojdka, B. Wagner, R. Knöchel, R. Adelung, and F. Faupel, "Microelectromechanical magnetic field sensor based on Δ e effect," *Applied Physics Letters*, volume 105, number 5, 2014, ISSN: 00036951. DOI: 10.1063/1.4891540 (cited on page 9).

[22] R. Jahns, H. Greve, E. Woltermann, E. Quandt, and R. Knöchel, "Sensitivity enhancement of magnetoelectric sensors through frequency-conversion," *Sensors and Actuators, A: Physical*, volume 183, pages 16–21, 2012, ISSN: 09244247. DOI: 10.1016/j.sna.2012.05.049 (cited on page 9).

[23] S. M. Gillette, A. L. Geiler, D. Gray, D. Viehland, C. Vittoria, and V. G. Harris, "Improved sensitivity and noise in magneto-electric magnetic field sensors by use of modulated AC magnetostriction," *IEEE Magnetics Letters*, volume 2, 2011, ISSN: 1949307X. DOI: 10.1109/LMAG.2011.2151178 (cited on page 9).

[24] J. Petrie, D. Gray, D. Viehland, G. Sreenivasulu, G. Srinivasan, S. Mandal, and A. S. Edelstein, "Shifting the operating frequency of magnetoelectric sensors," in *Journal of Applied Physics*, volume 111, 2012. DOI: 10.1063/1.3677840 (cited on page 9).

[25] E. Yarar, S. Salzer, V. Hrkac, A. Piorra, M. Höft, R. Knöchel, L. Kienle, and E. Quandt, "Inverse bilayer magnetoelectric thin film sensor," *Applied Physics Letters*, volume 109, number 2, 2016, ISSN: 00036951. DOI: 10.1063/1.4958728 (cited on page 9).

[26] Y. K. Fetisov, D. A. Burdin, D. V. Chashin, and N. A. Ekonomov, "High-sensitivity wideband magnetic field sensor using nonlinear resonance magnetoelectric effect," *IEEE Sensors Journal*, volume 14, number 7, pages 2252–2256, 2014, ISSN: 1530437X. DOI: 10.1109/JSEN.2014.2309718 (cited on page 10).

[27] C. Kirchhof, M. Krantz, I. Teliban, R. Jahns, S. Marauska, B. Wagner, R. Knöchel, M. Gerken, D. Meyners, and E. Quandt, "Giant magnetoelectric effect in vacuum," *Applied Physics Letters*, volume 102, number 23, 2013, ISSN: 00036951. DOI: 10.1063/1.4810750 (cited on page 10).

[28] D. A. Burdin, D. V. Chashin, N. A. Ekonomov, Y. K. Fetisov, and A. A. Stashkevich, "High-sensitivity dc field magnetometer using nonlinear resonance magnetoelectric effect," *Journal of Magnetism and Magnetic Materials*, volume 405, pages 244–248, 2016, ISSN: 03048853. DOI: 10.1016/j.jmmm.2015.12.079 (cited on page 10).

[29] L. Gutiérrez, R. Costo, C. Grüttner, F. Westphal, N. Gehrke, D. Heinke, A. Fornara, Q. A. Pankhurst, C. Johansson, S. Veintemillas-Verdaguer, and M. P. Morales, "Synthesis methods to prepare single- and multi-core iron oxide nanoparticles for biomedical applications," volume 44, number 7, pages 2943–2952, 2015, ISSN: 14779234. DOI: 10.1039/c4dt03013c (cited on page 10).

[30] M. Erbe, *Field free line magnetic particle imaging*. 2014, pages 1–154, ISBN: 9783658053376. DOI: 10.1007/978-3-658-05337-6 (cited on pages 11, 18).

[31] W. T. Coffey, P. J. Cregg, and Y. U. P. Kalmykov, "On the Theory of Debye and Néel Relaxation of Single Domain Ferromagnetic Particles," in, 1993, pages 263–464. DOI: 10.1002/9780470141410.ch5 (cited on page 12).

[32] M. I. Shliomis and V. I. Stepanov, "Theory of the Dynamic Susceptibility of Magnetic Fluids," in, 1994, pages 1–30. DOI: 10.1002/9780470141465.ch1 (cited on page 12).

[33] H. Albers, T. Kluth, and T. Knopp, *A simulation framework for particle magnetization dynamics of large ensembles of single domain particles: Numerical treatment of brown/néel dynamics and parameter identification problems in magnetic particle imaging*, 2020. arXiv: 2010.07772 [eess.IV] (cited on pages 13, 15, 29).

[34] J. Rahmer, A. Halkola, B. Gleich, I. Schmale, and J. Borgert, "First experimental evidence of the feasibility of multi-color magnetic particle imaging," *Physics in Medicine and Biology*, volume 60, number 5, pages 1775–1791, 2015, ISSN: 13616560. DOI: 10.1088/0031-9155/60/5/1775 (cited on pages 13, 42, 44, 109).

[35] A. Coene, J. Leliaert, M. Liebl, N. Löwa, U. Steinhoff, G. Crevecoeur, L. Dupré, and F. Wiekhorst, "Multi-color magnetic nanoparticle imaging using magnetorelaxometry," *Physics in Medicine and Biology*, volume 62, number 8, pages 3139–3157, 2017, ISSN: 13616560. DOI: 10.1088/1361-6560/aa5e90 (cited on pages 13, 18, 109).

[36] J. Weizenecker, B. Gleich, J. Rahmer, and J. Borgert, "Particle Dynamics of Mono-Domain Particles in Magnetic Particle Imaging," 2010, pages 3–15. DOI: 10.1142/9789814324687_0001 (cited on page 13).

[37] *Applications of magnetic nanoparticles in biomedicine*, 2003. DOI: 10.1088/0022-3727/36/13/201 (cited on pages 13, 21).

[38] Q. A. Pankhurst, N. K. Thanh, S. K. Jones, and J. Dobson, "Progress in applications of magnetic nanoparticles in biomedicine," *Journal of Physics D: Applied Physics*, volume 42, number 22, 2009, ISSN: 00223727. DOI: 10.1088/0022-3727/42/22/224001 (cited on page 13).

[39] V. F. Cardoso, A. Francesko, C. Ribeiro, M. Bañobre-López, P. Martins, and S. Lanceros-Mendez, *Advances in Magnetic Nanoparticles for Biomedical Applications*, 2018. DOI: 10.1002/adhm.201700845 (cited on page 13).

[40] K. Wu, D. Su, J. Liu, R. Saha, and J. P. Wang, "Magnetic nanoparticles in nanomedicine: A review of recent advances," *Nanotechnology*, volume 30, number 50, 2019, ISSN: 13616528. DOI: 10.1088/1361-6528/ab4241 (cited on page 13).

[41] H. Oliveira, E. Pérez-Andrés, J. Thevenot, O. Sandre, E. Berra, and S. Lecommandoux, "Magnetic field triggered drug release from polymersomes for cancer therapeutics," *Journal of Controlled Release*, volume 169, number 3, pages 165–170, 2013, ISSN: 18734995. DOI: 10.1016/j.jconrel.2013.01.013 (cited on page 13).

[42] R. Tietze, J. Zaloga, H. Unterweger, S. Lyer, R. P. Friedrich, C. Janko, M. Pöttler, S. Dürr, and C. Alexiou, *Magnetic nanoparticle-based drug delivery for cancer therapy*, 2015. DOI: 10.1016/j.bbrc.2015.08.022 (cited on page 13).

[43] S. M. Cromer Berman, P. Walczak, and J. W. Bulte, "Tracking stem cells using magnetic nanoparticles," *Wiley Interdisciplinary Reviews: Nanomedicine and Nanobiotechnology*, volume 3, number 4, pages 343–355, 2011, ISSN: 19395116. DOI: 10.1002/wnan.140 (cited on page 13).

[44] B. Zheng, T. Vazin, P. W. Goodwill, A. Conway, A. Verma, E. Ulku Saritas, D. Schaffer, and S. M. Conolly, "Magnetic particle imaging tracks the long-term fate of in vivo neural cell implants with high image contrast," *Scientific Reports*, volume 5, 2015, ISSN: 20452322. DOI: 10.1038/srep14055 (cited on pages 13, 17).

[45] T. Sasaki, N. Iwasaki, K. Kohno, M. Kishimoto, T. Majima, S. I. Nishimura, and A. Minami, "Magnetic nanoparticles for improving cell invasion in tissue engineering," *Journal of Biomedical Materials Research - Part A*, volume 86, number 4, pages 969–978, 2008, ISSN: 15493296. DOI: 10.1002/jbm.a.31724 (cited on page 13).

[46] A. Ito and M. Kamihira, "Tissue engineering using magnetite nanoparticles," in *Progress in Molecular Biology and Translational Science*, volume 104, 2011, pages 355–395. DOI: 10.1016/B978-0-12-416020-0.00009-7 (cited on page 13).

[47] A. J. Giustini, A. A. Petryk, S. M. Cassim, J. A. Tate, I. Baker, and P. J. Hoopes, "Magnetic Nanoparticle Hyperthermia in Cancer Treatment," *Nano LIFE*, volume 01, number 01n02, pages 17–32, 2010, ISSN: 1793-9844. DOI: 10.1142/s1793984410000067 (cited on page 13).

[48] M. Bañobre-López, A. Teijeiro, and J. Rivas, *Magnetic nanoparticle-based hyperthermia for cancer treatment*, 2013. DOI: 10.1016/j.rpor.2013.09.011 (cited on page 13).

[49] A. E. Deatsch and B. A. Evans, *Heating efficiency in magnetic nanoparticle hyperthermia*, 2014. DOI: 10.1016/j.jmmm.2013.11.006 (cited on page 13).

[50] T. L. Kalber, K. L. Ordidge, P. Southern, M. R. Loebinger, P. G. Kyrtatos, Q. A. Pankhurst, M. F. Lythgoe, and S. M. Janes, "Hyperthermia treatment of tumors by mesenchymal stem cell-delivered superparamagnetic iron oxide nanoparticles," *International Journal of Nanomedicine*, volume 11, pages 1973–1983, 2016, ISSN: 11782013. DOI: 10.2147/IJN.S94255 (cited on pages 13, 106).

[51] A. Rajan and N. K. Sahu, *Review on magnetic nanoparticle-mediated hyperthermia for cancer therapy*, 2020. DOI: 10.1007/s11051-020-05045-9 (cited on page 13).

[52] M. Douek, J. Klaase, I. Monypenny, A. Kothari, K. Zechmeister, D. Brown, L. Wyld, P. Drew, H. Garmo, O. Agbaje, Q. Pankhurst, B. Anninga, M. Grootendorst, B. Ten Haken, M. A. Hall-Craggs, A. Purushotham, and S. Pinder, "Sentinel node biopsy using a magnetic tracer versus standard technique: The SentiMAG multicentre trial," *Annals of Surgical Oncology*, volume 21, number 4, pages 1237–1245, 2014, ISSN: 15344681. DOI: 10.1245/s10434-013-3379-6 (cited on page 13).

[53] M. Thill, A. Kurylcio, R. Welter, V. van Haasteren, B. Grosse, G. Berclaz, W. Polkowski, and N. Hauser, "The Central-European SentiMag study: Sentinel lymph node biopsy with superparamagnetic iron oxide (SPIO) vs. radioisotope," *Breast*, volume 23, number 2, pages 175–179, 2014, ISSN: 15323080. DOI: 10.1016/j.breast.2014.01.004 (cited on page 13).

[54] A. Karakatsanis, P. M. Christiansen, L. Fischer, C. Hedin, L. Pistioli, M. Sund, N. R. Rasmussen, H. Jørnsgård, D. Tegnelius, S. Eriksson, K. Daskalakis, F. Wärnberg, C. J. Markopoulos, and L. Bergkvist, "The Nordic SentiMag trial: a comparison of super paramagnetic iron oxide (SPIO) nanoparticles versus Tc99 and patent blue in the detection of sentinel node (SN) in patients with breast cancer and a meta-analysis of earlier studies," *Breast Cancer Research and Treatment*, volume 157, number 2, pages 281–294, 2016, ISSN: 15737217. DOI: 10.1007/s10549-016-3809-9 (cited on page 13).

[55] J. Haegele, J. Rahmer, B. Gleich, J. Borgert, H. Wojtczyk, N. Panagiotopoulos, T. M. Buzug, J. Barkhausen, and F. M. Vogt, "Magnetic particle imaging: Visualization of instruments for cardiovascular intervention," *Radiology*, volume 265, number 3, pages 933–938, 2012, ISSN: 00338419. DOI: 10.1148/radiol.12120424 (cited on pages 13, 17).

[56] A. C. Bakenecker, M. Ahlborg, C. Debbeler, C. Kaethner, T. M. Buzug, and K. Lüdtke-Buzug, *Magnetic particle imaging in vascular medicine*, 2020. DOI: 10.1515/iss-2018-2026 (cited on page 13).

[57] T. F. Sattel, T. Knopp, S. Biederer, B. Gleich, J. Weizenecker, J. Borgert, and T. M. Buzug, "Single-sided device for magnetic particle imaging," *Journal of*

Physics D: Applied Physics, volume 42, number 2, 2009, ISSN: 00223727. DOI: 10.1088/0022-3727/42/2/022001 (cited on pages 13, 18).

[58] T. F. Sattel, M. Erbe, S. Biederer, T. Knopp, D. Finas, K. Diedrich, K. Lüdtke-Buzug, J. Borgert, and T. M. Buzug, "Single-sided magnetic particle imaging device for the sentinel lymph node biopsy scenario," in *Medical Imaging 2012: Biomedical Applications in Molecular, Structural, and Functional Imaging*, volume 8317, 2012, 83170S, ISBN: 9780819489661. DOI: 10.1117/12.912733 (cited on pages 13, 17, 18).

[59] A. Tonyushkin, "Single-Sided Field-Free Line Generator Magnet for Multi Dimensional Magnetic Particle Imaging," *IEEE Transactions on Magnetics*, volume 53, number 9, 2017, ISSN: 00189464. DOI: 10.1109/TMAG.2017.2718485. arXiv: 1701.03838 (cited on pages 13, 18).

[60] F. Ludwig, C. Balceris, C. Jonasson, and C. Johansson, "Analysis of AC Susceptibility Spectra for the Characterization of Magnetic Nanoparticles," *IEEE Transactions on Magnetics*, volume 53, number 11, 2017, ISSN: 00189464. DOI: 10.1109/TMAG.2017.2693420 (cited on page 14).

[61] R. E. Rosensweig, "Heating magnetic fluid with alternating magnetic field," *Journal of Magnetism and Magnetic Materials*, volume 252, number 1-3 SPEC. ISS. Pages 370–374, 2002, ISSN: 03048853. DOI: 10.1016/S0304-8853(02)00706-0 (cited on page 14).

[62] F. Ludwig, D. Eberbeck, N. Löwa, U. Steinhoff, T. Wawrzik, M. Schilling, and L. Trahms, *Characterization of magnetic nanoparticle systems with respect to their magnetic particle imaging performance*, 2013. DOI: 10.1515/bmt-2013-0013 (cited on page 14).

[63] F. Ludwig and H. Remmer, "Rotational dynamics of magnetic nanoparticles in different matrix systems," *Physical Sciences Reviews*, 2020, ISSN: 2365659X. DOI: 10.1515/psr-2019-0115 (cited on page 14).

[64] D. Cabrera, A. Coene, J. Leliaert, E. J. Artés-Ibáñez, L. Dupré, N. D. Telling, and F. J. Teran, "Dynamical Magnetic Response of Iron Oxide Nanoparticles Inside Live Cells," *ACS Nano*, volume 12, number 3, pages 2741–2752, 2018, ISSN: 1936086X. DOI: 10.1021/acsnano.7b08995 (cited on pages 14, 75).

[65] S. Biederer, *Magnet-Partikel-Spektrometer*. 2012. DOI: 10.1007/978-3-8348-2407-3 (cited on page 15).

[66] J. Zhong, M. Schilling, and F. Ludwig, "Excitation frequency dependence of temperature resolution in magnetic nanoparticle temperature imaging with a scanning magnetic particle spectrometer," *Journal of Magnetism and Magnetic Materials*, volume 471, pages 340–345, 2019, ISSN: 03048853. DOI: 10.1016/j.jmmm.2018.09.112 (cited on pages 15, 18).

[67] S. Draack, N. Lucht, H. Remmer, M. Martens, B. Fischer, M. Schilling, F. Ludwig, and T. Viereck, "Multiparametric Magnetic Particle Spectroscopy of CoFe2O4 Nanoparticles in Viscous Media," *Journal of Physical Chemistry C*, volume 123, number 11, pages 6787–6801, 2019, ISSN: 19327455. DOI: 10.1021/acs.jpcc.8b10763 (cited on pages 15, 29, 99).

[68] T. Knopp and T. M. Buzug, *Magnetic particle imaging: An introduction to imaging principles and scanner instrumentation*. 2012, volume 9783642041990, pages 1–204, ISBN: 9783642041990. DOI: 10.1007/978-3-642-04199-0 (cited on pages 17, 18).

[69] M. Graeser, T. Knopp, P. Szwargulski, T. Friedrich, A. Von Gladiss, M. Kaul, K. M. Krishnan, H. Ittrich, G. Adam, and T. M. Buzug, "Towards Picogram Detection of Superparamagnetic Iron-Oxide Particles Using a Gradiometric Receive Coil," *Scientific Reports*, volume 7, number 1, 2017, ISSN: 20452322. DOI: 10.1038/s41598-017-06992-5. arXiv: 1704.01789 (cited on page 17).

[70] J. Weizenecker, B. Gleich, J. Rahmer, H. Dahnke, and J. Borgert, "Three dimensional real-time in vivo magnetic particle imaging," *Physics in Medicine and Biology*, volume 54, number 5, 2009, ISSN: 00319155. DOI: 10.1088/0031-9155/54/5/L01 (cited on page 17).

[71] J. Haegele, S. Biederer, H. Wojtczyk, M. Gräser, T. Knopp, T. M. Buzug, J. Barkhausen, and F. M. Vogt, "Toward cardiovascular interventions guided by magnetic particle imaging: First instrument characterization," *Magnetic Resonance in Medicine*, volume 69, number 6, pages 1761–1767, 2013, ISSN: 15222594. DOI: 10.1002/mrm.24421 (cited on page 17).

[72] B. Ruhland, K. Baumann, T. Knopp, T. Sattel, S. Biederer, K. Lüdtke-Buzug, T. Buzug, K. Diedrich, and D. Finas, "Magnetic Particle Imaging durch Superparamagnetische Nanopartikel zur Sentinellymphknotendetektion beim Mammakarzinom," *Geburtshilfe und Frauenheilkunde*, volume 69, number 09, 2009, ISSN: 0016-5751. DOI: 10.1055/s-0029-1239012 (cited on page 17).

[73] D. Finas, B. Ruhland, K. Baumann, T. Knopp, T. Sattel, S. Biederer, K. Lüdtke-Buzug, T. Buzug, and K. Diedrich, "Sentinal lymphnode detection in breast cancer by magnetic particle imaging using superparamagnetic nanoparticles," in *International Workshop on Magnetic Particle Imaging*, volume 1, 2010, page 35 (cited on page 17).

[74] K. Gräfe, T. F. Sattel, K. Lüdtke-Buzug, D. Finas, J. Borgert, and T. M. Buzug, "Magnetic-particle-imaging for sentinel lymph node biopsy in breast cancer," in *Springer Proceedings in Physics*, volume 140, 2012, pages 237–241, ISBN: 97836422 41321. DOI: 10.1007/978-3-642-24133-8_38 (cited on page 17).

[75] M. Muta, S. Hamanaga, N. Tanaka, T. Sasayama, T. Yoshida, and K. Enpuku, "Three-dimensional imaging of magnetic nanoparticles using multiple pickup coils and field-free line," *Japanese Journal of Applied Physics*, volume 57, number 2, 2018, ISSN: 13474065. DOI: 10.7567/JJAP.57.023002 (cited on page 18).

[76] M. Weber, J. Beuke, A. Gladiss, K. Grafe, P. Vogel, V. Behr, and T. Buzug, "Novel field geometry using two halbach cylinders for ffl-mpi," 2019 (cited on page 18).

[77] A. C. Bakenecker, J. Schumacher, P. Blümler, K. Gräfe, M. Ahlborg, and T. M. Buzug, "A concept for an mpi scanner with halbach arrays," *International Journal on Magnetic Particle Imaging*, volume 6, number 2, pages 1–3, 2020, ISSN: 23659033. DOI: 10.18416/IJMPI.2020.2009008 (cited on page 18).

[78] J. Zhong, M. Schilling, and F. Ludwig, "Spatial and temperature resolutions of magnetic nanoparticle temperature imaging with a scanning magnetic particle spectrometer," *Nanomaterials*, volume 8, number 11, 2018, ISSN: 20794991. DOI: 10.3390/nano8110866 (cited on pages 18, 116, 123).

[79] J. Zhong, M. Schilling, and F. Ludwig, "Magnetic nanoparticle temperature imaging with a scanning magnetic particle spectrometer," *Measurement Science and Technology*, volume 29, number 11, 2018, ISSN: 13616501. DOI: 10.1088/1361-6501/aae3bd (cited on pages 18, 116, 123).

[80] J. Zhong, M. Schilling, and F. Ludwig, "Magnetic nanoparticle-based biomolecule imaging with a scanning magnetic particle spectrometer," *Nanotechnology*, volume 31, number 22, 2020, ISSN: 13616528. DOI: 10.1088/1361-6528/ab776a (cited on page 18).

[81] M. Liebl, U. Steinhoff, F. Wiekhorst, J. Haueisen, and L. Trahms, "Quantitative imaging of magnetic nanoparticles by magnetorelaxometry with multiple excitation coils," *Physics in Medicine and Biology*, volume 59, number 21, pages 6607–6620, 2014, ISSN: 13616560. DOI: 10.1088/0031-9155/59/21/6607 (cited on pages 18, 91).

[82] D. P. Rühmer, "Zweidimensionale scanning-magnetrelaxometrie mit fluxgate sensoren," PhD thesis, Berlin, 2012. DOI: 10.24355/dbbs.084-201302151009-0. [Online]. Available: http://www.digibib.tu-bs.de/?docid=00049175 (cited on pages 18, 19, 123).

[83] A. Jaufenthaler, P. Schier, T. Middelmann, M. Liebl, F. Wiekhorst, and D. Baumgarten, "Quantitative 2D magnetorelaxometry imaging of magnetic nanoparticles using optically pumped magnetometers," *Sensors (Switzerland)*, volume 20, number 3, 2020, ISSN: 14248220. DOI: 10.3390/s20030753 (cited on page 18).

[84] A. Coene, J. Leliaert, L. Dupré, and G. Crevecoeur, "Quantitative model selection for enhanced magnetic nanoparticle imaging in magnetorelaxometry," *Medical Physics*, volume 42, number 12, pages 6853–6862, 2015, ISSN: 00942405. DOI: 10.1118/1.4935147 (cited on pages 19, 129).

[85] P. Schier, M. Liebl, U. Steinhoff, M. Handler, F. Wiekhorst, and D. Baumgarten, "Optimizing Excitation Coil Currents for Advanced Magnetorelaxometry Imaging," *Journal of Mathematical Imaging and Vision*, volume 62, number 2, pages 238–252, 2020, ISSN: 15737683. DOI: 10.1007/s10851-019-00934-8 (cited on pages 19, 40, 91, 129).

[86] A. Coene, G. Crevecoeur, J. Leliaert, and L. Dupré, "Toward 2D and 3D imaging of magnetic nanoparticles using EPR measurements," *Medical Physics*, volume 42, number 9, 2015, ISSN: 00942405. DOI: 10.1118/1.4927374 (cited on page 19).

[87] A. Coene, G. Crevecoeur, and L. Dupré, "Magnetic nanoparticle imaging using multiple electron paramagnetic resonance activation sequences," *Journal of Applied Physics*, volume 117, number 17, 2015, ISSN: 10897550. DOI: 10.1063/1.4906948 (cited on pages 19, 129).

[88] A. Coene, J. Leliaert, G. Crevecoeur, and L. Dupré, "Sensor fusion of electron paramagnetic resonance and magnetorelaxometry data for quantitative magnetic nanoparticle imaging," *Journal of Physics D: Applied Physics*, volume 50, number 8, 2017, ISSN: 13616463. DOI: 10.1088/1361-6463/aa5771 (cited on page 19).

[89] D. Rühmer, E. Heim, T. Wawrzik, F. Ludwig, and M. Schilling, "Magnetic relaxation imaging of magnetic nanoparticle distributions," in *IFMBE Proceedings*, volume 25, 2009, pages 418–420, ISBN: 9783642038846. DOI: 10.1007/978-3-642-03885-3_116 (cited on pages 19, 123).

[90] N. G. Sepúlveda, I. M. Thomas, and J. P. Wikswo, "Magnetic Susceptibility Tomography for Three-Dimensional Imaging of Diamagnetic and Paramagnetic Objectcts," *IEEE Transactions on Magnetics*, volume 30, number 6, pages 5062–5069, 1994, ISSN: 19410069. DOI: 10.1109/20.334296 (cited on page 19).

[91] B. W. Ficko, P. M. Nadar, P. J. Hoopes, and S. G. Diamond, "Development of a magnetic nanoparticle susceptibility magnitude imaging array," *Physics in Medicine and Biology*, volume 59, number 4, pages 1047–1071, 2014, ISSN: 00319155. DOI: 10.1088/0031-9155/59/4/1047 (cited on pages 19, 123, 129).

[92] B. W. Ficko, P. M. Nadar, and S. G. Diamond, "Spectroscopic AC susceptibility imaging (sASI) of magnetic nanoparticles," *Journal of Magnetism and Magnetic Materials*, volume 375, pages 164–176, 2015, ISSN: 03048853. DOI: 10.1016/j.jmmm.2014.10.011 (cited on pages 19, 129).

[93] B. W. Ficko, P. Giacometti, and S. G. Diamond, "Extended arrays for nonlinear susceptibility magnitude imaging," *Biomedizinische Technik*, volume 60, number 5, pages 457–463, 2015, ISSN: 00135585. DOI: 10.1515/bmt-2015-0048 (cited on pages 19, 129).

[94] R. Van Durme, A. Coene, G. Crevecoeur, and L. Dupre, "Model-based optimal design of a magnetic nanoparticle tomographic imaging setup," in *Proceedings - International Symposium on Biomedical Imaging*, volume 2018-April, 2018, pages 369–372, ISBN: 9781538636367. DOI: 10.1109/ISBI.2018.8363595 (cited on pages 19, 129).

[95] G. Hu and B. He, "Magnetoacoustic imaging of magnetic iron oxide nanoparticles embedded in biological tissues with microsecond magnetic stimulation," *Applied Physics Letters*, volume 100, number 1, pages 3–5, 2012. DOI: 10.1063/1.3675457 (cited on pages 20, 129).

[96] J. Oh, M. D. Feldman, J. Kim, C. Condit, S. Emelianov, and T. E. Milner, "Detection of magnetic nanoparticles in tissue using magneto-motive ultrasound," *Nanotechnology*, volume 17, number 16, pages 4183–4190, 2006, ISSN: 09574484. DOI: 10.1088/0957-4484/17/16/031 (cited on page 20).

[97] M. Mehrmohammadi, M. Qu, L. L. Ma, D. K. Romanovicz, K. P. Johnston, K. V. Sokolov, and S. Y. Emelianov, "Pulsed magneto-motive ultrasound imaging to detect intracellular accumulation of magnetic nanoparticles," *Nanotechnology*, volume 22, number 41, 2011, ISSN: 09574484. DOI: 10.1088/0957-4484/22/41/415105 (cited on page 20).

[98] L. Mariappan, Q. Shao, C. Jiang, K. Yu, S. Ashkenazi, J. C. Bischof, and B. He, "Magneto acoustic tomography with short pulsed magnetic field for in-vivo imaging of magnetic iron oxide nanoparticles," *Nanomedicine: Nanotechnology, Biology, and Medicine*, volume 12, number 3, pages 689–699, 2016, ISSN: 15499642. DOI: 10.1016/j.nano.2015.10.014 (cited on page 20).

[99] A. L. Oldenburg, F. J.-J. Toublan, K. S. Suslick, A. Wei, and S. A. Boppart, "Magnetomotive contrast for in vivo optical coherence tomography," *Optics Express*, volume 13, number 17, page 6597, 2005, ISSN: 1094-4087. DOI: 10.1364/opex.13.006597 (cited on page 20).

[100] R. John, R. Rezaeipoor, S. G. Adie, E. J. Chaney, A. L. Oldenburg, M. Marjanovic, J. P. Haldar, B. P. Sutton, and S. A. Boppart, "In vivo magnetomotive optical molecular imaging using targeted magnetic nanoprobes," *Proceedings of the National Academy of Sciences of the United States of America*, volume 107, number 18, pages 8085–8090, 2010, ISSN: 10916490. DOI: 10.1073/pnas.0913679107 (cited on page 20).

[101] A. L. Oldenburg, V. Crecea, S. A. Rinne, and S. A. Boppart, "Phase-resolved magnetomotive OCT for imaging nanomolar concentrations of magnetic nanoparticles in tissues," *Optics Express*, volume 16, number 15, page 11 525, 2008, ISSN: 1094-4087. DOI: 10.1364/oe.16.011525 (cited on page 20).

[102] P. Cimalla, J. Walther, C. Mueller, S. Almedawar, B. Rellinghaus, D. Wittig, M. Ader, M. O. Karl, R. H. Funk, M. Brand, and E. Koch, "Improved imaging of magnetically labeled cells using rotational magnetomotive optical coherence tomography," *Applied Sciences (Switzerland)*, volume 7, number 5, 2017, ISSN: 20763417. DOI: 10.3390/app7050444 (cited on page 20).

[103] A. L. Oldenburg, J. R. Gunther, and S. A. Boppart, "Imaging magnetically labeled cells with magnetomotive optical coherence tomography," *Optics Letters*, volume 30, number 7, page 747, 2005, ISSN: 0146-9592. DOI: 10.1364/ol.30.000747 (cited on page 20).

[104] A. L. Oldenburg, G. Wu, D. Spivak, F. Tsui, A. S. Wolberg, and T. H. Fischer, "Imaging and elastometry of blood clots using magnetomotive optical coherence tomography and labeled platelets," *IEEE Journal on Selected Topics in Quantum Electronics*, volume 18, number 3, pages 1100–1109, 2012, ISSN: 1077260X. DOI: 10.1109/JSTQE.2011.2162580 (cited on page 20).

[105] P. Cimalla, T. Werner, K. Winkler, C. Mueller, S. Wicht, M. Gaertner, M. Mehner, J. Walther, B. Rellinghaus, D. Wittig, M. O. Karl, M. Ader, R. H. W. Funk, and E. Koch, "Imaging of nanoparticle-labeled stem cells using magnetomotive optical coherence tomography, laser speckle reflectometry, and light microscopy," *Journal of Biomedical Optics*, volume 20, number 3, page 036 018, 2015, ISSN: 1083-3668. DOI: 10.1117/1.jbo.20.3.036018 (cited on page 20).

[106] C. Rümenapp, B. Gleich, and A. Haase, *Magnetic nanoparticles in magnetic resonance imaging and diagnostics*, 2012. DOI: 10.1007/s11095-012-0711-y (cited on page 21).

[107] D. T. Huong Giang, D. X. Dang, N. X. Toan, N. V. Tuan, A. T. Phung, and N. H. Duc, "Distance magnetic nanoparticle detection using a magnetoelectric sensor for clinical interventions," *Review of Scientific Instruments*, volume 88, number 1, 2017, ISSN: 10897623. DOI: 10.1063/1.4973729 (cited on page 21).

[108] H. Xi, X. Qian, M. C. Lu, L. Mei, S. Rupprecht, Q. X. Yang, and Q. M. Zhang, "A Room Temperature Ultrasensitive Magnetoelectric Susceptometer for Quantitative Tissue Iron Detection," *Scientific Reports*, volume 6, 2016, ISSN: 20452322. DOI: 10.1038/srep29740 (cited on pages 21, 129).

[109] N. Lukat, R. M. Friedrich, B. Spetzler, C. Kirchhof, C. Arndt, L. Thormählen, F. Faupel, and C. Selhuber-Unkel, "Mapping of magnetic nanoparticles and cells using thin film magnetoelectric sensors based on the delta-E effect," *Sensors and Actuators, A: Physical*, volume 309, 2020, ISSN: 09244247. DOI: 10.1016/j.sna.2020.112023 (cited on pages 21, 125, 128).

[110] G. M. Wing, *A Primer on Integral Equations of the First Kind*. 1991. DOI: 10.1137/1.9781611971675 (cited on page 30).

[111] J. Banaś and M. Pasławska-Południak, "Monotonie solutions of urysohn integral equation on unbounded interval," *Computers and Mathematics with Applications*, volume 47, number 12, pages 1947–1954, 2004, ISSN: 08981221. DOI: 10.1016/j.camwa.2002.08.014 (cited on page 33).

[112] M. A. Darwish, J. Banaś, and E. O. Alzahrani, "The existence and attractivity of solutions of an urysohn integral equation on an unbounded interval," *Abstract and Applied Analysis*, volume 2013, 2013, ISSN: 10853375. DOI: 10.1155/2013/147409 (cited on page 33).

[113] P. C. Hansen, *Discrete Inverse Problems: Insight and Algorithms*. 2010, ISBN: 978-0-89871-696-2 (cited on pages 33, 35, 36, 38, 39, 65, 70, 104, 131).

[114] E. A. Larsen, "Depth Resolution in 3D Imaging," Master's thesis, Technical University of Denmark, 2010, pages 11–20 (cited on page 33).

[115] R. J. Blakely, *Potential Theory in Gravity and Magnetic Applications*. 1995. DOI: 10.1017/cbo9780511549816 (cited on page 33).

[116] P. C. Hansen, "Deblurring Images: Matrices, Spectra and Filtering," *Journal of Electronic Imaging*, volume 17, number 1, page 019 901, 2007, ISSN: 1017-9909. DOI: 10.1117/1.2900557 (cited on page 35).

[117] G. Nakamura and R. Potthast, *Inverse modeling: An introduction to the theory and methods of inverse problems and data assimilation*. 2015, pages 1–509, ISBN: 9780750312189. DOI: 10.1088/978-0-7503-1218-9 (cited on page 35).

[118] H. Zou and T. Hastie, "Regularization and variable selection via the elastic net," *Journal of the Royal Statistical Society. Series B: Statistical Methodology*, volume 67, number 2, pages 301–320, 2005, ISSN: 13697412. DOI: 10.1111/j.1467-9868.2005.00503.x (cited on page 36).

[119] A. Kirsch, "An introduction to the mathematical theory of inverse problems," in *Applied Mathematical Sciences (Switzerland)*, volume 120, 2011, pages 1–307 (cited on page 39).

[120] X. Zhang, "An Inverse Problem Solution Scheme for Solving the Optimization Problem of Drug-Controlled Release from Multilaminated Devices," *Computational and Mathematical Methods in Medicine*, volume 2020, 2020, ISSN: 17486718. DOI: 10.1155/2020/8380691 (cited on page 39).

[121] E. Bolduc, G. C. Knee, E. M. Gauger, and J. Leach, "Projected gradient descent algorithms for quantum state tomography," *npj Quantum Information*, volume 3, number 1, 2017, ISSN: 2056-6387. DOI: 10.1038/s41534-017-0043-1. arXiv: 1612.09531. [Online]. Available: http://dx.doi.org/10.1038/s41534-017-0043-1 (cited on page 40).

[122] A. Beck, *First-Order Methods in Optimization*. 2017. DOI: 10.1137/1.9781611974997 (cited on page 41).

[123] T. M. Hansen, K. S. Cordua, B. H. Jacobsen, and K. Mosegaard, "Accounting for imperfect forward modeling in geophysical inverse problems - Exemplified for crosshole tomography," *Geophysics*, volume 79, number 3, H1–H21, 2014, ISSN: 19422156. DOI: 10.1190/GEO2013-0215.1 (cited on page 45).

[124] R. G. De Peralta Menendez, S. L. Gonzalez Andino, and B. Lütkenhöner, "Figures of merit to compare distributed linear inverse solutions," *Brain Topography*, volume 9, number 2, pages 117–124, 1996, ISSN: 08960267. DOI: 10.1007/BF01200711 (cited on page 62).

[125] M. An, "A simple method for determining the spatial resolution of a general inverse problem," *Geophysical Journal International*, volume 191, number 2, pages 849–864, 2012, ISSN: 0956540X. DOI: 10.1111/j.1365-246X.2012.05661.x (cited on page 62).

[126] S. S. Chen, D. L. Donoho, and M. A. Saunders, "Atomic decomposition by basis pursuit," *SIAM Review*, volume 43, number 1, pages 129–159, 2001, ISSN: 00361445. DOI: 10.1137/S003614450037906X (cited on pages 62, 86).

[127] M. Bertero and P. Boccacci, *Introduction to Inverse Problems in Imaging*. 1998. DOI: 10.1887/0750304359 (cited on page 62).

[128] W. B. (https://scicomp.stackexchange.com/users/393/wolfgang-bangerth), *A notion of resolution in inverse problems*, Computational Science Stack Exchange, URL:https://scicomp.stackexchange.com/q/36537 (version: 2020-12-18). eprint: https://scicomp.stackexchange.com/q/36537. [Online]. Available: https://scicomp.stackexchange.com/q/36537 (cited on page 66).

[129] N. Löwa, F. Wiekhorst, S. Metzkow, A. Ludwig, and L. Trahms, "Magnetic Particle Spectroscopy for the Quantification of Magnetic Nanoparticles in Living Cells," *Biomedical Engineering / Biomedizinische Technik*, 2013, ISSN: 0013-5585. DOI: 10.1515/bmt-2013-4138 (cited on pages 75, 106, 116).

[130] L. I. Rudin, S. Osher, and E. Fatemi, "Nonlinear total variation based noise removal algorithms," *Physica D: Nonlinear Phenomena*, volume 60, number 1-4, pages 259–268, 1992, ISSN: 01672789. DOI: 10.1016/0167-2789(92)90242-F (cited on page 86).

[131] J. Weizenecker, B. Gleich, and J. Borgert, "Magnetic particle imaging using a field free line," *Journal of Physics D: Applied Physics*, volume 41, number 10, 2008, ISSN: 00223727. DOI: 10.1088/0022-3727/41/10/105009 (cited on page 91).

[132] D. Baumgarten, R. Eichardt, G. Crevecoeur, E. Supriyanto, and J. Haueisen, "Magnetic nanoparticle imaging by random and maximum length sequences of inhomogeneous activation fields," in *Proceedings of the Annual International Conference of the IEEE Engineering in Medicine and Biology Society, EMBS*, 2013, pages 3258–3260, ISBN: 9781457702167. DOI: 10.1109/EMBC.2013.6610236 (cited on page 91).

[133] R. Jahns, H. Greve, E. Woltermann, E. Quandt, and R. H. Knöchel, "Noise performance of magnetometers with resonant thin-film magnetoelectric sensors," in *IEEE Transactions on Instrumentation and Measurement*, volume 60, 2011, pages 2995–3001. DOI: 10.1109/TIM.2011.2122410 (cited on page 95).

[134] R. Jahns, A. Piorra, E. Lage, C. Kirchhof, D. Meyners, J. L. Gugat, M. Krantz, M. Gerken, R. Knöchel, and E. Quandt, "Giant magnetoelectric effect in thin-film composites," *Journal of the American Ceramic Society*, volume 96, number 6, pages 1673–1681, 2013, ISSN: 00027820. DOI: 10.1111/jace.12400 (cited on page 95).

[135] E. Yarar, V. Hrkac, C. Zamponi, A. Piorra, L. Kienle, and E. Quandt, "Low temperature aluminum nitride thin films for sensory applications," *AIP Advances*, volume 6, number 7, 2016, ISSN: 21583226. DOI: 10.1063/1.4959895 (cited on page 96).

[136] R. Jahns, R. Knochel, H. Greve, E. Woltermann, E. Lage, and E. Quandt, "Magnetoelectric sensors for biomagnetic measurements," in *MeMeA 2011 - 2011 IEEE International Symposium on Medical Measurements and Applications, Proceedings*, 2011, pages 107–110, ISBN: 9781424493388. DOI: 10.1109/MeMeA.2011.5966676 (cited on page 96).

[137] W. C. Poller, N. Löwa, F. Wiekhorst, M. Taupitz, S. Wagner, K. Möller, G. Baumann, V. Stangl, L. Trahms, and A. Ludwig, "Magnetic particle spectroscopy reveals dynamic changes in the magnetic behavior of very small superparamagnetic iron oxide nanoparticles during cellular uptake and enables determination of cell-labeling efficacy," *Journal of Biomedical Nanotechnology*, volume 12, number 2, pages 337–346, 2016, ISSN: 15507041. DOI: 10.1166/jbn.2016.2204 (cited on page 106).

[138] A. Yanai, U. O. Häfeli, A. L. Metcalfe, P. Soema, L. Addo, C. Y. Gregory-Evans, K. Po, X. Shan, O. L. Moritz, and K. Gregory-Evans, "Focused Magnetic Stem Cell Targeting to the Retina Using Superparamagnetic Iron Oxide Nanoparticles," *Cell Transplantation*, volume 21, number 6, pages 1137–1148, 2012, ISSN: 09636897. DOI: 10.3727/096368911X627435 (cited on page 106).

[139] D. Robert, N. Pamme, H. Conjeaud, F. Gazeau, A. Iles, and C. Wilhelm, "Cell sorting by endocytotic capacity in a microfluidic magnetophoresis device," *Lab on a Chip*, volume 11, number 11, pages 1902–1910, 2011, ISSN: 14730189. DOI: 10.1039/c0lc00656d (cited on page 106).

[140] A. S. Arbab, G. T. Yocum, L. B. Wilson, A. Parwana, E. K. Jordan, H. Kalish, and J. A. Frank, "Comparison of transfection agents in forming complexes with ferumoxides, cell labeling efficiency, and cellular viability," *Molecular Imaging*, volume 3, number 1, pages 24–32, 2004, ISSN: 15353508. DOI: 10.1162/1535350 04773861697 (cited on page 106).

[141] C. Stehning, · . B. Gleich, and J. Rahmer, "Simultaneous magnetic particle imaging (MPI) and temperature mapping using multi-color MPI," *International Journal on Magnetic Particle Imaging*, 2016, ISSN: 2365-9033 (cited on page 109).

[142] M. Möddel, C. Meins, J. Dieckhoff, and T. Knopp, "Viscosity quantification using multi-contrast magnetic particle imaging," *New Journal of Physics*, volume 20, number 8, 2018, ISSN: 13672630. DOI: 10.1088/1367-2630/aad44b (cited on page 109).

[143] J. Winand, "Optimization and Characterization of Magnetic Particle Mapping Using Magnetoelectric Sensors," Master's thesis, 2020 (cited on page 118).

[144] N. Lukat, "Zellldynamik und detektion magnetisch markierter zellen," de, PhD thesis, 2020 (cited on pages 128, 129).

[145] M. Yalaz, A. Teplyuk, G. Deuschl, and M. Hoft, "Dipole Fit Localization of the Deep Brain Stimulation Electrode Using 3D Magnetic Field Measurements," *IEEE Sensors Journal*, volume 20, number 16, pages 9550–9557, 2020, ISSN: 15581748. DOI: 10.1109/JSEN.2020.2988067 (cited on page 130).

[146] M. Yalaz, G. Deuschl, M. Butz, A. Schnitzler, A. K. Helmers, and M. Höft, "Investigation of magnetoelectric sensor requirements for deep brain stimulation electrode localization and rotational orientation detection," *Sensors*, volume 21, number 7, 2021, ISSN: 14248220. DOI: 10.3390/s21072527 (cited on page 130).

[147] S. Boyd and L. Vandenberghe, *Convex Optimization*. 2004. DOI: 10.1017/cbo9780511804441 (cited on pages 131, 132).

[148] S. Gazzola, P. C. Hansen, and J. G. Nagy, "IR Tools: a MATLAB package of iterative regularization methods and large-scale test problems," *Numerical Algorithms*, volume 81, number 3, pages 773–811, 2019, ISSN: 15729265. DOI: 10.1007/s11075-018-0570-7. arXiv: 1712.05602 (cited on page 133).

[149] Y. Wang, T. D. Onuta, C. J. Long, Y. Geng, and I. Takeuchi, "Colossal magnetoelectric effect induced by parametric amplification," *Applied Physics Letters*, volume 107, number 19, 2015, ISSN: 00036951. DOI: 10.1063/1.4935332 (cited on page 138).

[150] L. Y. Fetisov, D. A. Burdin, N. A. Ekonomov, D. V. Chashin, J. Zhang, G. Srinivasan, and Y. K. Fetisov, "Nonlinear magnetoelectric effects at high magnetic field amplitudes in composite multiferroics," *Journal of Physics D: Applied Physics*, volume 51, number 15, 2018, ISSN: 13616463. DOI: 10.1088/1361-6463/aab384 (cited on page 138).

[151] P. Durdaut, "Ausleseverfahren und rauschmodellierung für magnetoelektrische und magnetoelastische sensorsysteme," PhD thesis, November 2019. DOI: 10.13140/RG.2.2.17043.84009 (cited on page 139).

[152] M. Gerken, "Resonance line shape, strain and electric potential distributions of composite magnetoelectric sensors," *AIP Advances*, volume 3, number 6, 2013, ISSN: 21583226. DOI: 10.1063/1.4811369 (cited on page 139).

[153] S. Zabel, "Vom e-effekt zum sensorsystem," de, PhD thesis, 2018. [Online]. Available: https://macau.uni-kiel.de/receive/diss_mods_00026079 (cited on page 140).

[154] Z. Chu, C. Dong, C. Tu, Y. He, X. Liang, J. Wang, Y. Wei, H. Chen, X. Gao, C. Lu, Z. Zhu, Y. Lin, S. Dong, J. McCord, and N. X. Sun, "Voltage-Driven Nonlinearity in Magnetoelectric Heterostructures," *Physical Review Applied*, volume 12, number 4, 2019, ISSN: 23317019. DOI: 10.1103/PhysRevApplied.12.044001 (cited on page 140).

[155] B. Spetzler, J. Su, R. M. Friedrich, F. Niekiel, S. Fichtner, F. Lofink, and F. Faupel, "Influence of the piezoelectric material on the signal and noise of magnetoelectric magnetic field sensors based on the delta-E effect," *APL Materials*,

volume 9, number 3, 2021, ISSN: 2166532X. DOI: 10.1063/5.0042448 (cited on page 140).

[156] M. J. Brennan, I. Kovacic, A. Carrella, and T. P. Waters, "On the jump-up and jump-down frequencies of the Duffing oscillator," *Journal of Sound and Vibration*, volume 318, number 4-5, pages 1250–1261, 2008, ISSN: 10958568. DOI: 10.1016/j.jsv.2008.04.032 (cited on page 141).

[157] Y. Jia, J. Yan, K. Soga, and A. A. Seshia, "Parametric resonance for vibration energy harvesting with design techniques to passively reduce the initiation threshold amplitude," *Smart Materials and Structures*, volume 23, number 6, 2014, ISSN: 1361665X. DOI: 10.1088/0964-1726/23/6/065011 (cited on page 143).

E F A K U L T
S-UNIVERSITÄT ZU K
T K I E L